

A FIELD STUDY OF TURBULENT FLOWS IN SHALLOW GRAVEL-BED RIVERS

THÈSE N° 3393 (2005)

PRÉSENTÉE À LA FACULTÉ ENVIRONNEMENT NATUREL, ARCHITECTURAL ET CONSTRUIT

Institut des infrastructures, des ressources et de l'environnement

SECTION DE GÉNIE CIVIL

ÉCOLE POLYTECHNIQUE FÉDÉRALE DE LAUSANNE

POUR L'OBTENTION DU GRADE DE DOCTEUR ÈS SCIENCES

PAR

Mário Jorge Rodrigues Pereira da FRANCA

Ingénieur diplômé en Génie Civil et Maître en Hydraulique et Ressources Hydriques,
Instituto Superior Técnico, Lisboa, Portugal
et de nationalité portugaise

acceptée sur proposition du jury:

Prof. U. Lemmin, directeur de thèse
Prof. H. De Vriend, rapporteur
Prof. M. Parlange, rapporteur
Dr E. A. Terray, rapporteur

Lausanne, EPFL
2005

Ah, que ninguém me dê piedosas intenções!

(...)

Não sei por onde vou,

Não sei para onde vou,

Sei que não vou por aí.

José Régio in "Cântico Negro"

ACKNOWLEDGEMENTS

I wish to express my gratitude to:

- My supervisor, Ulrich Lemmin, who provided me excellent conditions and a great scientific environment for my research, for his patience, helpfulness and friendship.
- All the members of my PhD committee for their helpful comments and suggestions.
- Mustafa Altınakar who invited me to pursue a Ph.D. at the LHE, for his friendship, support and trust.
- Christophe Ancey for giving me the institutional framework as the director of the LHE.
- Włodzimierz Czernuszenko, for the fruitful discussions on the mean velocity profile, and for inviting me to a short stay in the Institute of Geophysics of the Polish Academy of Sciences (visit in the framework of the GEODEV project).
- Gene Terray, for his comments and discussions, for defying me into the wavelet world, for the hospitality when I visited Woods Hole and for allowing me to present my work to his group in the Woods Hole Oceanographic Institution.
- For the comments, discussions and suggestions contributing to improvements in the dissertation, Steve Thorpe, Tom Osborn (introduced me to the EMD), Huib de Vriend, Heidi Nepf (gave me the opportunity to present my work to her group in the MIT and provided me the valuable “blending height” suggestion), Wim Uijtewaal, Marc Parlange, Walter Graf, David Hurther, Fernando Porté-Agel and Emil Hopfinger.
- John Beck (Hydram-EPFL) for providing precious hydraulic and topographic information.
- LMS-EPFL for the use of the laboratory facilities in the riverbed gravel analysis.
- All the ones within the LHE which along these years collaborated with me and provided me a good working atmosphere: my good friend Baris Ozen, Lars Umlauf, Koen Blanckaert, Adhy Kurniawan, Laurent Glasson, Claude Perrinjaquet, René Fontanellaz, Barbara Tinguely, Yiquin Guan, Zhaosong Qu, Damien Bouffard, Ismail Albayrak, Cecilia Harvey, Adeline Amouroux, Philippe Aviolat, Sylvain Chesneau, Sébastien Rotté-Capet, Michel Teuscher, Jean-Marc Terraz, Steve Cochard, Sébastien Wiederseiner, Peter Vollmöller, Martin Rentschler.
- All the colleagues in the EPFL gravitation field who also contributed to a good spirit.
- The luso/brasilian/malayan/etc community in Lausanne, which helped me keeping up a good spirit (Rui, Cátia, Bruno, Intan, Janina, Luís, Ana, Marcelo, and many more).
- My good friend Pedro Manso, with whom it is a pleasure to share technical and personal problems.

Finally I thank my family and friends that in numerous ways helped me during my PhD, visiting me, calling, writing emails, letters, inviting me for weddings, etc...

Agradeço ao meu irmão Alberto e à Ana, pela sua amizade e encorajamento nas minhas decisões. À Luísa por me ter sempre apoiado, pelo seu carinho, por ter vindo comigo para a Suíça e por aturar o meu mau humor e negativismo quotidiano. Aos meus pais, a quem dedico este trabalho, por me incentivarem a esforçar-me por aquilo que gosto e em que acredito, e por serem um exemplo de como o empenho e a honestidade compensam na vida.

This research was only possible due to the support of the Portuguese Science and Technology Foundation (FCT/BD 6727/2001) and the Swiss National Science Foundation (2000-063818).

ABSTRACT

The study of turbulent flows has always been a challenge for scientists. Turbulent flows are common in nature and have an important role in several geophysical processes related to a variety of phenomena such as river morphology, landscape modeling, atmospheric dynamics and ocean currents. At present, new measurement and observation techniques suitable for fieldwork can be combined with laboratory and theoretical work in order to advance in the understanding of river processes.

In this Ph.D. dissertation, an Acoustic Doppler Velocity Profiler (ADVP) suspended from a deployable structure allowed the investigation of turbulent gravel-bed river flows. The ADVP, which was developed by the Laboratoire d'Hydraulique Environnementale (LHE), permits to obtain over the entire water depth, three-dimensional quasi-instantaneous information on the fluctuating velocity flow field in the production and inertial subranges of the spectral space. Improvements on the ADVP data quality were made with the implementation of a correction methodology for errors due to data aliasing. This reduced the range-velocity ambiguity in Doppler-based instruments.

The results presented in this dissertation contribute to the understanding of transport and mixing processes in river flows. They are based on three sets of field measurements made in gravel-bed rivers with blockage ratios of $h/D_{84} \approx 3.0$ and aspect ratios B/h between 23 and 32. The measurements were made during low-water periods. The fieldwork provided results on the mean and instantaneous velocity field.

The flow was divided into three inviscid vertical layers with different mean field and Reynolds stress characteristics: the roughness layer, the blending or intermediate layer and the surface layer. In the lower layers of the flow three types of mean velocity profile were found: mono-logarithmic, s-shaped due to bed perturbations and double-logarithmic downstream bed perturbations. The determination of the shear stress distribution for each of these profile types is studied. In double-log profiles, the friction velocity and roughness length determined for the outer logarithmic layer are required for the velocity profile parameterization. The s-shaped profiles are described by a tangent-hyperbolic function in the lower layers compatible with an external log layer. Limitations of 2D open-channel theories to parameterize the velocity distribution and to characterize the bottom drag are discussed. Bottom drag occurs in the predominant momentum direction. The direction changes as a function of the local bed forms. To estimate bottom drag one has to consider the actual momentum transport direction which varies with the flow depth.

The wall effect of the riverbank is visible until $y/h \approx 5$. Bottom topography produces important secondary mean motion in the flow. A permanent structure of the flow was described in the upper layers, near the surface ($z/h > 0.80$): the Surface Layer Organized Movement – SLOM. It is composed by local jets (CH regions) and by lower velocity regions (CL regions) associated with a compensatory secondary motion with streamwise vorticity. Lateral momentum transfer exists between adjacent CL and CH regions. In one river, the bed form presented signatures of possible streamwise ridges. All the turbulent characteristics of the flow respond to the periodic riverbed morphology. The strips were produced during high water events affecting river processes on the long-term. The D-shaped profiles are investigated. They relate to the CL regions and are formed where the velocity is lower near the surface. The maximum velocity is situated at around $z_{U_{max}}/\delta \sim 0.80$. The occurrence of D-shaped profiles shows a dependence on the local Froude number; the SLOM might be an inviscid response to the bed forms.

Two distinct approaches in the study of the turbulent velocity field were made: an analysis of the mean turbulence characteristics and the analysis of particular instantaneous features in the turbulent flow. The normal Reynolds stress distributions are anisotropic because streamwise turbulent intensity (TI) dominates the TKE (50 to 80% of the total energy with maximum at $z/h \approx 0.70$). Spanwise and vertical contributions vary along the flow depth. The surface and the

bottom layers exert a strong influence on the vertical TI profile inducing a parabolic distribution. Self-similarity of the flow is only found inside the blending layer. In the roughness layer all Reynolds shear stresses become equally important. Empirical formula established by previous authors to describe the Reynolds stress tensor components are analyzed. The diffusive terms in the TKE budget equation are negligible and consequently the pseudo-dissipation may be considered equal to the actual dissipation $\tilde{\epsilon} \approx \epsilon$. Production mostly happens inside the boundary layer and is mainly due to the gradients of the streamwise component. Dissipation is more widely spread in the flow with a maximum value near the bottom. Production and dissipation follow the exponential laws $e^{-5.1z/h}$ and $e^{-3.9z/h}$, respectively. The repartition of the flow energy through the eddy scales is studied and a characteristic curve is found having as parameters the scale corresponding to the peak energy (Λ_{\max}), and a dimensionless parameter representing the energy dispersion through the scales (σ^+). Empirical power laws are presented for the turbulence scales, Taylor (λ), Kolmogorov (η), integral (L), energetic (Λ) and mixing length (l_m). The relationship between the different scales is also studied.

With conditional sampling techniques, particular features of the turbulent velocity and their role in flow dynamics were described: detection and analysis of bursting packets inside the boundary layer and the study of the passage of large-scale uniform momentum regions (UMR), which here were called Streamwise Velocity Pulsation (SVP). Innovative tools are applied in the study of the instantaneous velocity measurements: wavelet decomposition and multiresolution analysis, empirical mode decomposition (EMD) and phase averaging based on the Hilbert transform.

SVP corresponds to a non-periodic passage of large-scale UMR with streamwise velocities alternately higher or lower than the mean. This phenomenon was identified and characterized. The SVP Strouhal number is within the range $0.13 < S_{\text{SVP}} < 0.32$ (defined with the local depth averaged velocity). A vertical linear phase shift of $\approx -3/4\pi$ of the front exists. The front has a first quarter moon shape with an apex at $z/h \approx 0.35$. It scales with h in the vertical and with $3.1-7.3h$ in the streamwise direction. In the lower layer the fronts have an average angle of 15° . In phase with the SVP, cycles of large-scale sweeps and ejections exist. Ejections dominate shear stress production with higher instantaneous amplitude and lower permanence. A periodic variation of the bottom drag is related nonlinearly with the SVP (direct effect). Due to the 3D bursting process triggered by the passage of an UMR, the bottom drag is enhanced (indirect effect). The SVP may be generated by the combined shedding effect produced by boulders which are randomly and widely spaced in the riverbed.

Several identical bursting packets composed of sequential ejections and sweeps ($\{x-z\}$ shear events) linked to spanwise vortical cells were visualized and characterized. The feedback of these was evaluated in the velocity profile, Reynolds stresses and TKE budget. These packets are highly energetic. The sampled bursting packets are independent. The time interval between packets is stable and the most probable value corresponds to a Strouhal number of $S_i = 2.5$ (defined with the local friction velocity). The bursting Strouhal number is $S_b = 12.5$. Fronts from large-scale high- and low-speed wedges are associated with the bursting packets. Near the bottom the fronts have a concave shape and an angle of 18° with the horizontal.

Key words: gravel-bed rivers; turbulent flow; river hydraulics; mean velocity profile; 3D mean velocity; acoustic Doppler velocity profiler (ADV); coherent structures; bursting processes; streamwise velocity pulsation (SVP)

RESUMO

Os escoamentos turbulentos têm sido desde sempre um desafio para a comunidade científica. Estes são comuns na natureza e têm um papel importante em processos geofísicos tais como morfologia fluvial, modelação de paisagens, dinâmica atmosférica e correntes oceânicas. Actualmente existem técnicas de investigação no terreno que, em conjunto com trabalho laboratorial e teórico, permitem analisar os processos de transporte e de mistura em rios.

Nesta tese investigaram-se escoamentos turbulentos em rios de leito de gravilha com um perfilador de velocidades acústico de efeito Doppler (Acoustic Doppler Velocity Profiler - ADVP). O ADVP foi desenvolvido no Laboratoire d'Hydraulique Environnementale e permite a medição 3D de um perfil quasi-instantâneo de velocidades. A frequência das medições feitas com o ADVP permite a visualização das regiões produtivas e de inércia nos espectros de energia das velocidades instantâneas. Apresenta-se um método de correcção de erros de dobragem, reduzindo a ambiguidade distância/velocidade comum a medições baseadas no efeito Doppler.

O escoamento é dividido em três camadas não-viscosas com diferentes distribuições de velocidades e de tensão tangencial de Reynolds: camada rugosa ($z/h < 0.20$), camada intermédia ($0.20 < z/h < 0.80$) e camada de superfície ($z/h > 0.80$). Três tipos de perfil de velocidades foram identificados: mono-logarítmico, em forma de “s” devido à inflexão do perfil de velocidades causada por perturbações no leito e duplamente logarítmico (2xlog) a jusante das perturbações no leito. Nos perfis 2xlog, a velocidade de arrastamento e a rugosidade absoluta correspondente à segunda camada limite são necessárias na descrição da distribuição de velocidades. Os perfis “s” são descritos por uma lei tangente-hiperbólica nas camadas inferiores, compatibilizada com uma lei logarítmica na camada exterior. O perfil de tensão tangencial correspondente aos três tipos de distribuição de velocidades é analisado. São discutidas limitações de teorias 2D na parametrização do perfil de velocidades e na determinação da tensão de arrastamento no fundo. A tensão de arrastamento é exercida na direcção predominante de transporte de quantidade de movimento, variável com as configurações de fundo e na vertical.

O efeito das margens dos rios é visível até uma distância normalizada de $y/h \approx 5$. As configurações de fundo produzem significativo escoamento secundário. Uma estrutura permanente do escoamento existente na camada de superfície ($z/h > 0.80$) foi identificada e descrita: movimento organizado na camada de superfície (Surface Layer Organized Motion - SLOM). Esta estrutura é constituída por zonas de velocidade superior à média (regiões CH) compensada por zonas de velocidade inferior à média (regiões CL), ambas associadas por um escoamento secundário de compensação de massa com vorticidade longitudinal. Entre as regiões CH e CL dá-se troca lateral de quantidade de movimento. No fundo de um dos rios investigados existem indícios de acumulação de sedimentos no sentido do escoamento que condicionam toda a estrutura média e turbulenta do escoamento. Estas configurações de fundo são produzidas em períodos de cheia condicionando o escoamento a longo prazo. Na vertical correspondente às regiões CL os perfis de velocidade têm a forma de “D”. Nestes, a velocidade máxima corresponde à profundidade $z/h \approx 0.80$. A ocorrência dos perfis “D” está relacionada com o número de Froude local, indicando que o SLOM pode ser uma resposta não-viscosa às formas de fundo.

Nesta tese duas abordagens são feitas ao estudo do campo instantâneo de velocidades: análise das características turbulentas médias do escoamento e análise de processos individuais nos sinais turbulentos de velocidade. A distribuição das tensões normais de Reynolds é anisotrópica: as intensidades turbulentas (IT) na direcção longitudinal dominam a produção de energia cinética turbulenta (ECT) – entre 50 e 80% da energia total com máximo valor a $z/h \approx 0.70$. As contribuições de IT vertical e transversal para a ECT variam ao longo da coluna de água. A superfície e o fundo influenciam marcadamente a distribuição de IT vertical induzindo nesta um perfil parabólico. A distribuição da tensão de Reynolds é semelhante apenas na camada intermédia. Dentro da camada rugosa, todas as tensões tangenciais de

Reynolds são igualmente importantes. Formulações empíricas estabelecidas por outros autores para a distribuição do tensor das tensões de Reynolds são analisadas. Os termos de difusão na equação de balanço da ECT são negligenciáveis e conseqüentemente a pseudo-dissipação pode ser considerada igual à dissipação real $\tilde{\varepsilon} \approx \varepsilon$. A produção turbulenta ocorre maioritariamente na camada limite e é devida principalmente aos gradientes da componente longitudinal da velocidade. A dissipação encontra-se mais dispersa pelo escoamento, com valor máximo junto ao fundo. A produção e a dissipação têm distribuições verticais exponenciais proporcionais a $e^{-5.1z/h}$ e $e^{-3.9z/h}$, respectivamente. A repartição da ECT pelas escalas energéticas é caracterizada por uma curva parametrizada com um valor de escala correspondente à energia máxima (Λ_{\max}) e um parâmetro adimensional representando a dispersão de energia pelas diversas escalas (σ^+). São apresentadas leis empíricas de potências de z/h para a distribuição das seguintes escalas turbulentas: micro-escala de Taylor (λ), Kolmogorov (η), integral (L), energética (Λ) e comprimento de mistura (l_m).

Foram utilizadas diversas técnicas de amostragem condicionada do sinal instantâneo de velocidade para estudar determinados fenómenos instantâneos e o seu papel na dinâmica turbulenta do escoamento: detecção e análise de grupos de eventos no plano $\{x-z\}$ dentro da camada limite e passagem de regiões de quantidade de movimento uniforme (RQMU), intitulada pulsação de velocidade longitudinal (Streamwise Velocity Pulsation - SVP). Para o estudo do sinal instantâneo de velocidades aplicaram-se ferramentas matemáticas inovadoras no estudo de mecânica dos fluidos: decomposição e análise multiresolucional recorrendo a onduletas, decomposição empírica em modos (Empirical Mode Decomposition – EMD) e determinação da média na fase recorrendo à transformada de Hilbert do sinal instantâneo.

A SVP corresponde à passagem não periódica mas regular de RQMU de grande escala onde as velocidades são maiores ou menores que a média. O número de Strouhal da SVP encontra-se no intervalo $0.13 < S_{SVP} < 0.32$ (definido com velocidade média na coluna de água). Existe uma diferença de fase vertical na frente de uma RQMU de $\approx 3/4\pi$. Uma frente de SVP tem a forma de um quarto crescente com o vértice situado a $z/h \approx 0.35$. A RQMU tem dimensão vertical igual a h e dimensão longitudinal entre 3.1 e $7.3h$. As frentes de RQMU fazem em média um ângulo com a horizontal de 15° . Verificou-se que, em fase com um ciclo de SVP, existe um ciclo de varrimentos e ejeções abrangendo toda a coluna de água. Existe uma resposta não-linear da tensão de arrastamento associada a um ciclo de SVP: efeito directo. Devido ao processo tri-dimensional de desencadeamento de eventos induzido pela passagem de uma RQMU, a tensão de arrastamento é influenciada: efeito indirecto de SVP. A eventual origem da SVP está na aglomeração de vórtices desencadeados pelas diversas saliências existentes no fundo do rio.

Identificaram-se e caracterizaram-se vários grupos idênticos de eventos tangenciais no plano $\{x-z\}$ idênticos, compostos por uma sequência de ejeções e varrimentos ligados entre si por vórtices de eixo transversal. São analisadas as implicações da ocorrência destes grupos no perfil de velocidades instantâneo, nas tensões de Reynolds e no balanço da ECT. Estes grupos de estruturas são muito energéticos e verificou-se que são independentes uns dos outros. O intervalo de tempo mais provável entre diferentes grupos corresponde a um número de Strouhal de $S_i = 2.5$ (definido com a velocidade de arrastamento). O número de Strouhal correspondente à duração dos grupos de eventos é de $S_b = 12.5$. Associados aos grupos de eventos, observa-se uma frente correspondente à separação entre duas RQMU com velocidades maiores e menores que a média. Estas frentes têm uma forma côncava junto ao fundo e fazem um ângulo com a horizontal de 18° .

Palavras-chave: rios com leito de gravilha; escoamento turbulento; hidráulica fluvial; perfil médio de velocidade; velocidade média 3D; perfilador de velocidades acústico de efeito Doppler (ADVP); estruturas coerentes; desencadeamento de eventos tangenciais; pulsação da velocidade longitudinal (SVP)

RESUMÉ

L'étude des écoulements turbulents représente toujours un défi pour la communauté scientifique. De nombreuses études ont mis en évidence l'importance des écoulements turbulents pour les fluides géophysiques. Ainsi, la morphologie fluviale, la modélisation des paysages, la dynamique atmosphérique ou les courants océaniques peuvent tous être influencés par des écoulements turbulents. Actuellement, les techniques de mesures et observations in situ, couplées avec des travaux expérimental et théorique, permettent d'analyser certains processus de transport et de mélange dans les rivières.

Dans cette thèse, l'étude des écoulements turbulents dans les rivières au lit de gravier a été effectuée grâce à un profileur acoustique à effet Doppler à haute résolution (Acoustic Doppler Velocity Profiler - ADVP). Cet appareil, développé au Laboratoire d'Hydraulique Environnementale (LHE), permet la mesure en 3D d'un profil quasi-instantané de vitesses avec des fréquences de mesures largement suffisantes pour visualiser les régions d'inertie et de production du spectre d'énergie. Afin de réduire l'ambiguïté distance/vitesse inhérentes aux mesures Doppler une méthode de correction des erreurs de crénelage a été développée.

Les résultats présentés dans cette thèse se divisent en deux groupes : champ des vitesses moyennes et champ des vitesses instantanées. Les relations de blocage des écoulements étudiés étaient $h/D_{84} \approx 3.0$ et le rapport largeur/profondeur (B/h) se situait entre 23 et 32. Les mesures ont été faites pendant des périodes d'écoulement peu profond.

L'écoulement peut être divisé en trois couches non-visqueuses caractérisées par des différences au niveau des distributions de vitesses et des tensions tangentielles de Reynolds: la couche rugueuse ($z/h < 0.20$), la couche intermédiaire ($0.20 < z/h < 0.80$) et la couche de surface ($z/h > 0.80$). On a identifié et caractérisé trois types de profils de vitesse : mono-logarithmique (monolog), en forme de "s" dû à l'inflexion du profil causé par une perturbation du fond et double-logarithmique (2xlog) à l'aval d'une perturbation du fond. La distribution de la tension tangentielle de Reynolds pour chaque un de ces profils est analysée. Pour les profils 2xlog on a besoin des paramètres de rugosité de la deuxième couche limite pour la description de la distribution de vitesses. Les profils "s" sont décrits par une loi tangente hyperbolique dans les couches inférieures de l'écoulement compatible avec une loi logarithmique dans la couche extérieure. Les limitations des théories bidimensionnelles pour la description du profil de vitesse et la détermination des effets de frottement au fond sont discutées. Le frottement au fond est exercé selon la direction prédominante du transport de quantité de mouvement qui varie avec la profondeur et la forme du fond.

L'effet de paroi exercé par les berges est visible jusqu'à une distance normalisée de $y/h \approx 5$. La morphologie du fond génère un écoulement secondaire significatif. On a identifié et décrit une structure permanente de l'écoulement existant dans la couche supérieure de l'écoulement ($z/h > 0.80$) : mouvement organisé dans la couche de surface (Surface Layer Organized Motion - SLOM). Cette structure est constituée de jets localisés (régions CH) et par des zones de vitesse inférieure à la moyenne (régions CL) associées à un écoulement secondaire de compensation avec vorticités longitudinales. Entre les régions CH et CL on vérifie un échange latéral de quantité de mouvement. Dans le fond d'une des rivières étudiées on a des indices de structures de fond longitudinales conditionnant toute la structure moyenne et turbulente de l'écoulement. Ces configurations de fond produites en périodes de crues, vont postérieurement conditionner à long terme l'écoulement. Correspondant aux régions CL, les profils de vitesse ont la forme en "D". En cela, la vitesse maximale correspond à la profondeur $z/h \approx 0.80$. L'occurrence des profils "D" est liée avec le régime d'écoulement local, ce qui justifie la réponse non-visqueuse du SLOM aux formes de fond.

Dans cette thèse, on étudie le champ instantané de vitesses en regardant les caractéristiques moyennes de la turbulence et des processus individuels dans les signaux de vitesses turbulentes. La distribution des termes diagonaux du tenseur de Reynolds est anisotrope: les intensités turbulentes (IT) selon la direction de l'écoulement dominant la production

d'énergie cinétique turbulente (ECT) – entre 50 et 80% de l'énergie totale avec la valeur maximale à $z/h \approx 0.70$. Les contributions des IT verticale et transversale pour l'ECT changent selon la verticale. La surface et le fond influencent la distribution verticale de l'IT induisant un profil parabolique. La distribution de la tension de Reynolds est similaire seulement dans la couche intermédiaire. Dans la couche rugueuse, tous les autres termes du tenseur de Reynolds deviennent également importants. On analyse des formules empiriques établies par d'autres chercheurs pour la distribution du tenseur des tensions de Reynolds. Les termes de diffusion dans l'équation de l'ECT sont négligeables et par conséquent la pseudo-dissipation peut-être considérée égale à la dissipation réelle $\bar{\varepsilon} \approx \varepsilon$. La production turbulente existe en majorité dans la couche limite et est due principalement aux gradients de vitesse longitudinale. La dissipation est épanouie par l'écoulement, avec la valeur maximale près du fond. La production et la dissipation ont des distributions verticales proportionnelles à $e^{-5.1z/h}$ et $e^{-3.9z/h}$. La répartition de ECT par des échelles énergétiques de l'écoulement est caractérisée par une courbe avec comme paramètres l'échelle la plus énergétique (Λ_{\max}) et un paramètre adimensionnel représentant la dispersion de l'énergie par les échelles (σ^+). On présente des lois empiriques pour la description des échelles turbulentes suivantes: micro-échelle de Taylor (λ), Kolmogorov (η), intégrale (L), énergétique (Λ) et longueur de mélange (l_m).

On utilise plusieurs techniques d'échantillonnage conditionné d'un signal instantané de vitesse pour isoler des phénomènes et étudier son rôle dans la dynamique turbulente de l'écoulement, notamment: détection et analyse des groupements des événements de cisaillement $\{x-z\}$ dans la couche limite et passage des régions de quantité de mouvement uniforme (RQMU) nommé pulsation de vitesse longitudinale (Streamwise Velocity Pulsation - SVP). Des outils mathématiques innovateurs en mécanique des fluides ont été appliqués: décomposition par ondelettes, décomposition empirique en modes (Empirical Mode Decomposition – EMD) et moyenne dans la phase en utilisant la transformé d'Hilbert.

La SVP correspond au passage non-périodique de RQMU à grande échelle où les vitesses sont inférieures et supérieures à la moyenne. Le nombre de Strouhal de la SVP est dans l'intervalle $0.13 < S_{SVP} < 0.32$ (défini avec la vitesse moyenne dans le profil). Il y a une différence de la phase verticale d'environ $\approx 3/4\pi$. Les fronts de SVP ont la forme de « croissant de lune » avec le point d'inflexion situé à $z/h \approx 0.35$. La RQMU a une dimension verticale h et une dimension longitudinale $3.1-7.3h$. Les fronts de RQMU font en moyenne un angle avec l'horizontale de 15° . On observe en phase avec la SVP un cycle d'éjections et de balayages sur toute la hauteur de l'écoulement. On vérifie une réponse non-linéaire du frottement au fond associé à la SVP: effet direct. Dues au processus 3D de déclenchement des événements induit par le passage d'une RQMU, le frottement au fond est influencé: effet indirect. L'éventuelle origine de la SVP est l'agglomération de tourbillons déclenchés par des divers obstacles au fond de la rivière.

Plusieurs groupements identiques des événements de cisaillement dans le plan $\{x-z\}$, constitué par une séquence d'éjections et balayages connectées par des tourbillons d'axe transversal, ont été identifiés et caractérisés. On analyse les implications de ces groupes sur le profil instantané de vitesse, les tensions de Reynolds et dans le bilan de ECT. Ces groupements sont très énergétiques et indépendants. L'intervalle de temps le plus probable entre ces groupements correspond à un nombre de Strouhal de $S_f = 2.5$ (défini avec la vitesse de frottement). Le Strouhal correspondant à la durée d'un groupement est de $S_b = 12.5$. Associé aux groupements d'interactions, il existe un front de séparation entre deux RQMU avec des vitesses inférieures et supérieures à la moyenne. Ces fronts ont une forme concave et un angle de 18° avec l'horizontal près du fond.

Mots-clés: rivières à lit de gravier; écoulement turbulent; hydraulique fluviale; profil de vitesse moyenne; vitesse moyenne 3D; profileur vélocimétrique acoustique Doppler de haute résolution (ADVP); structures cohérentes; processus de déclenchement des événements de cisaillement; pulsation de vitesse longitudinale (SVP)

TABLE OF CONTENTS

1. Introduction

2. Instrumentation and methods

- 2.1 Methods and field measurements
- 2.2 Eliminating velocity aliasing in acoustic Doppler velocity profiler data

3. Fieldwork

- 3.1 Mean streamwise velocity in gravel-bed river flows
- 3.2 3D mean velocity distribution in gravel-bed rivers
- 3.3 The occurrence of s-shaped velocity profiles in gravel-bed river flows
- 3.4 Flow resistance characterization in shallow gravel-bed rivers
- 3.5 Streamwise Velocity Pulsation (SVP) in gravel-bed rivers
- 3.6 Boundary layer bursting packets associated with high- and low-speed wedges detected through a wavelet multiresolution analysis
- 3.7 Evaluation of energetic scales in turbulent gravel-bed rivers based on wavelet analysis
- 3.8 TKE budget analysis in gravel-bed river flow

4. Conclusions

- 4.1 Main results
- 4.2 Suggestions for future research

A. Appendices

- A.1 A field study of extremely rough, three-dimensional river flow (conference paper)
- A.2 Flow dynamics over a gravel riverbed (conference paper)
- A.3 Cross-section periodicity of turbulent gravel-bed river flows (conference paper)
- A.4 Annex to Subchapter 3.2
- A.5 Annex to Subchapter 3.4
- A.6 Curriculum Vitae

1. INTRODUCTION

1	MOTIVATION	1.1
2	FRAMEWORK	1.1
2.1	Introduction	1.1
2.2	ADVP – Acoustic Doppler Velocity Profiler	1.2
2.3	Mean velocity field	1.2
2.4	Fluctuating velocity field	1.3
3	OBJECTIVES	1.4
4	TEXT ORGANIZATION	1.5
	REFERENCES	1.5

1 MOTIVATION

This dissertation presents a study of turbulent flow in shallow gravel-bed rivers. Shallow river flows are characterized by large aspect ratios (B/h , where B is the river width and h the water depth) and are usually described by 2D theories where the flow is depth averaged. However, with low blockage ratios (h/D , where D is a characteristic gravel diameter), shallow water 2D assumptions are no longer valid since the form effect changes the flow structure and 3D turbulent effects are produced. The three-dimensionality of shallow flows and the limitations of 2D theories are still an important topic in fluid mechanics. Some of the present results have similarities with large-scale geophysical shallow flows where bed forms are important such as in atmospheric and oceanic flows around obstacles.

Better prediction tools of sediment transport and river dynamics processes are needed to provide optimal river management decisions. Presently, well-controlled laboratory experiments or numerical simulations are the main source of information on open-channel turbulence and are used in the interpretation of river phenomena. However, laboratory open-channel studies are typically carried out under idealized conditions of uniform flow and flat beds with a fairly homogeneous bed roughness distribution rarely found in rivers. Thus, discrepancies are observed between concepts used in routine engineering applications and actual field measurements.

Few field studies have been made in fluvial hydraulics mainly due to the lack of adequate instrumentation. However, these measurements are essential to confirm hypothesis and models used regularly by engineers. Field observations of natural processes allow us to identify and characterize unknown or lesser known features, and consequently upgrade the existing knowledge. The research deals with the turbulence mechanisms closely related to water quality, sediment transport and river morphology.

2 FRAMEWORK

2.1 Introduction

Ever since turbulence as a research topic was introduced by Reynolds in 1883, many investigations have been made on the subject. Nevertheless, turbulence still constitutes a challenge given its complexity and the variety of phenomena involved.

In fluvial hydraulics research, field data are of major importance. Recent publications on field studies provide some information on certain flow features in rivers or artificial channels (AC). These studies analyze mean velocities, turbulence intensities, shear stresses, bed shear, friction velocity, roughness parameters and velocity spectra (González et al. (1996-AC), Smart (1999) and Babaeyan-Koopaei et al. (2002)). Powell et al. (1999-AC) observed a strong variation of the bed-load transport along the cross section. Nikora and Smart (1997) studied the vertical distribution of turbulent energy dissipation and characteristic turbulent scales. Nikora and Goring (2000-AC) investigated turbulence feature differences of weakly mobile and fixed gravel bed cases. Buffin-Bélanger et al. (2000a) and Hurther et al. (2002) documented the existence of coherent structures in rivers and their influence on transport and mixing. Buffin-Bélanger and Roy (1998), Tritico and Hotchkiss (2005) and Tritico et al. (2002) analyzed the turbulence structure in the wake of obstructions. Roy et al. (2004) described and characterized flow structures present in gravel-bed rivers.

2.2 ADVP – Acoustic Doppler Velocity Profiler

The ADVP (Acoustic Doppler Velocity Profiler) has been used in several laboratory and field measurements due to the flexibility of the instrument configuration (Lemmin and Rolland (1997) and Hurther et al. (2002)). Acoustic Doppler instruments are widely applied in water studies as well as in meteorology (Doviak and Zrnic 1993). However certain limitations remain due to the range-velocity ambiguity problem (Lhermitte 1983), leading to aliasing data spikes. Recent proposals to solve the ambiguity were presented by Joe and May (2003), Holleman and Beekhuis (2003) and Goring and Nikora (2002). James and Houze (2001) presented an overview of the up-to-date developments in dealiasing techniques applied to weather radar measurements.

2.3 Mean velocity field

One of the main topics in the study of turbulent geophysical flows is the form of the velocity profile. Recently, Wosnik et al. (2000) presented an extension of the classic analysis of the mean velocity profile in the streamwise direction of open-channel flows. Some remarks can be made: the logarithmic longitudinal mean velocity profile is present to some extent; the inertial subrange in the spectral space of the turbulence domain is also present; there is an influence from the sidewall drag on the vertical distribution of the velocity which indicates that the two-dimensional concept may not be applicable to all the cross sections since significant scattering of the equivalent roughness parameter is observed.

In shallow gravel-bed rivers the mean velocity in the lower regions of the flow assumes two kinds of profiles, logarithmic and s-shaped (Marchand et al. (1984) and Bathurst (1988)). The wake effect formed by the presence of bed forms and boulders is responsible for the delay effects observed in the velocity profiles of gravel-bed rivers (Robert et al. (1992), Nelson et al. (1993), Baiamonte et al. (1995), Buffin-Bélanger and Roy (1998) and Carravetta and Della Morte (2004)). Katul et al. (2002) investigated the similarity between the inflected profiles in atmospheric flows above canopy and the s-profiles in river flows. Downstream singular obstacles, the velocity distribution gradually reacquires the log-shape in the inner layer, but the wake effect may produce a second boundary layer (Chriss and Caldwell (1982), Lueck and Lu (1997) and Sanford and Lien (1999)). Both boundary layers of this transitory type of profile have a logarithmic distribution. The shear controlling the inner log layer is due to the bottom drag, whereas the shear from the outer log layer is due to the upstream bed form (Chriss and Caldwell (1982), Lueck and Lu (1997) and Sanford and Lien (1999)).

Nikora and Smart (1997) referred to a three-dimensional inner region of the flow where deviations from the log-law occur as the roughness sublayer. Nevertheless, a log layer can be found in the majority of the velocity profiles (Nikora and Smart (1997) and Smart (1999)).

The resistance parameterization of rivers is also an open subject in environmental fluid mechanics. Biron et al. (2004) recently presented an analysis of the best methods to evaluate bed shear stress from simple measurements. Another feature of the mean velocity distribution observed in shallow open-channel flows is the velocity dip in the upper layers. This deviation from the logarithmic mean velocity profile is called the D-shaped profile, and has already been described by Cardoso et al. (1989), Ferro and Baiamonte (1994) and Yang et al. (2004).

2.4 Fluctuating velocity field

The modelling of hydraulic flows with complex large-scale bed forms is still difficult. Random distribution of large gravel grains and low blockage ratios provide additional problems in turbulence closure methods due to the complex geometry and three-dimensionality (Nicholas (2001) and Rodi (1984)). Nevertheless, several attempts have been made to include randomly distributed bed-forms in turbulence models, mainly in cases with high blockage ratios (Czernuszenko and Rylov 2004). Actual river measurements of the turbulent mean characteristics such as Reynolds stress tensor, turbulence scales and TKE budget components will allow complementing some of the closure and boundary condition gaps in turbulence modelling.

Fluctuations of flow velocity are responsible for sediment suspension and pollutant dispersion processes in river flows. According to Chassaing (2000), physically coherent motion exists when turbulent structure properties (geometric, cinematic and dynamic) change slowly with respect to their representative scale domain. Coherent structures are macroscale organized features belonging to the productive range of the spectral space. Coherent structures are formed typically in shear zones such as the bottom layer, and their generation is due to the interaction between large-scale and small-scale uniform momentum regions, known as the bursting process (Nakagawa and Nezu (1981) and Adrian et al. (2000a)). The mean field transports coherent structure properties.

Ashworth et al. (1996) summarized the main research that was done on coherent structures. From 33 studies presented, only seven correspond to field studies and of those, five relate to turbulence in estuaries and two to rivers. Hinze (1975), Yalin (1992), Nezu and Nakagawa (1993), Holmes et al. (1998), Métais and Lesieur ed. (1989) and Chassaing (2000) deal with coherent structures. Knowledge about the dynamics of coherent structures in rivers is very limited.

Coherent structures dominated by sweeps and ejections are found over the entire water depth (Hurther and Lemmin 2000). A link exists between the bursting process and surface boils near the surface which is an active layer for gas transfer (Jackson (1976), Kumar et al. (1998), Hurther and Lemmin (2000), Troiani et al. (2004) and Yoshida and Nezu (2004)); burst motions transport turbulent kinetic energy to the surface creating active zones for gas transfer. For shallow rivers, the inviscid response of the flow to bottom roughness is visible in the free surface. An interaction between the bottom-generated structures and the air-water transfer in the surface is expected. It is accepted that coherent structures distribute particles and pollutants across the whole water column much faster than small-scale turbulence (Falco (1977) and Hurther et al. (2002)). Cellino and Lemmin (2004) demonstrated the importance of ejection and sweep events in sediment suspension and transport.

Large- and small-scale coherent motion within the coherent structure range can still be distinguished. Large-scale motion typically scales with multiples of the dimension of the boundary layer (eddies scaling with the flow depth in open-channel flows), whereas small-scale motion, with parcels of the boundary layer (eddies scaling with dimensions comparable with the roughness sizes). Each of these groups acts differently but eventually jointly in the flow energy balance.

The existence of large-scale uniform momentum regions at low frequencies in gravel bed flows was reported by: Williams et al. (1989), Kirkbride and Ferguson (1995), Ferguson et al. (1996), Buffin-Bélanger et al. (2000b), Roy et al. (2004) and Hofland (2004). Interaction between these large-scale regions and small-scale coherent motion is accepted (Lu and Willmarth (1973), Brown and Thomas (1977), Antonia et al. (1990), Nakagawa and Nezu (1981) and Adrian et al. (2000a)). They may dominate instantaneous velocity signals and thus interfere with practical data evaluation such as discharge measurements and sediment transport processes (Dinehart 1999). The implication of low-frequency large-scale uniform momentum regions on the turbulent structure of the flow is an open research topic. Useful information is needed on the interaction of large- and small-scale processes.

Conditional statistics techniques have been developed recently which can be applied to instantaneous velocity samples (Antonia and Atkinson (1973), Nakagawa and Nezu (1977), Hurther and Lemmin (2000) and Adrian et al. (2000b)).

3 OBJECTIVES

This dissertation has two main objectives: the verification of existing theories which practitioners of river engineering use on a regular basis, and the observation and characterization of unknown or lesser known processes in gravel-bed rivers, where bed forms play an important role. This investigation will make use of detailed field measurements. Advances in the understanding of geophysical processes are only possible with observations made in natural environments. New observation techniques allow discovering new processes, which in turn require laboratory and numerical research for their verification. The investigation of basic processes is essential in order to understand these complex geophysical phenomena.

The present work on turbulent gravel-bed river flows seeks to contribute to the fluid mechanics domain, with results in the mean and instantaneous velocity field. The aims of the mean field analysis are:

- Validation of the 2D concept on mean velocity profile parameterization, assuming that the longitudinal plane shear stress determines the bottom drag.
- Validation and limitations of the logarithmic-law concept to represent the velocity distribution in the profile. Identification and eventual parameterization of different velocity distributions caused by local effects.
- Determination of the influence of riverbank drag, bed forms and bed roughness in the mean flow structure.
- Evaluation of the best form to define the bottom equivalent roughness parameter as a function of the local river conditions.
- Verification of organized and permanent secondary motion identifying possible local causes and consequences. Determination of 3D permanent features of the flow with their typical scales and the influence on transport and mixing processes. Interaction with the turbulent structure of the flow will be assessed.
- Study of the division of the flow depth with respect to fluid mechanics.
- Interaction between 3D organized flow and actual morphological structure at the river boundaries.

The turbulent flow is investigated either by analysis of temporal mean turbulent characteristics of the flow or by analysis of individual momentary features that contribute to flow dynamics. This study proposes to make the following contributions to the turbulent velocity field:

- Verification of the actual theories on the vertical distribution of such turbulence parameters as Reynolds stress tensor and cross-correlation factors. Determination of new trends and distribution forms resulting from local effects.
- Estimates of the TKE budget terms and their characterization in terms of turbulent flow dynamics; qualitative and quantitative study of the TKE distribution in the profile and contribution to the modelling of empirical results.
- Analysis of the energy repartition through the eddy scales present in the flow and distribution of the main turbulence scales, namely: Taylor microscale, Kolmogorov, integral and energetic scales. Determination of the relationship between local conditions and the scale distribution.

- Study of the distribution of such mixing parameters in the flow as the eddy viscosity and mixing length.
- Verification of the concepts on coherent structure dynamics and associated bursting processes identified and studied by previous researchers in open-channel laboratory studies.
- Detection, reconstruction and characterization of 3D coherent motion in the instantaneous velocity field and verification of its impact on turbulence dynamics, namely the contribution to the Reynolds stress tensor, to the transport and mixing processes and to the TKE total budget.
- Geometric definition of typical coherent motion, namely scales and spatial distribution within the 3D flow field. Analysis of the persistence and duration of coherent motion in the flow.
- Identification of the relationship between coherent motions of different scales.
- Interaction between the morphology and turbulent features.

New mathematical tools are applied to river hydraulics research, such as wavelets multiresolution analysis (Fargé (1992) and Fofoula-Georgiou and Kumar (1994)), and phase averaging techniques based on the signal Hilbert transform and Empirical Mode Decomposition (EMD) (Huang et al. (1998) and Huang et al. (1999)).

4 TEXT ORGANIZATION

This Ph.D. dissertation is composed of four major chapters:

- 1) The introduction gives details of the motivation, the research subjects and the objectives.
- 2) The second chapter describes the methods used in the research: the field measurements and instrumentation (2.1); and presentation of a dealiasing technique for the improvement and elimination of aliasing errors from the ADV data (2.2).
- 3) In the third chapter, the 3D ADV field data are analyzed in terms of mean and instantaneous velocity fields. Eight subchapters were elaborated, some in the form of scientific papers. Subchapters 3.1 to 3.4 analyze the mean velocity field and subchapters 3.5 to 3.8, the instantaneous velocity field.
- 4) The main conclusions of the research are summarized in 4.1, and ideas for future field and laboratory research are given in 4.2.

Three scientific articles published in conference proceedings can be found in the appendices. They provide complementary information to the main chapters. In the subchapters, written as articles, the necessary theoretical and experimental framework has been given. Therefore information about methods and field measurements may be repeated. A cover page gives a summary of the contents of each subchapter. Since certain subchapters have already been submitted, some formatting inconsistency will appear.

REFERENCES

- Adrian R.J., Meinhart C.D. and Tomkins C.D. (2000a), Vortex organization in the outer region of the turbulent boundary layer, *J. Fluid Mech.*, 422, 1-54.
- Adrian R.J., Christensen K.T. and Liu Z.-C. (2000b), Analysis and interpretation of instantaneous turbulent velocity fields, *Exper. Fluids*, 29, 275-290.

- Antonia R.A. and Atkinson J.D. (1973), High-order moments of Reynolds shear stress fluctuations in a turbulent boundary layer, *J. Fluid Mech.*, 58(3), 581-593.
- Antonia R.A., Bisset D.K. and Browne L.W.B. (1990), Effect of Reynolds number on the topology of the organized motion in a turbulence boundary layer, *J. Fluid Mech.*, 213, 267-286.
- Ashworth P.J., Bennett S.J., Best J.L. and McLelland S.J., ed. (1996), *Coherent flow structures in open channels*, John Wiley and Sons Ltd., West Sussex (UK).
- Babaeyan-Koopaei K., Ervine D.A., Carling P.A. and Cao Z. (2002), Velocity and turbulence measurements for two overbank flow events in river Severn, *J Hydr. Eng.* 128(10), 891-900.
- Baiamonte G., Giordano G. and Ferro V., (1995), Advances on velocity profile and flow resistance law in gravel bed rivers. *Excerpta*, 9, p. 41.
- Bathurst J.C. (1988), Velocity profile in high-gradient, boulder-bed channels. *Proc. Int. Conf. Fluv. Hydr.*, Budapest (Hungary).
- Biron P.M., Robson C., Lapointe M.F. and Gaskin S.J. (2004), Comparing different methods of bed shear stress estimates in simple and complex flow fields, *Earth Surf. Proc. and Landforms*, 29, 1403-1415.
- Brown G.L. and Thomas A.S.W. (1977), Large structure in a turbulent boundary layer, *Phys. Fluids*, 20(10), s243-252.
- Buffin-Bélanger T. and Roy A.G. (1998), Effects of a pebble cluster on the turbulent structure of a depth-limited flow in a gravel-bed river, *Geomorphology*, 25, 249-267.
- Buffin-Bélanger T., Roy A.G. and Kirkbride A.D. (2000a), On large-scale flow structures in a gravel-bed river, *Geomorphology*, 32, 417-435.
- Buffin-Bélanger T., Roy A.G. and Kirkbride A.D. (2000b), Vers l'intégration des structures turbulentes de l'écoulement dans la dynamique d'un cours d'eau à lit de graviers, *Géogr. Phys. Et Quaternaire*, 54(1), 105-117.
- Cardoso A.H., Graf W.H. and Gust G. (1989), Uniform flow in a smooth open-channel, *J. of Hydr. Res.*, 27(5), 45-57.
- Carravetta A. and Della Morte R. (2004), Response of velocity to a sudden change of the bed roughness in sub critical open channel flow, *Proc. Riverflow 2004*, Naples (Italy).
- Cellino M. and Lemmin U. (2004), Influence of coherent flow structures on the dynamics of suspended sediment transport in open-channel flow, *J. Hydr. Eng.*, 130(11), 1077-1088.
- Chassaing P. (2000), *Turbulence en mécanique des fluides*, Cépadués-Éditions, Toulouse (France).
- Chriss T.M. and Caldwell D.R. (1982), Evidence for the influence of form drag on bottom boundary layer flow, *J. Geoph. Res.*, 87 (C6), 4148-4154.
- Czernuszenko W. and Rylov A. (2004), 3D turbulent flow over irregular bed surfaces, *Proc. Riverflow 2004*, Naples (Italy).
- Dinehart R.L. (1999), Correlative velocity fluctuations over a gravel river bed, *Water Resour. Res.*, 35(2), 569-582.
- Doviak R.J. and Zrnic D.S. (1993), *Doppler radar and weather observations*, Academic Press, San Diego (USA).
- Falco R.E. (1977), Coherent motions in the outer region of turbulent boundary layers, *Phys. Fluids*, 20(10), s124-s132.

- Fargé M. (1992), Wavelet transforms and their applications to turbulence, *Annu. Rev. Fluid. Mech.*, 24, 395-458.
- Ferguson R.I., Kirkbride A.D. and Roy A.G. (1996), Markov analysis of velocity in gravel-bed rivers, *in* Coherent flow structures in open channels, ed. Ashworth P.J., Bennett S.J., Best J.L. and McLelland S.J., John Wiley and Sons Ltd., West Sussex (UK).
- Ferro V. and Baiamonte G. (1994), Flow velocity profiles in gravel-bed rivers, *J. Hydr. Eng.*, 120(1), 60-80.
- Foufoula-Georgiou E. and Kumar P. (1994), *Wavelets in geophysics*. Academic Press, San Diego (USA).
- González J.A., Melching C.S. and Oberg K.A. (1996), Analysis of open-channel velocity measurements collected with an acoustic Doppler currents profiler, *Proc. 1st Int. Conf. New/Emerging Concepts for Rivers*, Chicago (USA).
- Goring D.G. and Nikora V.I. (2002), Despiking acoustic Doppler velocimeter data, *J. Hydr. Eng.*, 128(1), 117-126.
- Hinze J.O. (1975), *Turbulence*, 2nd edition, McGraw-Hill Inc, (USA).
- Hofland B. and Booij R.R. (2004), Measuring the flow structures that initiate stone movement, *Proc. Riverflow 2004*, Naples (Italy).
- Holleman I. and Beekhuis H. (2003), Analysis and correction of dual PRF velocity data, *J. Atmosph. Ocean. Technol.*, 20, 443-453
- Holmes P., Lumley J.L. and Berkooz G. (1996), *Turbulence, coherent structures, dynamical systems and symmetry*, Cambridge University Press (UK).
- Huang N.E., Shen Z., Long S.R., Wu M.C., Shih H.H., Zheng Q., Yen N.C., Tung C.C. and Liu H.H. (1998), The empirical mode decomposition and the Hilbert spectrum for nonlinear and non-stationary time series analysis, *Proc. R. Soc. Lond. A*, 454, 903-995.
- Huang N.E., Shen Z. and Long S.R. (1999), A new view of nonlinear water waves: the Hilbert spectrum, *Ann. Rev. Fluid Mech.*, 31, 417-457.
- Hurther D. and Lemmin U. (2000), Shear stress statistics and wall similarity analysis in turbulent boundary layers using a high-resolution 3-D ADV, *IEEE J. Oc. Eng.*, 25(4), 446-457.
- Hurther D., Lemmin U. and Blanckaert K. (2002), A field study of transport and mixing in a river, using an acoustic Doppler velocity profiler *Proc. Riverflow 2002*, Louvain-la-Neuve (Belgium).
- Jackson R.G. (1976), Sedimentological and fluid-dynamic implications of the turbulent bursting phenomenon in geophysical flows, *J. Fluid Mech.*, 77(3), 531-560.
- James C.N. and Houze Jr. R.A. (2001), A real-time four-dimensional Doppler dealiasing scheme, *J. Atmosph. Ocean. Technol.*, 18(10), 1674-1683.
- Joe P. and May P.T. (2003), Correction of dual PRF velocity errors for operational Doppler weather radars, *J. Atmos. Ocean. Technol.*, 20, 429-442.
- Katul G., Wiberg P., Albertson J. and Hornberger G. (2002), A mixing layer theory for flow resistance in shallow streams, *Water Resour. Res.*, 38(11), 1250.
- Kirkbride A.D. and Ferguson R. (1995), Turbulent flow structure in a gravel-bed river: Markov chain analysis of the fluctuating velocity profile, *Earth Surf. Proc. and Landforms*, 20, 721-733.
- Kumar, S., R. Gupta, and S. Banerjee (1998) An experimental investigation of the characteristics of the free surface turbulence in open channel flows. *Phys. Fluids* 10: 437-456.

- Lemmin U. and Rolland T. (1997), Acoustic velocity profiler for laboratory and field studies, *J. Hydr. Eng.*, 123(12), 1089-1098.
- Lhermitte R. (1983), Doppler sonar observation of tidal flow, *J. Geophys. Res.*, 88, 725-742.
- Lu S.S. and Willmarth W.W. (1973), Measurements of the structure of the Reynolds stress in a turbulent boundary layer, *J. Fluid Mech.*, 60(3), 481-511.
- Lueck R.G. and Lu Y. (1997), The logarithmic layer in a tidal channel, *Cont. Shelf Res.*, 17(14), 1785-1801.
- Marchand J.P., Jarret R.D. and Jones L.L. (1984), Velocity profile, surface slope, and bed material size for selected streams in Colorado, U.S. Geol. Surv. Open File Rep., 84-733.
- Métais O. and Lesieur M. (ed.) (1989), *Turbulence and coherent structures*, Kluwer, Dordrecht (The Netherlands).
- Nakagawa H. and Nezu I. (1977). Prediction of the contributions to the Reynolds stress from bursting events in open-channel flows. *J. Fluid Mech.*, 80(1), p. 99.
- Nakagawa H. and Nezu I. (1981), Structure of space-time correlations of bursting phenomena in an open-channel flow, *J. Fluid Mech.*, 104, 1-43.
- Nelson J.M., McLean S.R. and Wolfe S.R. (1993), Mean flow and turbulence fields over two-dimensional bed forms, *Water Resour. Res.*, 29(12), 3935-3953.
- Nezu I. and Nakagawa H. (1993), *Turbulence in open-channel flows – IAHR monograph*, A. A. Balkema, Rotterdam (The Netherlands).
- Nicholas A.P. (2001), Computational fluid dynamics modelling of boundary roughness in gravel-bed rivers: an investigation of the effects of random variability in bed elevations, *Earth Surf. Proc. and Landforms*, 26, 345-362.
- Nikora V. and Smart G.M. (1997), Turbulence characteristics of New Zealand gravel-bed rivers, *J Hydr. Eng.*, 123(9), 764-773.
- Nikora V. and Goring D. (2000), Flow turbulence over fixed and weakly mobile gravel beds, *J. Hydr. Eng.*, 126(9), 679-690.
- Powell D.M., Reid I., and Laronne J.B. (1999), Hydraulic interpretation of cross-stream variations in bed-load transport, *J. Hydr. Eng.*, 125(12), 1243-1252.
- Robert A., Roy A.G. and De Serres B. (1992), Changes in velocity profiles at roughness transitions in coarse grained channels, *Sedimentology*, 39, 725-735.
- Rodi W. (1984), *Turbulence models and their application in hydraulics - a state of the art review*, IAHR - Section of Fundamentals of Division II.
- Roy A.G., Buffin-Belanger T., Lamarre H. and Kirkbride A.D. (2004), Size, shape and dynamics of large-scale turbulent flow structures in a gravel-bed river, *J. Fluid Mech.*, 500, 1-27.
- Sanford T.B. and Lien R.C. (1999), Turbulent properties in a homogeneous tidal bottom boundary layer, *J. Geoph. Res.*, 104(C1), p. 1245.
- Smart G.M. (1999), Turbulent velocity profiles and boundary shear in gravel bed rivers, *J. Hydr. Eng.*, 125(2), 106-116.
- Tritico H.M., Hotchkiss R.H. (2005), Unobstructed and obstructed turbulent flow in gravel bed rivers, *Journal of Hydraulic Engineering*, 131(8), 635-645.

- Tritico H.M., Stone M.C. and Hotchkiss R.H. (2002), Turbulence characterization in the wake of an obstruction in a gravel bed river, Proc. Hydr. Meas. Exp. Met., Estes Park (USA).
- Troiani G., Cioffi F. and Casciola C.M. (2004), Free-surface-vorticity interactions in an open channel flow, J. Hydr. Eng., 130(4), 313-323.
- Williams J.J., Thorne P.D. and Heathershaw A.D. (1989), Measurements of turbulence in the benthic boundary layer over a gravel bed, Sedimentology, 36, 959-971.
- Wosnik M., Castillo L. and George W.K. (2000), A theory for turbulent pipe and channel flows, J. Fluid Mech., 421, 115-145.
- Yalin M.S. (1992), River mechanics, Pergamon Press Ltd, Exeter (UK).
- Yang S.Q., Tan S.K. and Lim S.Y. (2004), Velocity distribution and Dip-phenomenon in smooth uniform open channel flows, J. Hydr. Eng., 130(12), 1179-1186.
- Yoshida K. and Nezu I. (2004), Experimental study on air-water interfacial turbulent hydrodynamics and gas transfer in wind-induced open channel-flows, Proc. 4th Int. Symp. Env. Hyd., IAHR, Hong Kong (China).

2. INSTRUMENTATION AND METHODS

2.1 – Methods and field measurements

2.2 – Eliminating velocity aliasing in acoustic Doppler velocity profiler data

2.1 METHODS AND FIELD MEASUREMENTS

Subchapter 2.1 is a brief introduction to the methods used in the present research: ADVP instrument and field measurements.

1	INTRODUCTION	2.1.1
2	ADVP WORKING PRINCIPLE	2.1.1
3	SCATTERING TARGETS IN CLEAR WATER FLOWS	2.1.3
4	EXPERIMENTAL SET-UP	2.1.4
5	FIELD MEASUREMENTS	2.1.5
	REFERENCES	2.1.7

1. INTRODUCTION

The present study is based on instantaneous velocity measurements made with the Acoustic Doppler Velocity Profiler (ADVP). The ADVP was developed at the Laboratoire d'Hydraulique Environnementale (LHE) and is the subject of the following PhD dissertation:

- Rolland T. (1994), Développement d'une instrumentation Doppler ultrasonore adaptée à l'étude hydraulique de la turbulence dans les canaux, PhD dissertation No. 1281, Swiss Federal Institute of Technology, Lausanne.
- Shen C. (1997), An acoustic instantaneous particle flux profiler for turbulence flow, PhD dissertation No. 1630, Swiss Federal Institute of Technology, Lausanne.
- Hurther D. (2001), 3-D acoustic Doppler velocimetry and turbulence in open-channel flow, PhD dissertation No. 2395, Swiss Federal Institute of Technology, Lausanne.

It is a non-intrusive ultrasonic instrument that is capable of measuring quasi-instantaneous three-dimensional velocity profiles of clear water open-channel flows. It is suitable for use in laboratory studies (laboratory flumes), or in field studies (rivers and lakes). The ADVP allows turbulence measurements that cover the inertial and the productive range of the spectral space.

In this chapter, a brief description of the ADVP working principle is given, as well as the field apparatus and location of the field measurement sites.

2. ADVP WORKING PRINCIPLE

The working principle of this Doppler based instrument is explained in detail in Lemmin and Rolland (1997) and in Section 2 of subchapter 2.2, "Eliminating velocity aliasing in acoustic Doppler velocity profiler data". Here, a specific description of the ADVP for bistatic and multistatic configurations is given.

Acoustic sonar uses the Doppler effect to measure the velocity of moving targets. The signal emitted by the ultrasonic emitter-transducer is scattered by moving particles and captured by a receiver-transducer; the Doppler shift between the emitted and the received signal is proportional to the target's velocity. A simple configuration of the ADVP will be considered first to provide an explanation of how the device uses the Doppler effect. An extension of the theory to the three-dimensional profiling system is subsequently made.

A simple configuration consists of two fixed transducers, one emitter and one receiver, called bistatic mode (Fig. 1). The emitter generates an ultrasonic wave with frequency f_0 and wavelength $\lambda_e = c/f_0$ (c is the sound speed of the considered environment) that propagates through the fluid. The scattering targets moving with velocity \vec{V} reflect the signal, which is afterwards detected by the receiver. Once the target moves with a certain velocity, the reflected signal frequency f_r (and consequently its wavelength λ_r) becomes different from the original, resulting in the so-called Doppler effect. The frequency shift between both the emitted and the received signal is called the Doppler frequency:

$$f_D = f_r - f_0 \quad (1)$$

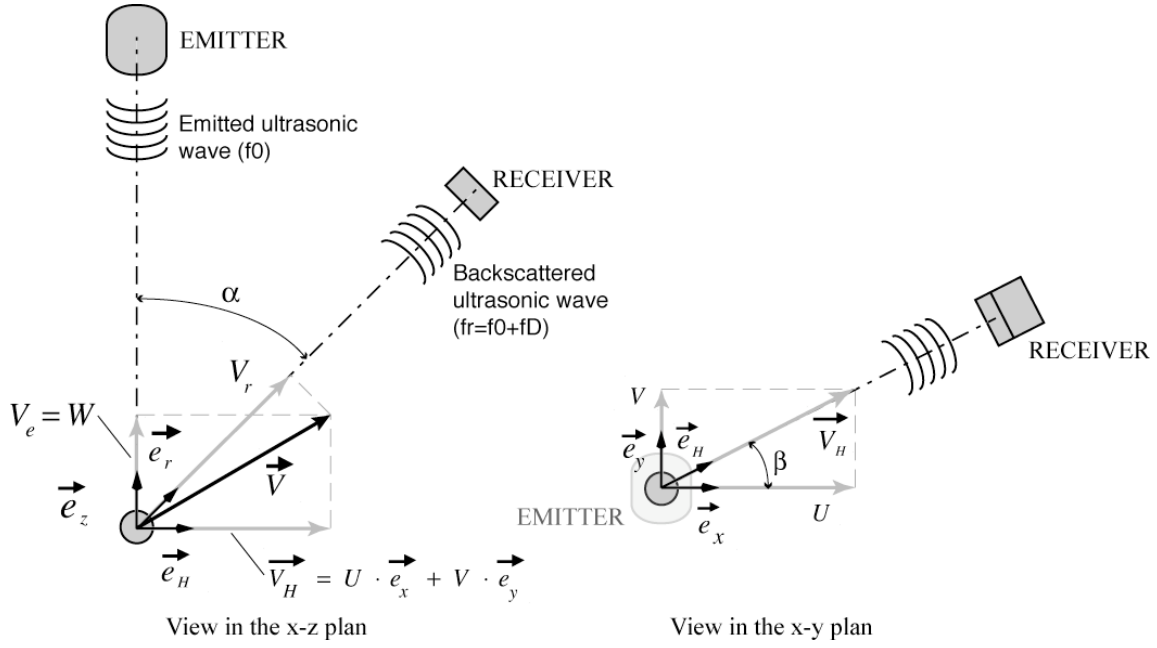


Figure 1 – Working principle of an acoustic Doppler sonar (from Blanckaert and Lemmin 2005)

If V_e and V_r are the velocity components of the target in the emitter-target and receiver-target directions, and f_t the frequency of the emitted signal as seen from the target, then it is possible to establish the following relations, with simple kinematic considerations:

$$f_t = f_0 + \frac{V_e}{c} f_0 = f_0 \left(\frac{c + V_e}{c} \right) \quad (2)$$

$$f_r = f_t \left(\frac{c}{c - V_r} \right) = f_0 \left(\frac{c + V_e}{c - V_r} \right) \quad (3)$$

From expression (3) it is now possible to establish a relationship between the Doppler frequency and each one of the velocity components in the emitter and receiver directions:

$$f_D = \frac{f_0}{c} (V_e + V_r) \quad (4)$$

To obtain the above expression, the velocity component along the receiver-target direction is assumed to be very small compared to the sound celerity ($V_r \ll c$). From Fig. 1 one can obtain an expression for the Doppler frequency as a function of the three velocity components of the moving target, based on geometrical considerations. In fact it is already known that $V_z = V_e$. The horizontal velocity vector \vec{V}_H is composed of components in the x and y directions:

$$V_H = U \cos \beta + V \sin \beta \quad (5)$$

Furthermore:

$$V_r = V_H \sin \alpha + V_z \cos \alpha \quad (6)$$

Putting the three latter equations into expression (1), it is possible to obtain the following expression for the Doppler frequency:

$$f_D = \frac{f_0}{c} [U \cos\beta \sin\alpha + V \sin\beta \sin\alpha + W(\cos\alpha + 1)] \quad (7)$$

In order to determine the three velocity components of the moving target from this expression, it is necessary and sufficient to have three geometrically independent measures of the Doppler frequency. In practice this is possible by having three transducers tilted horizontally, which receive the backscattered signal. The matrix equation system is the basis for the calculation of the 3D velocity field.

$$\begin{bmatrix} U(t) \\ V(t) \\ W(t) \end{bmatrix} = \frac{c}{f_0} \begin{bmatrix} \cos\beta_1 \sin\alpha & \sin\beta_1 \sin\alpha & \cos\alpha + 1 \\ \cos\beta_2 \sin\alpha & \sin\beta_2 \sin\alpha & \cos\alpha + 1 \\ \cos\beta_3 \sin\alpha & \sin\beta_3 \sin\alpha & \cos\alpha + 1 \end{bmatrix}^{-1} \begin{bmatrix} f_{D1}(t) \\ f_{D2}(t) \\ f_{D3}(t) \end{bmatrix} \quad (8)$$

The ADV configuration that will be adopted for the measurements in the present study is called the multistatic mode. It consists of four receivers that surround the emitter (Fig. 2) allowing one redundancy in the velocity component calculation. This redundancy is used to eliminate signal noise and to control the data quality (Hurther and Lemmin (2000) and Blanckaert and Lemmin (2005)).

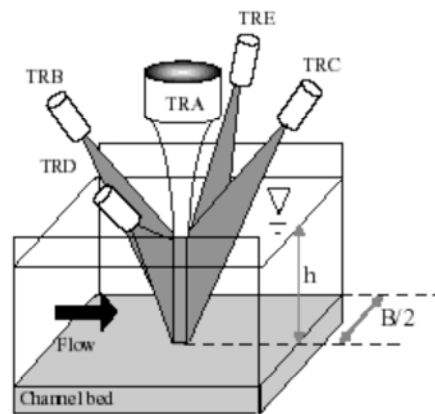


Figure 2 – Multistatic configuration of the ADV (in Hurther 2001)

Recently, Blanckaert and Lemmin (2005) presented an optimization of the ADV configuration that theoretically eliminates the noise from the measured velocity field. It also provides the algorithm to compute the instantaneous velocity components, as well as the different components of the Reynolds stress tensor (normal and shear stress), all as a function of the four Doppler frequencies acquired with the system. Franca and Lemmin (2005 – 2.2) describe a technique to improve the data quality by eliminating aliased data with an algorithm that takes into account the Doppler signal history.

3. SCATTERING TARGETS IN CLEAR WATER FLOWS

ADV measurements are based on the echo produced when an ultrasonic signal is scattered by moving targets. The quality of the signal obtained with the ADV measurements is closely related to the

scattering targets and their capability to follow the fluid motion. Shen and Lemmin (1997) studied several possible turbulence induced scattering sources:

- Turbulent velocity microstructures;
- Temperature microstructures;
- Concentration microstructures of fine particles;
- Concentration microstructures of fine air bubbles contained in normal tap water.

They studied clear water flows under conditions similar to those in the present study. Shen and Lemmin (1997) showed that in clear water flows, air bubble microstructures are mainly responsible for ultrasonic scattering. These structures, with a mean size of 750 μm , are ideal tracers of turbulent motion, without the interference of any inertial lag.

4. EXPERIMENTAL SET-UP

In order to undertake field measurements in rivers, a deployable 3D ADVP is used (Fig. 3).



Figure 3 – Deployable 3D ADVP placed in the river Venoge. The ADVP transducers are installed inside the grey housing

For the present study certain improvements were made on the system:

- An extension of the metal bridge, with a connectable beam, allowing to cover a river width of about 9 m.
- Reinforcement of the bridge to improve rigidity;
- Addition of a rail to slide the ADVP structure along the metal bridge to avoid lateral swaying;
- Installation of a longitudinal rail allowing the bridge displacement in the streamwise direction;
- Construction of a new transducer housing that allows having the four receivers in the water.

The structure permits the easy and stable displacement of the transducers in the field. The ADVP level is controlled by a wheel system with a fine lifting device. All transducers are mounted on a rigid plate. The transducers are installed inside a plastic housing (Fig. 4), which is filled with water. The plastic housing has a window in the bottom covered by a plastic film (Mylar), which does not interfere with the passage of the ultrasound waves. During the measurements, the Mylar barely touches the water surface. From the measurements it is possible to determine the influence of the boundary layer caused by the Mylar. Therefore the first measuring gates affected by this boundary layer are eliminated. It was experimentally verified that the boundary layer induced by the Mylar is negligible when compared with the measured flow depths.

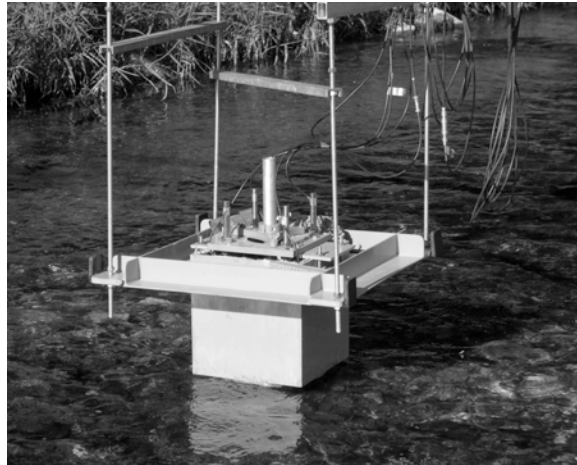


Figure 4 – Detail of the ADVP housing. The ADVP transducers are installed inside the grey housing

5. FIELD MEASUREMENTS

The velocity profiles were measured at three different sections of the Swiss rivers, Venoge and Chamberonne (canton of Vaud). Two sets of measurements were made in the Venoge (Venoge 1 and Venoge 2) and one in the Chamberonne. The hydraulic characteristics of each river at the time of the different measurements are described in the chapters where this information is pertinent. The cross sections are located at the following sites: in the river Venoge, 120 m and 90 m upstream from the Moulin de Lussery, and in the river Chamberonne, 385 m upstream from the river mouth. The main characteristics of the rivers are summarized in Table 1:

Table 1 – Rivers' main characteristics

River	Basin (km ²)	Maximum altitude (msl)	Minimum altitude (msl)	Slope (%)	Banks occupation	Riverbed
Venoge	243	1680 (Mont-Tendre)	374 (Lake Geneva)	<1	Rural and forest	Gravel/Sand
Chamberonne	40	610 (Cheseaux)	374 (Lake Geneva)	<1	Rural and urban	Gravel/Sand

Figs. 5 and 6 show the location of the measuring sections for both rivers.

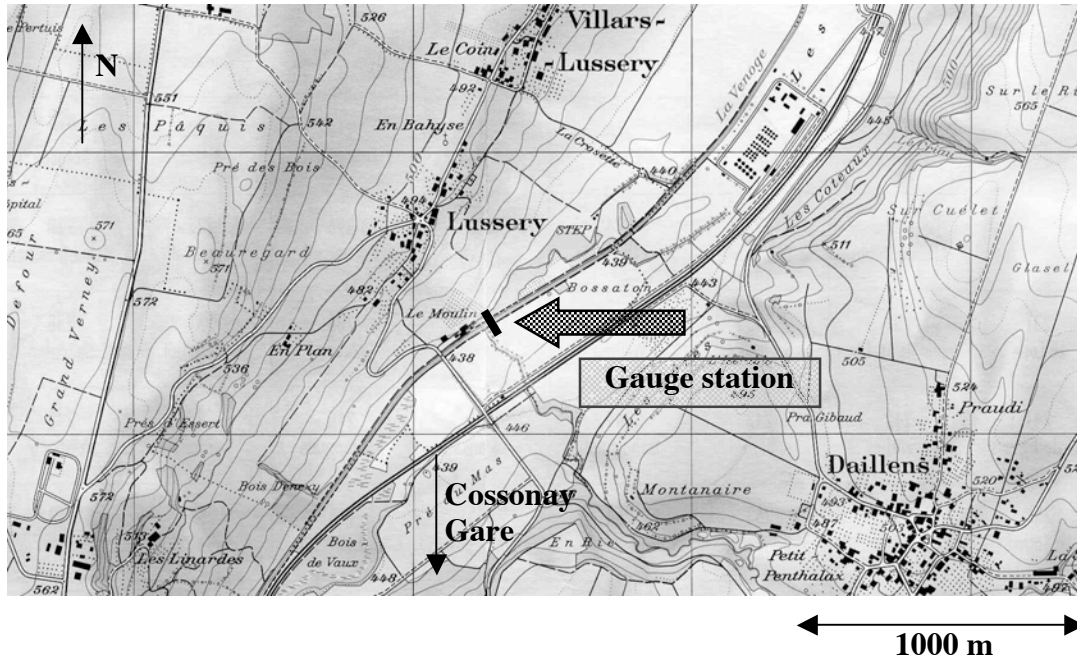


Figure 5 – Location of the gauge station in the river Venoge (extract from topographic map Nr. 1222, originally with the scale 1/25000, Office fédérale de topographie, Switzerland)

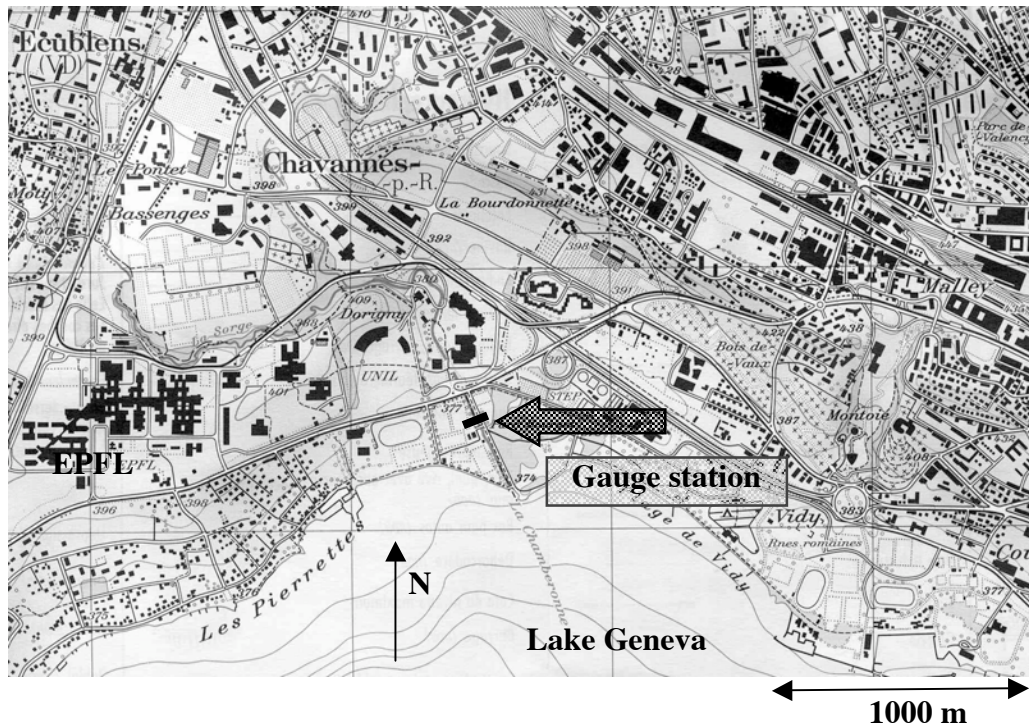


Figure 6 – Location of the gauge station in the river Chamberonne (extract from topographic map Nr. 1243, originally with the scale 1/25000, Office fédérale de topographie, Switzerland)

For the three measurement sets different ADVP configurations were used. Details of these configurations are given in Table 2.

Table 2 – ADVP configuration at the time of the measurements

Set of measurements	Angle α (°)	PRF (Hz)	Gates width (μ s)	Number of gates (-)
Venoge 1	35	2000	6	30
Chamberonne	35	2000	6	30 to 40
Venoge 2	30	1666.7	6	50

PRF is the Pulse Repetition Frequency. For more details on the definition of PRF and the measuring gates refer to subchapter 2.2.

REFERENCES

- Blanckaert K. and Lemmin U. (2005), Means of noise reduction in acoustic turbulence measurements. *J. Hydr. Res.*, (in press).
- Franca M.J. and Lemmin U. (2005 – 2.2), subchapter “Eliminating velocity aliasing in acoustic Doppler velocity profiler data”.
- Hurther D. and Lemmin U. (2000), A correction method for turbulence measurements with a 3D acoustic Doppler velocity profiler. *J. Atmosph. Ocean. Technol.*, 18, 446-458
- Hurther D. (2001), 3-D acoustic Doppler velocimetry and turbulence in open-channel flow, PhD dissertation No. 2395, Swiss Federal Institute of Technology, Lausanne.
- Lemmin U. and Rolland T. (1997), Acoustic velocity profiler for laboratory and field studies. *J. Hydr. Eng.*, 123(12), 1089-1098.
- Shen C. and Lemmin U. (1997), Ultrasonic scattering in highly turbulent clear water flow, *Ultras.*, 35, 57-64.

2.2 ELIMINATING VELOCITY ALIASING IN ACOUSTIC DOPPLER VELOCITY PROFILER DATA

Subchapter 2.2 accepted for publication in the journal, Measurement Science and Technology (IOP). The authors are M.J. Franca and U. Lemmin.

This paper deals with the improvement of the ADVF data analysis. It presents an efficient dealiasing method for acoustic Doppler velocity measurements which is directly carried out on the Doppler phase shift signal.

	ABSTRACT	2.2.1
1	INTRODUCTION	2.2.1
2	ACOUSTIC DOPPLER VELOCITY PROFILER	2.2.2
2.1	Principle of operation	2.2.2
2.2	Range-velocity ambiguity	2.2.4
2.3	Doppler frequency estimation	2.2.5
3	DEALIASING ALGORITHMS	2.2.6
3.1	Aliasing analysis	2.2.6
3.2	Dealiasing algorithm for the case of a known flow direction	2.2.9
3.3	Dealiasing algorithm following the signal history	2.2.11
4	SUMMARY AND CONCLUSION	2.2.15
	ACKNOWLEDGEMENTS	2.2.16
	REFERENCES	2.2.16

ELIMINATING VELOCITY ALIASING IN ACOUSTIC DOPPLER VELOCITY PROFILER DATA

ABSTRACT

We present an efficient dealiasing method for acoustic Doppler velocity measurements which is directly carried out on the Doppler phase shift signal. Corrections are applied to the Doppler frequency measured by the Acoustic Doppler Velocity Profiler receivers, before any transformation into the velocity domain is made. The method does not require knowledge of the flow direction. It consists of a first step in which a threshold analysis determines the need for dealiasing, and a second one in which the Doppler information is corrected. For the second step, an algorithm is developed which follows the complex signal history. It determines the correction to be applied to the instantaneous Doppler frequency in order to make it coherent with the neighbouring space/time points. The efficiency and improvement obtained with this algorithm are demonstrated using field measurement data with our ADVP.

Key-words: aliasing, acoustic Doppler velocity profiler, turbulence studies

1 INTRODUCTION

For open-channel turbulence studies, the use of Acoustic Doppler instrumentation has become common practice in laboratory and field measurements due to the flexibility of the instrumentation configuration (Lemmin and Rolland 1997, Hurther *et al.* 2002). Besides its application in water studies, measurements based on acoustic Doppler technology are widely used in meteorology (Doviak and Zrnic 1993).

Acoustic Doppler instruments determine the flow velocity from the frequency shift caused by targets in the flow. Doppler instrumentation is non-intrusive and in open-channel flows it often allows full depth *quasi*-instantaneous velocity profiling which permits comprehensive studies of the turbulent and mean flow fields. The spatial resolution is in the range of turbulent scales and it is reliable even in the presence of suspended sediment transport (Lemmin and Rolland 1997, Shen and Lemmin 1997 and Cellino and Lemmin 2004). In this paper we will focus on pulse-to-pulse coherent acoustic Doppler instruments.

The velocity range in acoustic Doppler measurements is determined by the choice of the corresponding pulse repetition frequency (PRF). The choice is actually constrained by a combination of the water depth range to be covered and the desired velocity range, thus resulting in the so-called range-velocity ambiguity. This leads to a compromise which limits the maximum measurable velocity. If the actual velocities are higher than this maximum velocity, aliasing (or folding) will occur which results in incorrect velocity estimates. The elimination of data spikes due to aliasing has been the topic of numerous publications. James and Houze (2001) present an overview of the latest developments in dealiasing techniques applied in weather radar measurements made with Doppler instrumentation. Other researchers (Joe and May 2003, Holleman and Beekhuis 2003) have recently proposed the use of dual

PRF techniques for meteorological applications. Lhermitte (1999) suggested a dual PRF sample technique for the use in tidal flow measurements. Existing dealiasing techniques most often deal with the analysis and correction of velocity values (Durden and Werner 1996, Gong et al. 2003, Gao et al. 2004, Gao and Droegemeier 2004). Goring and Nikora (2002) presented despiking methods based on the analysis of the measured velocity fields. James and Houze (2001) and Friedrich and Caumont (2004) consider the dimension time in their dealiasing algorithm, obtaining a so-called 4D scheme.

In this text we present an efficient dealiasing method which is directly carried out on the Doppler phase shift signal. Corrections are applied to the Doppler frequency measured by the ADVP receivers, before any transformation into the velocity field is made. The technique consists of a first step in which a threshold analysis determines the need for dealiasing, and a second one in which the Doppler information is corrected. The method falls into the domain of phase unwrapping.

The phase unwrapping is carried out by a simple technique based on a coherence relation between neighbouring data. Since ADVP measurements provide entire velocity profiles, a 2D approach to map the true phase of the signal is possible (Volkov and Zhu 2003). Phase unwrapping techniques are widely used and developed for reconstructing 2D phase surfaces (Ghiglia and Pritt 1998). These techniques are applied in such research fields as optics, resonance imaging, tomography, signal processing and solid-state physics. Costantini (1996) and Nico *et al.* (2000) distinguish two different methods for correcting the wrapped phase. The first one is based on edge detection and the second one uses least square estimates. The dealiasing herein presented belongs to the first method, assuming continuity or piecewise continuity of the phase surface (Strand and Taxt 1999) defined by the two dimensions, time and vertical direction.

The manuscript first resumes ADVP principles and discusses range-velocity limitations and Doppler frequency estimates. The aliasing problem is then visualized on a trigonometric circle. Two dealiasing algorithms are demonstrated: the first one is based on a known flow direction with certain limitations, and the second one is based on the signal history analysis. The feasibility of the method is demonstrated using data measured in a river.

2 ACOUSTIC DOPPLER VELOCITY PROFILER

2.1 Principle of operation

Acoustic sonar instruments use the Doppler frequency shift of ultrasonic waves to estimate the velocity of moving targets in the flow. This shift occurs between an emitted ultrasonic signal and the one which is scattered by the moving particles within the flow, and then captured by receiver-transducers (Fig. 1a).

The working principle of the acoustic Doppler Velocity Profiler (ADVP), its geometry and limitations are presented by Lemmin and Rolland (1997). Here we will briefly summarize the important steps in the calculation of the velocity which are necessary to understand the proposed dealiasing method. For most of our applications, the instrument is placed in a water-filled housing which touches the water surface. This allows instantaneous profile measurements over the whole water column without disturbing the flow. ADVP instrumentation is robust and can easily be displaced, allowing not only a multitude of laboratory studies but also field measurements (Fig. 2).

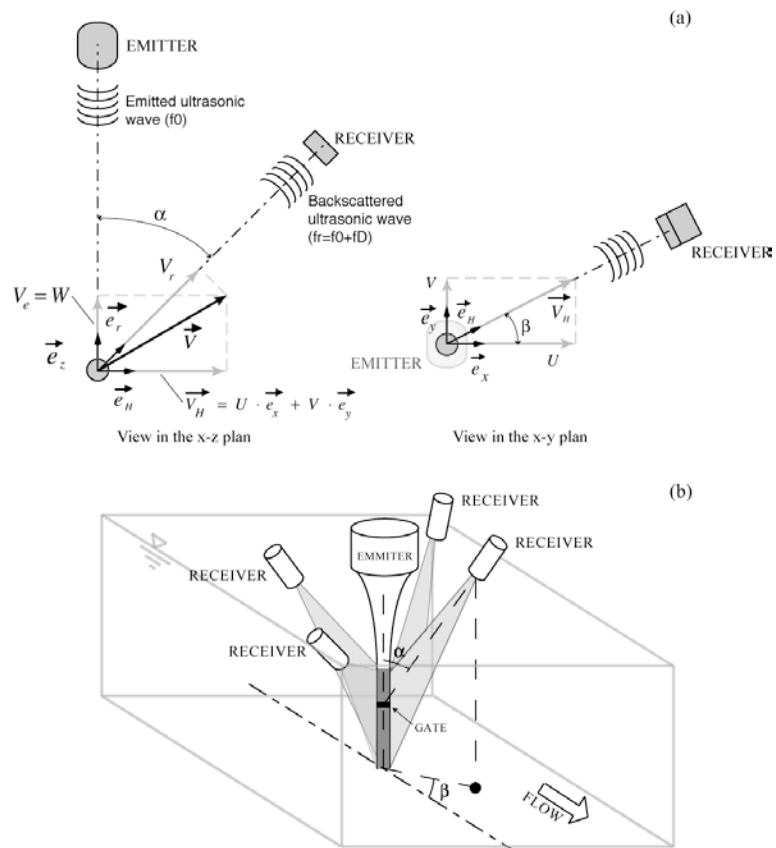


Figure 1, Acoustic Doppler Velocity Profiler (ADVP); (a) working principle of the multistatic configuration; (b) general scheme.

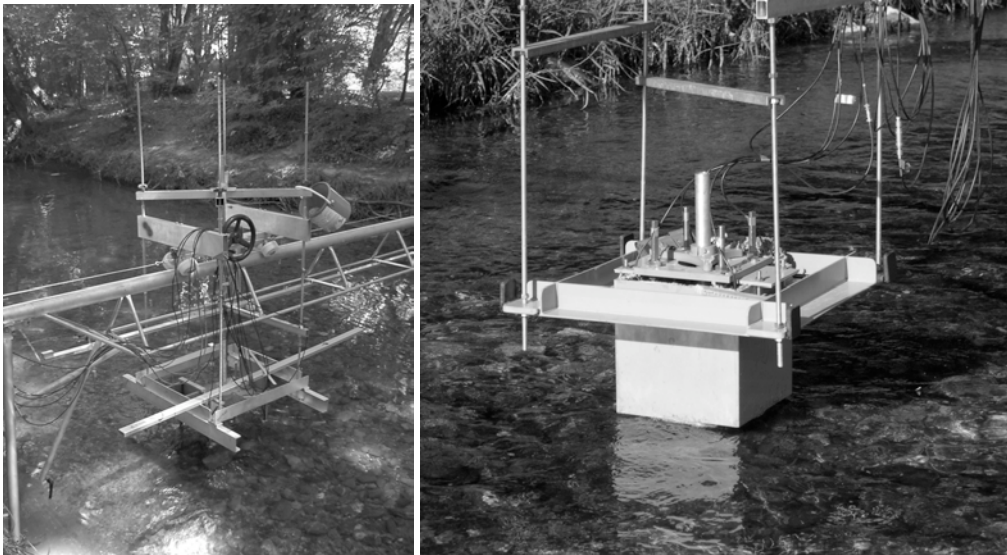


Figure 2: Field measurements with the Acoustic Doppler Velocity Profiler (ADVP).

In the ADVP, the Doppler frequency is estimated using the pulse-to-pulse coherent method (Lhermitte and Serafin 1984). The emitted signal consists of a short pulse of ultrasonic waves (typically four or eight sinusoidal waves with frequency f_0) repeated at the pulse repetition frequency (PRF) which is much lower than f_0 . Between two pulse emissions the receiver-transducers capture the backscattered waves of frequency f_r , which are gated to correspond to the pulse's time of flight to a certain depth. Thus, an almost instantaneous complete velocity profile can be obtained by consecutive gating over the total water column.

The Doppler frequency (f_D) which results from the difference between the emitted frequency and the one reflected by a moving target is proportional to the target's velocity in the target-receiver direction:

$$f_D = f_0 \left(\frac{\vec{V} \cdot (\vec{e}_e + \vec{e}_r)}{c - \vec{V} \cdot \vec{e}_r} \right) \quad (1)$$

where f_0 is the frequency of the sound wave emitted from a fixed source; \vec{V} is the target velocity; \vec{e}_e and \vec{e}_r are the unit vectors in the directions from the target to the emitter and from the target to the receiver respectively, and c is the speed of sound in the water. In most hydraulic applications, the target velocity component in the target receiver direction is negligible when compared to the speed of sound. Thus, the above expression can be simplified to:

$$f_D = \frac{f_0}{c} \vec{V} \cdot (\vec{e}_e + \vec{e}_r) \quad (2)$$

In a monostatic configuration, where the emitter and receiver are located at the same point, the unit vectors are equal. Therefore, the target velocity in the target-receiver direction (V_r) can be obtained from Eq. (2) as:

$$V_r = \frac{c}{2} \frac{f_D}{f_0} \quad (3)$$

In the present study a multistatic configuration of the ADVP as illustrated in Fig. 1b is used. It consists of four receivers that surround the emitter allowing one redundancy on the 3D velocity component calculation. This redundancy is used to eliminate signal noise and to control the data quality (Hurther and Lemmin 2000). The quality of the signal obtained with the ADVP measurements is closely related to the scattering targets and their capability to follow the fluid motion. Shen and Lemmin (1997) investigated several hypotheses for turbulence induced scattering sources.

2.2 Range-velocity ambiguity

As stated above, the value of the PRF is also conditioned by the desired water depth range. In fact, the time between two consecutive emissions of wave trains should be sufficiently long to allow the signal to travel the profiling water depth range and return back to the receiver. In open-channel measurements the last sampling gate is usually placed close to the bottom. This leads to limitations on the PRF. The PRF

must respect the condition $PRF \geq \frac{c}{d}$ (where d is the distance the signal travels along the emitter-bottom-receiver path) in order to cover a distance slightly beyond the flow depth. On the other hand, and according to Shannon's Sampling Theorem, the frequency range estimated from the measurements is equal to half the sampling frequency (PRF), and is called the Nyquist frequency (f_N):

$$\left| \hat{f}_D \right| \leq \frac{\text{PRF}}{2} = f_N \quad (4)$$

All Doppler frequencies higher than the Nyquist frequency are aliased, thus limiting the range of the instantaneous velocities. From this restriction and from expression (3) comes the maximum velocity limitation that leads to the so-called range-velocity ambiguity (Lhermitte 1983):

$$V_{\max} d_{\max} = \frac{c^2}{4f_0} \quad (5)$$

Therefore, any profiling has to be a compromise between the maximum profile depth and the maximum velocity. If the actual velocity in the flow is greater than the maximum velocity defined here, aliasing will occur. One way to overcome this limit is to use a dual PRF system (Lhermitte 1999).

2.3 Doppler frequency estimation

The Doppler frequency f_D is estimated by the pulse-pair algorithm (Lhermitte and Serafin 1984). The mean value of f_D corresponds to the phase angle of the autocorrelation function of the complex echo signal ($z(t) = I(t) + iQ(t)$), estimated for a sample of NPP consecutive values (Lemmin and Rolland 1997); where NPP is the number of pulse-pairs. The pulse-pair algorithm for the estimate of f_D on NPP values is given by the following expressions:

$$\hat{f}_D = \frac{1}{2\pi T_{\text{PRF}}} \arctan \left[\frac{\text{Im} \left(\hat{R}(T_{\text{PRF}}) \right)}{\text{Re} \left(\hat{R}(T_{\text{PRF}}) \right)} \right] \quad (6)$$

where T_{PRF} is the time between two emissions (inverse of the PRF) and \hat{R} is the complex autocorrelation function of the echo signal estimated for the time lag T_{PRF} . In the study of turbulent velocity fields, a high resolution (PRF/NPP) is desirable in order to increase the maximum velocity. However, the NPP has a limit below which the signal variance estimates are no longer stable. Lemmin and Rolland (1997) indicated $\text{NPP} \geq 32$. The imaginary and real parts of the function \hat{R} are estimated for NPP values as follows:

$$\text{Im} \left(\hat{R}(T_{\text{PRF}}) \right) = \sum_{i=1}^{\text{NPP}-1} (Q_i I_{i+1} - Q_{i+1} I_i) \quad (7)$$

$$\text{Re} \left(\hat{R}(T_{\text{PRF}}) \right) = \sum_{i=1}^{\text{NPP}-1} (I_i I_{i+1} + Q_i Q_{i+1}) \quad (8)$$

For a given range gate, the index i corresponds to a time step in the I and Q signal series, whose total number of elements is equal to PRF times the total time of acquisition. With Eqs (7) and (8) it is possible to obtain time series of $\text{Im} \left(\hat{R}(T_{\text{PRF}}) \right)$ and $\text{Re} \left(\hat{R}(T_{\text{PRF}}) \right)$ whose length is equal to the total number of I and Q time steps divided by NPP. From Eq. (6) it is obvious that the phase angle (θ) from

which the Doppler frequency is determined has to be in the range $-\pi$ to π . If it falls outside this range, aliasing will occur.

3 DEALIASING ALGORITHMS

3.1 Aliasing analysis

Here we present a dealiasing method based on the analysis of the complex function \hat{R} . This method takes into consideration the signal history by analysing the imaginary and real parts of the autocorrelation function. It is highly efficient in eliminating aliasing peaks. Access to the raw data which consist of the complex echo signal constituted by the in-phase I and the quadrature Q output series allows an early treatment of the data and provides the possibility to correct errors due to aliasing, before any higher level data treatment and analysis process is carried out. In our studies we record the raw data and we carry out the dealiasing in a post-measurement data treatment. The method can of course be adapted and directly incorporated into a real-time visualization system.

As indicated above, aliasing of the Doppler frequency occurs if the condition imposed by the Sampling Theorem is not satisfied. Considering the expression that relates the Doppler frequency to the autocorrelation function's phase angle, Eq. (6), and the Nyquist frequency limitation we obtain:

$$\left| \frac{1}{2\pi T_{\text{PRF}}} \arctan \left[\frac{\text{Im} \left(\hat{R}(T_{\text{PRF}}) \right)}{\text{Re} \left(\hat{R}(T_{\text{PRF}}) \right)} \right] \right| \leq \frac{\text{PRF}}{2} \quad (9)$$

By simplifying the expression we can link the aliasing restriction to the arctangent function limits (Fig. 3b):

$$|\arctan(\theta)| \leq \pi \quad (10)$$

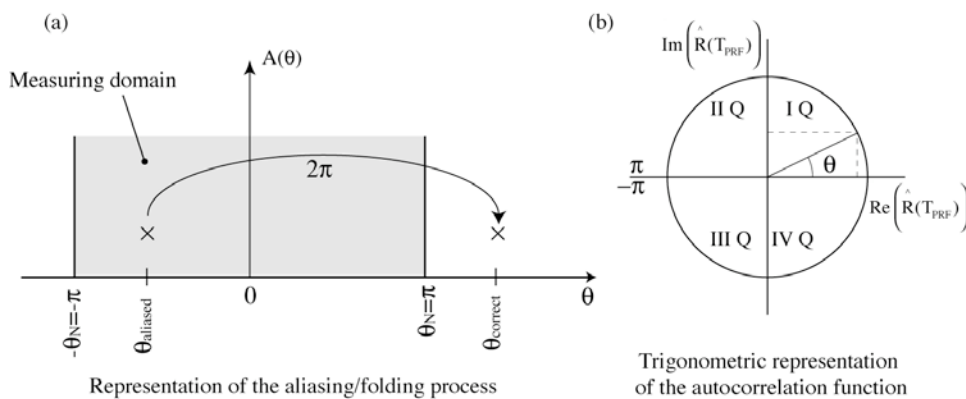


Figure 3: (a) Demonstration of aliasing in ADV measurements in terms of the autocorrelation phase angle; (b) Trigonometric interpretation of the autocorrelation phase angle.

Thus, with respect to its correct value, an aliased frequency has a lag of 2π in the autocorrelation phase angle (θ). This is demonstrated in Fig. 3a: the correct phase angle which is larger than π falls outside the measuring range. However, due to aliasing it will be found inside the measuring range and thus have the wrong phase angle. It also means that an aliased frequency is greater than zero when the true value is smaller, and *vice-versa*. Therefore, the dealiasing technique always consists of either adding or subtracting the value 2π to the value of the arctangent function in expression (6). The principle of aliasing can also be demonstrated with the help of the trigonometric circle (Fig. 4). Assuming that the neighbouring data are situated in the positive hemisphere, the Doppler frequency turns clockwise. Therefore, the point indicated in Fig. 4 falls into the negative hemisphere because its frequency has become too large and is aliased due to the range-velocity ambiguity (eq. 4). A value of 2π has to be added in order to bring the point back into the positive hemisphere.

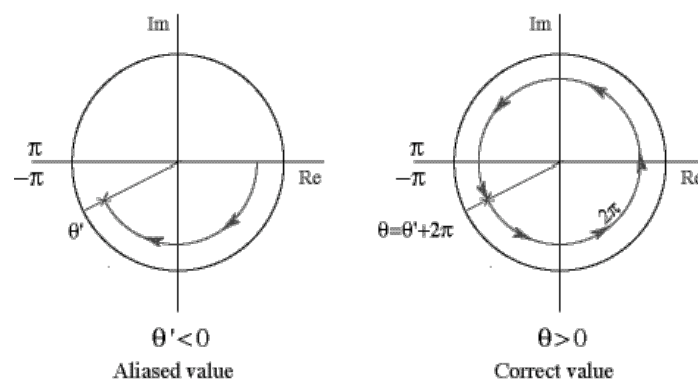


Figure 4: Trigonometric interpretation of the aliasing in ADVP measurements.

The aliasing effect can be demonstrated in a sequence of instantaneous Doppler frequency data (Fig. 5). The data presented in this paper were taken from field measurements during one campaign performed in the summer of 2003 in the river Venoge, Switzerland (Franca and Lemmin 2004 – A.1). Flow characteristics are detailed in Table 1. The measurements were made in a rough bottom river section. In these measurements a PRF of 2000 Hz was used ($T_{\text{PRF}} = 500 \mu\text{s}$), which corresponds to a Nyquist frequency of $f_N = 1000 \text{ Hz}$. The emitted frequency f_0 was equal to 1 MHz.

Table 1. Hydraulic characteristics of the river flow in the river Venoge, summer 2003.

Discharge (m^3/s)	River width (m)	Water depth (m)	Bulk mean velocity (m/s)	Channel slope (%)
0.80	6.3	0.21	0.60	0.13

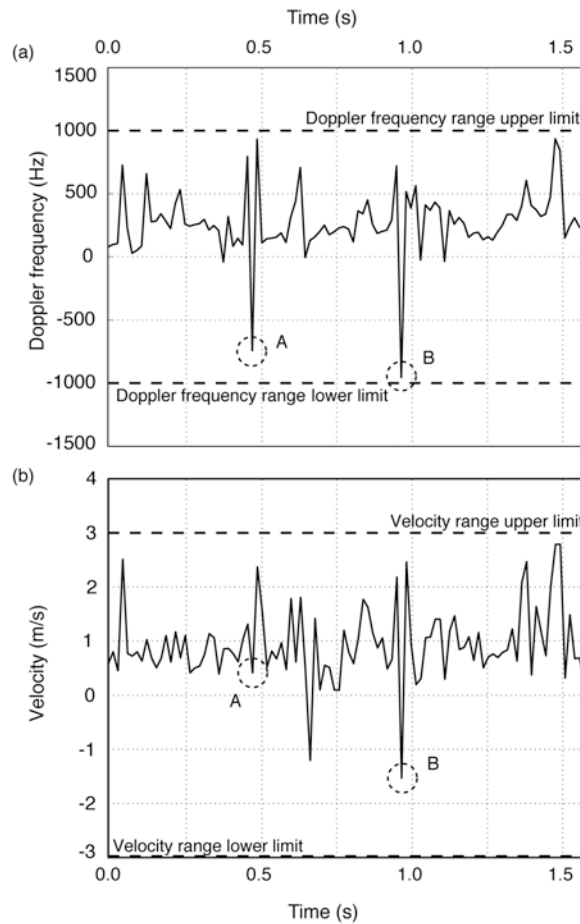


Figure 5: (a) aliasing on Doppler frequency data measured by one of the receivers – two spurious peaks (A and B) pointing downwards are marked by circles; (b) horizontal velocity data in the streamwise direction obtained by combining all four receiver data. Data obtained with a frequency $f_a=62.5$ Hz.

Two spurious peaks are visible in the Doppler frequency time series (Fig. 5a; indicated by circles). Peak B is obviously spurious in the instantaneous velocity data (Fig. 5b), demonstrating how aliasing in the Doppler frequency can directly affect velocity results. However, less obvious errors are also present in the velocity data such as the one corresponding to the Doppler frequency peak A. It should be noted that the ADVP multistatic configuration measures the Doppler frequency in four distinct directions since it uses four receiver-transducers. The velocity calculation in the Cartesian space results from an algorithm that integrates the four Doppler frequency data sets in order to determine the three velocity vector components. An aliasing error affecting only one of the receiver data series can be included in the velocity calculations without being apparent. This occurs at peak A of the Doppler frequency data in Fig. 5 where the resultant velocity seems to fall within the range of expected velocities. On the other hand, the negative velocity spike in the middle of the series (Fig. 5b) is due to aliasing at another receiver since no aliasing is observed in the series of the receiver shown in Fig. 5a. This example clearly indicates that it is very difficult or impossible to obtain unbiased and complete correction of aliasing errors in the velocity domain.

3.2 Dealiasing algorithm for the case of a known flow direction

We will first deal with a simple dealiasing technique, based on an *a priori* knowledge of the flow direction (Lemmin and Rolland 1997). This technique has been applied to the velocity data. In the present case, however, the correction is based on the complex autocorrelation function terms.

If the flow direction is known, the sign of the expected Doppler frequency is also known due to the given orientation of the instrument with respect to the flow. By definition, the Doppler frequency and therefore also the velocity according to expression (3) will acquire a positive value if a target particle approaches a receiver. Otherwise it will acquire a negative value (Fig. 1). In testing for aliasing, the sign of the imaginary term of the autocorrelation function ($\text{Im}\left(\hat{\mathbf{R}}(T_{\text{PRF}})\right)$) should be the same as the one expected for the Doppler frequency given that the arctangent function in Equation (6) only assumes positive values between 0 and π in the I and II quadrant (see Fig. 3b). If this is not the case, a correction can be made to the arctangent function by adding or subtracting 2π , according to the following algorithm:

$$f_D^{\text{expected}} > 0 \left\{ \begin{array}{l} \text{if } \text{Im}\left(\hat{\mathbf{R}}(T_{\text{PRF}})\right) > 0 \Rightarrow \arctan\left(\frac{\text{Im}\left(\hat{\mathbf{R}}(T_{\text{PRF}})\right)}{\text{Re}\left(\hat{\mathbf{R}}(T_{\text{PRF}})\right)}\right) = \arctan\left(\frac{\text{Im}\left(\hat{\mathbf{R}}(T_{\text{PRF}})\right)}{\text{Re}\left(\hat{\mathbf{R}}(T_{\text{PRF}})\right)}\right) \\ \text{if } \text{Im}\left(\hat{\mathbf{R}}(T_{\text{PRF}})\right) < 0 \Rightarrow \arctan\left(\frac{\text{Im}\left(\hat{\mathbf{R}}(T_{\text{PRF}})\right)}{\text{Re}\left(\hat{\mathbf{R}}(T_{\text{PRF}})\right)}\right) = \arctan\left(\frac{\text{Im}\left(\hat{\mathbf{R}}(T_{\text{PRF}})\right)}{\text{Re}\left(\hat{\mathbf{R}}(T_{\text{PRF}})\right)}\right) + 2\pi \end{array} \right. \quad (11)$$

$$f_D^{\text{expected}} < 0 \left\{ \begin{array}{l} \text{if } \text{Im}\left(\hat{\mathbf{R}}(T_{\text{PRF}})\right) > 0 \Rightarrow \arctan\left(\frac{\text{Im}\left(\hat{\mathbf{R}}(T_{\text{PRF}})\right)}{\text{Re}\left(\hat{\mathbf{R}}(T_{\text{PRF}})\right)}\right) = \arctan\left(\frac{\text{Im}\left(\hat{\mathbf{R}}(T_{\text{PRF}})\right)}{\text{Re}\left(\hat{\mathbf{R}}(T_{\text{PRF}})\right)}\right) + 2\pi \\ \text{if } \text{Im}\left(\hat{\mathbf{R}}(T_{\text{PRF}})\right) < 0 \Rightarrow \arctan\left(\frac{\text{Im}\left(\hat{\mathbf{R}}(T_{\text{PRF}})\right)}{\text{Re}\left(\hat{\mathbf{R}}(T_{\text{PRF}})\right)}\right) = \arctan\left(\frac{\text{Im}\left(\hat{\mathbf{R}}(T_{\text{PRF}})\right)}{\text{Re}\left(\hat{\mathbf{R}}(T_{\text{PRF}})\right)}\right) \end{array} \right. \quad (12)$$

We will demonstrate the use of this algorithm and its limitations on the data sample shown in Fig. 5. As seen in Fig. 6, the two spurious Doppler frequency peaks (circles) have been corrected by the dealiasing. However, several other correct data points are also modified, because their signs are not consistent with the expected target-receiver direction velocity. In the instantaneous velocity set in Fig. 6b, several other points have been corrected indicating the combined effect of the correction on all four receivers. It is rather difficult to decide whether in the velocity domain the proposed correction is correct or not. It has to be noted that in multistatic ADV configurations, a receiver may not necessarily be orientated in the streamwise direction, as is the case in Fig. 1. The target-receiver radial velocity V_r measured by each of

the transducers also contains spanwise and vertical components. Thus, even in cases where the streamwise flow velocity never becomes negative, it is not possible to assume that this is also true for V_r . This strongly depends on the intensity of the secondary flow components and in the present river measurements, a highly 3D flow field was observed (Franca and Lemmin 2004 – A.1). In these cases, the above described method is not sufficiently well defined and actually produces errors in the data since it introduces unjustified corrections.

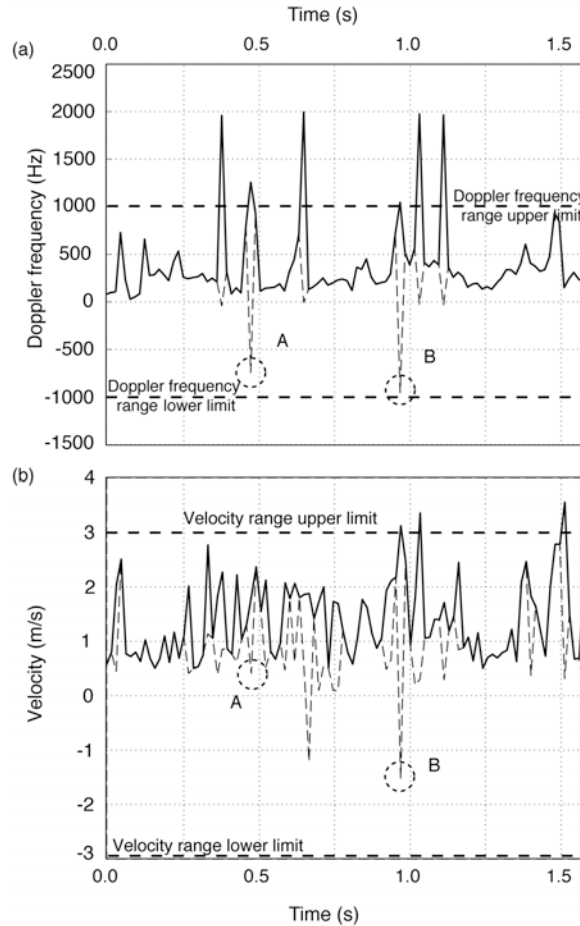


Figure 6, Example of dealiasing based on the known flow direction made directly on a Doppler frequency series (same data as in Fig. 5): (a) Doppler frequencies at one receiver; (b) horizontal velocity data in the streamwise direction obtained by combining all four receiver data. The original series are presented by dashed lines, the continuous lines correspond to the dealiased series. Data obtained with a frequency $f_a=62.5$ Hz.

Another limitation of the present method is due to the fact that this algorithm only allows the elimination of first order aliasing. This means that the Doppler frequency range is increased from $\left[-\frac{\text{PRF}}{2}, \frac{\text{PRF}}{2}\right]$ to $[-\text{PRF}, \text{PRF}]$. This limitation is particularly important in applications with low PRF and strongly varying flow fields.

This method fails when the actual flow velocity can acquire positive and negative values; errors may then be made in the instantaneous velocity computation which can lead to inaccuracies not only in the mean fields but particularly in the analysis of turbulence. Despite these limitations, this can be a valid

method in simple 1D cases or for simple instrument configurations such as a monostatic system which is well-oriented in the flow direction.

An important aspect in the application of dealiasing techniques is the starting point. Most dealiasing methods are based on a threshold analysis between neighbouring points. Thus the definition of the right boundary conditions for the initiation of the process is important. The methodology described in this section of the text may be useful for the definition of these boundary conditions. For example in the case of open-channel flows, the flow in the surface region of the water column will be positive in the streamwise direction. Therefore, the present method may be applied here in order to define the boundary condition for more sophisticated approaches. Below, an advanced method will be presented which is based on the analysis of time or space neighbouring data.

3.3 Dealiasing algorithm following the signal history

In situations without an *a priori* knowledge of the flow direction, the analysis and the possible correction of aliased Doppler velocity measurements will focus on the relationship between the imaginary and real terms of function \hat{R} in the arctangent function of the pulse-pair algorithm (Eq. 6). It is assumed that the data are sampled at a high frequency resulting in small steps between neighbouring values in terms of the autocorrelation phase angle. In this case, a dealiasing technique is proposed which is based on a threshold analysis of the difference between the value of the arctangent function at a given point (i) to a neighbouring one ($i+1$):

$$|\phi| = \left| \arctan \left(\frac{\text{Im} \left(\hat{R}(T_{\text{PRF}}) \right)}{\text{Re} \left(\hat{R}(T_{\text{PRF}}) \right)} \right)_{i+1} - \arctan \left(\frac{\text{Im} \left(\hat{R}(T_{\text{PRF}}) \right)}{\text{Re} \left(\hat{R}(T_{\text{PRF}}) \right)} \right)_i \right| < T\pi ? \quad (13)$$

where ϕ is the variable and T is the threshold considered. The latter is typically taken to be equal to the unity in ADVP measurements made in open-channel flows. In general, the choice of the threshold value T has to be carefully made in order to avoid unjustified dealiasing. The index i represents a time step or the distance between two gates. If the difference between two consecutive values is greater than the threshold value, then the dealiasing technique described below will be applied.

This method is based on a trigonometric analysis of the complex data, and is made following the signal on the trigonometric circle (Fig. 7). As mentioned, the dealiasing technique always consists of either adding or subtracting the value 2π to the value of the arctangent function in eq (6). In the present algorithm, in order to determine which operation should be applied, an analysis of both the imaginary and real terms of the autocorrelation function is made. For single level aliasing there are two possibilities, depending on the position of $\text{Im} \left(\hat{R}(T_{\text{PRF}}) \right)$ and $\text{Re} \left(\hat{R}(T_{\text{PRF}}) \right)$ of the starting point (i) on the trigonometric circle. This technique allows following the signal history indefinitely and can be used to several levels of aliasing since it moves freely around the trigonometric circle. It is a post-processing technique and can be applied to all Doppler based instruments.

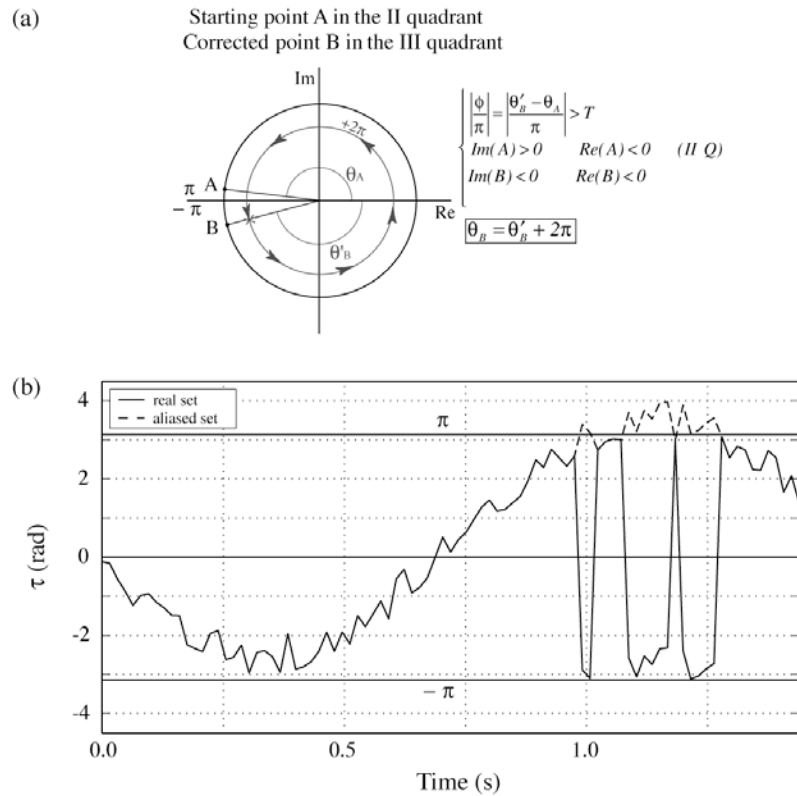


Figure 7, Scheme of the algorithm for dealiasing following the echo signal history: (a) A and B are the positions of the complex function \hat{R} on the trigonometric circle at the starting point and at the investigated point, respectively: $A = \text{Re}\left(\hat{R}(T_{\text{PRF}})_i\right) + i\text{Im}\left(\hat{R}(T_{\text{PRF}})_i\right)$ and $B = \text{Re}\left(\hat{R}(T_{\text{PRF}})_{i+1}\right) + i\text{Im}\left(\hat{R}(T_{\text{PRF}})_{i+1}\right)$; (b) Demonstration of the dealiasing; solid line: initial signal; dashed line: dealiased signal

The quadrant of the phase function of the starting value (i) and of the investigated value ($i + 1$) gives an indication as to whether aliasing has occurred, and consequently the sense in which the aliasing correction has to be made. The algorithm only considers values as aliased when they are not located in the same hemisphere as the starting point. As indicated in Fig. 7, starting point A is in the positive hemisphere and the neighbouring point B is in the negative hemisphere because the sense of rotation of the Doppler frequency is counterclockwise in this example. The distance between the two points is greater than the threshold and a correction, as indicated in the bottom panel of Fig. 7, has to be made by adding 2π to B.

Fig. 8 shows the application of the present dealiasing technique to the same Doppler frequency series presented before (Figs. 5 and 6). In this case, only the values that pass the established threshold between neighbouring points were dealiased ($T=1$ in this case). Comparing the velocity timeseries in Fig. 8b with the one obtained with the flow direction based dealiasing method (Fig. 6b), the improvement in the dealiasing procedure is quite obvious. The number of points which have been corrected is greatly reduced. Examining the four receivers Doppler frequency timeseries, we find that this method corrects the data well and is more robust than the method based on the known flow direction.

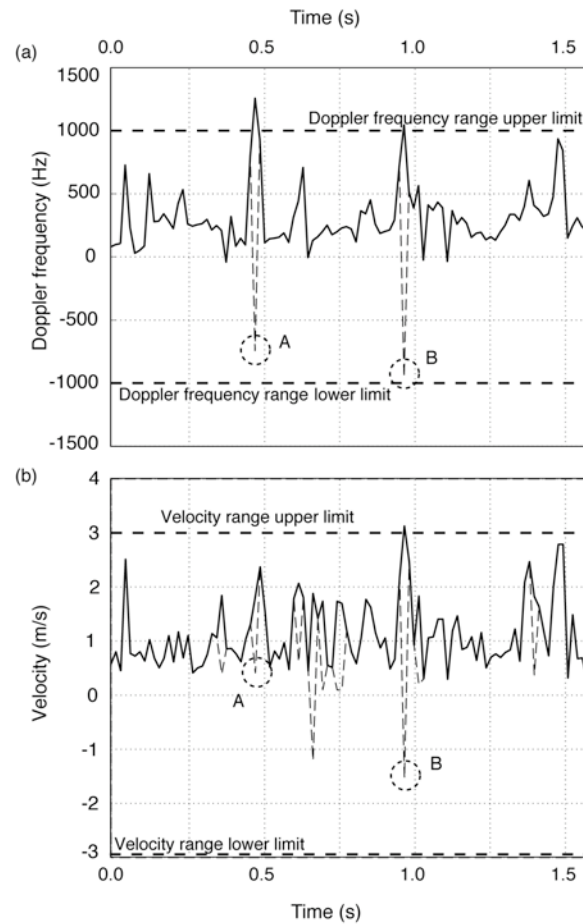


Figure 8, Example of dealiasing based on the signal history made on the Doppler frequency series (same data as in Figs. 5 and 6): (a) Doppler frequencies at one receiver; (b) horizontal velocity data in the streamwise direction obtained by combining all four receiver data. The continuous line corresponds to the dealiased series, the original data are presented with a dashed line. Data obtained with a frequency $f_a=62.5$ Hz.

For a mean velocity profile in the river, the results with and without the application of dealiasing are compared in Fig. 9. In the mean velocity profile, the untreated aliased data show a decrease of the velocity in the upper zone of the flow. When the data are corrected, the mean velocity profile approaches the expected logarithmic profile. This example indicates that, as expected, aliasing becomes more likely in the upper part of the profile where flow velocities are higher.

Fig. 10 shows the so-called dealiasing matrix for the same data set as in Fig. 9. This matrix is useful in visualising the degree of dealiasing in the data. Each cell of the matrix represents an instantaneous Doppler frequency in the space-time domain and a matrix corresponds to one profile measured by one of the receivers. Dealiased cells are represented in white.

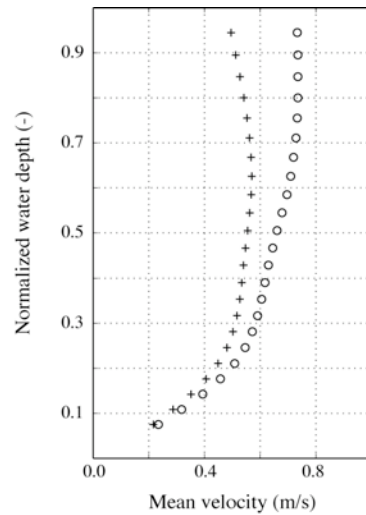


Figure 9: Example of open-channel mean velocity profile with and without application of the dealiasing algorithm based on the signal history. Dealised values are presented by circles whereas values obtained from the original data are presented by crosses. Data obtained with a frequency $f_a=62.5$ Hz.

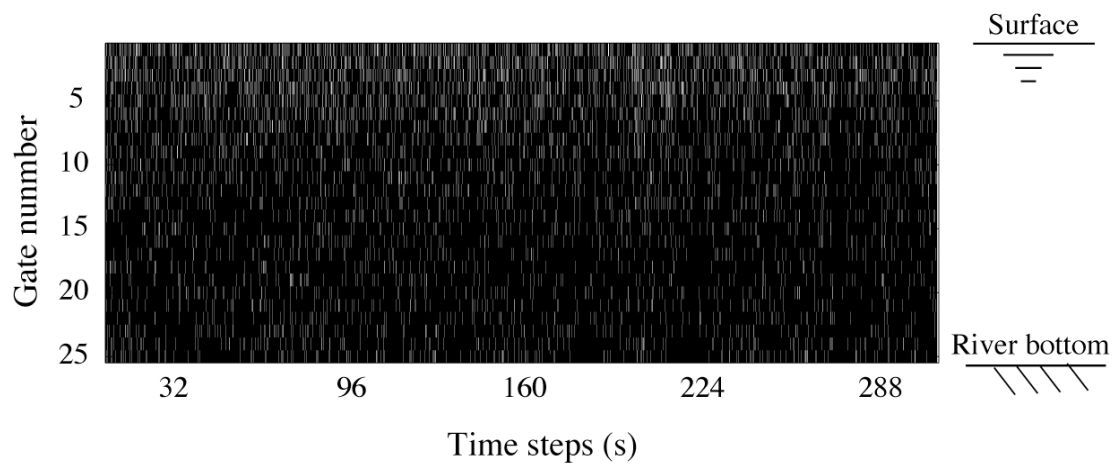


Figure 10: Example of the dealiasing matrix applied to the data of one of the four ADVP receivers; this matrix shows the position of the dealiased cells in the gate/time matrix of open-channel measurements (in white the corrected cells). The horizontal axis represents the time. The vertical axis represents the profile gates in the vertical with gate 1 close to the water surface and gate 25 near the river bottom. Data obtained with a frequency $f_a=62.5$ Hz.

An analysis of the dealiasing matrix allows to evaluate the data quality by its dealiasing level and to determine errors in the dealiasing process. In the present example, the dealiasing level (defined as the ratio between dealiased cells and the total number of cells) is about 6 %. As was already evident from the profile in Fig. 9, most of the aliasing occurs in the upper zone of the water column (Fig. 10) where velocities are higher and the Doppler frequency may exceed the Nyquist frequency. An aliasing gradient is found along the water column which may be explained by two factors: the decrease of angle α with

the water depth improves the velocity measuring performance (expression 2; Fig. 1) and the decrease of the local velocity with water depth. The above-mentioned 3-dimensionality of the flow may also explain the occurrence of aliasing since the range limit of the horizontal velocity is smaller than the limit for the streamwise component. The presence of large areas of aliasing in the dealiasing matrix may indicate that error sources other than aliasing are contaminating the signal.

Another possible source of error is the uncertainty related to the estimate of the Doppler frequency. This uncertainty is due to the phase angle introduced by the random variation of the relative location of scattering targets in the measuring volume. The most important sources of this Doppler spectral broadening are (Brumley *et al.* 1991): advection of the backscattered particles inside the volume (finite target residence time); local variation of the particles position resulting from turbulent movement inside the sampling volume; beam divergence; flow acceleration during the NPP-averaging period. Cabrera *et al.* (1987) discuss these contributions for the Doppler uncertainty and provide estimates for each of them. Lhermitte and Lemmin (1990) give estimates for the present ADVP. Hurther and Lemmin (1998) show how constant beam width transducers can improve the situation. Dealiasing will contribute to the reduction of spectral broadening.

4 SUMMARY AND CONCLUSION

The method of dealiasing presented here is a simple and easy implementation approach to the aliasing problem which occurs in acoustic Doppler instrumentation and affects velocity and turbulence measurements. The dealiasing procedure is based on the signal history and assumes that coherence must exist between subsequent Doppler estimates. In a first step, a threshold determines the necessity for dealiasing. In the second step, a dealiasing algorithm is applied if required. It is based on the analyses of the quadrant localization of a point pair using the complex autocorrelation function derived from the complex echo signal. This procedure is applied to the raw backscattered signal and corrects the instantaneous values of the Doppler frequency. Considering that it works directly on the Doppler frequency series of each of the ADVP receivers it avoids the problem of the so-called hidden errors, which occur when dealiasing is carried out in the velocity domain. It has to be remembered that in a multistatic ADVP configuration (Hurther and Lemmin 2000), aliasing does not necessarily occur in all receiver directions at the same time. Thus, dealiasing has to be carried out for each individual receiver signal separately.

Furthermore, this dealiasing method allows correcting several degrees of data aliasing. Since the method is based on the trigonometric position of a neighbouring complex autocorrelation, the algorithm can progress indefinitely in both directions of the trigonometric circle, if the threshold condition is respected.

The analysis has demonstrated the usefulness of access to raw data in the aliasing analysis of Doppler based velocity measurements. In fact, the analysis at the level of the phase angle of the autocorrelation function of the complex echo signal corrects the Doppler frequency values before their conversion into velocities. Applying the technique before estimating the Doppler frequency has the advantage of correcting at the same time not only the aliasing errors in the velocity in the longitudinal, but also in the transversal and vertical directions.

The treatment of the data in the early stage of the data acquisition brings obvious advantages when compared with standard dealiasing processes commonly applied to instantaneous velocities (Goring and Nikora 2002). Recently, Blanckaert and Lemmin (2005) presented for a multistatic ADVP configuration a noise-free calculation of the Reynolds stress tensor components (turbulent intensity and shear stress values) directly from the components of the Doppler frequency covariance matrix of the four receivers.

Combined with the application of the present dealiasing method in the raw data, the Reynolds stress tensor algorithm is then theoretically free of noise and also free of errors due to data aliasing.

The method of dealiasing presented is a simple but effective phase unwrapping procedure. Its feasibility was demonstrated in a data pre-treatment process. However, it can easily be implemented in a real time system.

ACKNOWLEDGEMENTS

The authors wish to acknowledge the financial support of FCT (BD 6727/2001) and the Swiss National Science Foundation (2000-063818). We thank David Hurther, Koen Blanckaert and Eugene Terray for the fruitful discussions and suggestions during the development of the methodology.

REFERENCES

- Blanckaert K. and Lemmin U. (2005), Means of noise reduction in acoustic turbulence measurements, *J. Hydr. Res.* (in press).
- Brumley B.H., Cabrera R.G., Deines K.L. and Terray E.A. (1991), Performance of a broad-band acoustic Doppler current profiler, *IEEE J. Oc. Eng.*, 16(4), 402-407.
- Cabrera R G, Deines K.L., Brumley B.H. and Terray E.A. (1987), Development of a practical coherent acoustic Doppler current profiler, *Proc. Oceans '87*, Halifax (Canada).
- Cellino M. and Lemmin U. (2004), Influence of coherent flow structures on the dynamics of suspended sediment transport in open-channel flow, *J. Hydr. Eng.*, 130(11), 1077-1088.
- Costantini M. (1996), A phase unwrapping method based on network programming, *FRINGE 96*, Zurich (Switzerland)
- Doviak R.J. and Zrnic D.S. (1993), *Doppler radar and weather observations*, Academic Press, San Diego (USA).
- Durden S.L. and Werner C.L. (1996), Application of an interferometric phase unwrapping technique to dealiasing of weather radar velocity fields, *J. Atmosph. Ocean. Technol.*, 13, 1107-1109.
- Franca MJ and Lemmin U. (2004 – A.1), A field study of extremely rough, three-dimensional river flow, *Proceedings 4th International Symposium Environmental Hydraulics - IAHR*, Hong Kong (China). Appendix A.1.
- Friedrich K. and Caumont O. (2004), Dealiasing Doppler velocities measured by a bistatic radar network during a downburst-producing thunderstorm, *J. Atmosph. Ocean. Technol.*, 21, 717-729.
- Gao J.D., Droegemeier K.K., Gong J.D. and Xu Q. (2004), A method for retrieving mean horizontal wind profiles from single-Doppler radar observations contaminated by aliasing, *Monthly Weather Rev.*, 132(6), 1399-1409.
- Gao J.D. and Droegemeier K.K. (2004), A variational technique for dealiasing Doppler radar velocity data, *J. Applied Meteor.*, 43(6), 934-940.
- Ghiglia D.C. and Spritt M.D. (1998), *Two-dimensional phase unwrapping. Theory algorithms and software*, John Wiley, New York (USA).
- Gong J.D., Wang L.L. and Xu Q. (2003), A three-step dealiasing method for Doppler velocity data quality control, *J. Atmosph. Ocean. Technol.*, 20, 1738-1748.

- Goring D.G. and Nikora V.I. (2002), Despiking acoustic Doppler velocimeter data, *J. Hydr. Eng.*, 128(1), 117-126.
- Holleman I. and Beekhuis H. (2003), Analysis and correction of dual PRF velocity data, *J. Atmosph. Ocean. Technol.*, 20, 443-453.
- Hurther D., Lemmin U. and Blanckaert K. (2002), A field study of transport and mixing in a river, using an acoustic Doppler velocity profiler, *Proc. Riverflow 2002*, Louvain-la-Neuve (Belgium).
- Hurther D. and Lemmin U. (2000), A correction method for turbulence measurements with a 3D acoustic Doppler velocity profiler, *J. Atmosph. Ocean. Technol.*, 18, 446-458.
- Hurther D. and Lemmin U. (1998), A constant-beam-width transducer for 3D acoustic Doppler profile measurements in open-channel flows, *Meas. Sci. Technol.*, 9, 1706-1714.
- James C.N. and Houze Jr. R.A. (2001), A real-time four-dimensional Doppler dealiasing scheme, *J. Atmosph. Ocean. Technol.*, 18(10), 1674-1683.
- Joe P. and May P.T. (2003), Correction of dual PRF velocity errors for operational Doppler weather radars, *J. Atmosph. Ocean. Technol.*, 20, 429-442.
- Lemmin U. and Rolland T. (1997), Acoustic velocity profiler for laboratory and field studies, *J. Hydr. Eng.*, 123(12), 1089-1098.
- Lhermitte R. (1983), Doppler sonar observation of tidal flow, *J. Geophys. Res.*, 88, 725-742.
- Lhermitte R. (1999), Tidal flow velocity and turbulence measurements, Internal publication Rosenstiel School of Marine and Atmospheric Science University of Miami.
- Lhermitte R. and Lemmin U. (1990), Probing water turbulence by high frequency Doppler sonar, *Geophys. Res. Letters*, 17, 1549-1552.
- Lhermitte R. and Serafin R. (1984), Pulse-to-pulse coherent signal processing techniques, *J. Atmos. Ocean. Technol.*, 4, 293-308.
- Nico G., Palubinskas G. and Datcu M. (2000), Bayesian approaches to phase-unwrapping: theoretical study, *IEEE Trans. Sign. Proc.*, 48(9), 2545-2556.
- Shen C. and Lemmin U. (1997), Ultrasonic scattering in highly turbulent clear water flow, *Ultrasonics*, 35, 57-64.
- Strand J. and Taxt T. (1999), Performance evaluation of two-dimensional phase unwrapping algorithms, *Applied Optics*, 38(20), 4333-4334.
- Volkov V.V. and Zhu Y. (2003), Deterministic phase unwrapping in the presence of noise. *Optics Letters*, 28(22), 2156-2158.

3. FIELDWORK

3.1 – Mean streamwise velocity in gravel-bed river flows

3.2 – 3D mean velocity distribution in gravel-bed rivers

3.3 – The occurrence of s-shaped velocity profiles in gravel-bed river flows

3.4 – Flow resistance characterization in shallow gravel-bed rivers

3.5 – Streamwise Velocity Pulsation (SVP) in gravel-bed rivers

3.6 – Boundary layer bursting packets associated with high- and low-speed wedges detected through a wavelet multiresolution analysis

3.7 – Evaluation of energetic scales in turbulent gravel-bed rivers based on wavelet analysis

3.8 – TKE budget analysis in gravel-bed river flow

3.1 MEAN STREAMWISE VELOCITY IN GRAVEL-BED RIVER FLOWS

Subchapter 3.1 was submitted for publication to the journal, Earth Surface Processes and Landforms (BGRG). The authors are M.J. Franca and U. Lemmin.

This paper presents results from the rivers Venoge and Chamberonne and focuses on the streamwise mean properties of the flow, namely the velocity profile, equivalent roughness, and bottom shear velocity.

	ABSTRACT	3.1.1
1	INTRODUCTION	3.1.1
2	FIELD STUDY	3.1.2
3	INSTRUMENTATION	3.1.3
4	RESULTS	3.1.3
4.1	Bottom roughness	3.1.3
4.2	Mean velocity profile	3.1.4
4.3	Bottom shear velocity	3.1.7
5	CONCLUSION	3.1.9
	ACKNOWLEDGEMENTS	3.1.10
	REFERENCES	3.1.10

MEAN STREAMWISE VELOCITY IN GRAVEL-BED RIVER FLOWS

ABSTRACT

Field measurements were made under stationary conditions during a low water period in the Swiss lowland rivers, Venoge and Chamberonne, using the deployable 3-D Acoustic Doppler Velocity Profiler (ADVP). In the river Venoge, 25 profiles were measured, and in the river Chamberonne, 24 profiles were measured. Both riverbeds are hydraulically rough, composed of coarse gravel and with randomly spaced protuberances as high as half the water depth. The analysis focuses on the streamwise mean properties of the flow, namely the velocity profile, equivalent roughness, and bottom shear velocity. The studied flows are highly three-dimensional compromising any approach on the flow description that does not account for local effects. The log-law approach to represent the mean velocity distribution proved to be quite robust (more than 65% of the measured profiles are log-shaped). Nevertheless, the results for shear velocities computed from the log-law approach do not always match with those determined from the analysis of the vertical shear stress distribution. Shear velocities obtained from the river mean slope assuming uniform flow conditions do not represent the actual energy loss in the flow. The equivalent roughness resulting from the application of the log-law constitutes a valid approach for the qualitative mapping of the local river roughness.

Key-words: 3D flow; gravel-bed rivers; mean velocity profile; 3D-ADVP

1 INTRODUCTION

Open-channel turbulence studies are essential for the development of engineering concepts and tools for river processes concerning sediment transport, morphology evolution, secondary flows and mixing and transport of matter. At present, carefully controlled laboratory experiments and numerical simulations are the main source of information for open-channel turbulence and for the interpretation of flow phenomena in rivers. These laboratory open-channel studies are typically carried out under idealized conditions of uniform flow and flat beds with fairly homogeneous bed roughness distribution. Such conditions, however, are rarely found in rivers. Although field studies in rivers are desirable, in contrast to the large number of existing laboratory studies, few field investigations in natural or canalized rivers have been made. This is mainly due to the lack of suitable instrumentation.

Recent field study publications provide information on certain flow features in rivers (R) or artificial channels (C). These studies analyze mean velocities, turbulence intensities, shear stresses, bed shear, friction velocity, roughness parameters and velocity spectra (González et al. (1996-C), Smart (1999-R) and Babaeyan-Koopaei et al. (2002-R)). Powell et al. (1999-C) observed a strong variation of the bed-load transport along the cross section. Nikora and Smart (1997-R) studied the vertical distribution of turbulent energy dissipation and characteristic turbulence scales. Nikora and Goring (2000-C) investigated differences of turbulence features between weakly mobile and fixed gravel bed cases. Buffin-Bélanger et al. (2000-R) and Hurther et al. (2002-R) documented the existence of coherent structures in rivers and their influence on transport and mixing. Tritico and Hotchkiss (2005) described

turbulence characteristics in the wake of obstructions. More recently, Roy et al. (2004-R) studied flow structures in gravel-bed rivers. Franca and Lemmin (2004 – A.1-R) focused on the three-dimensional character of the mean river flow and its implication on mixing and transport.

In the present study, results are presented from a field measurement campaign made in the Swiss rivers, Venoge and Chamberonne under stationary flow conditions. The results focus on mean velocity components. Theoretical approaches for the mean velocity profile are compared with the measurements. The friction velocity is calculated using three different methods: the log-law approach (profile method); using the river slope and water depth for an ideal two-dimensional uniform flow; and from the vertical shear stress distribution (eddy-correlation method).

2 FIELD STUDY

Field measurements of instantaneous velocity profiles were carried out during the summer of 2003, in the rivers Venoge and Chamberonne. Both are lowland rivers (Fig. 1) and are located in the canton of Vaud, Switzerland. Investigations were made along one cross-section on a straight river reach during a shallow water period. The cross sections are located at the following sites: in the river Venoge, 120 m upstream from the Moulin de Lussey and in the river Chamberonne, 385 m upstream from the river mouth. Table 1 summarizes the flow conditions.



FIGURE 1 – View of the study reaches of the rivers Venoge (left hand side) and Chamberonne (right hand side).

Table 1 – Summary of the rivers' flow characteristics

River	Mean slope – S (%)	Discharge – Q (m ³ /s)	Mean water depth – $\bar{\delta}$ (m)	Width – B (m)	Re = $\bar{U}\bar{\delta}/\nu$ (x10 ⁴)	Fr = $\bar{U}/\sqrt{g\bar{\delta}}$	D ₅₀ from the bottom ⁽¹⁾ (mm)
Venoge	0.33	0.80	0.21	6.30	3.0 – 14.4	0.20 – 0.90	40
Chamberonne	0.26	0.55	0.25	5.75	4.5 – 12.3	0.24 – 0.44	49

⁽¹⁾ D₅₀ obtained from a sample of the bottom material.

Re is the Reynolds number; \bar{U} , the vertical averaged streamwise velocity; ν , the cinematic viscosity (taken in the present study as being equal to $1.01 \times 10^{-6} \text{m}^2 \text{s}^{-1}$); Fr, the Froude number; g, the gravity acceleration and D₅₀, the bottom grain size diameter for which 50% of the grains have smaller diameters.

Based on the average water depth, the ratio $B/\bar{\delta}$ takes the values 30 and 23 for the rivers Venoge and Chamberonne, respectively. Both cases correspond to shallow water or wide channels. For the Venoge, the river slope was determined with topographic data obtained from IATE/HYDRAM (1996) and for the Chamberonne from the Gesrau system (SESA - Canton of Vaud). Both river bottoms have a gravel-armoured layer.

For each river, all measurements were taken on a single day. The discharge in the river sections was constant during the measurement time, as was confirmed by discharge data provided by the Swiss Hydrological and Geological Services. Assuming symmetrical conditions in the river, measurements were made only in one half of the cross section of the rivers, starting from the right riverbank in both cases. For the river Venoge 25 profiles were measured during a 5 minute period each with horizontal spacing of 10 to 12.5 cm, and for the river Chamberonne 24 profiles were measured, also of 5 minute duration each, with horizontal spacing of 5 to 12.5 cm. During the measurements no sediment transport was observed and this was confirmed by an analysis based on the Shields diagram.

3 INSTRUMENTATION

We used the 3-D ADVP which was developed at the LHE. This instrument allows the measurement of the 3-D quasi-instantaneous velocity field over the entire flow depth. Covering the production and the inertial ranges in the spectral space, it has sufficient space and time resolution to estimate the main turbulent parameters in open-channel flows. A detailed description of the ADVP system is given in the literature (Rolland and Lemmin 1997). In ADVP instruments, the signal emitted by the ultrasonic emitter-transducer is backscattered by moving targets and captured by a receiver-transducer. The quality of the signal depends on the scattering targets and their capability to follow the fluid motion (Shen and Lemmin 1997). The Doppler frequency shift observed between the emitted and the received signal is proportional to target's velocity in the receiver direction. The ADVP configuration used in the present measurements consists of four receivers that surround the emitter providing one redundancy in the three-dimensional velocity component calculation. This redundancy is used to eliminate signal noise and to control the data quality (Hurther and Lemmin 2000).

For both rivers, a Pulse Repetition Frequency (PRF) of 2000 Hz and a Number of Pulse Pairs (NPP) equal to 32 was used, which results in a sampling frequency of 62.5 Hz. Although a low degree of aliasing was expected, a dealiasing algorithm developed by the authors was applied to the data (Franca and Lemmin 2005 – 2.2). For the two-dimensional displacement of the ADVP system, a portable metal bridge structure was installed and is levelled so that the instrument always had the same distance from the water surface (Fig. 1). This set-up allowed efficient profiling and a minimum disturbance of the flow by the measuring installation, minimizing at the same time vibrations of the ADVP instrument.

4 RESULTS

4.1 Bottom roughness

For both rivers, riverbed sediments were sampled and analyzed according to the sample collection method for coarse rivers proposed by Wolman (1954). The bottom samples were taken from the armoured layer. The analysis was made using standard sieve sizes to obtain the weighted grain size distribution. The grain size distribution of the riverbed material is shown in Fig. 2. As indicated in Table 1, river Venoge sediments have a D_{50} of 40 mm and those of the Chamberonne a D_{50} of 49 mm. By definition, both riverbeds are composed of coarse gravel. The cumulative bed particle size distribution is

compared to the cumulative distribution of the equivalent roughness which is computed from the log-law applied to the measured profiles, assuming turbulent rough conditions.

Two distinct cases occur in the two rivers (Fig. 2). In the Venoge river, both the grain size and the equivalent roughness distributions collapse for values beyond the values $D_{50} \approx k_{50}$ (k_{50} is the equivalent roughness for which 50% of the roughness values are smaller). In the Chamberonne river, both curves only cross over once, for $D_{28} \approx k_{28}$. In this case the grain diameter distribution has a higher slope. The discrepancies in the distribution increase in the lower zones of the curves with a maximum difference of about 17% in both cases. The equivalent roughness k varies between 1.5 mm and 119.5 mm for the Venoge and between 5.0 mm and 212.8 mm for the Chamberonne. The equivalent roughness k_{50} for which 50% of the roughness values are smaller, corresponds to the values of D_{50} and D_{84} for the Venoge and Chamberonne rivers, respectively.

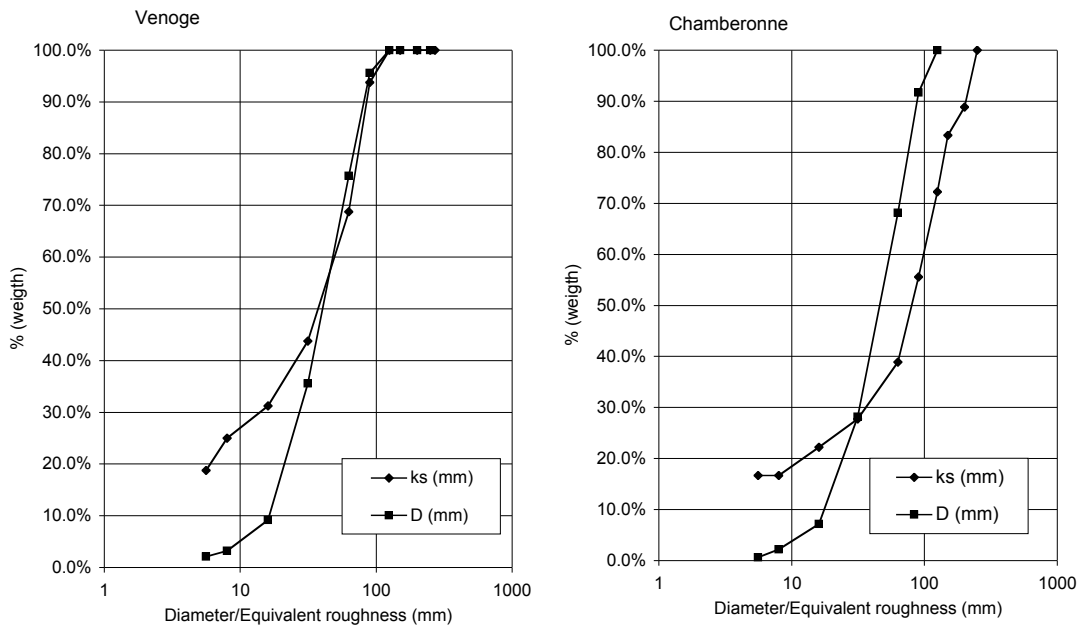


FIGURE 2 – Bottom grain diameter and equivalent roughness distribution for the two rivers.

4.2 Mean velocity profile

In this study, the measured mean velocity profiles are compared with the classic logarithmic approach. As indicated above, the riverbed is fully rough, and the following analysis will be carried out for completely rough flow. Considering the bulk mean velocity and a cross-section averaged water depth, the Reynolds numbers for the rivers, Venoge and Chamberonne are of the order of magnitude 10^5 and 10^4 , respectively. In both cases we deal with turbulent flow. The mean velocity (U) log-law approach was applied to $z/\delta < 0.20$ (z is the vertical direction and δ is the water depth) to the measured profiles:

$$U = C_1 \ln(z) + C_2 \quad (1)$$

The origin of the logarithmic profile was set on the top of the river bottom material situated in the measured profile. In the present study, the aim was to verify the suitability of the logarithmic approach for extremely rough flows and there was no intention to determine the best position for the origin of the

log-law profile. Coefficients C1 and C2 were obtained through a simple linear regression. The Nikuradse equivalent roughness (k) and the friction velocity (U^*) were calculated for each profile from the log-law expression for completely rough flows:

$$\frac{U}{U^*} = \frac{1}{\kappa} \ln\left(\frac{z}{k}\right) + A \quad (2)$$

where κ is the von Karman constant (taken as $\kappa = 0.41$), and A was set equal to 8.5 for turbulent rough flows (Kironoto and Graf 1994). The friction velocity and equivalent roughness were calculated by the profile method, regressing the velocity against the logarithm of the water depth (Bergeron and Abrahams 1992). The logarithmic layer is found to be valid in the majority of the profiles measured (Fig. 3). In about 65% of the profiles the log law can be applied without apparent deviations up to $z/\delta=0.4$. The distance from the bottom to $z/\delta=0.40$ corresponds roughly to the D_{90} of the riverbed material. In 92% of the measured profiles we find $k^+ > 70$ which corresponds to completely rough bed cases. k^+ is the dimensionless roughness defined as $k^+ = \frac{kU^*}{\nu}$ (Nezu and Nakagawa 1993).

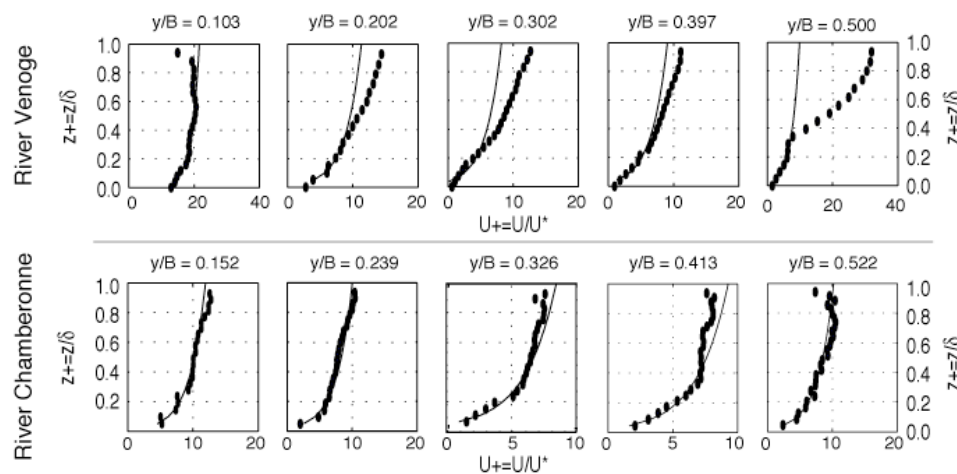


FIGURE 3 – Mean velocity profiles at several positions for both rivers. Points: measured data; line: logarithmic profile.

Above $z/\delta=0.40$ some of the mean velocity profiles show strong deviations from the logarithmic profile. It is difficult to establish a general tendency in the deviations, because they occur in both ways by increase or decrease of the flow velocity. For decelerated flow, the mean velocity profile sometimes acquires a so-called D-shape (Chamberonne at $y/B=0.522$, where y is the spanwise direction), common in gravel bed rivers, as reported by Ferro and Baiamonte (1994).

In some velocity profiles such as for $y/B=0.302$ (Venoge), a wake effect near the bottom is noted for $z/\delta < 0.20$ which may be caused by a sudden change of the bed level or roughness upstream from the measuring point as observed by Carravetta and Della Morte (2004). Such profiles correspond to the so-called s-profiles and they are widely observed in gravel-bed rivers in the presence of large obstacles (Marchand et al. 1984, Bathurst 1988). Nelson et al. (1993) and Buffin-Bélanger and Roy (1998) indicate that the wake effect formed by the presence of bed forms is responsible for the observed deviations in the lower layers of the velocity profile. Baiamonte et al. (1995) show the delay effect produced by boulder drag in gravel-bed rivers and Katul et al. (2002) compare the velocity deviations produced in gravel-bed rivers with the inflected profiles in atmospheric flows above canopy.

In the mean velocity profiles we observe shear zones which are not produced by bottom drag. For $y/B=0.50$ (Venoge), the mean gradient of the shear zone located between $z/\delta=0.30$ and $z/\delta=0.80$ is three times more intense than the bottom one. This suggests that turbulence production may exist throughout the water column and strong mixing can be expected.

Fig. 4 shows the distribution of the equivalent roughness computed with the log-law across the river sections, and the bottom profile. The variation of the equivalent roughness relates to bed forms, and is more obvious in the river Chamberonne (discussed in Franca and Lemmin 2005 – A.3). Although the log-law cannot be applied to describe the velocity distribution of all measured profiles, it may be argued that the k values obtained are still a useful order of magnitude indicator of the (form conditioned) roughness distribution across the river section.

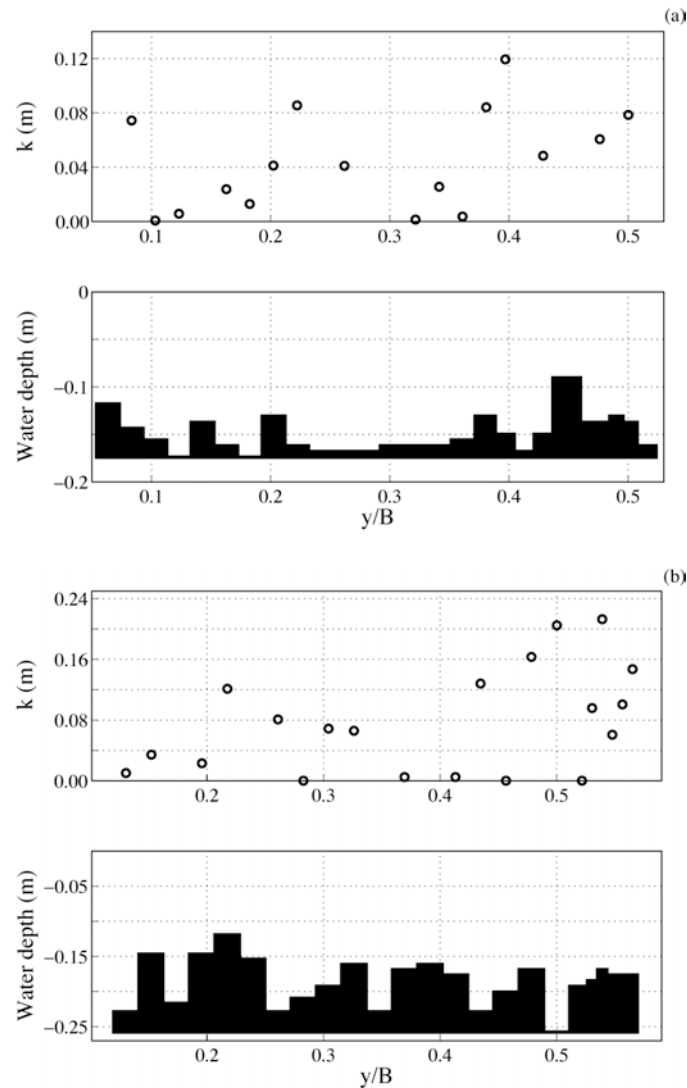


FIGURE 4 – Distribution of the local equivalent roughness across the river section determined from the log-law (top) and bottom profile (bottom); Venoge (a) and Chamberonne (b).

In completely rough flows, the following modified logarithmic formula is widely applied to the mean velocity profile in the inner region of the flow:

$$\frac{U}{U^*} = \frac{1}{\kappa} \ln\left(\frac{z}{Z_0}\right) \quad (3)$$

where Z_0 is generally called roughness length. From the relation $Z_0 = k/32.6$, obtained by equating eqs. (2) and (3), a representative roughness length relates to the grain diameter distribution as $0.03D_{50}$ or $0.03D_{84}$, according to the present results. The second value corresponds approximately to the lower value suggested by Smart (1999) based on van Rijn's (1982) results of $Z_0 = 0.03D_{85}$. As shown for the k values, there is a strong variation of the Z_0 values along the cross-section. Besides being related to the grain diameter, Z_0 (and consequently k) may also depend on bed form, bed load, lateral velocity gradients and upstream conditions (Smart 1999). In our study, lateral velocity gradients and upstream conditions are mainly responsible for the strong variability of k as seen in Fig. 4. The value of Z_0 corresponds to the distance from the local river bottom to the zero-plane displacement as defined by Nikora et al. (2002). In the present case, due to the highly variable riverbed, the zero-plane displacement has to be replaced by a zero-surface displacement.

4.3 Bottom shear velocity

The observed flow over macro-scale roughness is $3D$. However, since the logarithmic law fits more than half of the observed profiles, 2D concepts to calculate U^* may still be used.

The shear velocity along the cross-section can be calculated using the distribution of the Reynolds stress and the mean velocity gradient along the water column. The shear stress (τ_{xz}) in plane x-z is given by:

$$\frac{\tau_{xz}}{\rho} = -\overline{u'w'} + \nu \frac{\partial U}{\partial z} \quad (4)$$

The vertical shear distribution in 2D open-channel flows is assumed to be linear:

$$\frac{\tau_{xz}}{\rho} = \tau_{xz,b} \left(1 - \frac{z}{\delta}\right) \quad (5)$$

Therefore, with $\tau_{xz,b} = \rho U^{*2}$, U^* becomes:

$$U^{*2} = \frac{-\overline{u'w'} + \nu \frac{\partial U}{\partial z}}{\left(1 - \frac{z}{\delta}\right)} \quad (6)$$

This is the so-called eddy-correlation method (Monin and Yanglom 1971) and the U^* values obtained were taken as reference results for the shear velocity in the present study. For both rivers, the observed shear stress distribution is not always linear or with the expected tendency away from the bottom. As Wang et al. (2003), we only considered the linear layer close to the bottom, omitting some of the profiles. With the same approach, friction velocity values can also be calculated in the y-z plane, since we have 3D velocity profiles.

The calculation of the bottom shear velocity, or friction velocity (U^*), using the logarithmic mean velocity distribution approach was presented above. This concept is valid for 2D flows and will be applied to those profiles where the log law agreed with the mean velocity profile.

Assuming a uniform 2D open-channel flow, where the driving force (gravity term in the momentum equation) is in equilibrium with the shear force induced by bottom friction, the following expression for the calculation of the tension due to friction forces ($\tau_{xz,b}$) is given:

$$\tau_{xz,b} = \rho g R_h S \quad (7)$$

where ρ is the water mass per volume unit, g is the gravitational acceleration, R_h is the hydraulic radius and S is the mean river slope. From the definition of shear velocity ($U^{*2} = \frac{\tau_{xz,b}}{\rho}$), U^* can be estimated with the following expression for shallow water ($R_h \sim \delta$):

$$U^* = \sqrt{g\delta S} \quad (8)$$

The mean water depth is usually applied, giving a constant value of U^* along one river segment.

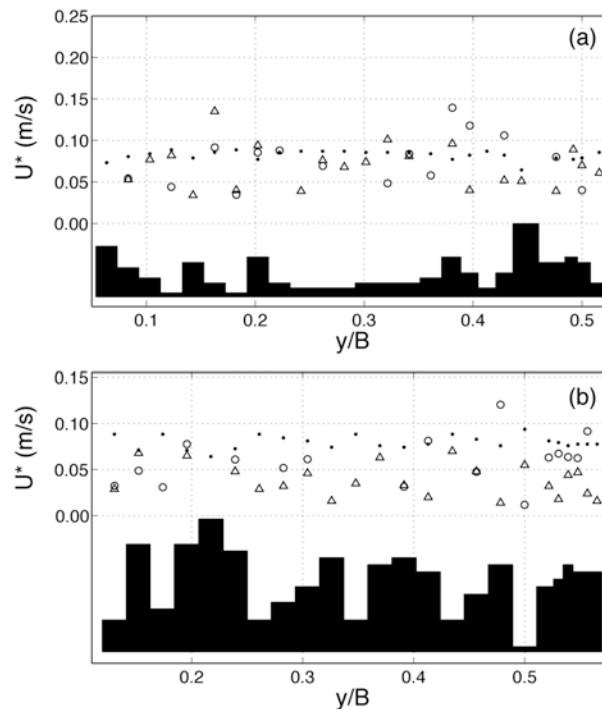


FIGURE 5 – Bottom friction velocity U^* for the Venoge (a) and the Chamberonne (b). Δ - friction velocity computed from the shear stress profiles; γ - friction velocity computed from the log-law approach; λ - friction velocity computed by expression (8).

The friction velocity obtained from the shear stress profile analysis provides the lowest estimates in most profile locations (Fig. 5). The values vary by a factor of two across the section in the river Venoge. In the Chamberonne river the amplitude of variation is even bigger. The amplitude of variation indicates that the flow field is far from uniform and 2D. In 2D uniform open-channel flows with rough beds and narrow grain size distribution, we have observed discrepancies typically smaller than 3% (Hurther and Lemmin 2000). The bed shear distribution seems to be related to bed form undulations as indicated by Powell et al. (1999) and Franca and Lemmin (2005 – A.3). The friction velocity estimates obtained from the log-law approach are generally slightly higher, but sometimes nearly coincide with those obtained by shear stress analysis. For the Venoge, the two results are closer than those for the Chamberonne flow.

Using Eq. (8), one obtains section-averaged values of 0.082 m/s and 0.080 m/s for the Venoge and the Chamberonne respectively (based on the average values from Table 1). These may be compared to the section averaged values for the eddy correlation method which are equal to 0.069 and 0.039 m/s with standard deviations of 0.026 and 0.018 m/s for the Venoge and Chamberonne, respectively. Considering only those profiles where the log-law represents the actual velocity distribution, the average shear velocity values calculated by the profile method are 0.076 and 0.059 m/s (with standard deviations of 0.030 and 0.026 m/s), respectively for the Venoge and Chamberonne. The large discrepancy between the three mean values shows that 2D section mean concepts cannot be applied to this flow. The application of expression (8) results in a strong overestimate, indicating that the energy loss in the flow cannot be described by the streamwise mean bed level gradient. Given the 3D character of the flow and the observed variability of the local resistance parameters, an analysis based on section-averaged values is not correct.

5 CONCLUSION

This paper presents the results of an intensive velocity measuring campaign made in the rivers, Venoge and Chamberonne with a deployable 3-D ADVP. In both cases, the riverbeds were composed of coarse gravel and the flow was rough, as confirmed by $k^+ > 70$ in 92% of the profiles. Based on the analysis of the mean flow characteristics, the following conclusions can be drawn:

The logarithmic law concept was applied to the measured mean velocity profiles. In 65% of the cases, it agreed well with the observed velocity data up to a water depth of $z/\delta = 0.4$ corresponding roughly to the D_{90} value of the riverbed material. Given the 3D flow character observed in both rivers, this approach proved to be relatively robust for the description of the vertical velocity distribution.

However, the log-law distribution is not adequate for bottom shear velocity calculations. The friction velocity was computed from the log-law approach (profile method) and from the shear stress distribution in the water column (eddy-correlation method which is considered the reference for the bottom shear velocity). The values obtained by the second method are generally smaller (by 10 to 33%, depending on profile location) than the ones obtained from the log-law approach. In the river Venoge, and for the measured logarithmic profiles, the average of both estimates agree better indicating that these profiles are approximately 2D. The Chamberonne flow is more 3D, and consequently the shear results diverge more from the reference values.

The determination of the shear velocity by applying the expression $U^* = \sqrt{g\delta S}$ for 2D uniform open-channel flows proved to be inadequate. Large deviations are observed in layer $z/\delta > 0.4$, indicating a 3D flow. This method generally overestimates when compared with the estimates based on shear measurements. The uniform flow conditions do not represent the actual energy loss in the flow.

The studied flows are clearly 3D and simplifications assuming 2D and uniform conditions fail in the determination of the overall estimate of the resistance parameters. Franca (2005 – A.2) showed the existence of three types of velocity profiles in measurements made in the river Venoge under similar hydraulic conditions: mono-log, s-type and 2xlog. Further research is being carried out to determine the best way to estimate the flow resistance in these three types of velocity distribution.

In the present measurements the Venoge flow is closer to 2D, since the bed variability is smaller than the Chamberonne case (Fig.5). It appears that it is not only the river apparent ratio which determines the three-dimensionality of the flow, but also the influence of the relative bed variability. This possibility should also be investigated. Further research should be carried out to define the ratio characterizing the three-dimensionality of the flow based on both: h (water depth) and χ , a length parameter representing the bed level variability (σ_h , σ_D , etc).

According to the measurements, the grain size corresponding to D_{50} or D_{84} of the riverbed material, respectively for the Venoge and Chamberonne rivers, can be taken as the equivalent roughness, called k_{50} . Using the relation $Z_0=k/32.6$, an equivalent roughness height relates to the grain diameter distribution differently for both rivers: $Z_0\approx 0.03D_{50}$ or $0.03D_{84}$. A large variation of k (or Z_0) along the cross section was found and the local k determined along the cross section has a strong contribution from the local bed forms. Although the values of k (or Z_0) computed with the measured data are only valid for the corresponding profile, they still allow to qualitatively map the riverbed roughness. However, a value for the total river equivalent roughness is not meaningful. It shows large discrepancies from the measured results across section, because the local bed forms which dominate the flow field are not taken into account. In both rivers, the bed forms may scale with $0.5\bar{\delta}$. This study shows that further detailed investigations should be carried out in order to establish a pattern for the distribution of k as function of the grain size distribution. This will result in a more realistic river roughness which is parameterized by a roughness distribution instead of a single k value.

The occurrence of D-shaped and s-shaped velocity profiles was identified. In the first case, the upper layers of the flow present strong local gradients of the streamwise velocity. In the second case, local constrictions due to sudden roughness changes induce an inflection of the velocity profile in the lower part of the water column. The existence of velocity profile inflections (s-shaped and D-shaped profiles) influences the spreading of matter, heat and momentum in the water column, because mixing is enhanced due to shear zones observed throughout the water column. Therefore, local velocity profiles depend on the bed geometry and large-scale bed forms which strongly affect mixing and transport in rivers.

ACKNOWLEDGEMENTS

Acknowledgements are due to S. Thorpe and W. Czernuszenko for the fruitful discussions, and to John Beck for helping with the topographic data. The authors acknowledge the financial support of the Portuguese Science and Technology Foundation (BD 6727/2001) and the Swiss National Science Foundation (2000-063818).

REFERENCES

- Babaeyan-Koopaei K., Ervine D.A., Carling P.A. and Cao Z. (2002), Velocity and turbulence measurements for two overbank flow events in river Severn, *J. Hydr. Eng.*, 128(10), 891-900.
- Baiamonte G., Giordano G. and Ferro V. (1995), Advances on velocity profile and flow resistance law in gravel bed rivers, *Excerpta*, 9, 41-89.
- Bathurst J.C. (1988), Velocity profile in high-gradient, boulder-bed channels, *Proc. Int. Conf. Fluv. Hydr.*, Budapest (Hungary).
- Bergeron N.E. and Abrahams A.D. (1992), Estimating shear velocity and roughness length from velocity profiles, *Water Resour. Res.*, 28(8), 2155-2158.
- Buffin-Bélanger T. and Roy A.G. (1998), Effects of a pebble cluster on the turbulent structure of a depth-limited flow in a gravel-bed river, *Geomorphology*, 25, 249-267.
- Buffin-Bélanger T., Roy A.G. and Kirkbride A.D. (2000), On large-scale flow structures in a gravel-bed river, *Geomorphology*, 32, 417-435.

- Carravetta A. and Della Morte R. (2004), Response of velocity to a sudden change of the bed roughness in sub critical open channel flow, Proc. Riverflow 2004, Naples (Italy).
- Ferro V. and Baiamonte G. (1994), Flow velocity profiles in gravel-bed rivers, J. Hydr. Eng., 120(1), 60-80.
- Franca M.J. (2005 – A.2), Flow dynamics over a gravel riverbed, Proc. of the XXXI IAHR Congress, Seoul (South Korea). Appendix A.2.
- Franca M.J. and Lemmin U. (2004 – A.1), A field study of extremely rough, three-dimensional river flow, Proc. 4th International Symposium Environmental Hydraulics - IAHR, Hong Kong (China). Appendix A.1.
- Franca M.J. and Lemmin U. (2005 – A.3), Cross-section periodicity of turbulent gravel-bed river flows, Proc. 4th RCEM, Urbana (IL - USA). Appendix A.3.
- Franca M.J. and Lemmin U. (2005 – 2.2). subchapter “Eliminating velocity aliasing in acoustic Doppler velocity profiler data”.
- González J.A., Melching C.S. and Oberg K.A. (1996), Analysis of open-channel velocity measurements collected with an acoustic doppler current profiler, Rivertech 96: Proc. 1st Int. Conf. New/Emerging Conc. Rivers, Chicago (USA).
- Hurther D., Lemmin U. and Blanckaert K. (2002), A field study of transport and mixing in a river, using an acoustic Doppler velocity profiler, Proc. Riverflow 2002, Louvain-la-Neuve (Belgium).
- Hurther D. and Lemmin U. (2000), A correction method for turbulence measurements with a 3D acoustic Doppler velocity profiler, J. Atmosph. Ocean. Technol., 18, 446-458.
- IATE/HYDRAM (1996), Profil en long, profils en travers, et courbes de tarage des sections relevées, Rapport d'étude du Bassin Versant de la Venoge - HYDRAM/EPFL, Lausanne (Switzerland).
- Katul G., Wiberg P., Albertson J. and Hornberger G. (2002), A mixing layer theory for flow resistance in shallow streams, Water Resour. Res., 38(11), 1250.
- Kironoto B.A. and Graf W.H. (1994), Turbulence characteristics in rough uniform open-channel flow, Proc. Instn. Civ. Engrs. Wat., Marit. & Energy, Vol. 106, p. 333-344.
- Marchand J.P., Jarret R.D. and Jones L.L. (1984), Velocity profile, surface slope, and bed material size for selected streams in Colorado, U.S. Geological Survey - Open File Rep. 84-733.
- Monin A.S. and Yaglom A.M. (1971), Statistical Fluid Mechanics: Mechanics of Turbulence - Vol. 1, The MIT Press, Cambridge (USA).
- Nezu I. and Nakagawa H. (1993), Turbulence in open-channel flows - IAHR monograph, A.A. Balkema, Rotterdam (The Netherlands).
- Nelson J.M., McLean S.R. and Wolfe S.R. (1993), Mean flow and turbulence fields over two-dimensional bed forms, Water Resour. Res., 29(12), 3935-3953.
- Nikora V. and Smart G.M. (1997), Turbulence characteristics of New Zealand gravel-bed rivers, J. Hydr. Eng., 123(9), 764-773.
- Nikora V. and Goring D. (2000), Flow turbulence over fixed and weakly mobile gravel beds, J. Hydr. Eng., 126(9), 679-690.
- Nikora V., Koll K., McLean S., Dittrich A. and Aberle J. (2002), Zero-plane displacement for rough-bed open-channel flows, Proc. Riverflow 2002, Louvain-la-Neuve (Belgium).
- Powell D.M., Reid I. and Laronne J.B. (1999), Hydraulic interpretation of cross-stream variations in bed load transport, J. Hydr. Eng., 125(12), 1243-1252.

- van Rijn L.C. (1982), Equivalent roughness of alluvial bed, *J. Hydr. Eng.*, 108(10), 1215-1218.
- Rolland T. and Lemmin U. (1997), A two-component acoustic velocity profiler for use in turbulent open-channel flow, *J. Hydr. Res.*, 35(4), 545-561.
- Roy A.G., Buffin-Belanger T., Lamarre H. and Kirkbride A.D. (2004), Size, shape and dynamics of large-scale turbulent flow structures in a gravel-bed river, *J. Fluid Mech.*, 500, 1-27.
- Shen C. and Lemmin U. (1997), Ultrasonic scattering in highly turbulent clear water flow, *Ultrasonics*, 35, 57-64.
- Smart G.M. (1999), Turbulent velocity profiles and boundary shear in gravel bed rivers, *J. Hydr. Eng.*, 125(2), 106-116.
- Tritico H.M. and Hotchkiss R.H. (2005), Unobstructed and obstructed turbulent flow in gravel bed rivers, *J. Hydr. Eng.*, 131(8), 635-645.
- Wang Z.Q., Cheng N.S., Chiew Y.M. and Chen X.W. (2003), Secondary flows in open channel with smooth and rough bed strips, *Proc. XXX IAHR Cong., Thessaloniki (Greece)*.
- Wolman M.G. (1954), A method of sampling coarse river-bed material, *Trans. Amer. Geoph. Un.*, 35(6), 951-956.

3.2 3D MEAN VELOCITY DISTRIBUTION IN GRAVEL-BED RIVERS

Subchapter 3.2 was submitted for publication to the journal *Geomorphology*. The authors are M.J. Franca and U. Lemmin.

This paper concerns results of the rivers Venoge and Chamberonne and it focuses on the 3D characteristics of the mean flow, namely bed forms influence, riverbank drag effect, organized secondary motion (SLOM) and D-profile.

	ABSTRACT	3.2.1
1	INTRODUCTION	3.2.1
2	FIELD STUDY AND INSTRUMENTATION	3.2.2
3	RESULTS	3.2.3
3.1	Mean velocity profile	3.2.3
3.2	Cross section mean velocity distribution	3.2.3
3.3	3D analysis of the mean flow	3.2.5
3.4	Bottom influence	3.2.7
3.5	Jets and low velocity regions in the upper layer (CH and CL regions)	3.2.8
3.6	The D-shaped velocity profile as a response to riverbed morphology	3.2.9
3.7	Horizontal Froude number analysis	3.2.11
4	CONCLUSIONS	3.2.11
	ACKNOWLEDGEMENTS	3.2.13
	REFERENCES	3.2.13

3D MEAN VELOCITY DISTRIBUTION IN GRAVEL-BED RIVERS

ABSTRACT

Results from 3D Acoustic Doppler Velocity Profiler (ADVP) measurements in shallow gravel-bed rivers are presented. The bed is composed of coarse gravel boulders scaling as high as half the water depth. Hydraulically, the river flows are turbulent and rough. The results focus on the 3D character of the river flow. The wall effect of the riverbank is shown. 3D features of the flow, mainly due to large-scale bottom roughness, are made evident. The bottom topography locally produces important secondary mean motion in the flow. A permanent flow structure is observed in the upper layer of the flow: local jets compensated by lower velocity regions were detected in the longitudinal velocity field, corresponding to an organized compensatory secondary motion with streamwise vorticity (Surface Layer Organized Movement – SLOM). This mechanism seems to be confined to $z/\delta > 0.80$ due to the macro-roughness effect. The so-called D-shaped profile distribution is formed near the surface where the velocity is lower. A relationship between the occurrence of D-shaped profiles and the local Froude number is established. The importance of the cross section variation of the flow regime is assessed and the response of the water surface to the riverbed morphology is investigated.

Key-words: 3D flow; gravel-bed rivers; mean velocity distribution; D-profile

1 INTRODUCTION

The extensive literature related to open-channel turbulent processes is mainly based on well-controlled laboratory experiments or numerical simulations. When compared to the available laboratory results, field studies on river phenomena are rare. This is mainly due to lack of suitable instrumentation. Fieldwork is needed to validate existing theories and develop new concepts. Knowledge of river processes related to sediment transport, morphology evolution, secondary flows and mixing and transport of matter is also desirable.

Some recent studies provide information on such river dynamics as mean velocities, turbulence intensities, shear stresses, bed shear, friction velocity, roughness parameters and velocity spectra (González et al. (1996), Smart (1999) and Babaeyan-Koopaei et al. (2002)); bed-load transport across the river section (Powell et al. 1999); vertical distribution of turbulent energy dissipation and characteristic turbulent scales (Nikora and Smart 1997); turbulence features between weakly mobile and fixed gravel bed cases (Nikora and Goring 2000); coherent structures in rivers and their influence on transport and mixing (Buffin-Bélanger et al. (2000) and Hurther et al. (2002)); turbulence in the wake of obstructions (Buffin-Bélanger and Roy (1998) and Tritico and Hotchkiss (2005)); flow structures present in gravel bed rivers (Roy et al. 2004).

2D concepts are no longer valid for shallow river flows over large-scale roughness (Franca and Lemmin 2004 – A.1). The three-dimensionality of these flows and their space and time variability are still an

open subject. Only instantaneous 3D data acquisition allows a correct interpretation of the hydraulic processes.

This paper presents results based on river measurements made with the deployable 3D ADVP instrument developed at the LHE-EPFL. The results focus on the 3D distribution of the mean velocity components. Several important aspects of the flow are assessed: cross-section velocity distribution; influence of the bed forms on the flow resistance; influence of the bed roughness on the velocity distribution; existence of D-shaped profiles, some with flow inversion; three-dimensionality of the flow; importance of the flow regime; and influence of the bed morphology on the surface layer.

2 FIELD STUDY AND INSTRUMENTATION

A detailed description of the present fieldwork is given by Franca and Lemmin (2005 – 3.1). The river measurements were made during the summer of 2003, in the Swiss rivers Venoge and Chamberonne. The fieldwork was carried out under stationary flow and shallow water conditions (Table 1).

Table 1 – Summary of the rivers' flow characteristics.

River	Mean slope – S (%)	Discharge – Q (m ³ /s)	Mean water depth – $\bar{\delta}$ (m)	Width – B (m)	Re = $\bar{U}\bar{\delta}/\nu$ (x10 ⁴)	Fr = $\bar{U}/\sqrt{g\bar{\delta}}$	D ₅₀ from the bottom ^(a) (mm)
Venoge	0.33	0.80	0.21	6.30	3.0 – 14.4	0.20 – 0.90	40
Chamberonne	0.26	0.55	0.25	5.75	4.5 – 12.3	0.24 – 0.44	49

^(a) D₅₀ obtained from a sample of the bottom material.

In Table 1, Re is the Reynolds number; \bar{U} , the vertically averaged streamwise velocity; ν , the kinematic viscosity (taken in the present study as being equal to $1.01 \times 10^{-6} \text{m}^2 \text{s}^{-1}$); Fr, the Froude number; g, the gravity acceleration and D₅₀, the bottom grain size diameter for which 50% of the grains have a smaller diameter. The riverbed material was sampled according to the Wolman method (Wolman 1954).

The data acquisition was made only in one half of the cross section of the rivers, starting from the right riverbank. For the Venoge, 25 profiles were measured with a horizontal spacing of 10.0 to 12.5 cm, and for the river Chamberonne, 24 with spacing between 5.0 to 12.5 cm. The distance between vertical positions was between 6 and 12 mm. The instantaneous velocity profiles were measured for 5 minutes. Measurements of the 3D quasi-instantaneous velocity field over the entire depth of the flow were made with the ADVP. The ADVP is a Doppler based sonar instrument which was developed at the LHE (Rolland and Lemmin 1997). The measuring configurations for both river measurements were indicated in Franca and Lemmin (2005 – 3.1). A Pulse Repetition Frequency (PRF) of 2000 Hz and a Number of Pulse Pairs (NPP) equal to 32 were used, resulting in a sampling frequency of 62.5 Hz. The multistatic ADVP configuration permitted signal noise elimination and the control of the data quality (Hurther and Lemmin 2000). A dealiasing algorithm based on the signal history was applied (Franca and Lemmin 2005 – 2.2). A metal bridge was built to support the ADVP. It allowed the easy and stable 2D displacement of the instrument.

3 RESULTS

3.1 Mean velocity profile

We previously investigated the mean streamwise velocity of these field measurements (Franca and Lemmin 2005 – 3.1) and concluded that despite the three-dimensionality of the flow, the log law still describes the mean velocity distribution for more than 50% of the profiles. For the determination of an overall value for the friction velocity however, the log-law approach (profile method) does not give satisfactory results. A relation between the distribution from grain diameter (D) and equivalent roughness (k) seems to exist. The equivalent roughness determined locally across the river section shows a strong contribution from the local bed forms. The Nikuradse equivalent roughness determined from the profile method can be used to qualitatively map the river bottom roughness.

3.2 Cross section mean velocity distribution

Considering the wide range of observed roughness heights and velocity profile deformation, we determined that the flows are 3D (Franca and Lemmin 2005 – 3.1). Figs. 1 and 2 present contour line graphics of the mean longitudinal velocity distribution in the two rivers. These figures also give the values of the following flow parameters: Nikuradse equivalent roughness (k) calculated with the logarithmic law distribution; Reynolds number (Re), computed with the vertically averaged velocity, and dimensionless roughness ($k^+ = \frac{kU^*}{\nu}$). As expected, the majority of the measured profiles corresponds to completely rough bed cases, where $k^+ > 70$ (Nezu and Nakagawa 1993). Values of the equivalent roughness for incompletely rough or smooth bed cases are omitted, since they have no significance in the present analysis.

The contour lines of the mean velocity strongly vary across the river section. The influence of the riverbank on the mean longitudinal flow structure is apparent in both cases for $y/B < 0.15$. Thus, the side wall effect disappears for $y/\bar{\delta}$ greater than 4.5 and 3.5, for the Venoge and Chamberonne respectively. Taking $y/\bar{\delta} = 5.0$ as the limit for the bank effect on the flow, the river width should be at least $10\bar{\delta}$ in order to be considered a shallow water river where a central area of the flow would not be affected by the riverbank drag influence. This is higher than the value of $6\bar{\delta}$ proposed by Ferro and Baiamonte (1994).

The structure of the mean flow is evidently 3D making any purely 2D approach questionable, notably, in the inner bank zone and near the most important bed forms (for instance in the vertical $y/B = 0.45$ of Fig. 1). Near the bank, the influence of the sidewall drag on the vertical distribution of the mean velocity is quite evident from the strong transversal gradient in the mean longitudinal velocity.

Both cases show a certain periodicity in the natural riverbed cross undulation and in the spanwise distribution of the mean flow characteristics. This periodicity has a wavelength of about two times the water depth. This cross-periodicity on the bottom shape corresponds to signatures of streamwise sediment strips (Franca and Lemmin 2005 – A.3). They originate during high water events when Prandtl's cellular motion of the second type occurs, conditioning the river hydraulic characteristics during low water periods.

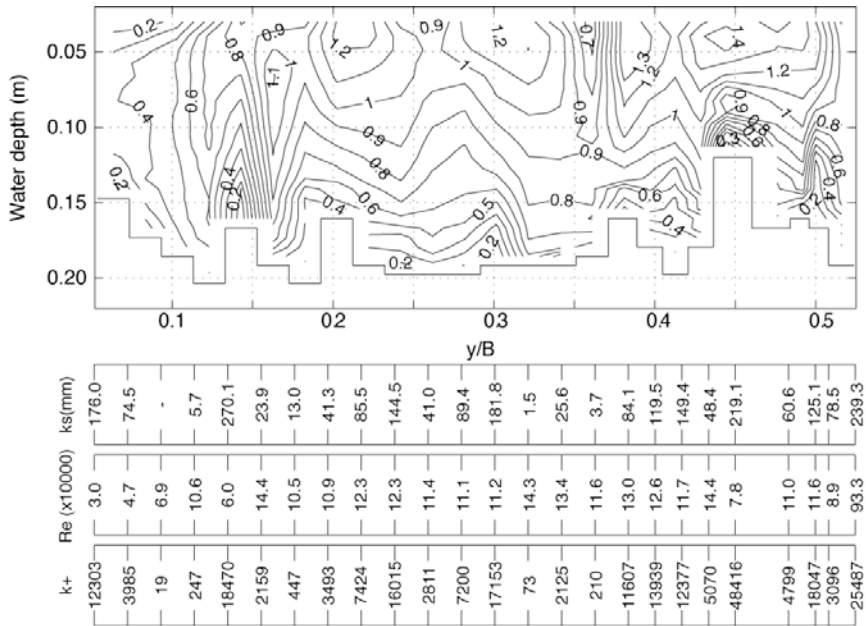


FIGURE 1 – Top: Mean longitudinal velocity field for the river Venoge section; bottom: equivalent roughness distribution (k); Reynolds number (Re); dimensionless roughness (k^+). The horizontal extent of the measurement section is 3.25 m ($y/B = 0.516$).

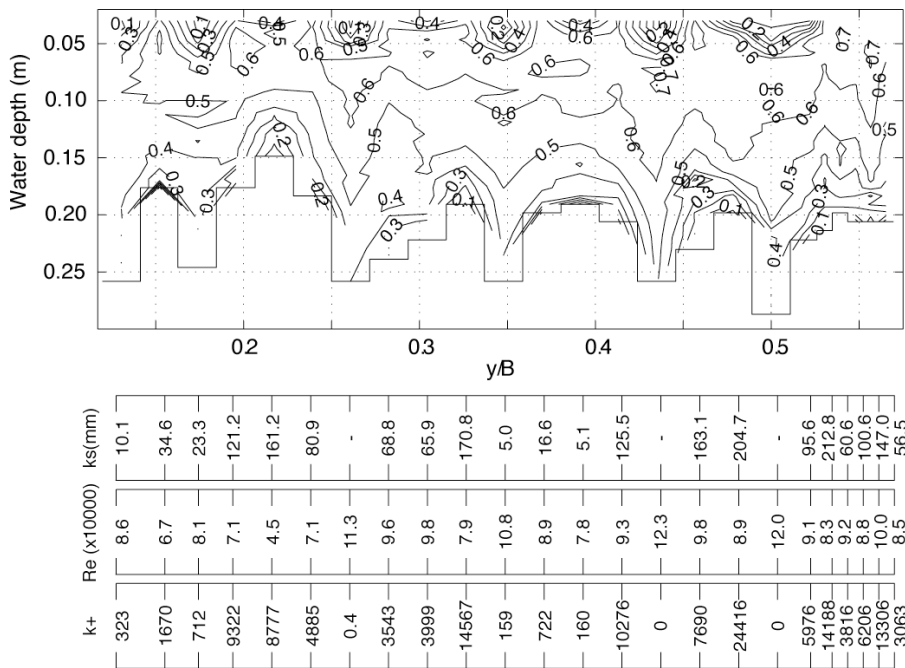


FIGURE 2 – Top: Mean longitudinal velocity field for the river Chamberonne section; bottom: equivalent roughness distribution (k); Reynolds number (Re); dimensionless roughness (k^+). The horizontal extent of the measurement section is 3.25 m ($y/B = 0.565$).

The measurements show periodically distributed deviations in the velocity profiles in the upper layers for both rivers. High velocity regions are more evident in the river Venoge (Fig. 1), whereas low velocity regions are dominant in the river Chamberonne (Fig. 2). Hereinafter we refer to the higher velocity regions corresponding to localized flow jets as CH regions or cells (H stands for high velocity), and CL regions or cells to the lower velocity regions (L stands for low velocity). A D-shaped profile corresponds to the CL regions, and is discussed in subsection 3.6.

3.3 3D analysis of the mean flow

The observed variability of the longitudinal velocity indicates that the velocity field is 3D over most of the cross section. In order to make the 3D flow structure evident, we investigated the distribution of the mean velocity vector field in the three Cartesian components. Figs. 3 and 4 illustrate the mean velocity vector fields for both rivers in the transversal plane and also in the longitudinal plane.

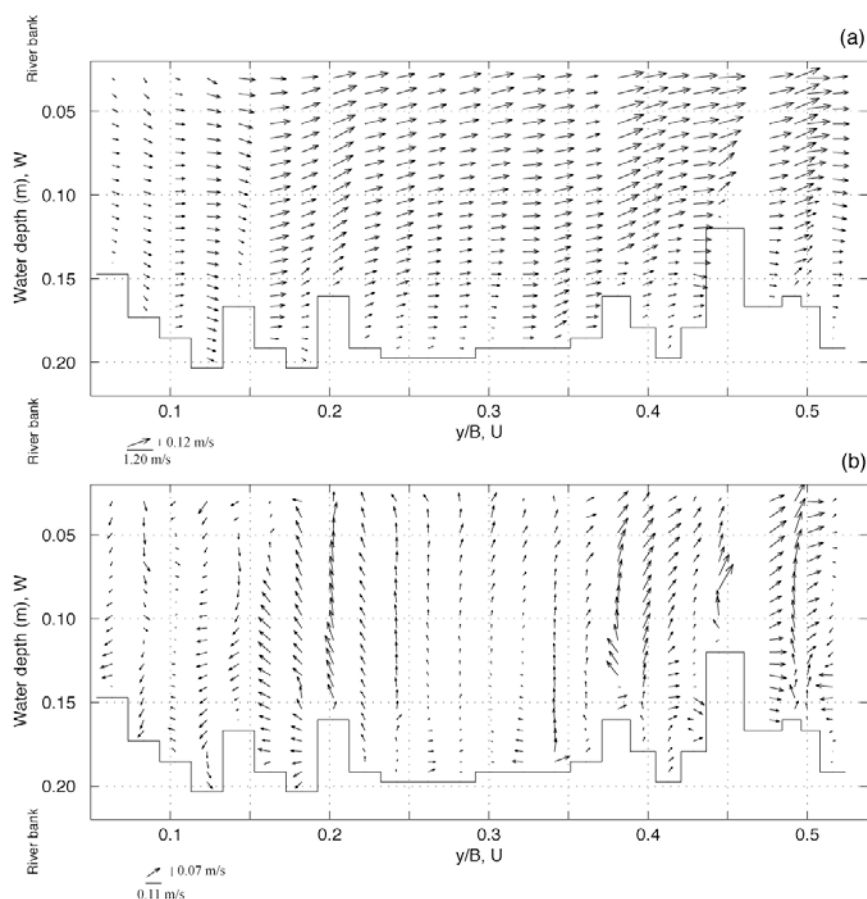


FIGURE 3 – Mean velocities represented in the cross section of the river Venoge: (a) longitudinal velocity mean vector field (x-z); (b) transversal velocity mean vector field (y-z).

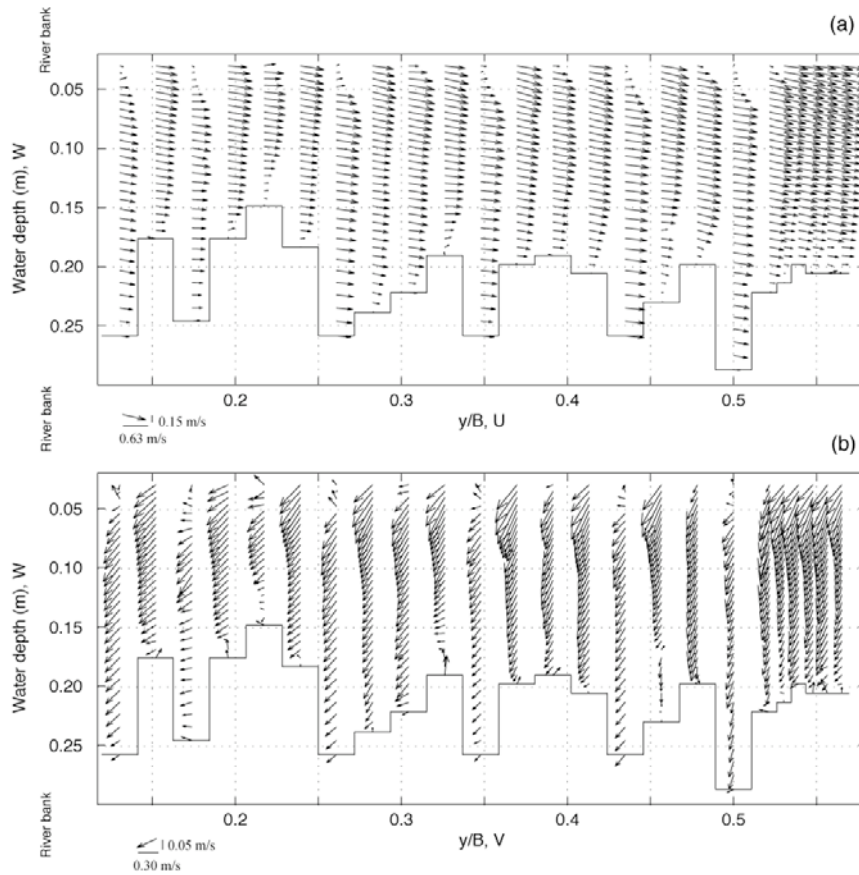


FIGURE 4 – Mean velocities represented in the cross section of the river Chamberonne: (a) longitudinal velocity mean vector field (x-z); (b) transversal velocity mean vector field (y-z).

In the river Venoge, the strong three-dimensionality of the flow and the influence of the riverbank and bottom contours on the mean velocity pattern are evident from the mean large-scale pattern in this river section (Fig. 3). The secondary flow velocities are small compared to the streamwise velocity component. Considering section-averaged mean values, the vertical velocity component represents about 7.5%, and the spanwise component 5.4% of the streamwise velocity. In the area between $y/B = 0.21$ and $y/B = 0.36$, the flow is more regular. In agreement with the contour lines (Fig. 1), the secondary flow reaches its lowest level in this area. The disturbances induced locally in the flow by the most prominent bed shapes are visible at around $y/B = 0.12$, 0.42 and 0.50 . The transversal flow field observed in the present measurements can be divided into three major zones:

- $y/B < 0.20$. The spanwise flow has a predominant component towards the bank. When approaching the bank, the vertical component turns the mean velocity field downwards. In this area flow recirculation seems to exist inducing lower longitudinal mean velocities and directing the spanwise component into the riverbank. For $y/B \sim 0.15$ (Fig. 1) the presence of an incompletely developed CH cell can be observed that is distorted by the bank influence, locally inducing a D-shaped mean velocity profile.
- Middle zone, $0.20 < y/B < 0.36$. The secondary flow reaches its minimum in the flow.
- $y/B > 0.36$. The presence of several obstacles disturbs the flow. The spanwise velocity is directed into the left bank and vertical velocities are mainly in the upward direction.

The riverbed configuration is responsible for 3D flow. The mass is not conserved within the flow cross motion, one evidence of the three-dimensionality of the flow. With the exception of the zone $y/B < 0.15$, the average vertical velocity component is mainly directed upwards.

A different situation is found in the river Chamberonne. The measuring section was situated downstream a smooth bend of river. The bend induced a strong spanwise velocity component in the direction of the right riverbank (Fig. 4). However, no circular flow which could produce lateral mass conservation was detected across the whole river section. We assume that in order to provide the necessary mass equilibrium, the spanwise component is compensated for by the two other velocity components. Only an analysis of a longitudinal river stretch would allow us to understand the interaction of the three velocity components in the present case. The absence of Prandtl's secondary flow of the first kind can be explained by the existence of macro-roughness elements in the riverbed. These may contribute to a reorientation of the flow cancelling the vorticity generated by the river curvature. The spanwise velocity increases in the bank direction and the vertical velocity is mainly orientated downwards. The secondary components of the mean velocity are higher than in the Venoge river; the section-averaged value of the vertical velocity represents 16.5% and the spanwise component 29.1% of the streamwise velocity.

3.4 Bottom influence

The influence of the bottom shape on the mean velocity contour lines and on the value of the equivalent bottom roughness is evident. In the Chamberonne river for example, the dimensionless value of the roughness is very low in the deepest zones of the flow situated at around $y/B = 0.26, 0.43$ and 0.5 , corresponding to smooth flow ($k^+ < \sim 5$). In these areas the velocity contour lines bend downwards which may be interpreted as a weaker influence of the bottom compared to other profiles (lower drag). In the Venoge river, the form dependence of the values of k^+ is more evident where big protuberances occur. For example, one can assume that the k^+ value in profile $y/B=0.321$ is entirely due to bed roughness, whereas in profile $y/B=0.143$ there is a strong bed form component in the k^+ value. In the vertical $y/B=0.103$, the weak value of k^+ may be due to the bank influence since it is inside the zone $y/B < 0.15$. The last vertical appears to be situated in a recirculation zone of the flow due to the riverbank effect. Based on Franca and Lemmin (2005 – 3.1), generally, the k value along the cross section has a strong contribution from the bed forms as seen in Fig. 5.

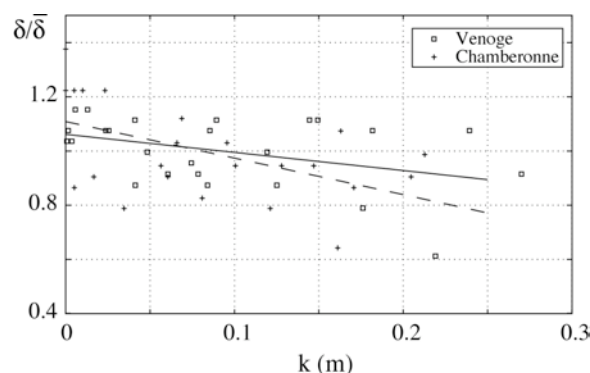


FIGURE 5 – Relation between the Nikuradse equivalent roughness (k) and the local water depth. Continuous line represents the mean trend for river Venoge; dashed line for river Chamberonne.

Apparently, the shallow water flow is conditioned by the cross section periodicity forms. These forms might be signatures of streamwise bed strips on the river reach which are produced during high water periods, when lateral transport conditions by cellular secondary currents are fulfilled within the river flow (Tsujiimoto 1989). The high water events will hence condition the flow characteristics during low water periods.

3.5 Jets and low velocity regions in the upper layer (CH and CL regions)

Both cases illustrate similar phenomena of velocity deviations in the upper layers of the flow. In the river Venoge (Fig. 1), and in agreement with observations made by Studerus (1982) and cited by Nezu and Nakagawa (1993), one can observe from the contour line representation that the mean velocity acquires larger values in the roughest profiles. This situation is demonstrated by the presence of a kind of local jet in the upper layers of the flow located approximately at the local dimensionless roughness maxima (k^+) profiles. Assuming that the unitary discharge tends to be constant across the river section, the jets compensate the local extra bed resistance given by the rougher profiles. As shown in subsection 3.4, the roughness determined locally is strongly influenced by the bed forms, thus by the local water depth. The reduction of the available flow depth has to be compensated for by a higher velocity in the upper layer. Between the jets one may distinguish low velocity regions in the upper layer of the flow (Fig. 1, $y/B \sim 0.26, 0.36$ and 0.41). These regions seem to correlate with local minima of dimensionless roughness. Fig. 1 shows a cross section density of about 2 cells per meter, randomly spaced. It is possible to find an interaction between the three velocity components, concentrated in the surface layer. For $y/B \sim 0.26$ and 0.35 , the discreet CL cells coincide with stagnation zones of spanwise velocities (a stagnation zone is defined as a transition between different flow orientations).

In the river Chamberonne, nine CL regions exist almost uniformly distributed across the section with a density of about 4 per meter (Fig. 2). This case was already discussed in Franca and Lemmin (2005 – A.3). CL cells seem to be the prevalent feature in this case. Higher velocity zones (CH) due to lateral momentum compensation are less intense and are situated in the limits of the CL cells. The CL-profile distribution is uniform and apparently periodic across the section, independent of the local values of k^+ . However, the cells have a stronger retarding effect where the water depth is greater (corresponding to the local minima of k^+). The presence of CL and CH cells in the flow has to be compensated by a secondary motion in order to assure the mass conservation (Ferro and Baiamonte 1994). Interaction between the different regions and the secondary flow exists, producing an organized cellular structure. This is called SLOM (Surface Layer Organized Motion) and is confined to $z/\delta > \sim 0.80$ where recirculation occurs. Low velocity regions coincide with retarding zones of the transversal plane and an inversion of the vertical mass flux is found in six out of nine cases (mainly in the deeper profiles – Fig. 4b). An increase of the vertical velocity in the downward direction exists adjacent to the CL cells, forming what resembles a vertical jet like flow. A lateral mass transfer from the CL to the CH cells in the top layer of the water column contributes to the extra momentum in the CH cell and an associated downward jet. This transfer creates a rotating movement (with streamwise vorticity) where the circulation cells scale with water depth in the spanwise direction (density of 4 cells per meter). Similar symmetrical rotating cells might be found under controlled laboratory conditions with more accurate measurements. Imamoto and Ishigaki (1986) described a similar non-permanent mechanism of cellular secondary currents with a 3D structure, scaling with water depth in the spanwise and vertical directions, and scaling with the double of the water depth in the streamwise direction.

The CL regions have different origins for the two rivers. Lateral momentum compensation due to the existence of local jets may explain the Venoge case. In the Chamberonne, we have CL regions directly associated with the periodically spaced deeper profiles (Franca and Lemmin 2005 – A.3). Adjacent to these, discreet CH regions are formed due to a compensatory secondary motion. Low intensity CL cells

exist due to mass conservation requirements when the cells assume a more stable configuration (secondary flow cells tend to be circular).

The SLOM mechanism may promote the gas transfer through the free surface. However, this only happens to a limited extent, i.e. $z/\delta > \sim 0.80$. Further studies will be made to investigate the nature of the non-permanent structures existing in this layer in order to determine how they may enhance gas transfer between the free surface and the inner flow areas. We will also focus on the possible turbulence enhancement by the existence of additional shear zones in the SLOM layer. From the observed mean field, areas near the higher protuberances and the riverbank are of major importance for the turbulence production over the whole cross section. Thus, one may expect a highly turbulent flow where large scale structures play an important role and where production is not exclusively limited to bottom shear. The importance of large-scale structures was suggested by Roy et al. (2004), indicating that they may play a key role in the turbulence dynamics in gravel-bed rivers. D-shaped and s-shaped profiles have different shear regions than log-profiles; differences in the turbulence distribution may be expected in both cases.

3.6 The D-shaped velocity profile as a response to riverbed morphology

The CL cells impose a deviation from the logarithmic mean velocity profile in the upper layers, the so-called velocity dip phenomenon described by Cardoso et al. (1989) and Yang et al. (2004). In the present case the effect causes a reduction of the velocity near the surface, resulting in what is known as the D-shaped velocity profile. Both field studies are good examples of the occurrence of D-shaped profiles in gravel-bed rivers, even though for each river they have different causes as discussed in subsection 3.5.

In Fig. 6 we plotted several mean velocity profiles taken from the Chamberonne data, normalized by the local maxima of velocity (U_{max}). The points collapse around a mean curve (continuous line), with the maximum velocity situated around $z_{U_{max}}/\delta \sim 0.78$. The difference between the near surface and the maximum velocities can be more than 80%. This is higher than observed in previous studies (Ferro and Baiamonte 1994). It appears that a reverse flow exists in the upper layer of the water column.

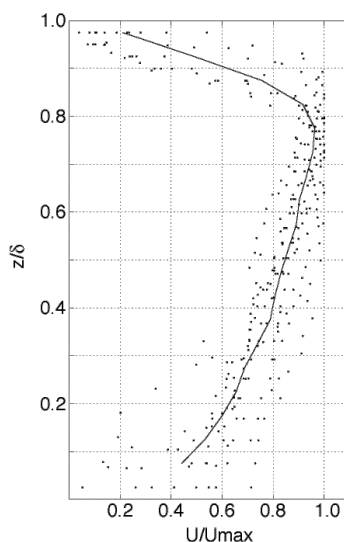


FIGURE 6 – River Chamberonne measurements: D-shaped mean velocity profiles normalized by the local maximum velocity (profiles: $y/B = 0.130, 0.174, 0.217, 0.261, 0.304, 0.348, 0.391, 0.435, 0.478, 0.500$ and 0.522).

In Franca and Lemmin (2005 – A.3) we defined a dimensionless variable (the velocity dip) to identify D-shaped profiles and to evaluate the magnitude of the velocity inflection:

$$dU(y) = U_{\max}(y)/U(y, z = 0.90\delta) \quad (1)$$

The velocity at $z/h=0.90$ is the velocity in the middle of the SLOM layer. In Fig. 7 the velocity dips from both rivers were plotted against the respective local Froude number:

$$Fr(y) = \bar{U}(y)/\sqrt{g\delta(y)} \quad (2)$$

\bar{U} is the depth averaged velocity for each profile. The variable dU allows us to evaluate the magnitude of the dip phenomenon.

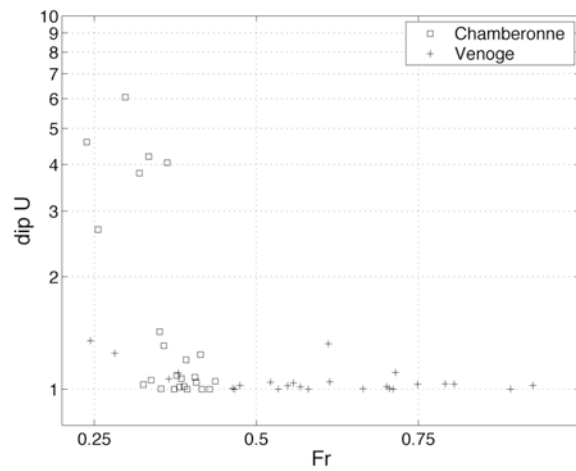


FIGURE 7 – Relation between the velocity dip (dU ratio) and the local Froude number (Fr) for both rivers.

There is a clear tendency of the velocity dip to be more intense with lower local Froude numbers, with a lower limit of $Fr \approx 0.35$ below which the flow velocity dip becomes more pronounced. Fr expresses the relation between the inertial and the gravity forces, and the occurrence of the CL cells is dependent on this relationship. The local characteristics of the mean flow are thus related to the flow regime. Given the Froude relationship, CL cells in the Chamberonne river may be attributed to different phenomena (Franca and Lemmin 2005 – A.3) such as the presence of stationary breaking surface waves, produced by boulders (ship- and lee-type waves) and stationary hydraulic jumps; or the inviscid response from the flow to the bed forms (potential flow assumption – barotropic flow). The latter process is more compatible with the observed local Froude number effect.

For modelling purposes, the specification of the bottom boundary conditions for the logarithmic velocity profile still constitutes a problem when the bed is rough and irregular. When conditions for the occurrence of D-shaped profiles exist, an additional boundary condition near the surface has to be included to represent the upper layer shear, and a new velocity law will be needed for the modelling of this upper layer ($z/\delta > \sim 0.80$). The ability of the river Chamberonne to produce D-shaped profiles is related to the sub-critical flow regime. An approach applicable to a river stretch requires further studies in a controlled laboratory environment.

3.7 Horizontal Froude number analysis

The influence of the cross section distribution of the horizontal Froude number on the mean velocity field is investigated. The horizontal Froude number (Fr_h) is calculated with the mean horizontal velocity component resulting from both the spanwise (V) and the streamwise (U) components. Fig. 8 shows the distribution of Fr_h across the river section.

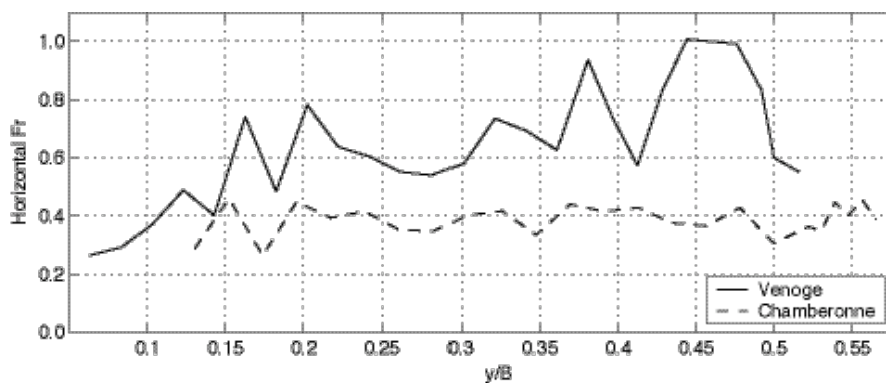


FIGURE 8 – Cross section distribution of the horizontal Froude number for both rivers.

For the Venoge river, the horizontal Froude number is equal to unity around profile $y/B=0.45$ suggesting that the flow is critical at this location. This indicates that at this location, a lateral drop in the flow above the riverbed obstacle occurs which is confirmed by observing Fig. 3b where a general outward mean transversal velocity tendency is found. In that figure we can see a transversal roll in the mean field at around $y/B = 0.50$. The existence of this flow feature implies a division of the measured cross section stretch into two regions. Each of these regions can be considered as a channel. In this particular case the inner channel seems to discharge laterally into the outer one. In fact, looking at the river flow as a whole, it can be suggested that several interconnected small channels exist, flowing between the extremely high riverbed protuberances, which sporadically meet and exchange fluxes.

The cross section distribution of the horizontal Froude number for the river Chamberonne is uniform and the flow is subcritical in all measured verticals. Based on the influence of the wave propagation speed and from the present Froude results, the development of the upper layer structured flow SLOM seems to relate to the flow regime.

4 CONCLUSIONS

In this paper results from ADVP measurements in the rivers Venoge and Chamberonne are presented. Both are gravel-bed rivers, with hydraulically rough flows. Important findings concerning the three-dimensionality of the mean flow were made.

The drag wall effect from the riverbanks is visible until $y/B=0.15$ in the mean velocity field, where a recirculation flow is observed. Near the riverbank, the vertical velocity distribution tends to be uniform along the water depth. According to the present results, the relationship between the river width (B) and its mean water depth ($\bar{\delta}$) should be at least $B/\bar{\delta}=10$ in order to be considered shallow water.

The analysis of the horizontal Froude number allowed visualizing lateral drops across the cross section, showing that this river stretch can be considered as being a composite of small river channels interacting laterally, converging and diverging occasionally. This analysis demonstrated the importance of both horizontal velocity components in the definition of the local flow regime in 3D flows.

In layer $z/\delta > 0.4$ large deviations from the log-law distribution are observed, in the positive direction of the flow or in the negative direction. This points towards the development of the so-called D-shaped velocity profile previously observed in gravel-bed rivers by other authors. The most prominent observation was the existence of localized flow areas of an organized permanent motion composed of high (CH) and low (CL) longitudinal velocity regions situated in the upper layer of the flow, $z/\delta > 0.80$ (jets compensated by adjacent low velocity regions). This type of flow pattern was detected differently in both rivers. In the Venoge case, CL regions seem to develop weakly from the uniformly distributed flow pattern based on a log-law structured flow. The presence of CH cells correlates roughly with the local maxima of the dimensionless roughness. The CL regions exist mainly due to lateral momentum transfer imposed by the presence of jets (CL regions). In the Chamberonne case, the CL cell distribution is uniform and periodic across the section. Higher intensity CL cells coincide with the minima positions of k^+ and are local Froude dependent. Lower intensity CL cells exist due to continuity and stability reasons.

The occurrence of D-shaped velocity profiles corresponds to the low velocity regions. Normalized plots of the detected D-shaped profiles were analysed and showed high consistency across the section. Good agreement between the normalized profiles was observed; the maximum velocity is situated around $z_{U_{max}}/\delta \sim 0.78$. It was verified that the local Froude number was correlated with the occurrence of a D-shaped type of profile, hence with the occurrence of a CL cell; the local flow regime is the local determinant characteristic of the phenomenon. Apparently this event is limited to subcritical flow regimes and the CH-CL cell structured flow seems to be related to the Froude number. However, the flow inversion verified in the D-shaped profiles of the river Chamberonne can only be explained by the presence of stationary breaking waves (in the upper layers, a 2D roll is observed in the vertical and vertical and streamwise mean flow). We believe that the combined effect of three kinds of surface waves may be at the origin of these profiles: wavy surface due to potential flow over the bed forms; boulder induced waves (ship- and lee-type waves); presence of hydraulic jumps due to local regime transitions.

Permanent motion in the transversal plane exists which is related to the flow cells generating an upper circulation layer in the flow with longitudinal vortical characteristics, i.e. the so-called SLOM, Surface Layer Organized Motion. These circular motion cells, with a longitudinal development, scale with the water depth in the spanwise direction. Previous authors described similar kinds of mechanisms that scaled vertically with the water depth. However, in the present case a vertical constraint exists, possibly due to the macro-roughness riverbed elements, that confines these motions to a layer near the surface deforming the flow cells in the spanwise direction. The origin of the present vortical structure concentrated in the upper layers is due to the coexistence of CH and CL regions, implying lateral momentum transfer.

In the two cases different intensities of the three-dimensionality of the flow, expressed by the ratio between the flow-averaged velocities of different Cartesian directions, were formed. On average, for the Venoge and for the Chamberonne the spanwise velocity intensity is about 5.4 and 29.1% of the longitudinal one, and the vertical one is about 7.5 and 16.5%, respectively. Besides the structured flow that was detected in the upper layer of both rivers, it was observed that local conditions such as high bed protuberances, proximity to the riverbank, and proximity to a river bend, induce isolated or widespread secondary motion. Large-scale bed roughness elements seen in these rivers (about half the size of the water depth) provide for a highly 3D character of the flow. This is confirmed by the lack of mass conservation within the cross section. The mass conservation can only be determined over a river stretch.

Periodic longitudinal strip signatures are found in the river Chamberonne, influencing the hydraulic characteristics. They may be produced during high water events, when longitudinal cellular secondary motion (Prandtl's cellular motion of the second type) has sufficient transport capacity to model the riverbed. Hence, high water events have long-term effects on the river processes during shallow water conditions.

Despite the presence of a smooth bend upstream from the Chamberonne measuring section, no Prandtl's secondary flow of the first kind cell was detected, only a strong spanwise velocity component in the direction of the right riverbank. The macro-roughness elements may contribute to a reorientation of the flow, thus cancelling the vorticity generated by the river curvature.

Mixing is widely present in the flow. The complex structure of the mean secondary flow shows the importance of this motion on mixing and transport processes. In fact, secondary motion induced by large-scale bottom forms has a strong influence on the spreading of matter, heat and momentum in the whole cross section. The cellular mechanism may also have a limiting effect on mixing and transport in rivers. Being situated near the surface, this phenomenon can create a stagnation zone in the upper layers of the flow ($z/\delta > 0.80$) where mass, heat or momentum inputs may accumulate and concentrate.

ACKNOWLEDGEMENTS

We would like to thank Steve Thorpe, Eugene Terray and Huib de Vriend for their fruitful discussions during the elaboration of the present paper. The authors acknowledge the financial support of the Portuguese Science and Technology Foundation (BD 6727/2001) and the Swiss National Science Foundation (2000-063818).

REFERENCES

- Babaeyan-Koopaei K., Ervine D.A., Carling P.A. and Cao Z. (2002), Velocity and turbulence measurements for two overbank flow events in river Severn, *J. Hydr. Eng.*, 128(10), 891-900.
- Bergeron N.E. and Abrahams A.D. (1992), Estimating shear velocity and roughness length from velocity profiles, *Water Resour. Res.*, 28(8), 2155-2158.
- Buffin-Bélanger T. and Roy A.G. (1998), Effects of a pebble cluster on the turbulent structure of a depth-limited flow in a gravel-bed river, *Geomorphology*, 25, 249-267.
- Buffin-Bélanger T., Roy A.G. and Kirkbride A.D. (2000), On large-scale flow structures in a gravel-bed river, *Geomorphology*, 32, 417-435.
- Cardoso A.H., Graf W.H. and Gust G. (1989), Uniform flow in a smooth open-channel, *J. Hydr. Res.*, 27(5), 603-616.
- Ferro V. and Baiamonte G. (1994), Flow velocity profiles in gravel-bed rivers, *J. Hydr. Eng.*, 120(1), 60-80.
- Franca M.J. and Lemmin U. (2004 – A.1), A field study of extremely rough, three-dimensional river flow, *Proc. 4th Int. Symp. Env. Hyd. - IAHR. Hong Kong (China)*. Appendix A.2.
- Franca M.J. and Lemmin U. (2005 – A.3), Cross-Section periodicity of turbulent gravel-bed river flows, *Proc. 4th RCEM - River Coastal and Estuarine Morphodynamics. Urbana (USA)*. Appendix A.3.
- Franca M.J. and Lemmin, U. (2005 – 2.2), subchapter “Eliminating velocity aliasing in acoustic Doppler velocity profiler data”.

Franca M.J. and Lemmin, U. (2005 – 3.1), subchapter “Mean streamwise velocity in gravel-bed river flows”.

González J.A., Melching C.S. and Oberg K.A. (1996), Analysis of open-channel velocity measurements collected with an acoustic Doppler current profiler, Rivertech 96: Proc. 1st Int. Conf. New/Emerging Conc. Rivers, Chicago (USA).

Hurther D. and Lemmin U. (2000), A correction method for turbulence measurements with a 3D acoustic Doppler velocity profiler, J. Atmosph. Ocean. Technol., 18, 446-458.

Hurther D., Lemmin U. and Blanckaert K. (2002), A field study of transport and mixing in a river, using an acoustic Doppler velocity profiler, Proc. Riverflow 2002, Louvain-la-Neuve (Belgium).

Imamoto H. and Ishigaki T. (1986), Visualization of longitudinal eddies in an open channel flow, Proc. IV Int. Symp. Flow Visual.. Paris (France).

Nezu I. and Nakagawa H. (1993), Turbulence in open-channel flows - IAHR monograph, A.A. Balkema, Rotterdam (The Netherlands).

Nikora V. and Smart G.M. (1997), Turbulence characteristics of New Zealand gravel-bed rivers, J. Hydr. Eng., 123(9), 764-773.

Nikora V. and Goring D. (2000), Flow turbulence over fixed and weakly mobile gravel beds, J. Hydr. Eng., 126(9), 679-690.

Powell D.M., Reid I. and Laronne J.B. (1999), Hydraulic interpretation of cross-stream variations in bed load transport, J. Hydr. Eng., 125(12), 1243-1252.

Rolland T. and Lemmin U. (1997), A two-component acoustic velocity profiler for use in turbulent open-channel flow, J. Hydr. Res., 35(4), 545-561.

Roy A.G., Buffin-Belanger T., Lamarre H. and Kirkbride A.D. (2004), Size, shape and dynamics of large-scale turbulent flow structures in a gravel-bed river, J. Fluid Mech., 500, 1-27.

Smart G.M. (1999), Turbulent velocity profiles and boundary shear in gravel bed rivers, J. Hydr. Eng., 125(2), 106-116.

Studerus X. (1982), Sekundärströmungen im offenen Gerinne über rauhen Längsstreifen, Ph.D. Thesis, Institut für Hydromechanik und Wasserwirtschaft – ETH Zurich (Switzerland).

Tritico H.M. and Hotchkiss R.H. (2005), Unobstructed and obstructed turbulent flow in gravel bed rivers, J. Hydr. Eng., 131(8), 635-645.

Tsujimoto T. (1989), Longitudinal stripes of alternate lateral sorting due to cellular secondary currents, Proc. XXX IAHR Cong., pp. B17-B24, Ottawa (Canada).

Wolman M.G. (1954), A method of sampling coarse river-bed material, Trans. Amer. Geoph. Un., 35(6), 951-956.

Yang S.Q., Tan S.K. and Lim S.Y. (2004), Velocity distribution and dip-phenomenon in smooth uniform open channel flows, J. Hydr. Eng., 130(12), 1179-1186.

3.3 THE OCCURRENCE OF S-SHAPED VELOCITY PROFILES IN GRAVEL-BED RIVER FLOWS

Subchapter 3.3 was submitted for publication to the Journal of Hydraulic Engineering (ASCE). The paper authors are M.J. Franca and U. Lemmin.

This subchapter concerns the occurrence of s-shaped profiles in gravel-bed river flows and the limits of the application of the logarithmic-law to the mean velocity profile description. The momentum distribution throughout the profile is discussed as well.

	ABSTRACT	3.3.1
1	INTRODUCTION	3.3.1
2	FIELD WORK AND INSTRUMENTATION	3.3.2
3	FIELD RESULTS	3.3.3
3.1	Mean velocity	3.3.3
3.2	Log shaped and s-shaped profiles in the lower layer of the flow	3.3.3
4	DEPTH-AVERAGED FLOW VELOCITIES	3.3.6
5	CONCLUSIONS	3.3.7
	ACKNOWLEDGEMENTS	3.3.8
	REFERENCES	3.3.8

THE OCCURRENCE OF S-SHAPED VELOCITY PROFILES IN GRAVEL-BED RIVER FLOWS

ABSTRACT

Based on ADV field measurements we discuss velocity profiles observed in two shallow gravel-bed rivers with low blockage ratio (h/D). Log profiles and s-shaped profiles simultaneously exist, indicating the possibility of 3D flow inside the roughness layer. However, away from the roughness layer in an intermediate region of the flow, a quasi-2D layer is always found. The log-law approach therefore will always lead to values of the friction velocity (u^*) and Nikuradse equivalent roughness (k). We found that above a certain limit of the relation k/h (h being the local water depth), the results obtained by the log approach are erroneous, since the velocity distribution in the lower profiles corresponds to an s-shaped profile. The log-law approach is no longer valid in this case. According to our measurements, s-shaped profiles occur for $k/h > \approx 0.6$. We also investigated the momentum distribution throughout the flow depth and concluded that the mean of the velocity profile roughly occurs at $z/h \approx 0.40$, for both log and s-shaped profiles.

Key-words: field measurements; gravel-bed river flows; s-shaped profile; depth-averaged velocity

1 INTRODUCTION

Existing open-channel theories are mainly based on laboratory experiments. In order to validate them in rivers, field measurements have to be carried out. Unfortunately, only a small number of field studies exist, mainly due to the lack of suitable instrumentation (Nikora and Goring (2000), Buffin-Bélanger et al. (2000), Babaeyan-Koopaei et al. (2002), Hurther et al. (2002), Tritico and Hotchkiss (2005), Roy et al. (2004), Kawanisi (2004) and Franca and Lemmin (2004 – A.1)). The classic logarithmic profile approach is often used to describe the mean velocity distribution in boundary layer flows (see Monin and Yaglom 1971). In shallow flows over rough surfaces, deviations from the logarithmic velocity profile may be expected in the lower layers due to the effect of bottom roughness. In such flows, velocity inflection is often observed leading to so-called s-shaped profiles (Marchand et al. 1984, Bathurst 1988 and Ferro and Baiamonte 1994). The occurrence of s-shaped profiles is common for flows with large-scale roughness elements. Usually these deviations are due to the wake effect resulting from the presence of bed forms that deform the mean velocity profile as observed by Nelson et al. (1993) and Buffin-Bélanger and Roy (1998). Nikora and Smart (1997) also found deviations from the log-law flow in the roughness sublayer which is a 3D inner layer of the flow in gravel-bed rivers. In the case of an s-shaped profile, the streamwise momentum is concentrated in the upper layers of the flow, where the velocity distribution becomes almost uniform (parallel streamlines; Franca (2005 – A.2)). Katul et al. (2002) compared the s-shaped profiles resulting from the drag effect on the canopy for atmospheric flows with the s-shaped profiles existing in gravel-bed rivers.

All these observations indicate that shear production is no longer limited to a log-based layer near the bottom. This will also affect the turbulence distribution due to the different forms of shear zones near the bottom. Based on Acoustic Doppler Velocity Profiler (ADVP) field measurements, we demonstrate the validity of the application of the log-law in the description of the velocity distribution. In all the measured profiles a log-layer seems to exist however with changing levels of origin. We could establish a relation between the results obtained from the “blind” application of the log-law in gravel-bed rivers and the occurrence of s-shaped profiles in the lower layer. An analysis of the momentum distribution throughout the flow depth for the different profiles is also presented.

2 FIELD WORK AND INSTRUMENTATION

This study is based on two sets of field measurements made in the Swiss lowland rivers, Venoge and Chamberonne, both located in the canton of Vaud. The measurements were made during the summer of 2003, under stationary shallow water conditions in straight river reaches. The measuring position for the Venoge was about 120 m upstream of the Moulin de Lussery and for the Chamberonne, 385 m upstream from the river mouth. The hydraulic characteristics of the two rivers during the measurement period are summarized in Table 1.

Table 1 – Summary of the rivers’ flow characteristics.

River	Mean slope (%)	Discharge (m ³ /s)	Mean water depth (m)	Width (m)	Re = $\bar{U}h/\nu$ (x10 ⁴)	Fr = \bar{U}/\sqrt{gh}	D ₅₀ from the bottom ⁽¹⁾ (mm)
Venoge	0.33	0.80	0.21	6.30	3.0 – 14.4	0.20 – 0.90	40
Chamberonne	0.26	0.55	0.25	5.75	4.5 – 12.3	0.24 – 0.44	49

⁽¹⁾D₅₀ obtained from a sample of the bottom material.

Re is the Reynolds number; \bar{U} , the vertically averaged streamwise velocity; ν , the kinematic viscosity; Fr, the Froude number; g, the gravity acceleration and D₅₀, the bottom grain size diameter for which 50% of the grain diameters are smaller. The riverbed was composed of coarse gravel with randomly spaced macro-roughness elements. The gravel-bed material was sampled by the Wolman method (Wolman 1954). Considering the average water depth, the ratio width/h takes the values 30.0 and 23.0 for the Venoge and Chamberonne, respectively. Both rivers correspond to shallow water conditions. The river flow was turbulent and rough. Based on the blockage ratio h/D_{50} equal to 5.25 and 5.10 respectively for Venoge and Chamberonne, the rivers are of intermediate scale roughness (Bathurst 1981). No sediment transport occurred during the measurements. The velocity profile measurements were made across river sections in both cases. For the Venoge, 25 velocity profiles were spaced horizontally with 10 to 12.5 cm distance; for the Chamberonne, 24 profiles were measured with horizontal spacing of 5 to 12.5 cm. Velocities were recorded for 5 minutes at each position. The deployable 3D ADVP developed at the LHE-EPFL was used to measure 3D quasi-instantaneous velocity profiles at each position. The ADVP system is described in the literature (Rolland and Lemmin 1997 and Shen and Lemmin 1997). For both measurements a Pulse Repetition Frequency (PRF) of 2000 Hz was used for the Doppler shift estimates. We applied a correcting algorithm to prevent aliasing problems in the data (Franca and Lemmin 2005 – 2.2).

3 FIELD RESULTS

3.1 Mean velocity

For the river flows discussed here, Franca and Lemmin (2005 – 3.1) found that the lower 40% of the profile could be matched by a logarithmic profile in about 65% of the profiles taken. However, in some profiles, deviations from the log-law occurred in the lower layer of the flow. We investigated whether these deviations could be explained by an s-shaped profile (Franca (2005 – A.2) and Franca and Lemmin (2005 – 3.4)). We parameterized the s-shaped velocity profiles by a tangent-hyperbolic function, with a reference velocity u_0 ($u_0 \approx u_\infty/2$) and a geometric parameter scaling with the mean size of the larger coherent structures inside the roughness layer ($L \approx \bar{L}_{int}(z < Z_{RL})$). L may be related to the bottom gravel distribution, $L = \alpha D_{84}$ ($\alpha = 0.25$) and the flow resistance is characterized by a resistance coefficient $C_u = 1/\kappa \cdot \ln(\alpha' D_{84} / z_{0,s})$, where $\alpha' = 0.21$ (Franca and Lemmin (2005 – 3.4)).

In this study the river bottom zero reference level corresponds to the shallowest part of the solid bed, this being at times a rock or boulder, in the vertical of the measured profile. The roughness length (Z_0) corresponds to the position where the log-law description of the mean velocity reaches the value zero. Due to the strongly variable bottom topography, the Z_0 coordinate defines a 3D surface near the riverbed. We call it the zero-surface displacement in analogy with the zero-plane displacement defined by Nikora et al. (2002). The roughness sublayer ($z < Z_{RL}$) is referred to as the zone near the bottom where the flow is highly 3D and deviations from the log-law shape on the mean velocity profile are expected (Nikora and Smart 1997). The upper limit of the roughness layer again defines a 3D surface above the top of the local riverbed.

3.2 Log shaped and s-shaped profiles in the lower layer of the flow

Based on the velocity distribution in the inner layer, most of the measured velocity profiles fall into two groups: one with a log-shaped lower layer (36 profiles), and the other one with an s-shaped lower layer (13 profiles). In our case, as shown in Fig. 1, the roughness sublayer scales with $Z_{RL}/h = 0.30$. This scale is nearly equivalent to the D_{75} of the grain size distribution.

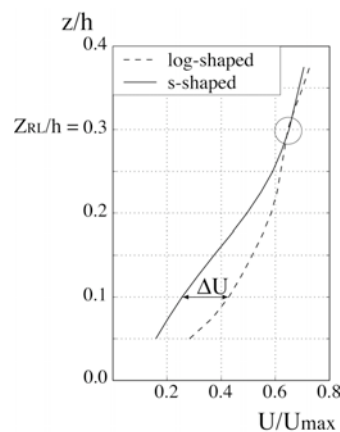


Figure 1 – Representation of the average mean velocity profiles normalized by the local maximum velocity corresponding to log-shaped and s-shaped lower layer profiles; circle: identification of the height of the roughness sublayer

The simultaneous occurrence of these two types of velocity profiles in both rivers indicates that lateral momentum transfer exists in the lower layers of the flow and that a 3D inner layer develops in the flow (Nikora and Smart 1997). The velocity discrepancy of about $\Delta U \approx 0.20$ for $z/h=0.10$ suggests that this exchange may be important (Fig.1). In both river flows two regions can be observed where significant lateral exchange of momentum takes place. Near the bottom log and s-shaped profiles coexist and near the surface, jets and compensating low velocity regions are found (Franca and Lemmin 2005 – A.3). Between these two regions a buffer region exists, where no significant lateral exchange occurs.

Bathurst (1988) and Ferro and Baiamonte (1994) investigated the influence of bottom roughness on the shape of the profiles. As a parameter Bathurst (1988) took the ratio h/D_{84} , and Ferro and Baiamonte (1994) used h/D_{50} , both ratios being the inverse of a measure of the relative bottom roughness represented by the characteristic diameters D_{84} and D_{50} . Although the log law cannot describe some of the velocity profiles, the Nikuradse equivalent roughness (k) calculated from the logarithmic law approach (taking the geometry parameter $B=8.5$) may give an indication of the local roughness (Franca and Lemmin 2005 – 3.1). The Nikuradse equivalent roughness represents a measure of the wake effect locally felt in the velocity measurements, caused by some upstream perturbation of the bottom. For these river flows, Franca and Lemmin (2005 – 3.2) demonstrated the dependence of the k values on the riverbed forms. Therefore, we assume that the equivalent roughness values can be used to qualitatively map the local roughness of the riverbed. Fig. 2 shows the distribution of the ratio corresponding to the local Nikuradse relative roughness (k/h) for log-shaped and s-shaped cases. The distinction between the profiles was made by visual observation.

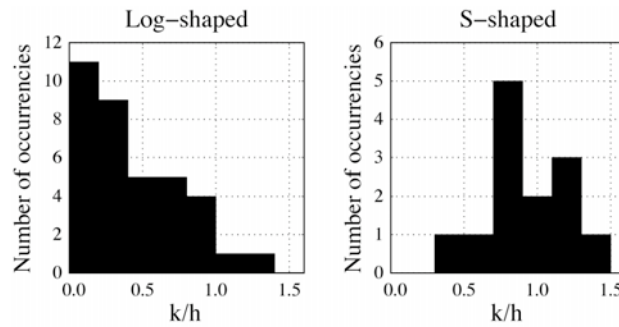


Figure 2 – Distribution of the relative roughness (k/h) for the case of log-shaped (left) and s-shaped (right) lower layer profiles. Note the change in vertical scales.

The rougher profiles denote a slightly higher tendency to be s-shaped, which is in agreement with previous authors. It appears that $k/h \approx 0.5-0.6$ constitutes a limit above which the lower layer profiles become s-shaped. In order to investigate the s-shaped profile, two dimensionless variables are used: the normalized velocity discrepancy between a log-based profiles and the measured profile, calculated for $z/h=0.10$ (Fig. 1); and the normalized low-layer unitary discharge discrepancy, calculated for $z/h < 0.30$.

$$\frac{\Delta U_{0.10}}{U_{\max}} = \frac{\left| U_{\log}\left(\frac{z}{h} = 0.10\right) - U_{\text{meas}}\left(\frac{z}{h} = 0.10\right) \right|}{U_{\max, \text{meas}}} \quad (1)$$

$$\frac{\Delta q_{0.30}}{q} = \frac{\left| q_{\log}\left(\frac{z}{h} < 0.30\right) - q_{\text{meas}}\left(\frac{z}{h} < 0.30\right) \right|}{q_{\text{meas}}\left(\frac{z}{h} < 1.00\right)} \quad (2)$$

The subscript $_{\log}$ means taken from the log-law based profile and the subscript $_{\text{meas}}$ means taken directly from the measurements. In Fig. 3 we plot these two non-dimensional variables against the relative roughness. Log-shaped and s-shaped profiles were identified visually and are plotted with different symbols.

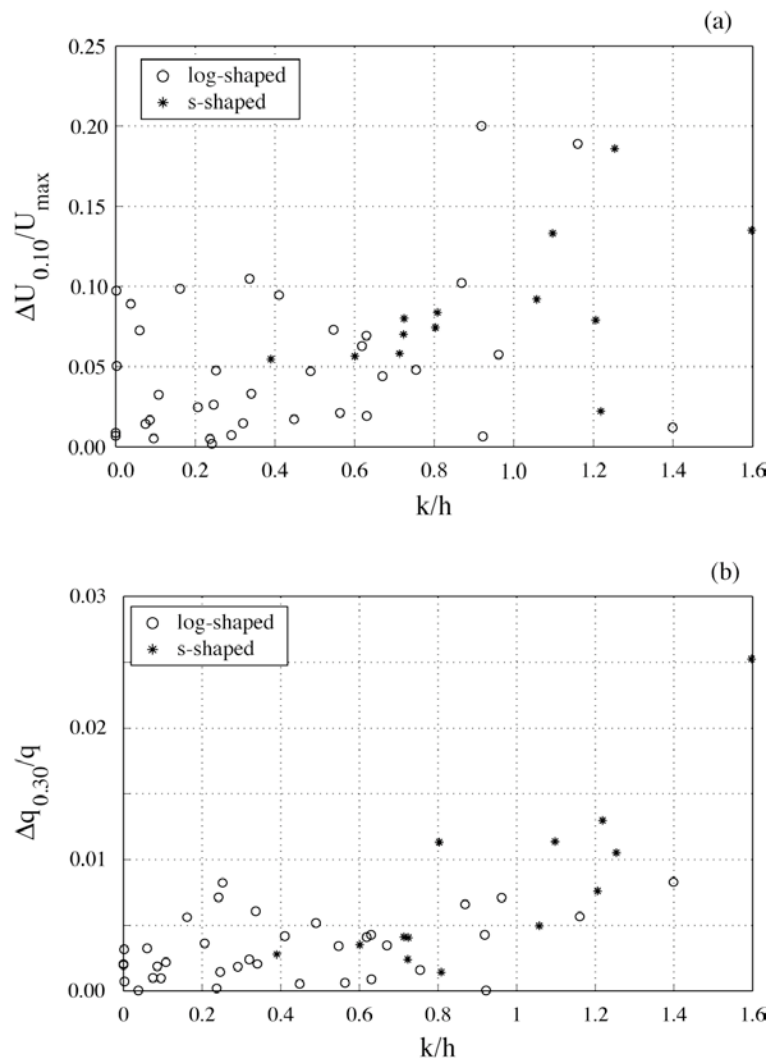


Figure 3 – (a) Normalized velocity discrepancy calculated for $z/h=0.10$ plotted against local relative roughness, and (b) normalized low-layer unitary discharge discrepancy calculated for $z/h<0.30$ plotted against local relative roughness.

In both cases there is a clear tendency for the occurrence of s-shaped profiles for $k/h > 0.5-0.6$. The cloud formed by the points belonging to the s-shaped profiles has an increasing trend with the relative roughness. The use of the low-layer unitary discharge discrepancy ($\frac{\Delta q_{0.30}}{q}$) seems better suited for identifying this kind of profile. These results confirm the importance of the relative roughness as characteristic parameter for the occurrence of s-shaped profiles (Bathurst (1988) and Ferro and Baiamonte (1994)).

Although evident in the velocity profile analysis, the influence of the roughness layer deviations do not greatly affect the estimate of the local unitary discharge. In Fig. 3b we find a maximum error of less than 3% for these calculations. In terms of mean velocity discrepancy, the error made by using the log law is about 25% of the local maximum velocity as shown in Fig. 3.

4 DEPTH-AVERAGED FLOW VELOCITIES

Practical applications in hydraulic and hydrological engineering often require a rapid estimate of the river discharge from simple, in-situ velocity measurements. These are often made with such point measuring instruments as propellers and Pitot tubes. Existing methods for discharge estimates usually consider a perfect logarithmic distribution of the velocity throughout the water depth. It is thus important to understand the differences which exist between the momentum distribution within the water depth for the different types of velocity profiles in order to assess possible measuring errors. Simplified methods which only depend on simple point velocity measurements made in well-chosen positions are widely used for easy application in the field. Well-known formulae are summarized in Graf and Altinakar (1998).

In this section we analyze measured profiles away from the influence of the bank ($y/h > 5$). In Fig. 4 we plotted the depth where the velocity value equalled the depth-averaged value against the spanwise location of the measured profiles. $Z_{\bar{U}}$ is the water depth for which the mean velocity value equals the local mean:

$$\bar{U}_i = U_i(z = z_{\bar{U}}) = \int_0^h U_i(z) dz \quad (3)$$

\bar{U} is the depth-averaged velocity; $U(z)$ is the vertical velocity distribution, and h is the total water depth. The index i denotes the corresponding measured profile.

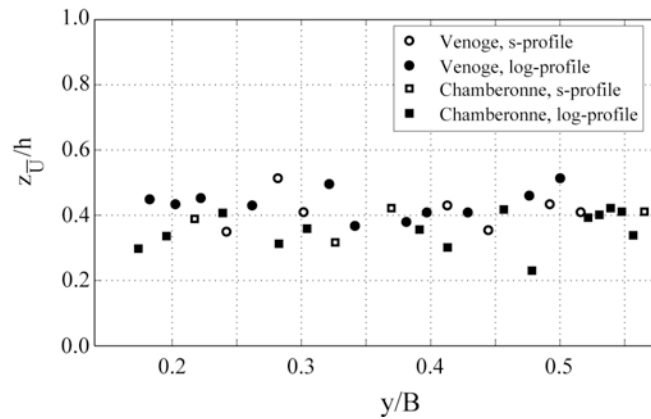


Figure 4 - Cross section distribution of $Z_{\bar{U}}$ normalized by the local water depth.

For our river measurements, the local mean velocity \bar{U} corresponds to a level of $z_{\bar{U}}/h = 0.39$ (standard deviation of 0.06), which is in accordance with the value of $z_{\bar{U}}/h = 0.40$ suggested by Graf and Altinakar (1998). For practical applications, we suggest the application of the following formula for the

calculation of the local mean velocity and local unitary discharge, based on simple point velocity measurements made for $y_i/h > 5$ (Fig. 5):

$$\bar{U}_i = U_i(y/h > 5, z/h = 0.40) \quad (4)$$

$$q_i = U_i(z/h = 0.40) h_i \quad (5)$$

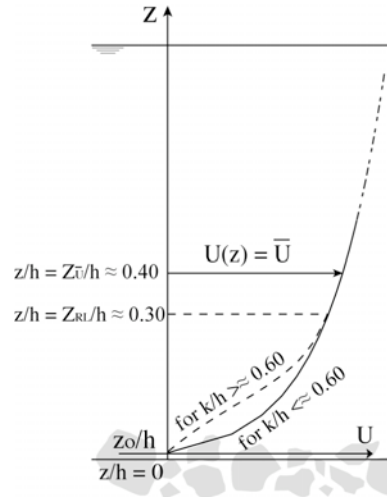


Figure 5 – Definition of the vertical position of the velocity gauge points that allow the estimate of the local mean velocity and the section averaged velocity.

We did not find a relationship between the occurrence of the mean velocity deviations in the lower layers and the variation of $z_{\bar{v}}$ values. This implies that in s-shaped profiles, a secondary compensatory flow exists in the longitudinal plane, which allows maintaining a nearly constant momentum across the section.

5 CONCLUSIONS

In this paper we discussed the presence of s-shaped profiles in shallow gravel-bed river flows and the limitations of the log-law to represent them. The research was based on ADV field measurements taken under stationary conditions during shallow water periods.

The classic logarithmic law to describe the velocity profile may be used, to some extent, as demonstrated by Franca and Lemmin (2005 – 3.1). Therefore, the Nikuradse equivalent roughness (k) determined from the measured profiles can be used as a first qualitative indication of the local roughness.

Log and s-shaped velocity profiles coexist in the lower layers of the flow indicating that 3D flow may occur in the inner layer. Nevertheless a log layer can be formed in most profiles, however, with different starting levels. The “blind” application of the log law may induce errors in the velocity distribution description. For Nikuradse equivalent roughness values of $k/h \approx 0.6$, the velocity distribution in the lower layers is probably s-shaped and a logarithmic approach is no longer valid. This is in accordance with previous references stating that relative roughness is the determinant parameter for the verification of the s-shaped profiles.

For the identification of the different types of profiles the local unitary discharge discrepancy may be used. However, the errors committed by not considering s-shaped profiles in river flow modelling are less evident in terms of unitary discharge than in terms of velocity vertical distribution.

We discuss the repartition of the momentum throughout the flow depth. We observed that the mean velocity measured at $z/h \approx 0.40$ corresponds to the depth-average velocity, independent of the type of velocity distribution. This relation allows straightforward and rapid calculations of the river discharge and unitary discharge cross distribution with simple point measurements made in the river. Uncomplicated river modelling can be done by using the lateral distribution of the mean velocity or of the unitary discharge. An estimate of the cross section momentum distribution and of the presence of secondary motion is possible from the analysis of the local mean velocity values.

This paper presents typical mean features of gravel-bed river flows, and suggests future research topics to be developed either in the laboratory or in the field. These results are useful for practitioners since they show the limits and errors which may occur when using the log-law in field studies.

ACKNOWLEDGEMENTS

The authors acknowledge the financial support of the Portuguese Science and Technology Foundation (BD 6727/2001) and the Swiss National Science Foundation (2000-063818).

REFERENCES

- Babaeyan-Koopaei K., Ervine D.A., Carling P.A. and Cao Z. (2002), Velocity and turbulence measurements for two overbank flow events in river Severn, *J. Hydr. Eng.*, 128(10), 891-900.
- Bathurst J.C., Li R.M. and Simons D.B. (1981), Resistance equation for large-scale roughness, *J. Hydr. Eng.*, 107(12), 1593-1613.
- Bathurst J.C. (1988), Velocity profile in high-gradient, boulder-bed channels, *Proc. Int. Conf. Fluv. Hydr.*, Budapest (Hungary).
- Buffin-Bélanger T. and Roy A.G. (1998), Effects of a pebble cluster on the turbulent structure of a depth-limited flow in a gravel-bed river, *Geomorphology*, 25, 249-267.
- Buffin-Bélanger T., Roy A.G. and Kirkbride A.D. (2000), On large-scale flow structures in a gravel-bed river, *Geomorphology*, 32, 417-435.
- Ferro V. and Baiamonte G. (1994), Flow velocity profiles in gravel-bed rivers, *J. Hydr. Eng.*, 120(1), 60-80.
- Franca M.J. (2005 – A.2), Flow dynamics over a gravel riverbed, *Proc. XXXI IAHR Congress*, Seoul (South Korea). Appendix A.2.
- Franca M.J. and Lemmin U. (2004 – A.1), A field study of extremely rough, three-dimensional river flow, *Proc. 4th Int. Symp. Env. Hyd. - IAHR*, Hong Kong (China). Appendix A.1.
- Franca M.J. and Lemmin U. (2005 – A.3), Cross-Section periodicity of turbulent gravel-bed river flows, *Proc. 4th RCEM. Urbana - Illinois (USA)*. Appendix A.3.
- Franca M.J. and Lemmin U. (2005 – 2.2), subchapter “Eliminating velocity aliasing in acoustic Doppler velocity profiler data”.

- Franca M.J. and Lemmin U. (2005 – 3.1), subchapter “Mean streamwise velocity in gravel-bed river flows”.
- Franca M.J. and Lemmin U. (2005 – 3.2), subchapter “3D mean velocity distribution in gravel bed rivers”.
- Graf W.H. and Altinakar M.S. (1998), *Fluvial Hydraulics*, John Wiley and Sons, West Sussex (UK).
- Hurther D., Lemmin U. and Blanckaert K. (2002), A field study of transport and mixing in a river, using an acoustic Doppler velocity profiler, *Proc. Riverflow 2002*, Louvain-la-Neuve (Belgium).
- Katul G., Wiberg P., Albertson J. and Hornberger G. (2002), A mixing layer theory for flow resistance in shallow streams, *Water Resour. Res.*, 38(11), 1250.
- Kawanisi K. (2004), Structure of turbulent flow in a shallow tidal estuary, *J. Hydr. Eng.*, 130(4), 360-370.
- Marchand J.P., Jarret R.D. and Jones L.L. (1984), Velocity profile, surface slope, and bed material size for selected streams in Colorado, U.S. Geol. Surv. Open File Rep., 84-733.
- Monin A.S. and Yaglom A.M. (1971), *Statistical Fluid Mechanics: Mechanics of Turbulence - Vol. 1*, The MIT Press, Cambridge (USA).
- Nelson J.M., McLean S.R. and Wolfe S.R. (1993), Mean flow and turbulence fields over two-dimensional bed forms, *Water Resour. Res.*, 29(12), 3935-3953.
- Nikora V. and Smart G.M. (1997), Turbulence characteristics of New Zealand gravel-bed rivers, *J. Hydr. Eng.*, 123(9), 764-773.
- Nikora V. and Goring D. (2000), Flow turbulence over fixed and weakly mobile gravel beds, *J. Hydr. Eng.*, 126(9), 679-690.
- Nikora V., Koll K., McLean S., Dittrich A. and Aberle J. (2002), Zero-plane displacement for rough-bed open-channel flows, *Proc. Riverflow 2002*, Louvain-la-Neuve (Belgium).
- Rolland T. and Lemmin U. (1997), A two-component acoustic velocity profiler for use in turbulent open-channel flow, *J. Hydr. Res.*, 35(4), 545-561.
- Roy A.G., Buffin-Belanger T., Lamarre H. and Kirkbride A.D. (2004), Size, shape and dynamics of large-scale turbulent flow structures in a gravel-bed river, *J. Fluid Mech.*, 500, 1-27.
- Shen C. and Lemmin U. (1997), Ultrasonic scattering in highly turbulent clear water flow, *Ultrasonics*, 35, 57-64.
- Tritico H.M. and Hotchkiss R.H. (2005), Unobstructed and obstructed turbulent flow in gravel bed rivers, *J. Hydr. Eng.*, 131(8), 635-645.
- Wolman M.G. (1954), A method of sampling coarse river-bed material, *Trans. Amer. Geoph. Un.*, 35(6), 951-956.

3.4 FLOW RESISTANCE CHARACTERIZATION IN SHALLOW GRAVEL-BED RIVERS

Subchapter 3.4 was submitted for publication to the journal, Water Resources Research (AGU). The authors are M.J. Franca and U. Lemmin.

This subchapter concerns the characterization of flow resistance in shallow gravel-bed rivers. Three types of velocity distribution within the roughness length are studied: mono-logarithmic, s-shaped and double logarithmic. The division of the flow in three inviscid outer layers is proposed: roughness layer, blending layer and surface layer.

	ABSTRACT	3.4.1
1	INTRODUCTION	3.4.1
2	RIVER CHARACTERISTICS	3.4.2
3	INSTRUMENTATION	3.4.4
4	MONOLOG, S AND 2XLOG VELOCITY PROFILES	3.4.4
5	VELOCITY PROFILE PARAMETERIZATION	3.4.5
5.1	Mono-logarithmic profile	3.4.5
5.2	Double logarithmic boundary layer	3.4.7
5.3	S-shaped profile	3.4.8
5.4	Eddy correlation method	3.4.11
6	DISCUSSION AND CONCLUSIONS	3.4.13
	ACKNOWLEDGEMENTS	3.4.15
	REFERENCES	3.4.15

FLOW RESISTANCE CHARACTERIZATION IN SHALLOW GRAVEL-BED RIVERS

ABSTRACT

Flow energy loss is one of the most important parameters needed to model mixing and transport processes of geophysical flows. This paper is based on 3D ADVP gravel-bed river measurements and contributes to the understanding of the resistance determination in shallow macro-rough flows. Three types of velocity distribution may be found in these kinds of flows: logarithmic (monolog), s-shaped and double logarithmic layer (2xlog). The s-shaped profiles are due to the presence of large-scale bed perturbations that inflect the velocity profile. Downstream of the bed perturbation, double boundary layers occur: an inner logarithmic layer is formed near the bottom by redistribution of the momentum throughout the depth; a second boundary layer is formed due to the upstream wake effect. Monolog and 2xlog profile flow resistance is determined by the riverbed drag. For monolog profiles, the velocity distribution is only parameterized by the bottom friction velocity (u^*) and roughness height (z_0). In 2xlog profiles, the friction velocity and roughness length determined from the outer logarithmic layer are also required. The friction velocity determined from the classic log-law approach does not necessarily correspond to the actual bottom drag, since bottom drag depends on the dominant momentum direction which is locally highly variable. The s-shaped velocity profiles are described by a tangent-hyperbolic function, parameterized with a reference velocity u_0 ($u_0 \approx u_\infty/2$) and a geometric parameter scaling with the mean size of the larger coherent structures inside the roughness layer ($L \approx \bar{L}_{int}(z < Z_{RL})$). L may be related to the bottom gravel distribution, $L = \alpha D_{84}$ ($\alpha = 0.25$, in the present case). According to our data, the flow resistance is characterized by a resistance coefficient $C_u = 1/\kappa \cdot \ln(\alpha' D_{84}/z_{0,s})$, where $\alpha' = 0.21$. In the intermediate layer, the shear stress distribution is self-similar, independent of local bottom roughness conditions. The flow field may be divided into three different inviscid layers: 1) a roughness layer ($z < Z_{RL} \approx 0.20h$), where the flow is 3D and deviations from a linear shear stress distribution occur; 2) a blending layer ($Z_B \approx 0.20h < z < Z_{SL} \approx 0.80h$), where the shear stress distribution is linear and similar; and 3) the surface layer ($z > Z_{SL} \approx 0.80h$), where the flow is 3D again and deviations from a linear shear stress occur.

Key-words: friction velocity; shallow gravel-bed river; log-profile; s-profile; double boundary layer

1 INTRODUCTION

The present research deals with gravel-bed river flows under shallow water conditions in the presence of large-scale roughness on the riverbed (relative roughness $D_{84}/h \approx 0.45$). Shallow river flows with large

obstacles, are an important subject in geophysical fluid mechanics, because their mixing and transport dynamics are similar to other shallow flows over irregular bottoms, such as atmospheric winds and ocean currents around obstacles. The best way to determine bed shear stress is still an open subject in fluid mechanics (Biron et al. 2004).

In these flows, the mean velocity in the lower regions assumes two kinds of profiles, logarithmic and s-shaped (Marchand et al. 1984). Bathurst (1988), Ferro and Baiamonte (1994) and Franca and Lemmin (2005 – 3.3) discussed the role of relative roughness defined as D/h (where D is a roughness characteristic length scale and h the water depth) in the occurrence of s-shaped profiles. The wake effect formed by the presence of individual riverbed boulders causes local deviations in the velocity profile (Robert et al. (1992), Nelson et al. (1993), Baiamonte et al. (1995), Buffin-Bélanger and Roy (1998), Carravetta and Della Morte (2004) and Franca (2005 – A.2)).

Katul et al. (2002) studied the similarity between the inflected velocity profiles found in flows over gravel riverbeds and in atmospheric canopy flow. We observed however that a continuous inflection of velocity does not exist in gravel-bed river flows, and that s and log profiles coexist. Downstream of a singular river obstacle, the velocity distribution gradually reacquires the log-shape in the inner layer, but due to the wake effect, a second boundary layer is generated (Chriss and Caldwell (1982), Lueck and Lu (1997) and Sanford and Lien (1999)). Both boundary layers of this transitory type of profile have a logarithmic distribution. The shear controlling the inner log layer is due to the bottom drag, whereas the shear in the outer log layer is due to the upstream bed form (Chriss and Caldwell (1982), Lueck and Lu (1997) and Sanford and Lien (1999)).

The roughness sublayer ($z < z_{RL}$) is the region of the flow where deviations from the logarithmic law in the velocity profiles are expected and the flow is 3D (Nikora and Smart 1997). Based on field measurements, Nikora and Smart (1997), Smart (1999) and Franca and Lemmin (2004 – A.1) showed that the log-law may be used to describe the velocity distribution in gravel-bed river flows.

However, for highly 3D flows such as the present one, local variations in the velocity distribution, with consequences on the local bottom shear and the momentum distribution, are important with respect to mixing and transport processes to be considered for modelling purposes. It is therefore necessary to evaluate bed friction as a function of the local characteristics.

In the present paper, methods for determining friction velocity are analyzed: the profile method applied to single boundary-layer profiles; the profile method applied to double boundary layer profiles; and the eddy-correlation method. The s-profile is parameterized with a tanh function using local turbulent scales. We assess the roughness coefficients given by Katul et al. (2002) in order to characterize the flow resistance.

The notation adopted for the Reynolds velocity decomposition is streamwise, $u = \bar{u} + u'$; spanwise, $v = \bar{v} + v'$; and vertical, $w = \bar{w} + w'$ ($\bar{\quad}$ temporal mean and $'$ instantaneous value).

2 RIVER CHARACTERISTICS

The present measurements were taken during the summer of 2004, in the Swiss river Venoge (canton of Vaud). The instantaneous velocity profiles were measured in a single day under stationary shallow water flow conditions, as confirmed by the discharge data provided by the Swiss Hydrological and Geological Services. The measuring position was located about 90 m upstream of the Moulin de Lussery. The river hydraulic characteristics at the time of the measurements are shown in Table 1.

Table 1 - Summary of the river hydraulic characteristics.

Discharge	Slope	Mean depth	Width	\bar{U}	Re	Fr	D_{50}	D_{84}
Q	S	\bar{h}	B					
(m^3/s)	%	(m)	(m)	(m/s)	($\times 10^{-4}$)	(-)	(mm)	(mm)
0.76	0.33	0.20	6.30	0.60	5.9 - 8.7	0.32 - 0.61	68	89

\bar{U} is the section-averaged streamwise velocity; Re, the Reynolds number; Fr, the Froude number; D_{50} and D_{84} , the bed grain size diameter for which 50% and 84% of the grain diameters are smaller. The riverbed material was sampled according to the Wolman method (1954), and analyzed using standard sieve sizes to obtain the weighted grain size distribution. Considering the average water depth, the ratio B/h is 31.5, which corresponds to wide channels. Given the ratio $h/D_{50}=2.94$, the river is of intermediate scale roughness as defined by Bathurst et al. (1981). The riverbed is hydraulically rough, composed of coarse gravel and randomly spaced macro-roughness elements as high as half the water depth ($0.5h$). The slope and Froude number are within the normal range referred to by Bathurst et al. (1981) for boulder-bed rivers. There was no sediment transport during the measurements.

The measurements were made on a 3×5 rectangular horizontal grid (x-y). Fifteen velocity profiles were equally spaced in the spanwise direction with a distance of 10 cm, and in the streamwise direction with a distance of 15 cm. The vertical resolution of the measurements is around 0.5 cm. A measuring grid covering a 3D control volume was defined. 2D mass conservation was checked in the boundaries of the control volume. Water mass flux in the upstream and downstream boundaries was 0.031 and $0.030 \text{ m}^3\text{s}^{-1}$, respectively. The lateral water flux was small, 0.0008 and $0.001 \text{ m}^3\text{s}^{-1}$, for the right and left lateral boundaries, respectively and the flow is mainly in the streamwise direction. The volume is sufficiently large to smooth out local 3D features in a global analysis. Given the streamwise fluxes, the flow under the detected riverbed (within the bed material) has no significance in this case or may be constant.

The data between all the fifteen positions of the measurement grid were obtained through 3D interpolation using a cubic spline fitting. The level of the riverbed was determined by the sonar-backscattered response (Fig. 1). The profiles were measured for 3.5 min.

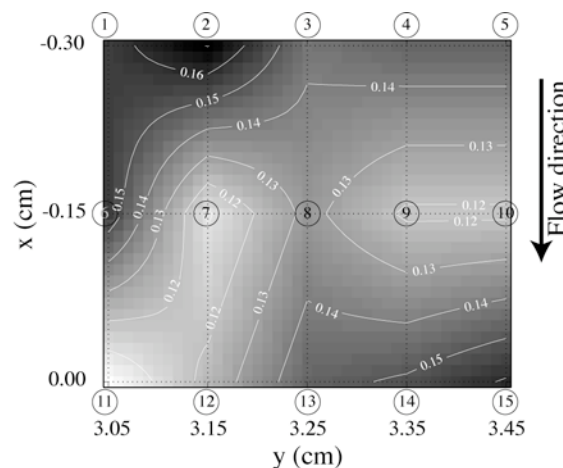


Figure 1 – Riverbed elevation in the measured control volume and location of the measured profiles. The spanwise distances are measured from the right riverbank.

3 INSTRUMENTATION

The deployable ADVP developed at the LHE-EPFL, allows measuring 3D quasi-instantaneous velocity profiles over the entire depth of the flow in rivers. Its resolution permits evaluating the main turbulent flow parameters. The detailed ADVP working principle is given in Rolland and Lemmin (1997). Doppler acoustic sonar instrumentation is based on the sound backscattered by movable targets in the water, responding to an emitted ultrasonic pulse. According to the Doppler principle, the shift between the emitted and the received sound signal is proportional to the target's velocity. We used a configuration of the ADVP consisting of four receivers to one emitter, which provides one redundancy in the 3D velocity profile measurements. This is used for noise elimination and data quality control (Hurther and Lemmin 2000). A Pulse Repetition Frequency (PRF) of 1666 Hz and a Number of Pulse Pairs (NPP) of 64 were used for the estimate of the Doppler shift, resulting in a sampling frequency of 26 Hz. We implemented a dealiasing methodology, which corrects the instantaneous Doppler frequencies measured in the four receivers (Franca and Lemmin 2005 – 2.2). A bridge which supported the ADVP instrument allowed the easy displacement of the system across the section and along the river streamwise direction (Fig. 2). It reduced the vibration of the ADVP and flow disturbance.

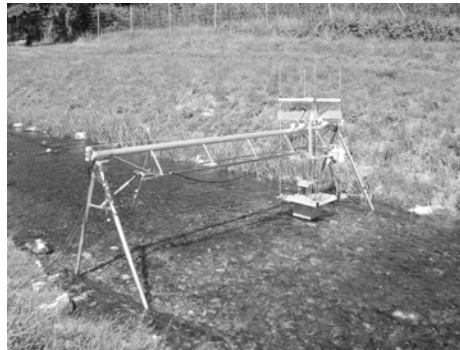


Fig. 2 – Deployable 3D ADVP system placed for measurements.

4 MONOLOG, S AND 2XLOG VELOCITY PROFILES

In all the 15 measured profiles, the three types of velocity distribution were detected, log, s and 2xlog (Table 2).

Table 2 – Classification of the measured velocity profiles according to the distribution.

Mono-logarithmic velocity profiles	S-shaped velocity profiles	Double-logarithmic velocity profiles
P3, P5, P7, P11, P13	P2, P4, P8, P9, P10, P12	P1, P6, P14, P15

Although no systematic distribution of the three types of profile is observed (Table 2 and Fig. 1), their occurrence is a direct consequence of the bed form distribution. Amongst the five longitudinal planes that compose the measurement grid, one example showing the transition between the three velocity distributions (monolog-s-2xlog) is found in plane P5-P10-P15 ($y=3.45$ m, Fig. 1). Franca (2005 – A.2) described this case in detail. The dynamics of the flow were investigated taking into account the spanwise mean velocity component, the Reynolds turbulent stresses and a coherent structure analysis. An individual bed perturbation scaling with D_{84} (Fig. 3) is responsible for the velocity inflection. In the

presence of the obstacle, three regions of the flow are identified, corresponding to the transition between the three profiles (Fig. 3): (A) convergence of the flow in the outer layers above the boulder; (B) separation of the flow due to the boulder creating a shielded inner zone, where the mean velocity distribution is inflected; (C) a double boundary layer profile indicating momentum redistribution throughout the water depth. Low momentum regions are laterally conveyed into the lee of the bed perturbations by the mean spanwise field, contributing to the inner log law layer in the downstream profile. The shear zone in the upper logarithmic layer is due to the form drag caused by the upstream obstacle.

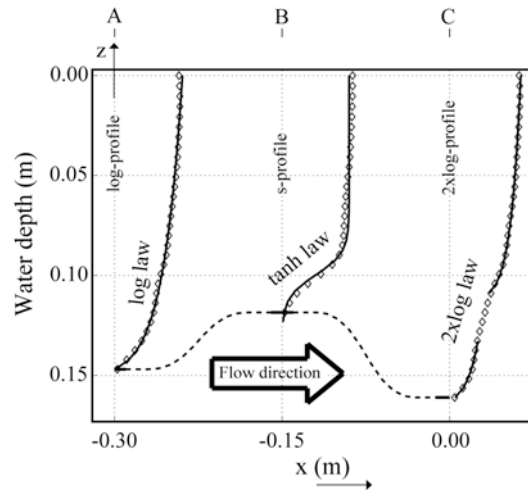


Fig. 3 – Example of the transition between log-s-2xlog velocity profiles.

5 VELOCITY PROFILE PARAMETERIZATION

5.1 Mono-logarithmic profile

We parameterized the bed roughness of the monolog profiles based on the classic logarithmic law approach for open-channel flow (Monin and Yaglom 1971). The log-law, for hydraulically rough flows, is parameterized by the bottom friction velocity (u^*_{\log}) and by a geometric parameter (the roughness length – z_0) that accounts for both the actual bed roughness and form:

$$\frac{\bar{u}(z)}{u^*_{\log}} = \frac{1}{\kappa} \ln\left(\frac{z}{z_0}\right) \quad (1)$$

κ is the Von Karman constant, $\kappa = 0.41$. The bottom detected by the ADV was considered as the origin of the z -coordinate for each measured profile. The logarithmic function fits are shown in Fig. 4 against the measured data. In the lower layer, the velocity profiles present only one slope in the logarithmic representation. In Fig. 4 we can confirm the suitability of the monolog fits to explain most parts of the velocity distribution. Mono-logarithmic profiles are only sheared by the bottom roughness. It should be emphasized that the friction velocity values which correspond to the best fits in Fig. 4 do not necessarily represent the actual bottom friction, since the main friction may not occur in the downstream direction. As indicated above, these flows over macro-rough beds present deviations from the log-law in the upper layers. Thus only the lower layers of the flow shall be used in the bed roughness characterization.

Only the lowest 40% of the flow depth was used in the regression for the profile parameterization since deviations from the log-law may occur in the outer layer (Bathurst (1988), Ferro and Baiamonte (1994) and Franca and Lemmin (2005 – A.3)). u^*_{log} and $z_{0,log}$ were calculated by regressing the velocity against the logarithm of the water depth, as proposed by Bergeron and Abrahams (1992). The results obtained for each measured profile are presented in Fig. 5 and in Table 3.

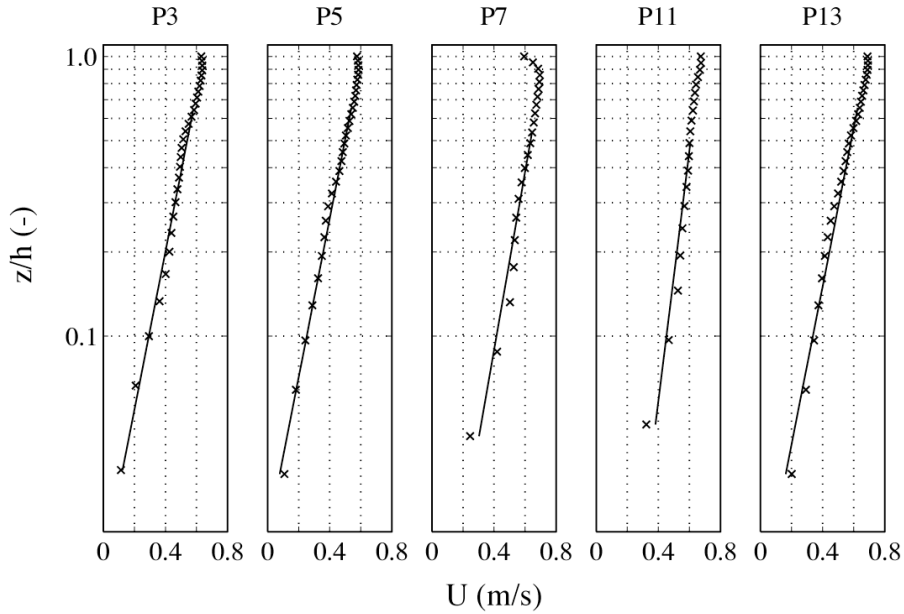


Figure 4 – Best fits for the monolog velocity profiles.

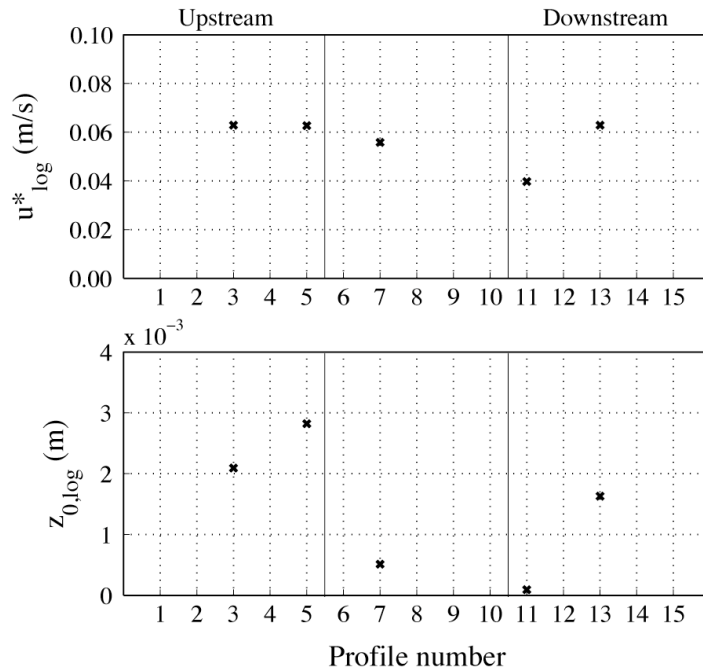


Figure 5 – Results of friction velocity and roughness length using the profile method.

Table 3 – Friction parameterization of the monolog profiles using the log-law approach.

	P3	P5	P7	P11	P13	Average	St. dev.
u^*_{\log} (m/s)	0.0629	0.0627	0.0558	0.0397	0.0629	0.057	0.010
$z_{0,\log}$ (m)	0.0021	0.0028	0.0005	0.0001	0.0016	0.001	0.001

A certain variability of the local values of the friction parameters is observed, in particular for the roughness length. Gravel-bed shallow river flows are often 3D, so that the local friction velocity has to be determined for the dominant momentum advection direction (Franca and Lemmin 2005 – 3.1). Nevertheless, an average value provides an overall estimate of the resistance exerted by the bed in the downstream flow direction.

5.2 Double logarithmic boundary layer

In geophysical flows, the existence of upstream singular perturbations in the flow bed may induce deformations in the logarithmic velocity profile, thus generate the so-called s-shaped profile. Downstream the perturbation, a double boundary layer exists corresponding to the transition from s to mono-logarithmic profiles (Sanford and Lien 1999). Two logarithmic layers form, an inner and an outer layer, in the velocity distribution. The inner layer is sheared by the actual riverbed roughness, whereas the outer layer is conditioned by the form drag induced by the upstream obstacle. Four 2xlog profiles were detected in the present data set (Table 2). The regression fits are shown in Fig. 6 against the measured data.

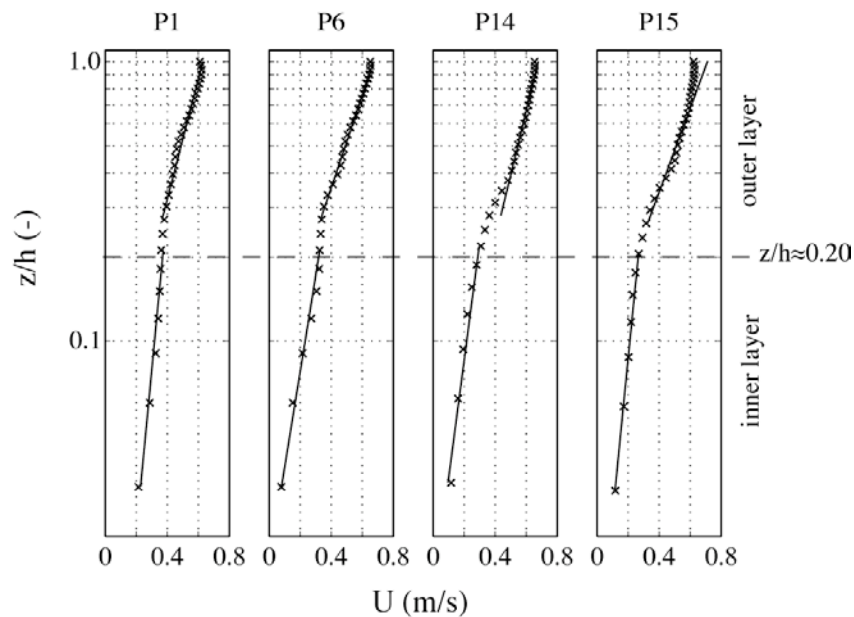


Figure 6 – Best fits for the 2xlog velocity profiles.

The velocity distributions clearly have two linear segments of different slopes, indicating the existence of the two boundary layers. The double fit in Fig. 6 better follows the observations than a single linear

slope. The position of the second boundary layer is conditioned by the wake-scale resulting from the upstream perturbation and by the convection field (Franca 2005 – A.2). The transition between the two boundary layers is found at $z/h \approx 0.20$ where the change in the velocity distribution slope is obvious. The profile method was applied to parameterize the friction in both boundary layers. Fig. 7 and Table 4 show the individual results for the four velocity profiles.

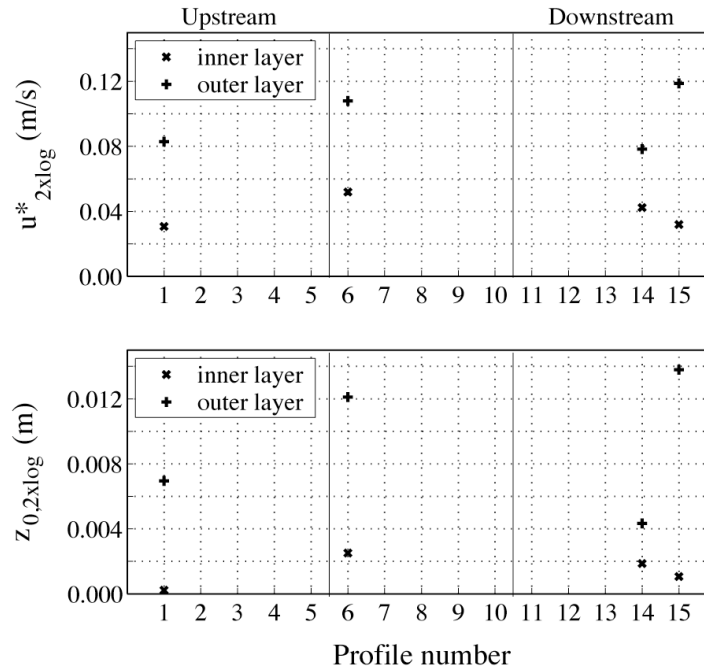


Figure 7 – Results of friction velocity and roughness length using the profile method for the 2xlog velocity profiles.

Table 4 – Friction parameterization of the double boundary layer profiles.

		P1	P6	P14	P15	Average	St. dev.
Lower layer	u^*_{2xlog} (m/s)	0.0307	0.0519	0.0424	0.0319	0.039	0.01
	$z_{0,2xlog}$ (m)	0.0002	0.0025	0.0019	0.0011	0.001	0.001
Upper layer	u^*_{2xlog} (m/s)	0.0829	0.1080	0.0782	0.1188	0.097	0.020
	$z_{0,2xlog}$ (m)	0.0070	0.0121	0.0043	0.0138	0.009	0.004

The friction velocity corresponding to the inner layer (bed roughness drag) is about 40% of the value for the outer layer (form drag). The form effect imposes a more intense slope in velocity distribution than the bed friction.

5.3 S-shaped profile

Inflected velocity profiles with an s-shape are due to individual riverbed perturbations producing localized wakes (Buffin-Bélanger and Roy 1998), or to the continuous effect of the bed roughness as in

the case of atmospheric canopy flow (Raupach et al. 1996). Katul et al. (2002) presented a mixing layer theory for the calculation of the flow resistance in shallow flows where the velocity has an inflection point and may be described by a tangent-hyperbolic function. Franca (2005 – A.2) parameterized one of the s-profiles from the present measurements with a tanh function, where the independent parameters are an energetic eddy size L and a reference velocity u_o :

$$\frac{\bar{u}}{u_o} = \tanh\left(\frac{z - Z_o}{L}\right) + B' \quad (2)$$

Z_o is a reference depth, corresponding to the inflection point in the tanh function; L is an energetic eddy size (Katul et al. 2002) representing the velocity decay; u_o is a reference velocity at the level $z=Z_o$; and B' defines the translation imposed on the tanh asymptote. The following relations were established between Z_o and L , assuming a no-slip condition and that the velocity slope tends to infinity near the bed:

$$\bar{u} = 0 \Rightarrow \frac{z - Z_o}{L} = a \tanh(-1) \Rightarrow Z_o \approx L\pi \quad (3)$$

$$\bar{u} = u_o \Rightarrow \frac{z - Z_o}{L} = a \tanh(0) \Rightarrow z = Z_o \quad (4)$$

The geometric parameter L represents a characteristic eddy size produced by Kelvin-Helmholtz type instabilities at the interface Z_o (Michalke (1964) and Katul et al. (2002)). Franca (2005 – A.2) analyzed the characteristic eddy sizes inside the roughness layer and concluded that the parameter L scales with the mean integral scale ($L \approx \bar{L}_{int}(z < Z_{RL})$). The reference velocity u_o corresponds to half of the constant velocity in the outer “potential layer” ($u_o = u_\infty/2$). Setting $B'=1$, the positive asymptote will converge to the “quasi” constant velocity in the outer layer of the flow, whereas the negative asymptote will converge to zero for $z \rightarrow 0$ (no-slip boundary condition).

In the present analysis however, a tanh function does not describe the velocity throughout the flow depth. In the case analyzed before, the velocity distribution in the outer layers of the flow was close to that of potential flow. From the remaining data, it appears that the outer layer of the flow is better described by a logarithmic law. As in the case of the 2xlog profiles, a second boundary layer exists corresponding to an outer logarithmic layer above the velocity inflection in the s-profile. In Fig. 8 we represent the s-profiles identified earlier (Table 2), fitted with a tanh law for the inner layer (an averaged fit curve was chosen for all the profiles) and an external log-law for the outer layer (profile method).

Two layers can be distinguished in the velocity profile: an outer-logarithmic with linear distribution in the log scale, and an inner where an inflection of the velocity profiles forms the so-called s-shape profile ($z/h \approx 0.20$). Based on Franca (2005 – A.2) results, the tanh-law was parameterized as $Z_o/h=0.16$, $L/h=0.12$ $u_o = u_\infty/2$ and $B'=1$. The geometric parameter L may be related to a gravel characteristic diameter, D as $\alpha = \frac{L}{D}$. Using $D=D_{84}$, α becomes $\alpha \approx 0.25$. This is smaller than the value given by Katul et al. (2002) who assumed that the eddy sizes related to instabilities caused by the velocity inflection would be D_{84} ($\alpha \approx 1$). This proved not to be the case in the present data set. The description of the s-profiles in the lower layer using the parameters suggested by Franca (2005 – A.2) fits the present data well. Table 5 shows the roughness parameterization of the outer-log layer of the flow.

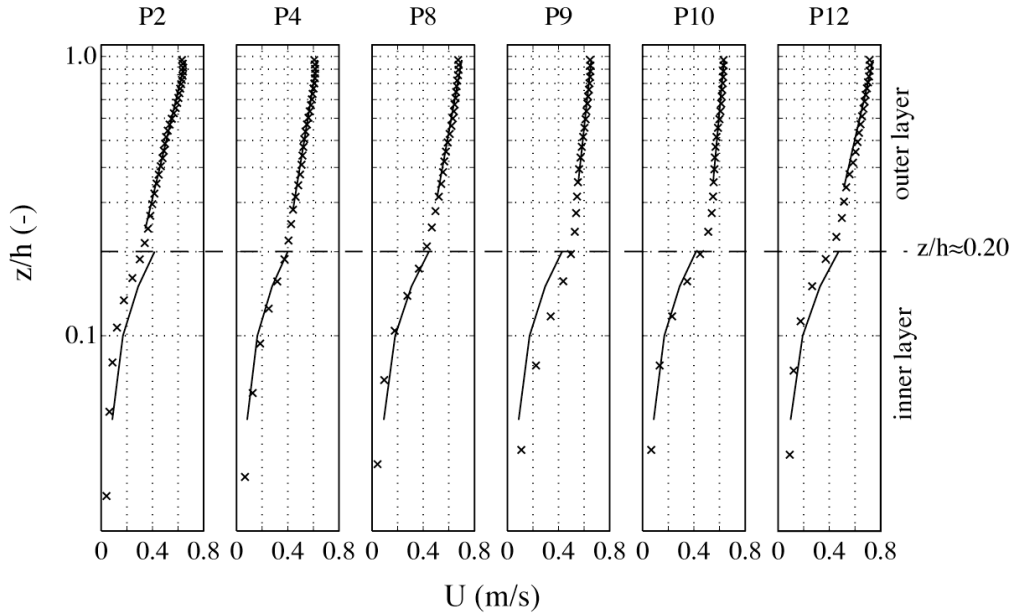


Figure 8 – Data and best fits for s-shaped velocity profiles, tanh-law for the inner layer and log-law for the outer layer.

Table 5 – Friction parameterization of the outer boundary layer for the s-shaped profiles.

		P2	P4	P8	P9	P10	P12	Average	St. dev.
Upper layer	u^*_s (m/s)	0.0925	0.0633	0.0701	0.0414	0.0347	0.0891	0.065	0.024
	$z_{0,s}$ (m)	0.009	0.002	0.002	0.0002	0.0001	0.004	0.003	0.003

The friction velocity corresponding to the outer layer is on the average ≈ 1.5 the value estimated from the eddy correlation method (see subsection 5.4). The determination of the shear stress slope by a log regression to the s-shaped velocity profiles will thus induce errors.

Katul et al. (2002) characterized the flow resistance by the coefficient C_u , defined as:

$$C_u = \frac{u_o}{u^*} \quad (5)$$

Considering an average reference velocity $u_o \approx 0.29$ m/s and an average friction velocity calculated for the outer layer, we obtain $C_u = 4.5$. This value is of the order of magnitude of the value suggested by Raupach et al. (1996) and Katul et al. (1998) for dense canopies and validates the assumptions made by Katul et al. (2002). Assuming that the log and tanh curves match at a flow depth of $z=D$, we may estimate the coefficient C_u by equating the log-law (1) and the tanh-law (2) expressions (Katul et al. 2002):

$$C_u = \frac{1}{\kappa} \ln \left(\frac{D}{z_{0,s}} \right) \quad (6)$$

Given the resistance coefficient $C_u = 4.5$, and using the corresponding average value of $z_{0,s} = 0.003$ m, we find $D = 0.019$ m $\approx \alpha' D_{84}$, where $\alpha' = 0.21$.

5.4 Eddy correlation method

ADVP measurements give access to instantaneous 3D velocities throughout the water depth. Therefore all six Reynolds stress tensor components can be calculated. It is possible to obtain the friction velocity using the so-called eddy correlation method (Franca and Lemmin 2005 – 3.1) from the x-z plane Reynolds shear stress ($\overline{u'w'}$). In turbulent flows with sufficiently high Reynolds numbers, the friction velocity corresponds to the slope of the distribution of the turbulent shear stress $\overline{u'w'}$:

$$u_*^2 = \frac{-\overline{u'w'}}{\left(1 - \frac{z}{h}\right)} \quad (7)$$

Fig. 9 shows the Reynolds shear stress profiles ($\overline{u'w'}$) for the measured profiles.

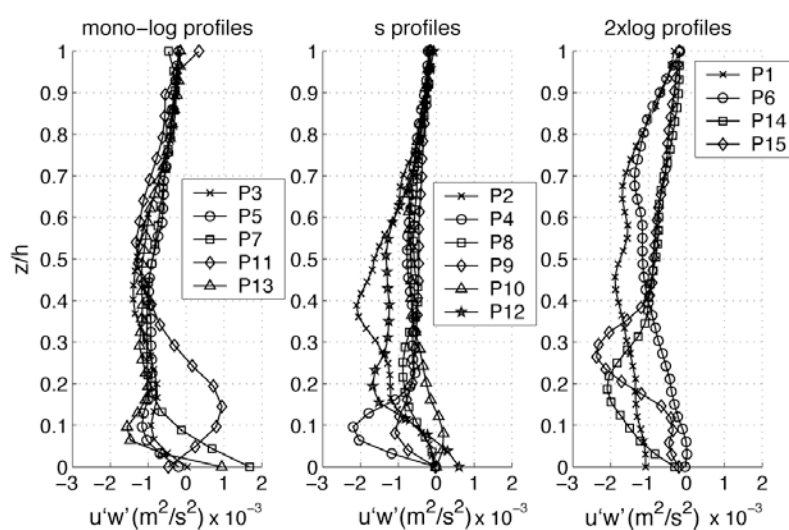


Figure 9 – Reynolds shear stress profiles in plane x-z ($\overline{u'w'}$), obtained from instantaneous ADVP velocity measurements throughout the water depth.

Inside the roughness layer the Reynolds shear stress distribution is hardly linear and has major deviations. Nevertheless, the shear stress generally increases with depth. Positive shear stress is found in some profiles due to local flow perturbations. Franca (2005 – A.2) explained the positive values of $\overline{u'w'}$ near the bottom in profile 10 as the result of the wake effect that changes the dominant coherent structure distribution. Two of the 2xlog profiles show unusual shear stress distributions (P1 and P6), probably due to the interference of the upstream obstacle and the subsequent redistribution of turbulence throughout the flow depth. The second shear layer in 2xlog profiles is situated roughly at $z/h \approx 0.25$. It can induce instability leading to turbulence production in the upper layer.

The linearity of the Reynolds shear stress distribution throughout the depth can be evaluated by plotting the evolution of u_* as expressed by equation (7). The distribution of the square root of the right hand term in equation (7) is presented in Fig. 10.

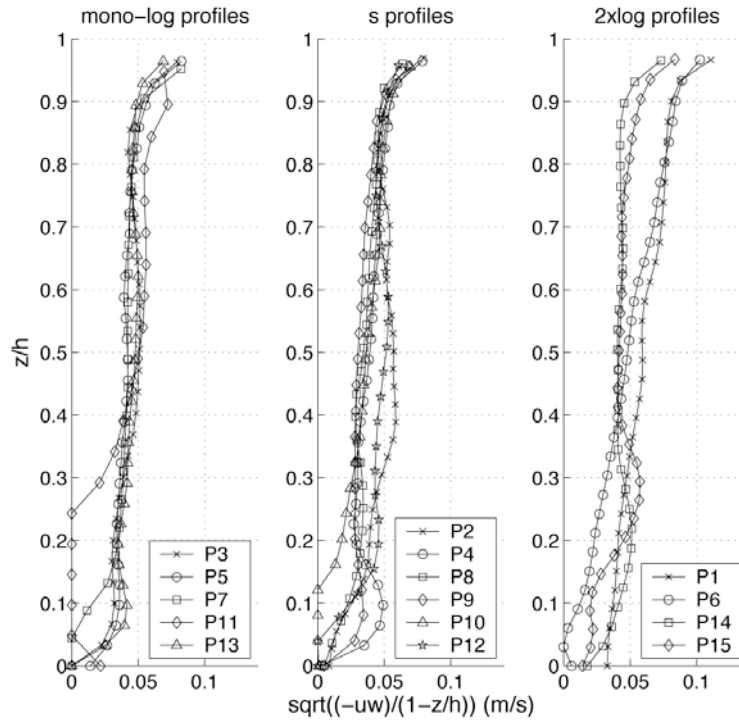


Figure 10 – Vertical distribution of the Reynolds shear stress linearity (plane x-z), as defined by

$$\text{expression (7) - } \sqrt{\frac{-\overline{u'w'}}{\left(1 - \frac{z}{h}\right)}}.$$

From Fig. 10 the Reynolds shear stress $\overline{u'w'}$ distribution is fairly linear throughout the water depth with the exception of layers $z/h \approx 0.20$ and $z/h \approx 0.80$, where perturbations occur close to the riverbed and near the surface as expected. The trend of $\overline{u'w'}$ has the same linear slope for all measured profiles. This indicates that independent of the inner boundary conditions, self-similarity of the shear stress distribution with the velocity scale u^* exists above a determined height. A surface layer can be defined as where deviations from the linear shear stress occur again ($z/h \approx 0.80$). The intermediate region of the flow where shear stress self-similarity is observed, we call the blending layer, in analogy with the concept of blending height used in atmospheric flows (Wieringa 1976). Inside the blending layer, the boundary effects of the surface layer and the rough riverbed on the shear stress distribution are smoothed out and “blended” into one combined effect. From our measurements, the blending layer is situated within $0.20 \approx z/h \approx 0.80$ where to $z_B \approx 0.20h$ is called the blending height. The upper value corresponds to the limit of the SLOM (Surface Layer Organized Motion) described by Franca and Lemmin (2005 – A.3). The fact that shear stress distributions are not self-similar in the lower layers of the flow is another indication that a 2D friction velocity is not suitable for the description of bed drag. To determine the bed drag, we shall look at the predominant momentum advection direction. Using equation (7) we only considered the linear layer as Wang et al. (2003) did. Profiles 1 and 6 were not considered because no linear segment was detected in the shear stress distribution. Fig. 11 and Table 6 show the results of the bottom friction velocity for all profiles.

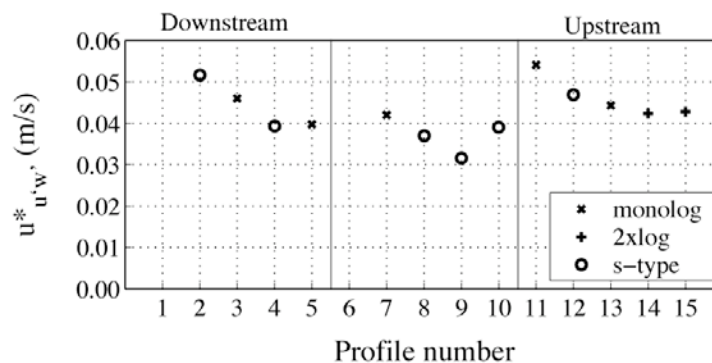


Figure 11 – Results of friction velocity estimated with the eddy correlation method.

Table 6 – Friction velocities estimated with the eddy-correlation method.

Profile	2	3	4	5	7	8	9	10
$u^*_{u,w'}$ (m/s)	0.052	0.046	0.039	0.040	0.042	0.037	0.032	0.039

Profile	11	12	13	14	15	Av.	Std.
$u^*_{u,w'}$ (m/s)	0.054	0.047	0.044	0.042	0.043	0.043	0.006

The friction velocity variation between individual profiles is lower than in the previous analysis. This confirms that self-similarity exists inside the blending layer. However, when compared with the results given by the profile method in the previous two subsections, large differences are observed. The slope of the downstream velocity inflection in the lower layers can be determined by the log-law. However no direct link can be established between this value and the actual bottom drag, since the downstream direction may not be the main momentum direction of the flow. For the double logarithmic profiles, the eddy-correlation method always gives friction velocities lower than the outer layer values estimated by the profile method in accordance with the results of Biron et al. (2004). The interface roughness-intermediate layer determines the shear stress distribution.

6 DISCUSSION AND CONCLUSIONS

An estimate of flow energy loss is important in geophysical flow modelling. This paper deals with the determination of friction velocity in shallow gravel-bed river flows. It is shown that logarithmic, s-shaped and double logarithmic velocity distributions coexist in gravel-bed rivers.

The friction velocities determined with the eddy-correlation method, falls into a narrow range. In all measured profiles, the Reynolds shear stress distribution is roughly linear within $0.20 < z/h < \approx 0.80$, and with a comparable linear slope ($u^*_{u,w'} = 0.043 \text{ ms}^{-1}$). The turbulent shear throughout the water depth is similar for the different types of profiles. This suggests that self-similarity exists with a certain velocity scale in this intermediate layer. We consider the eddy-correlation results for the friction velocity as a reference (as suggested by Biron et al. 2004), since they correspond to the region of the flow where the influence of the highly perturbed bottom is reduced.

Logarithmic profiles are only sheared by riverbed drag, and the velocity distribution may be parameterized by the bottom friction velocity (u^*) and roughness height (z_0). The profile method generally overestimated the values of the friction velocity in these cases.

When the roughness element height increases relative to the total flow depth, wake effects are formed and the effect of the bed protuberances extends downstream. In this case, the velocity near the bed is inflected and the log-law no longer describes its distribution. The velocity distribution thus becomes s-shaped near the riverbed and reacquires a logarithmic configuration above the roughness length. The lower layer of these inflected velocity profiles can be described by a tangent-hyperbolic function, parameterized with a reference velocity u_o ($u_o \approx u_{oc}/2$) and a geometric parameter of the same order of magnitude as the mean integral scale of the eddies present inside the roughness sublayer ($L \approx \bar{L}_{int}(z < Z_{RL})$). L is related to the bed material as $L = \alpha D_{84}$ ($\alpha = 0.25$). The flow resistance is

characterized by the coefficient $C_u = \frac{u_o}{u^*} = 4.5$ or $C_u = \frac{1}{\kappa} \ln \left(\frac{\alpha' D_{84}}{z_{0,s}} \right)$, where $\alpha' = 0.21$.

Downstream of the bed perturbation, momentum is redistributed throughout the flow depth and a logarithmic layer is formed again near the bottom. However, the upstream influence of the bed form creates a second boundary layer at a height determined by the upstream wake effect. The description of the flow velocity distribution requires the definition of the parameters friction velocity (u^*) and roughness height (z_0) for both logarithmic layers, whereas the flow resistance is only determined by the inner layer parameters. The inner logarithmic layer is sheared by the local bottom roughness, and the outer logarithmic layer shear is due to the form drag in the flow. Lateral momentum transfer occurs between the upstream and downstream regions of the bed perturbations, contributing to the inner boundary layer. The analysis of the double boundary layers indicates that the shear in the second log-layer has a small influence on the flow resistance determination. The form shear is locally important in the description of the vertical distribution. However, the actual friction effect in the flow is determined by the bottom shear. The influence of the bed perturbation in the downstream profile is due to coherent structures generated in the velocity inflection (Kelvin-Helmholtz type instabilities described by Michalke (1964)) and advected downstream. The inner roughness length of $z_{0,inn} \approx 0.007h \approx 1\% D_{84}$ is small when compared to the outer scales of the flow. The outer roughness length is about 10 % of the grain diameter D_{84} .

The friction velocities calculated here probably do not correspond to the actual drag acting at the interface flow-riverbed. The local roughness parameterization based on the logarithmic law, considering the downstream direction, only provides an indication of the velocity slope in this direction. However, the actual drag occurs in the predominant momentum direction, which changes locally. This explains the scatter of the results obtained. Away from the bed, the roughness effects blend and the shear stress slope is more uniform, suggesting that the flow here is less 3D. Nevertheless only a combined investigation of all the tangential Reynolds stresses will allow determining the actual bottom drag and how its effect is transmitted throughout the water column.

In the s-shaped and double boundary layer profiles, the transition between the inner layer and the outer layer defines the roughness layer which is $z_{RL} \approx 0.20h$ in outer scales. It is $z_{RL} \approx 0.30D_{84}$ as a function of the bed grains distribution. We suggest the division of the flow into three inviscid layers: 1) the roughness layer ($z < z_{RL} \approx 0.20h$); 2) the blending layer ($z_B \approx 0.20h < z < z_{SL} \approx 0.80h$); and 3) the surface layer ($z > z_{SL} \approx 0.80h$). In the blending layer the shear stress distribution is self-similar, independent of the position in the river; here the influence of the bed roughness and of the surface are smoothed out and a combined shear effect is exerted.

Further research should be carried out in shallow flows to determine under which conditions of relative roughness (D/h) the deviation of the predominant momentum direction no longer allows the log-law 2D approach. A complete turbulence flow study of the inviscid layers is necessary to determine their

interaction and the bottom influence at the near surface layer. An understanding of geophysical flows within large roughness environments is of major importance since it affects mixing and transport processes. This phenomenon is common to shallow river flows, atmospheric winds around mountains, buildings etc, and oceanic currents around underwater bottom forms.

ACKNOWLEDGEMENTS

The authors acknowledge the financial support of the Portuguese Science and Technology Foundation (BD 6727/2001) and the Swiss National Science Foundation (2000-063818).

REFERENCES

- Baiamonte G., Giordano G. and Ferro V. (1995), Advances on velocity profile and flow resistance law in gravel bed rivers, *Excerpta*, 9, 41-89.
- Bathurst J.C., Li R.M. and Simons D.B. (1981), Resistance equation for large-scale roughness, *J. Hydr. Eng.*, 107(12), 1593-1613.
- Bathurst J.C. (1988), Velocity profile in high-gradient, boulder-bed channels, *Proc. Int. Conf. Fluv. Hydr.*, Budapest (Hungary).
- Bergeron N.E. and Abrahams A.D. (1992), Estimating shear velocity and roughness length from velocity profiles, *Water Resour. Res.*, 28(8), 2155-2158.
- Biron P.M., Robson C., Lapointe M.F. and Gaskin S.J. (2004), Comparing different methods of bed shear stress estimates in simple and complex flow fields, *Earth Surf. Proc. and Landforms*, 29, 1403-1415.
- Buffin-Bélanger T. and Roy A.G. (1998), Effects of a pebble cluster on the turbulent structure of a depth-limited flow in a gravel-bed river, *Geomorphology*, 25, 249-267.
- Carravetta A. and Della Morte R. (2004), Response of velocity to a sudden change of the bed roughness in sub critical open channel flow, *Proc. Riverflow 2004*, Naples (Italy).
- Chriss T.M. and Caldwell D.R. (1982), Evidence for the influence of form drag on bottom boundary layer flow, *J. Geoph. Res.*, 87 (C6), 4148-4154.
- Ferro V. and Baiamonte G. (1994), Flow velocity profiles in gravel-bed rivers, *J. Hydr. Eng.*, 120(1), 60-80.
- Franca M.J. (2005 – A.2), Flow dynamics over a gravel riverbed, *Proc. XXXI IAHR Congress*, Seoul (South Korea). Appendix A.2.
- Franca M.J. and Lemmin U. (2004 – A.1), A field study of extremely rough, three-dimensional river flow, *Proc. 4th Int. Symp. Env. Hyd. - IAHR*, Hong Kong (China). Appendix A.1.
- Franca M.J. and Lemmin U. (2005 – A.3), Cross-Section periodicity of turbulent gravel-bed river flows, *Proc. 4th RCEM. Urbana - Illinois (USA)*. Appendix A.3.
- Franca M.J. and Lemmin U. (2005 – 2.2), subchapter “Eliminating velocity aliasing in acoustic Doppler velocity profiler data”.
- Franca M.J. and Lemmin U. (2005 – 3.1), subchapter “Mean streamwise velocity in gravel-bed river flows”.
- Franca M.J. and Lemmin U. (2005 – 3.3), subchapter “The occurrence of s-shaped velocity profiles in gravel-bed river flows”.

- Hurther D. and Lemmin U. (2000), A correction method for turbulence measurements with a 3D acoustic Doppler velocity profiler, *J. Atmosph. Ocean. Technol.*, 18, 446-458.
- Katul, G. G., Geron C.D., Hsieh C.I., Vidakovic B., and Guenther A.B. (1998), Active turbulence and scalar transport near the land-atmosphere interface, *J. Appl. Meteorol.*, 37, 1533–1546.
- Katul G., Wiberg P., Albertson J. and Hornberger G. (2002), A mixing layer theory for flow resistance in shallow streams, *Water Resour. Res.*, 38(11), 1250.
- Lueck R.G. and Lu Y. (1997), The logarithmic layer in a tidal channel, *Cont. Shelf Res.*, 17(14), 1785-1801.
- Marchand J.P., Jarret R.D. and Jones L.L. (1984), Velocity profile, surface slope, and bed material size for selected streams in Colorado, U.S. Geol. Surv. Open File Rep., 84-733.
- Michalke A. (1964), On the inviscid instability of the hyperbolic-tangent velocity profile, *J. Fluid Mech.*, 19, 543-556.
- Monin A.S. and Yaglom A.M. (1975), *Statistical Fluid Mechanics: Mechanics of Turbulence - Vol. 2*, The MIT Press, Cambridge (USA).
- Nikora V. and Smart G.M. (1997), Turbulence characteristics of New Zealand gravel-bed rivers, *J. Hydr. Eng.*, 123(9), 764-773.
- Nelson J.M., McLean S.R. and Wolfe S.R. (1993), Mean flow and turbulence fields over two-dimensional bed forms, *Water Resour. Res.*, 29(12), 3935-3953.
- Nezu I. and Nakagawa H. (1993), *Turbulence in open-channel flows - IAHR monograph*, A.A. Balkema, Rotterdam (The Netherlands).
- Pope S.B. (2001), *Turbulent Flows*, Cambridge University Press (UK).
- Raupach M.R., Finnigan J.J., and Brunet Y. (1996), Coherent eddies and turbulence in vegetation canopies: the mixing-layer analogy, *Boundary-Layer Meteo.*, 78, 351-382.
- Robert A., Roy A.G. and De Serres B. (1992), Changes in velocity profiles at roughness transitions in coarse grained channels, *Sedimentology*, 39, 725-735.
- Rolland T. and Lemmin U. (1997), A two-component acoustic velocity profiler for use in turbulent open-channel flow, *J. Hydr. Res.*, 35(4), 545-561.
- Sanford T.B. and Lien R.C. (1999), Turbulent properties in a homogeneous tidal bottom boundary layer, *J. Geoph. Res.*, 104(C1), 1245-1257.
- Smart G.M. (1999), Turbulent velocity profiles and boundary shear in gravel bed rivers, *J. Hydr. Eng.*, 125(2), 106-116.
- Wang Z.Q., Cheng N.S., Chiew Y.M. and Chen X.W. (2003), Secondary flows in open channel with smooth and rough bed strips, *Proc. XXX IAHR Cong.*, Thessaloniki (Greece).
- Wieringa, J. (1976), An objective exposure correction method for average wind speeds measured at a sheltered location, *Q. J. R. Meteorol. Soc.*, 102, 241– 253.
- Wolman M.G. (1954), A method of sampling coarse river-bed material, *Trans. Amer. Geoph. Un.*, 35(6), 951-956.

3.5 STREAMWISE VELOCITY PULSATION (SVP) IN GRAVEL-BED RIVERS

This subchapter concerns the identification and characterization of the passage of large-scale uniform momentum regions (SVP) at low frequency. The implications of the SVP on the turbulent structure of the flow are studied. Analysis methods based on the Hilbert transform and Empirical Mode Decomposition are described.

	ABSTRACT	3.5.1
1	INTRODUCTION	3.5.1
2	FIELD MEASUREMENTS	3.5.2
2.1	Flow characterization	3.5.2
2.2	Instrumentation	3.5.4
3	SVP DETECTION	3.5.4
3.1	Turbulent velocity field	3.5.4
3.2	Low-pass filtered data	3.5.6
3.3	Analysis of the space and time correlations in the flow depth	3.5.7
3.4	Analysis of filtered data	3.5.10
3.5	The Hilbert transform	3.5.11
3.6	Empirical mode decomposition - EMD	3.5.12
4	THE EFFECT OF SVP	3.5.15
4.1	Phase-averaged signal based on the Hilbert transform	3.5.15
4.2	Analysis of the SVP throughout the flow depth	3.5.16
4.3	SVP effect in bottom drag	3.5.18
4.4	SVP effect in the TKE budget	3.5.21
5	THE INTERACTION OF FREE SURFACE WAVES AND SVP	3.5.23
6	DISCUSSION AND CONCLUSIONS	3.5.25
	ACKNOWLEDGEMENTS	3.5.28
	REFERENCES	3.5.28

STREAMWISE VELOCITY PULSATION (SVP) IN GRAVEL-BED RIVERS

ABSTRACT

Large-scale uniform momentum regions (UMR) travelling in the streamwise direction were reported by several authors for gravel-bed river flows. In this paper we analyzed the fluctuating velocity of one velocity profile measured with the 3D ADV in a river with a blockage ratio of $h/D_{84}=2.25$. We identified a low-frequency pulsation in the streamwise velocity corresponding to large-scale regions of velocity alternately higher or lower than the mean. We called it Streamwise Velocity Pulsation (SVP). We applied Huang's Empirical Mode Decomposition to isolate the SVP and with phase averaging techniques based on a Hilbert transform of the velocity signal we were able to characterize the geometry of UMR corresponding to SVP and to evaluate the feedback of the SVP on the turbulent structure of the flow. The SVP Strouhal number is within the range $0.13 < S_{SVP} < 0.32$. The main geometric characteristics of the UMR are: a vertical linear phase shift of $\approx -3/4\pi$ of the front; the front has the shape of a first quarter moon with the apex situated at $z/h \approx 0.35$; in the vertical it scales with the flow depth (h) and in the streamwise direction with $3.1-7.3h$; in the lower layer the fronts have an average angle of 15° with the horizontal. A large-scale sweep-ejection sequence is in phase with the SVP cycle. Though less permanent in the cycle, ejections dominate the shear stress production with higher instantaneous amplitudes. SVP has direct and indirect effects on the bottom drag. A periodic nonlinear variation of the bottom drag of 0.90 to 1.10 times the mean value is related with the SVP (direct). An increase is due to the 3D bursting process triggered by the SVP (indirect). A suggested model for the description of the drag cycle directly related to SVP is presented. The passage of a UMR is not directly related to an increase in the production levels, but to higher frequency productive events. The dissipation rate is due to background small-scale turbulence distributed nearly homogeneously within the flow, and it is not influenced by the SVP. Through an analysis of the linear wave theory applied to the velocity measurements, we concluded that a relationship exists between the SVP and free surface ripples travelling within the UMR. The origin of the SVP is still not clear. In our opinion it is due to a combined shedding effect produced by the large number of boulders, randomly placed in the riverbed. SVP has a regular, non-periodic phase distribution due to the variety of boulder sizes and the interaction between different shedding vortices.

Key-words: Streamwise Velocity Pulsation; large-scale motion; gravel-bed rivers; bursting process

1 INTRODUCTION

The present research concerns large-scale motions covering the whole flow depth found in gravel-bed rivers. In our measurements we observed the passage of a low frequency uniform momentum region

(UMR) scaling with the flow depth and acting jointly with the lower and the surface layers. It is important to understand UMR dynamics and its implications in such processes as suspension, bed-load, mixing and air-water gas exchange. We named the phenomenon Streamwise Velocity Pulsation (SVP).

The occurrence of large-scale regions of uniform momentum in open-channel turbulent flows is reported by several authors from field and laboratory experiments of flows over gravel bed (Williams et al. (1989), Kirkbride and Ferguson (1995), Buffin-Bélanger (2000), Roy et al. (2004), and Hofland (2004)). Theories mention the passage of large UMR's as the trigger of the bursting process in the lower layers leading to 3D turbulence interactions. Adrian et al. (2000) presented a concept where, in the logarithmic layer, larger UMR's contain consecutively smaller UMR's. Lu and Willmarth (1973), Antonia et al. (1990) and Nakagawa and Nezu (1981) observed a link between the passage of organized motions of the order of magnitude of the boundary layer and small-scale bursting. Falco (1977) pointed out the importance of these coherent motions in the momentum exchanges across the boundary layer. Brown and Thomas (1977) showed that due to streamline curvature imposed by the passage of large-scale UMR, the production of Taylor-Görtler instabilities is possible in the lower layer of the flow. Dinehart (1999) mentioned that these large-scale motions will dominate the instantaneous velocity signals and that they might interfere with discharge and sediment transport processes. The implications of the SVP on the turbulence structure of the flow is thus essential in order to provide useful information on the interaction between large- and small-scale processes that need to be taken into account in gravel-bed river modelling.

We observed the SVP phenomenon in field measurements of the flow in gravel-bed rivers (Franca and Lemmin 2004 – A.1). Alternating periods of faster and slower streamwise velocity with respect to the mean velocity occurred regularly at a frequency of about 1 Hz, with a quasi-stationary cycle. Apparently a large part of the water column was affected.

In this paper we use one instantaneous velocity profile to identify and isolate the SVP in the turbulent signal, and characterize its implications in the turbulent structure of the flow. The paper is organized as follows: field measurements and instrumentation description; detection and isolation of the SVP using space and time correlations, filtering processes, and empirical mode decomposition as described by Huang et al. (1998); and using phase averaging based on the identification of the instantaneous signal phase (related to the Hilbert transform), reconstruction of the 3D SVP cycle and investigation of the geometry and the implications in bottom drag, production and dissipation processes.

2 FIELD MEASUREMENTS

2.1 Flow characterization

The field measurements used in the present investigation have already been exhaustively described in Franca and Lemmin (2005 – 3.4). The river hydraulic characteristics at the time of the measurements are shown on Table 1.

Table 1 - Summary of the river flow characteristics.

Discharge	Slope	Mean depth	Width	\bar{U}	Re	Fr	D ₅₀	D ₈₄
Q	S	\bar{h}	B					
(m ³ /s)	%	(m)	(m)	(m/s)	(x10 ⁻⁴)	(-)	(mm)	(mm)
0.76	0.33	0.20	6.30	0.60	5.9 - 8.7	0.32 - 0.61	68	89

\bar{U} is the section-averaged streamwise velocity; Re, the Reynolds number; Fr, the Froude number; D_{50} and D_{84} , the bed grain size diameter for which 50% and 84% of the grain have smaller diameters. The grain diameter distribution was based on the Wolman method (1954) for coarse material. According to Bathurst et al. (1981), this is considered a wide river ($B/h=31.5$) with intermediate scale roughness ($h/D_{50}=2.94$). The riverbed is composed of coarse gravel, with randomly spaced elements as high as half the water depth ($0.5h$). There was no sediment transport during the measurements. 15 instantaneous velocity profiles were measured in a 3×5 rectangular horizontal grid (Fig. 1) for about 3.5 min. The vertical resolution of the measurements is around 0.5 cm. The flow under the riverbed has no significance in this case. The riverbed was detected from the sonar-backscattered response (Fig. 1).

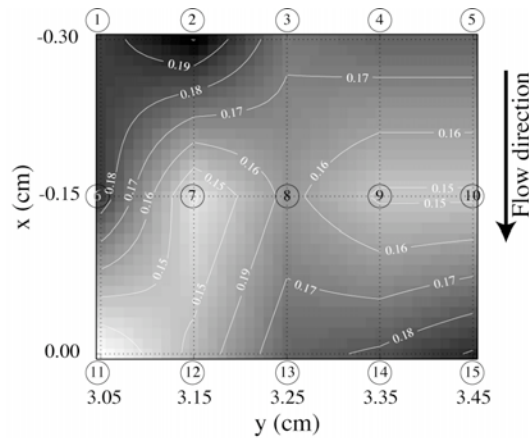


Figure 1 – Riverbed elevation in the measured control volume and location of the measured profiles. The spanwise distances are measured from the right riverbank.

We chose profile 13 for the SVP study. The flow characteristics of profile 13 are summarized in Table 2:

Table 2 - Summary of the flow characteristics of profile 13.

Linear discharge	Flow depth - h	U	Re	Fr	u^*
(m^2/s)	(m)	(m/s)	($\times 10^4$)	(-)	(m/s)
0.09	0.17	0.52	8.75	0.40	0.044

U is the depth-averaged streamwise mean velocity; and u^* is the shear velocity estimated from the eddy-correlation method (Franca and Lemmin 2005 – 3.4). Fig. 2 shows the main hydraulic characteristics of the measured profile: mean velocity profile and Reynolds stress ($\overline{v_i'v_j'}$).

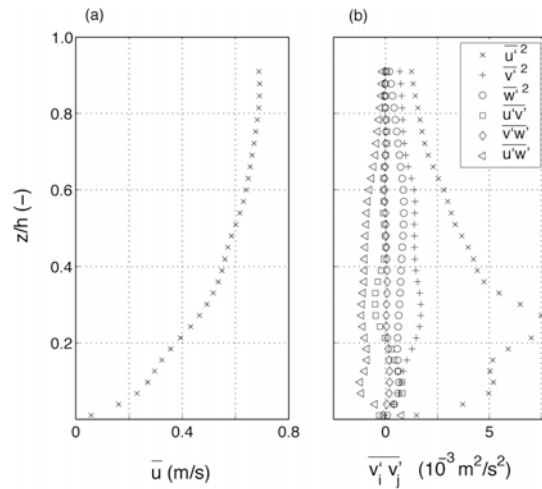


Figure 2 – (a) Mean velocity profile \bar{u} . (b) Distribution of the different components of the Reynolds stress tensor ($\overline{v_i'v_j'}$).

The mean velocity has a logarithmic distribution (Franca and Lemmin 2005 – 3.4). The extremely rough riverbed induces major deviations in the turbulence structure of the flow. Reynolds stress distributions have an increasing trend when approaching the riverbed until roughly $z/h < 0.25$. Below this level, local roughness effects impose random variations. The maximum turbulent kinetic energy (TKE) is situated near $z/h \approx 0.20$, the upper limit for the roughness layer (Franca and Lemmin 2005 – 3.8). Nicholas (2001) observed a similar displacement of the turbulence maximum in gravel-bed flows. Above the roughness layer is the blending layer where the random effects of both the water surface and the riverbed merge and the flow becomes approximately 2D and self-similar (Franca and Lemmin 2005 – 3.4).

2.2 Instrumentation

A deployable ADVP developed at the LHE-EPFL was used for the velocity profile measurements. It allows measuring 3D quasi-instantaneous velocity profiles over the entire depth of the flow in rivers. The ADVP is suitable for field and laboratory measurements. Details on the ADVP are given in chapter 2. A Pulse Repetition Frequency (PRF) of 1666 Hz and a Number of Pulse Pairs (NPP) of 64 were used to estimate the Doppler shift, resulting in a sampling frequency of 26 Hz. A bridge which supported the ADVP instrument allowed the easy displacement of the system across the section and along the river streamwise direction.

3 SVP DETECTION

3.1 Turbulent velocity field

ADVP measurements allow a Eulerian observation of the 3D instantaneous velocities, simultaneously throughout the flow depth. The main momentum transport direction of the flow is streamwise. Earlier observations (Williams et al. (1989), Buffin-Bélanger et al. (2000a), Franca and Lemmin (2004 – A.1))

showed that vertically-correlated large-scale motions occurring in the flow are mainly anisotropic in the streamwise direction. Thus, the SVP detection process will be made in the streamwise instantaneous velocity signal. Fig. 3 shows the streamwise instantaneous velocity profile (u') for a period of 20 s.

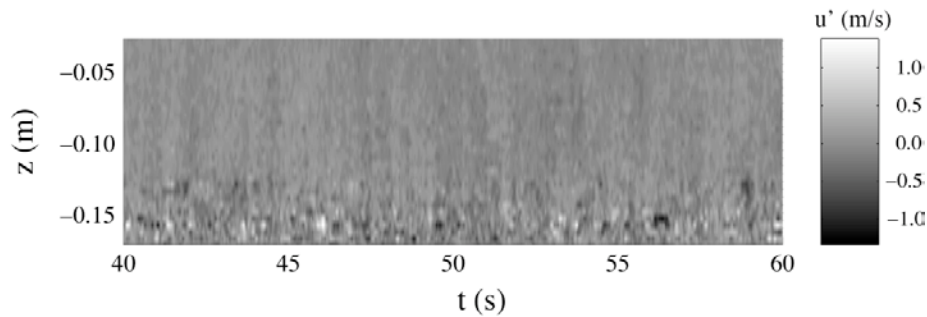


Figure 3 – Instantaneous streamwise velocity (u') profile (P13); sample frequency $f_a=26$ Hz.

From such images, high and low intensity events in the water column can already be detected, indicating the presence of organized motion coherent. Main turbulence activity develops near the bottom (roughly below $z=-0.13$ m). In the upper layers of the flow we observe background turbulence with larger scales involved. Nevertheless, a certain vertical character of the velocity distribution may be observed, indicating large UMR in time. Fig. 4 presents typical energy density spectra in the streamwise direction as a function of the frequency, averaged for three different layers of the flow.

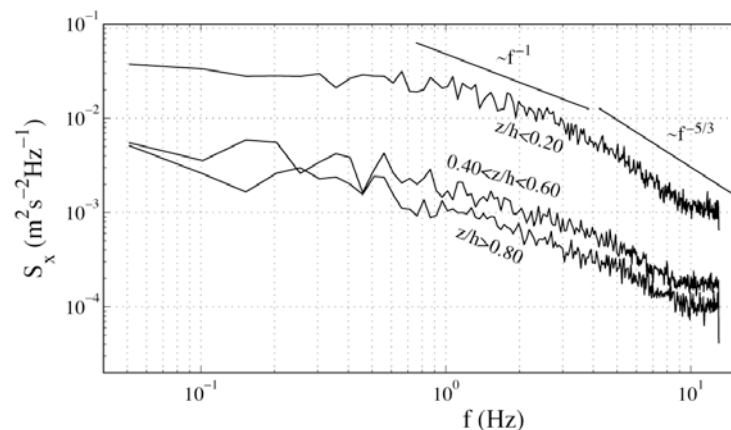


Figure 4 – Power spectrum density (S_x) of the streamwise instantaneous velocity, averaged in three different regions of the flow: near the bed, middle of the flow depth and near the surface. The sample frequency was $f_a=26$ Hz. For the calculation of S_x , the data was split into blocks of NFFT values corresponding to a time interval of 20 s, and the Welch method with 50% overlapping was used.

The differences in the energy content at different flow depths reflect the streamwise turbulence intensity distribution (Fig. 2). The Kolmogorov $-5/3$ spectrum decay law characterizing the inertial range (Kolmogorov 1941) is present in all three cases, though more evident near the bottom. The inertial range starts earlier in the frequency domain near the bottom; in other words, eddy sizes belonging to the productive range near the bottom already correspond to the inertial range near the surface (Franca and

Lemmin 2005 – 3.8). The spectrum transition through the -1 decay law (Nikora 1999) is also observed in the three spectra. The inertial subrange lower limit $f \approx 3$ Hz characterizes the beginning of the large-scale motions (lower frequencies). In Franca and Lemmin (2005 – 3.7), from a wavelet analysis of the energy partition throughout the motion scales, we showed that for these profiles the most productive scales correspond to periods between 0.25 and 0.50 s within $z/h \approx 0.10$ to 0.80 (2 to 4 Hz).

3.2 Low-pass filtered data

As a first approach, we isolated several frequency ranges in the velocity signal where the SVP should be found. Large-scale/low frequency motions observed by previous authors corresponding to the herein called SVP, have shown different velocity wave frequencies (f_{SVP}): 0.20 Hz (Williams et al. 1989); 0.33 – 3.33 Hz (Kirkbride and Ferguson 1995); 0.03 – 0.10 Hz (Dinehart 1999); and 0.15 Hz (Buffin-Bélanger et al. 2000b). In the SVP Strouhal number,

$$S_{SVP} = \frac{f_{SVP} h}{U} \quad (1)$$

h is an outer variable, usually the flow depth; U , a typical flow velocity, usually the free-stream velocity. Previous results range from 0.15 to 2.5 (Jackson (1976), Falco (1977), Williams et al. (1989), Kirkbride and Ferguson (1995) and Buffin-Bélanger et al. (2000b)). According to these results and to the profile hydraulic characteristics of the measurements ($U_\infty = 0.69$ m/s and $h = 0.17$ m), we may expect that SVP occurs with a frequency in the range $f \approx 0.6 - 12.6$ Hz. According to the previous observations, our experience and the analysis of several gravel-bed river data, we first decided to low-pass filter the data with a cut-off frequency of $f_c = 3$ Hz, using a Hamming window of length equivalent to 20 s. Fig. 5 presents the streamwise filtered instantaneous velocity profile (\tilde{u}) for the same 20 s shown in Fig. 3.

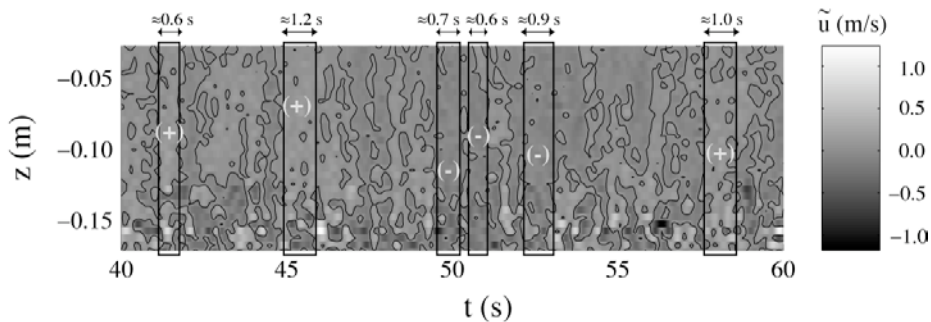


Figure 5 – Instantaneous streamwise velocity profile filtered with low-pass cut-off frequency of 3 Hz, using a Hamming window of length equivalent to 20 s in time. The continuous line corresponds to the limit between positive and negative velocity variations. Positive and negative UMR are marked by (+) and (-), respectively.

In the low-pass filtered data we observe regions of uniform streamwise momentum, where velocities are higher or lower than the temporal mean (herein called positive and negative UMR, respectively). These seem to correspond to the previously described large-scale fronts where the instantaneous velocity is above or below the average (Jackson (1976), Falco (1977), Nakagawa and Nezu (1981), Yalin (1992), Shen and Lemmin (1999), Buffin-Bélanger et al. (2000a) and Roy et al. (2004)). We marked the most prominent regions with the symbols + and -, respectively for momentum higher or lower than the mean. The duration of the motions is situated between 0.7 and 1.2 s, corresponding to frequencies within 0.8

and 1.7 Hz (inside the predetermined range). Some of the regions of uniform streamwise momentum, such as the three middle negative regions, have badly defined borders signifying that they may constitute a single merged structure.

From Fig. 5 the large-scale motions are correlated throughout the flow depth, mainly in the upper region $z > \approx 0.14$ m ($\approx 80\%$ of the flow depth). In fact, Kirkbride and Ferguson (1995) already argued that for the near-bed regions (inside the roughness layer visible in Fig. 3, $z/h < \approx 0.20$) the wake effect of the roughness dominated. Thus small-scale background turbulence in the roughness layer hides the large-scale structures footprints.

3.3 Analysis of the space and time correlations in the flow depth

We found vertical UMR's in the streamwise velocity signal indicating the existence of organized large-scale motions throughout most of the flow depth. From visual observation, large-scale motions seem to be vertically correlated in layer $z/h > \approx 0.80$. Spatial and time correlations allow us to verify the extent of the SVP in the flow depth, and also to more accurately estimate the frequencies at which it occurs in the flow. In this section we will use the streamwise instantaneous record, filtered by the low-pass filter with $f_c = 3$ Hz.

We define as follows the streamwise velocity time and space cross-correlation functions, for time lags equal to τ and between two vertical positions distant in the profile of a normalized space lag of r/h (r is the distance between two measuring positions):

$$R_{xx}(r/h, \tau) = \frac{\overline{u'(z/h, t) \cdot u'(z/h + r/h, t + \tau)}}{\sqrt{\overline{u'^2(z/h)} \cdot \overline{u'^2(z/h + r/h)}}} \quad (2)$$

R_{xx} is the time and space cross-correlation function. Fig. 6 shows a map of the peak values of the cross-correlation function ($R_{xx, \max}$) for each spatial lag r/h , within the normalized flow depth positions.

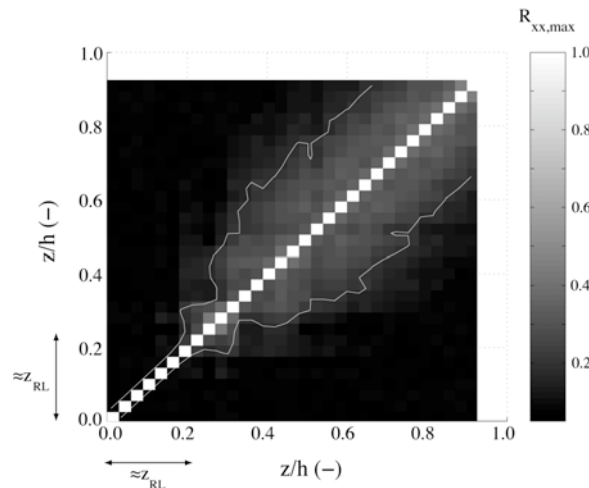


Figure 6 – Peak time cross-correlations between the instantaneous streamwise velocity data of two positions in the profile. The white line defines the boundary between the regions above and below the threshold level defined by $R_{xx, \max} = 0.20$.

The position of the large-scale correlated dominant structures in the time series is mainly in layer $z/h > 0.2$, outside the roughness layer (z_{RL}). The poor correlation between the adjacent measuring positions within the roughness layer is obvious, corroborating the observations of Kirkbride and Ferguson (1995). The local effects of the random bed form distribution create a lower layer where the flow becomes 3D and major deviations occur in the turbulence characteristics (the roughness layer according to Nikora and Smart (1997) and Franca and Lemmin (2005 – 3.8)). Inside the roughness layer the flow is thus particularly well mixed in the three directions, corresponding to the benthic layer described for such large-scale geophysical flows as marine and aeolian (Kantha and Clayson 2000).

Let us now analyze the instantaneous spatial auto-correlation function in the vertical direction defined for each time step t of the entire record:

$$R_z(r/h,t) = \frac{\overline{u'(z/h,t) \cdot u'(z/h + r/h,t)}}{\sqrt{\overline{u'^2(z/h,t)} \cdot \overline{u'^2(z/h + r/h,t)}}} \quad (3)$$

Fig. 7 is a 2D map of the spatial auto-correlation function in the vertical direction, where units in the vertical axis represent a lag of a measuring position or gate (roughly a distance of 5 mm), and units in the horizontal axis the instantaneous time steps:

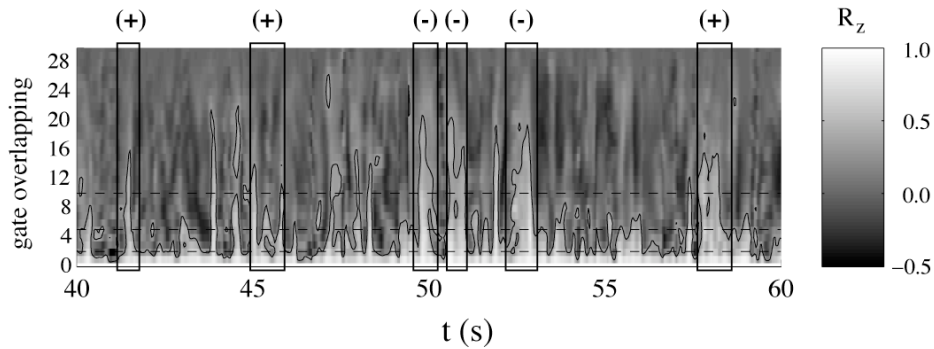


Figure 7 – Instantaneous vertical spatial cross-correlation function of the filtered streamwise velocity (low-pass cut-off frequencies of 3 Hz). The continuous line corresponds to the limit between correlation values above and below $R_z=0.30$. The positive and negative UMR identified earlier are indicated by (+) and (-), respectively.

High auto-correlation is associated with the positive and negative UMR indicated in Fig. 5. The higher auto-correlation patches confirm that the large-scale SVP motions are important over the full flow depth. We may now use the time series corresponding to the determined vertical spatial lags to detect and characterize the SVP structures in time. Three time series of R_z were defined corresponding to three vertical overlapping lags shown in Fig. 7 by the horizontal dashed lines. The spatial lags correspond to 2, 5 and 10 measuring positions, roughly to 1, 2.5 and 5 cm. In Fig. 8 we represent 20 s of the three time series defined by these horizontal lines.

As expected, in the positive and negative UMR the correlation functions present local maxima for the three time series in Fig. 8. We consider that the most representative correlation functions correspond to gate overlapping of 1 to 5. Thus the energy spectrum of the time record corresponding to R_z averaged for these 5 positions should indicate the important frequencies in the SVP phenomenon. The energy spectrum was calculated using the Welch method by two methods: with the whole time record and no

overlapping; and for NFFT=256 with 50% of overlapping, allowing us to better detect the most energetic frequencies (Fig. 9).

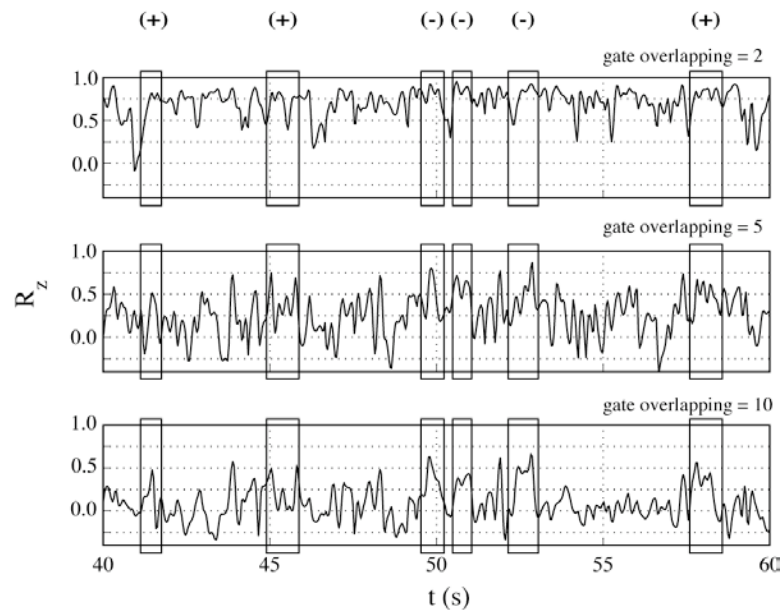


Figure 8 – Instantaneous spatial cross-correlation function of the filtered streamwise velocity (low-pass cut-off frequencies of 3 Hz), corresponding to three specific vertical space lags, 2, 5 and 10. The time position of the positive and negative momentum regions identified earlier are marked by (+) and (-), respectively.

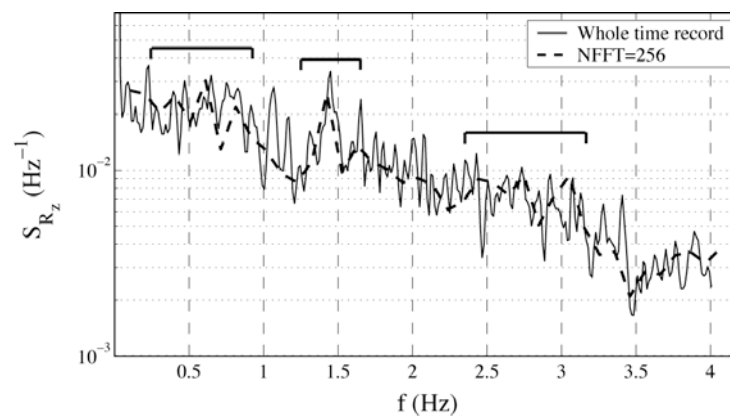


Figure 9 – Power spectrum density of the instantaneous spatial cross-correlation function (S_{R_z}), averaged for the vertical space lags 1 to 5. The spatial cross-correlation functions are calculated for the filtered streamwise velocity (low-pass cut-off frequencies of 3 Hz). For the calculation of S_{R_z} , we used the Welch method for the whole time record with no overlapping and for NFFT=256 with 50% of overlapping. Enhancement of the S_{R_z} for certain frequencies is indicated.

Three groups of higher frequencies are identified in Fig. 9. They are roughly centred on the frequencies 0.65, 1.4 and 2.7 Hz, which may belong to the same harmonic in the FFT transform (0.65×1 , 0.65×2 and 0.65×4).

3.4 Analysis of filtered data

Having verified the apparent harmonic, we analyzed three time series corresponding to the instantaneous velocities filtered with low- and band-pass filters of $f_{c1} < 1.00$, $f_{c2} \in [1.25 \ 1.75]$ and $f_{c3} \in [2.25 \ 3.25]$ Hz – Fig. 10:

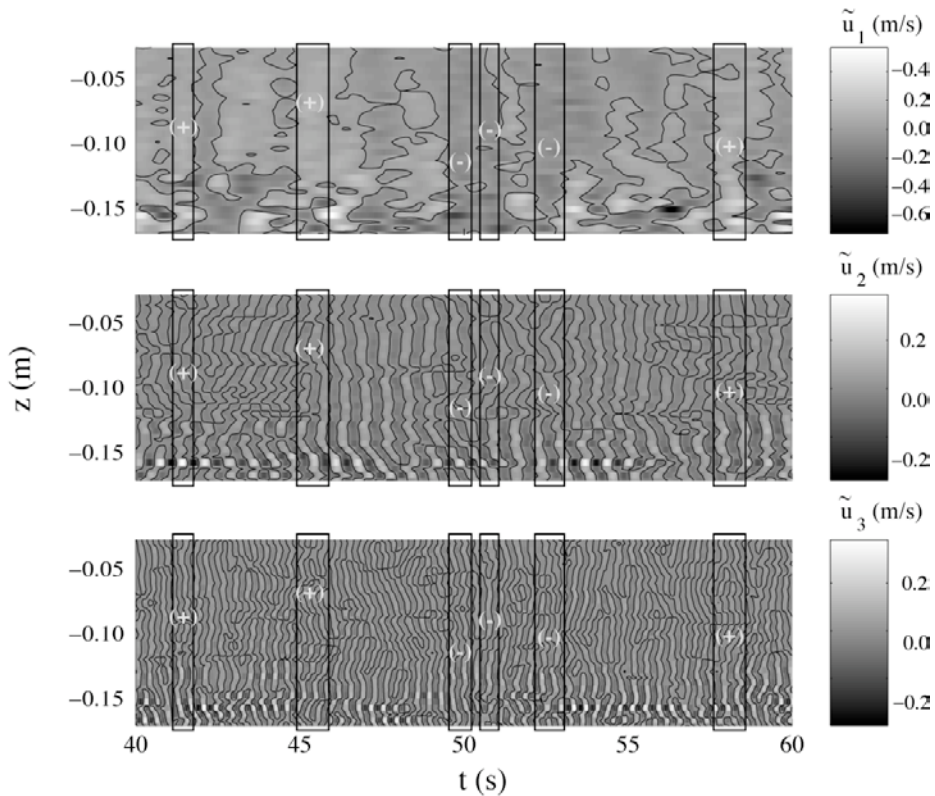


Figure 10 – Instantaneous streamwise velocity profile filtered with three band-pass cut-off frequencies of $f_{c1} \in]0 \ 1.0]$ Hz (low-pass filter), $f_{c2} \in [1.25 \ 1.75]$ Hz and $f_{c3} \in [2.25 \ 3.25]$ Hz. We used a Hamming window of length equivalent to 20 s in time. The continuous line corresponds to the limit between positive and negative velocity variations. The time position of the positive and negative UMR identified earlier are signalled by (+) and (-), respectively.

The low-pass filter corresponding to the filtered velocity \tilde{u}_1 ($f_{c1} = 1$ Hz) offers a better representation of the detected UMR. By applying the filter, it also becomes evident that some of the observed smaller UMR are actually one merged cluster, with small-scale interference in between. The large-scale structures still present the vertical orientation in the instantaneous observed velocity as mentioned before, and the main vertical correlation region is situated above $z/h \approx 0.20$. The following research will be conducted in the frequency range defined by $f_{c1} < 1$ Hz. We believe that the SVP will have a well-defined frequency in the time domain. Thus it will correspond to a stable and regular monochromatic harmonic in the streamwise velocity signal (monocomponent function, Cohen (1995)).

3.5 The Hilbert transform

The Hilbert transform of an instantaneous velocity signal is defined as (Huang et al. (1998) and Huang et al. (1999)):

$$H(t) = \frac{1}{\pi} \int_{-\infty}^{+\infty} \frac{u'(t')}{\underbrace{t-t'}_P} dt' \quad (4)$$

P is the Cauchy principle value. $u'(t)$ and $H(t)$ form a complex time series:

$$Z(t) = u'(t) + iH(t) \quad (5)$$

Therefore the real part of $Z(t)$ corresponds to the actual instantaneous velocity data and the instantaneous phase angle of the oscillation ($\Phi(t)$) may be deduced as:

$$\Phi(t) = \arctan\left(\frac{H(t)}{u'(t)}\right) \quad (6)$$

The calculation of the instantaneous angular frequency ($\omega(t)$) of an oscillatory signal may be estimated from:

$$\omega(t) = \frac{d\Phi(t)}{dt} \quad (7)$$

This expression is valid for monochromatic (monocomponent) or narrow-band signals, i.e. well-behaved Hilbert transforms. Since the Hilbert transform provides local phase angles, it is valid for even non-stationary and nonlinear signals. Let us now look at the Hilbert transform of the low-pass filtered streamwise velocity data (\tilde{u}_1). In Fig. 11 the real, instantaneous Φ and unwrapped Φ_{un} phase angle of $Z(t)$, for the measuring position $z/h=0.45$ are shown. This flow depth will be used as the detection level of the UMR.

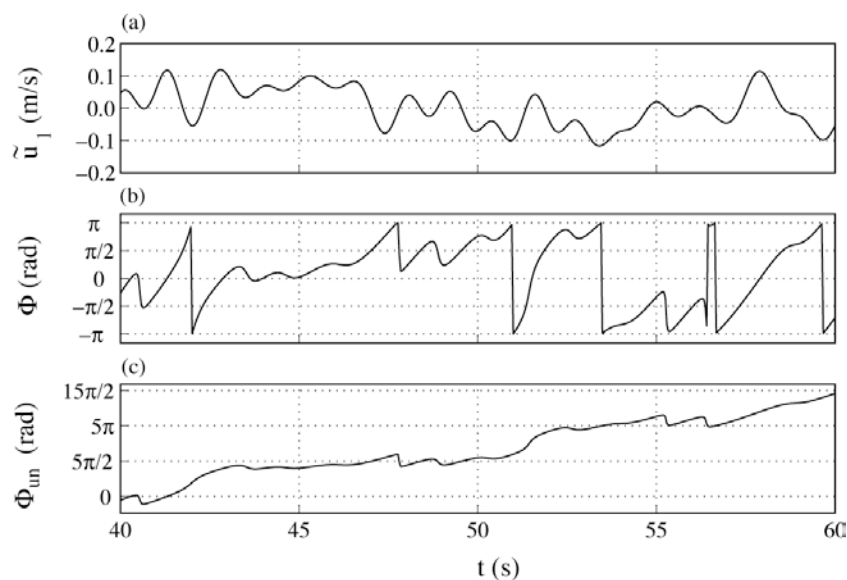


Figure 11 – Discrete Hilbert transform analysis of the instantaneous streamwise velocity at the position $z/h=0.45$, filtered with the low-pass cut-off frequency of 1.0 Hz: (a) real function corresponding to the original velocity signal; (b) phase function and (c) unwrapped phase function.

The phase angle varies largely and irregularly in the time domain and does not have a narrow-band; this is considered to be an ill-behaved Hilbert transform. The unwrapped phase angle series presents discontinuities in the gradient that will not allow an estimate of a close range of angular frequencies (ω) from the time differentiation of Φ_{un} . We therefore need to decompose our signal in proper modes to eliminate the irregularities in series $\Phi(t)$ and to obtain a smooth signal for the frequency determination. We will use the empirical mode decomposition.

3.6 Empirical mode decomposition - EMD

Empirical mode decomposition (EMD) introduced by Huang et al. (1998) allows the decomposition of any time series into a finite number of intrinsic mode functions (IMF), or details, that admit well-behaved Hilbert transforms. Each IMF corresponds to a narrow frequency band. EMD sifting is adaptive and efficient even in a non-stationary and nonlinear case since it is based on the local time scale of the data. In addition to the examples provided by Huang et al. (1998 and 1999), EMD has been applied with success to solve engineering and scientific problems such as signal detrending and denoising (Flandrin et al. 2004), ocean acoustic problems (Ooninx and Hermand 2004), analysis of the effect of ocean waves in turbulence (Osborn et al. 2005) and ultrasonic signal identification (Chen et al. 2005).

EMD adapts entirely to our search for a quasi-monochromatic time series. The sifting process that allows the progress from the original series to the first IMF consists in subtracting the mean of the envelopes of the extreme values from the original time series. The next lower level IMF is calculated using the same scheme and so on until the final signal trend is achieved. The reconstruction of the original signal is simply made by the addition of all the IMF's. In the present research we followed the improved EMD sifting algorithm presented by Rilling et al. (2003). In Fig. 12 we illustrate the application of the EMD sifting to determine the first IMF corresponding to the instantaneous filtered velocity signal \tilde{u}_1 ($f_{C1}=1$ Hz, subsection 3.4) at position $z/h=0.45$.

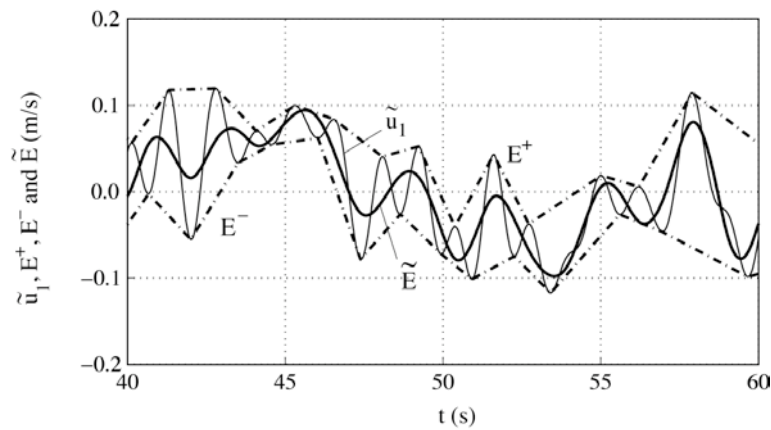


Figure 12 – Illustration of EMD sifting to the instantaneous streamwise velocity at position $z/h=0.45$, filtered with the low-pass cut-off frequency of 1.0 Hz. The thin line represents the filtered velocity signal; the dashed dotted lines represent upper and lower extreme envelopes, E^+ and E^- ; the thick line represents the envelope average \tilde{E} .

Fig. 13 presents the final results of EMD decomposition of the same signal. The final IMF corresponds to the signal trend, which is zero in the present case.

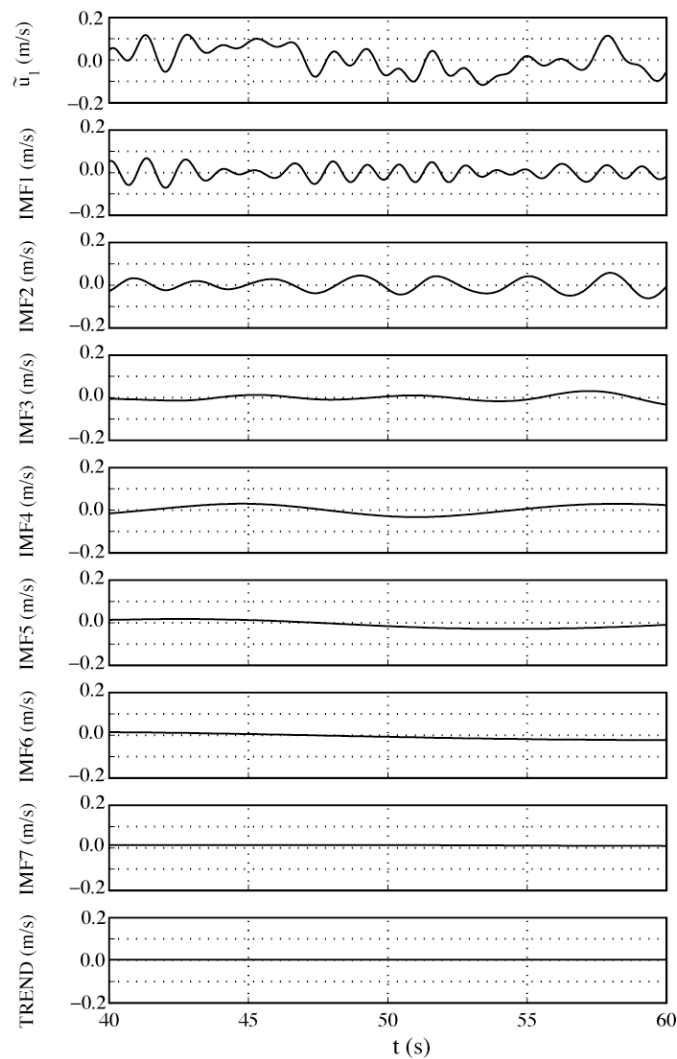


Figure 13 – EMD of the instantaneous streamwise velocity at position $z/h=0.45$, filtered with the low-pass cut-off frequency of 1.0 Hz. The first set corresponds to the original velocity signal and the remaining ones relate to the IMF's and the trend.

In the first mode (IMF1) the phase angle seems reasonably well-behaved, assuring a continuous Hilbert transform. Beyond the mode IMF3, little energy is left in the signal, which may be confirmed by the energy spectra of the \tilde{u}_1 and each of the corresponding IMF's (Fig. 14).

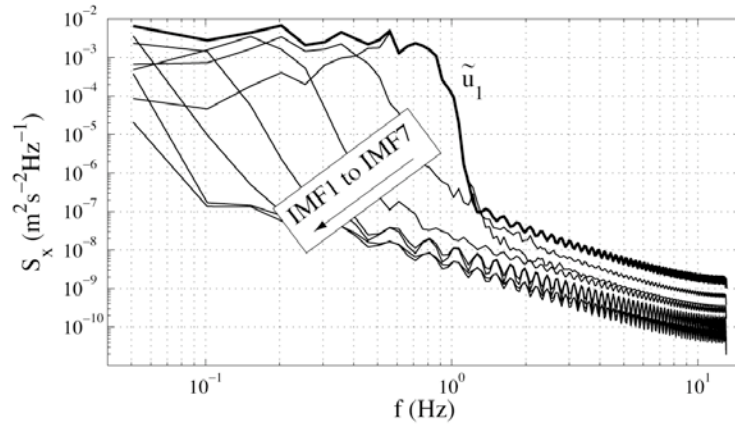


Figure 14 – Power spectrum density of the original velocity signal and of the 7 IMF's. For the calculation of the spectrum density, the data was split into blocks of NFFT values corresponding to a time interval of 20 s. We used the Welch method with 50% overlapping.

Since EMD is an orthogonal-basis decomposition, the total energy is preserved and partitioned throughout the different IMF, each one corresponding to a narrow frequency band in the original signal. Since IMF1 and IMF2 contain almost the total energy of the signal, the IMF1 Hilbert transform is well behaved, and given the frequency band of the large-scale structures detected earlier, we assume that the SVP is represented by the mode IMF1. Fig. 15 shows the Hilbert transform for the time series corresponding to IMF1.

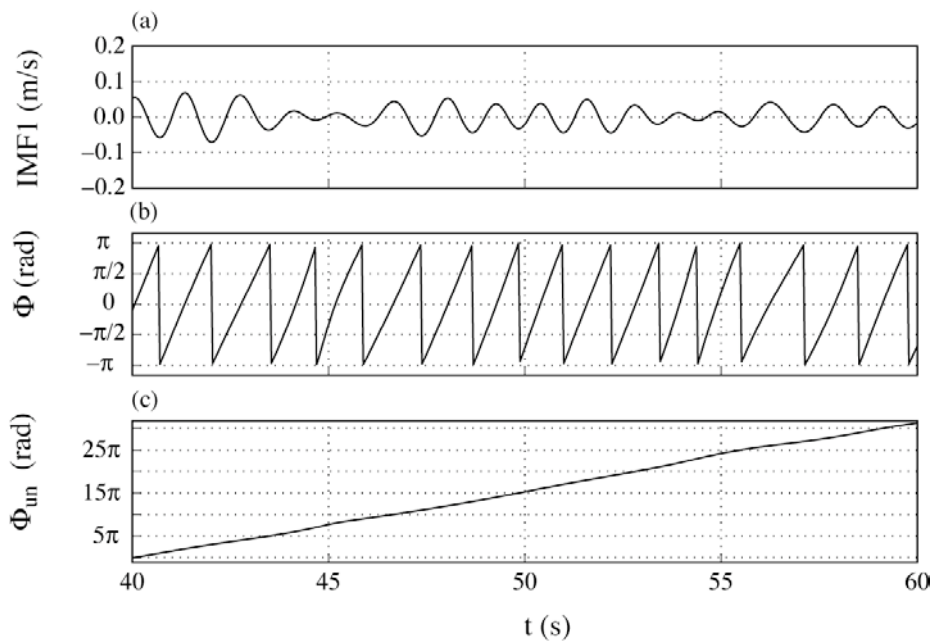


Figure 15 – Discrete Hilbert transform analysis of the IMF1: (a) real function corresponding to the IMF1 signal; (b) phase function and (c) unwrapped phase function.

Since the Φ is regular and Φ_{un} continuous, Φ_{un} admits a stable time derivative corresponding to the angular frequency of the signal. The maximum positive and negative velocity variations are 0.094 and -0.090 m/s (amplitude equal to 0.184 m/s), respectively, and the mean angular frequency estimated with expression (7) and corresponding to the slope of Φ_{un} is $\omega=4.40$ rad/s. This mean angular frequency is the centre of the narrow frequency band $\omega \in [2.66 \ 6.13]$ rad/s, where the energy from the instantaneous signal of IMF1 is situated. Using expression (8), the linear frequency attributed to the SVP is $f_{SVP} \approx 0.70$ Hz ($f_{SVP} \in [0.42 \ 0.98]$ Hz), which is within our primary range of observations.

$$f = \frac{\omega}{2\pi} \quad (8)$$

The corresponding time period is $T_{SVP} \approx 1.43$ s ($T_{SVP} \in [1.02 \ 2.38]$ s). The time interval in which the SVP is situated is within the order of magnitude expected from the previous observations, and corresponds typically to a large-scale motion. The SVP Strouhal number calculated with the flow depth h and profile mean velocity U is within $0.14 < S_{SVP} < 0.32$. Defining the Strouhal as a function of the friction velocity ($S_{SVP}^* = \frac{f_{SVP} h}{u^*}$), we have $1.54 < S_{SVP}^* < 3.78$. This interval contains the Strouhal number corresponding to the time interval between bursting packets observed by Franca and Lemmin (2005 – 3.6) $S_f = 2.5$. The high- and low- speed wedges associated to the bursting packets detected for different profiles but under similar turbulent conditions (Franca and Lemmin 2005 – 3.6) might be due to the passage of a SVP UMR.

4 THE EFFECT OF SVP

4.1 Phase-averaged signal based on the Hilbert transform

Having established the IMF corresponding to the SVP cycle for one position in the flow depth ($z/h=0.45$), we may now come back to the time series \tilde{u}_1 and reconstruct it for one SVP phase period (Hristov et al. (1998) and Osborn et al. (2005)). For that, we sample conditionally in phase the original \tilde{u}_1 data, i.e. using the instantaneous Hilbert transform phase angle Φ calculated for the IMF1 as a data marker. In Fig. 16 we represent the phase cycles of the IMF1 series and the corresponding \tilde{u}_1 data sampled within one period corresponding to a phase angle range of $[-\pi \ \pi]$.

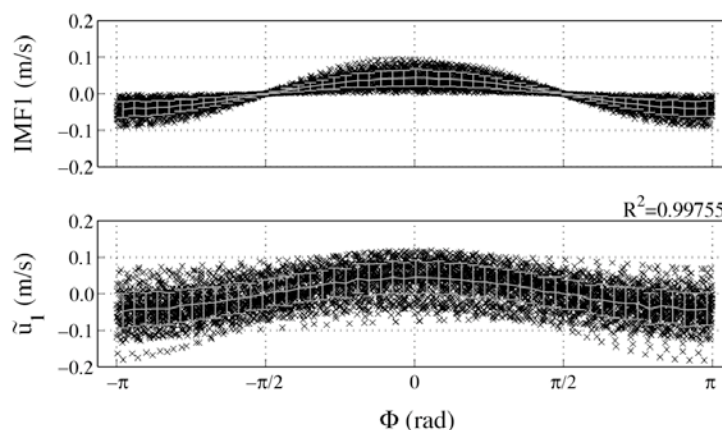


Figure 16 – IMF1 and \tilde{u}_1 time series conditionally sampled in phase for one SVP period. In white, phase averaged IMF1 and \tilde{u}_1 .

IMF1 and phase averaged \tilde{u}_1 fit well a cosine function within one SVP phase period. Despite the higher scattering observed for the \tilde{u}_1 data, its main in-phase trend is still in good agreement within the cycle and the SVP dominates the signal. This phase conditioned analysis may be applied now for the fluctuating components of the flow involving all the frequencies in the signal, in order to evaluate the SVP feedback in the turbulent flow structure.

4.2 Analysis of the SVP throughout the flow depth

The phase conditioned averaging to the SVP cycle is now applied to the streamwise velocity throughout the flow depth to evaluate and characterize the SVP behaviour in the space (vertical direction) and time domain (front advection). Figs. 17a and 17b represents the SVP phase-averaged streamwise filtered velocities (\tilde{u}_1) along the flow depth.

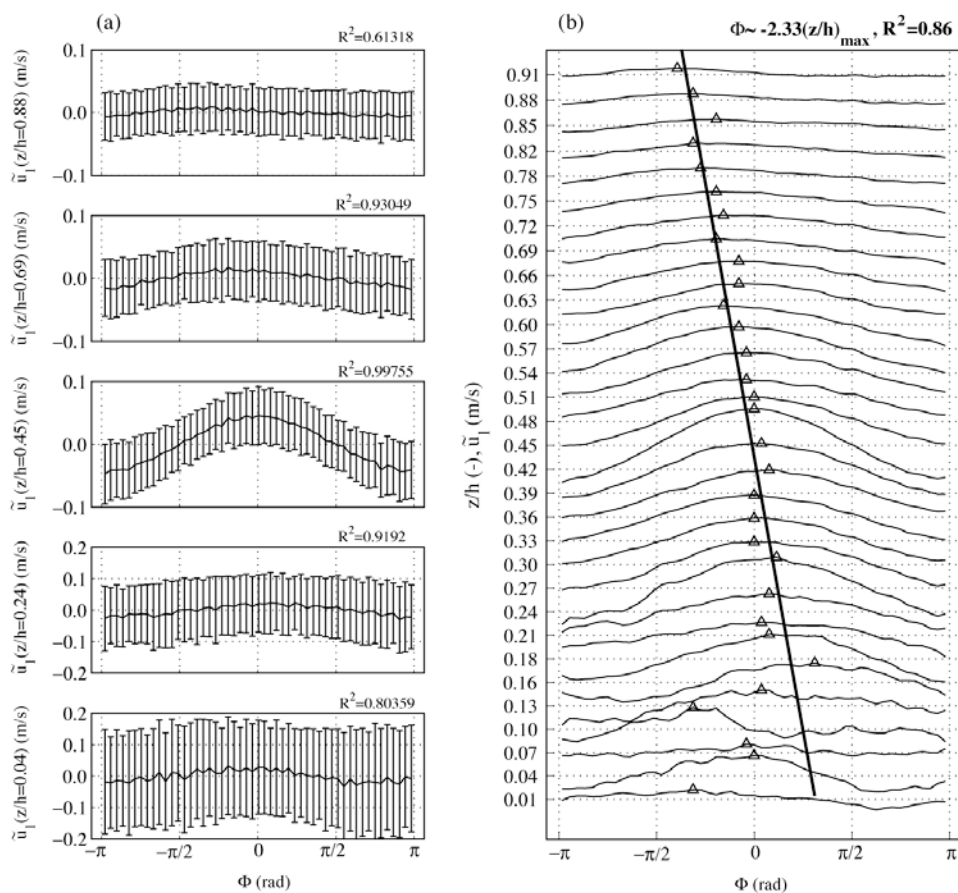


Figure 17 – \tilde{u}_1 phase averaged in the SVP cycle: (a) for the positions $z/h = 0.04, 0.24, 0.45, 0.69$ and 0.88 , R^2 is the correlation coefficient with the IMF1 series; (b) for the whole flow depth with the position of the local maxima signalled. The thick line represents the phase evolution of the SVP front.

In Fig. 17a we observe that for the low-pass filtered data (\tilde{u}_1), the correlation with the determined IMF1 corresponding to the SVP is very high. Thus a phase movement exists in the low frequencies with a large correlation in the vertical. Near the surface, the correlation factor between the phase-averaged series is poorer than in the near bed regions, although the scatter around the mean is more reduced in these latter. Fig. 17a indicates that the effect of the SVP exists throughout the flow depth confirming Kirkbride and Ferguson (1995) and Buffin-Bélanger (2000a) descriptions of the large-scale structures, even if the correlation between measuring gates in the lower layers is poor (Fig. 6). The small-scale background processes that proliferate in the lower layers of the flow eventually hide the large-scale coherency of the signal.

Fig. 17b shows that the SVP front position presents a slope of $-2.33(z/h)$ in the phase domain and that its vertical trend is roughly linear; the phase shift between the bed and the surface regions corresponds thus to $\approx 3/4\pi$. Our Eulerian observation of the flow, registers first the UMR waves in the lower layers. The position indicated in Fig. 17b corresponds to the maxima velocity within the SVP period (centre area of a positive UMR). Major scatter of the front position is verified above $z/h \approx 0.18$, inside the roughness layer. The geometric form of the SVP front may be determined first by expressing the cycle in the time domain and the subsequent application of the Taylor frozen hypothesis using the advection velocity $\bar{u}(z)$ (Fig. 18).

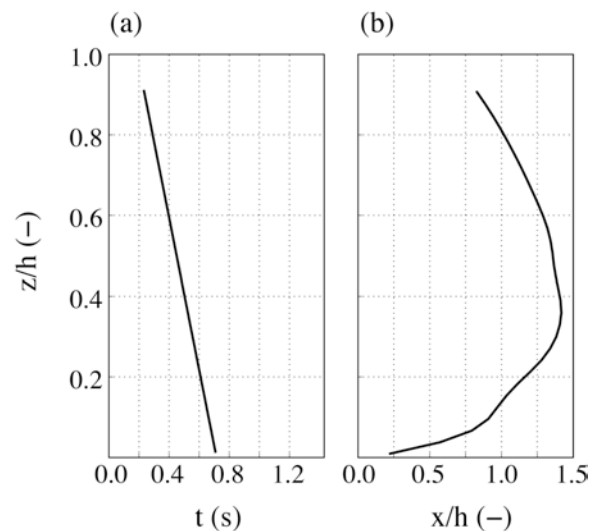


Figure 18 – SVP front description (a) in the time and (b) in the space domain. The front in the space domain was obtained by multiplying of the time position of the front (a) by the advection field (mean velocity profile in Fig. 2a).

Several authors described these large-scale coherent motions as the trigger for the bursting process in the inner layers of the flow. Buffin-Bélanger (2000b) reported a time response of the flow throughout the flow depth with a similar inclination from Fig. 18a. The mean convective field with logarithmic shape distorts the phase shift in the SVP progression, providing the UMR front with the shape of a first quarter moon as presented in Fig. 18b, with the apex situated at $z/h \approx 0.35$. Given its geometry, the UMR are best defined in the intermediate and upper parts of the flow where streamlines become eventually less curved in accordance with Kirkbride and Ferguson (1995). The geometry of the front is dependent on the vertical evolution of the phase shift and on the mean velocity profile. Kirkbride and Ferguson

(1995) suggested a front geometry with the logarithmic form, exclusively conditioned by the mean convection. Nakagawa and Nezu (1981) described the interface between high- and low-speed large-scale regions of the flow responsible for the bursting process as a surface concave towards the wall. We observed in Franca and Lemmin (2005 – 3.6) two interfaces linked to a bursting packet, one similar to Nakagawa and Nezu's and a second convex front similar to the present. According to the SVP shape in Fig. 18b, several UMR of opposite direction will not cluster.

Given the SVP period range and the profile mean velocity ($U=0.52$ m/s), the large-scale motions scale with 3.1-7.3h in the horizontal (distance between SVP consecutive fronts). Previous authors observed the following lengths for the large-scale motions over gravel beds: Falco (1977) 1.6h; Brown and Thomas (1977) 2h; Nakagawa and Nezu (1981) 2-3h; Kirkbride and Ferguson (1995) 0.3-3.3h; Buffin-Bélanger et al. (2000a and 2000b) 7-8h; and Hofland (2004) 4h. In the lower layers the inclined interface has a mean angle of $\theta \approx \arctan(0.4/1.5) = 15^\circ$ with the horizontal, which is compatible with the results from Brown and Thomas (1977) $\theta = 18^\circ$, Nezu and Nakagawa (1993) $\theta = 20^\circ$, Buffin-Bélanger (2000b) $\theta = 15^\circ$ for the near the bed region and Franca and Lemmin (2005 – 3.6) $\theta = 18.2^\circ$ for a front directly connected to the existence of a bursting packet.

To better understand the SVP influence on the turbulence structure of the flow, the local flow characteristics conditioning the vertical phase shift (Fig. 18a) have to be determined. This defines the type of front geometry to expect in the flow, inclined downstream or inclined upstream, which will determine the interaction between large-scale motions and the inner layer bursting. Further studies shall focus on the bursting process during the passage of UMR for different geometric configurations.

4.3 SVP effect in bottom drag

One important question about the SVP is their implication in sediment and mass transport processes. Although a low amplitude phenomenon, if acting as bursting trigger in the boundary layer, SVP may have a major effect on the turbulent mechanisms. Similarly, with the ADV data we may now analyze the phase averaged 3D components throughout the flow depth. In Fig. 19 we present the SVP phase-averaged streamwise, vertical and spanwise velocities (u' , w' and v') for three different vertical positions, and the corresponding bottom friction velocity cycle. The velocities were normalized by the maximum amplitude in the time record; the instantaneous friction velocity u^* was normalized by the mean value. It was calculated from the slope of the instantaneous shear stress profile within the blending layer ($0.30 < z/h < 0.80$, Franca and Lemmin 2005 – 3.4).

The SVP cycle is related to a large-scale bursting sequence; a large-scale sweep-ejection sequence (IIQ and IVQ shear events marked in Fig. 19) is in phase with the passage of the UMR. The sweep is associated with the positive UMR and the ejection with the negative. This is mainly evident in detection position $z/h=0.45$ (Fig. 19c), though we may observe it in the phase-averaged signals nearer the bed and the surface with the respective phase shifts. Both u' and w' components cross the zero line at exactly $\Phi = \pm\pi/2$ for $z/h=0.45$. The spanwise component does not seem to be correlated and with low activity associated with the UMR passage. Thus the large-scale coherent structures associated with the SVP are mainly 2D. Falco (1997) and Kirkbride and Ferguson (1995) described a similar association between both vertical and streamwise components with the passage of the high- and low-speed regions and Cellino and Lemmin (2004) verified that sweeps and ejections occur in the outer layer of the flow momentarily affecting the velocity profile.

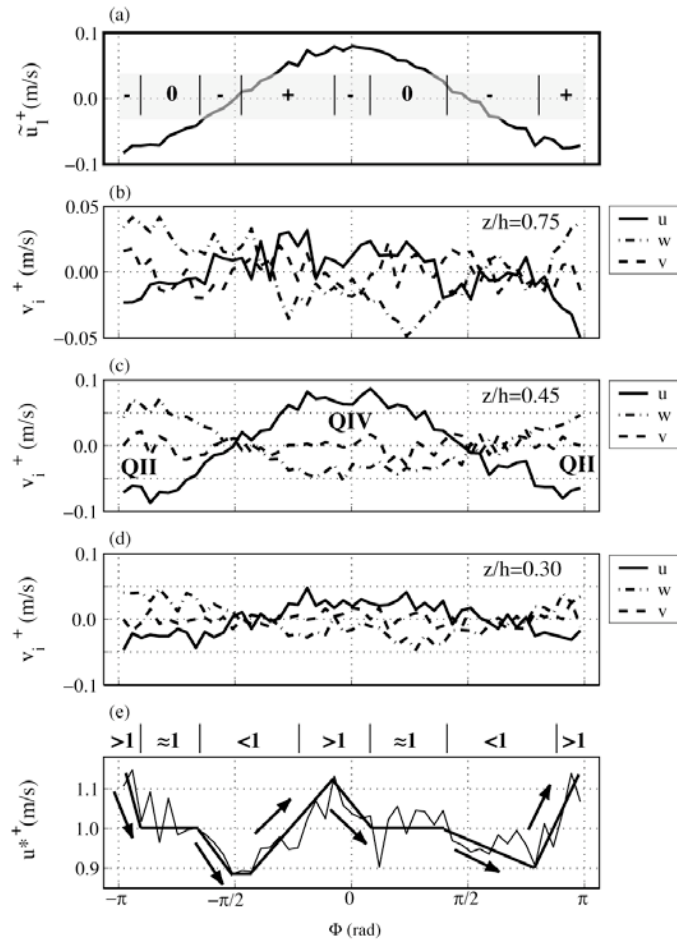


Figure 19 – SVP phase-averaged 3D instantaneous velocities: (a) filtered time series \tilde{u}_1^+ , reference cycle with indication of the bottom friction velocity derivative trend; (b) to (d) 3D instantaneous velocities for $z/h=0.30, 0.45$ and 0.75 ; and (e) friction velocity estimated from the instantaneous shear stress slope within the blending layer (the thick line is an interpretation of the mean trend within the SVP period).

Data from (a) to (d) are normalized by the maxima instantaneous signal amplitude and (e) by the temporal mean friction velocity.

Brown and Thomas (1977) and Buffin-Bélanger (2000a) observed a close relationship between the passage of the high-speed regions and the bottom drag variation. From Fig. 19e, a periodic enhancement/reduction of bed drag occurs associated with the SVP (a trend is indicated with the thick line). Two peaks exist in the phase-averaged u^{*+} with amplitudes of $1.10u^*$, corresponding both to the occurrence of the extreme values of the streamwise velocity and coinciding with sweep (S) and ejection (E). The lower values of u^{*+} occur when the u' and w' series cross the zero line (Fig. 19c). The phase gradients of the friction velocity are indicated in Fig. 19a. Fig. 20 shows a reconstructed phase plot of the interaction of both normalized streamwise and the bed friction velocities. In Table 3 we present a tentative model based on the results from Fig. 19 for the friction velocity SVP cycle.

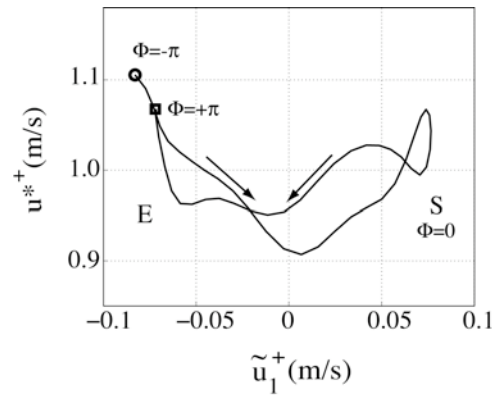


Figure 20 – SVP phase plot of the reconstructed normalized streamwise velocity for $z/h=0.45$ and normalized bed friction velocity. The circle and the square indicate the beginning and the end of the SVP period. The positions of the sweep and ejection are identified in Fig. 19 by S and E, respectively.

Table 3 – Bottom drag variation within one SVP period.

Φ (π rad)	-1, E	-1.00 to -0.89	-0.89 to -0.63	-0.63 to -0.42	-0.42 to 0.00	0, S
\tilde{u}_1 (m/s)	min	<0	≤ 0	≥ 0	>0	max
u^{*+}	1.1	1.1 to 1.0	1.0	1.0 to 0.9	0.9 to 1.1	1.1
$du^{*+}/d\Phi$ (rad^{-1})	-	-0.30	0	-0.15	+0.15	-
Φ (π rad)	0, S	0.00 to 0.14	0.14 to 0.43	0.42 to 0.81	0.81 to 1.00	1, E
\tilde{u}_1 (m/s)	max	>0	>0	>0 to <0	<0	min
u^{*+}	1.1	1.1 to 1.0	1.0	1.0 to 0.9	0.9 to 1.1	0.9 to 1.1
$du^{*+}/d\Phi$ (rad^{-1})	-	-0.23	0	-0.08	0.34	-

The convex shape of the curve in Fig. 20, with the maxima occurring roughly in both left and right extremes, confirm the relation between the u^* and SVP cycle specified in the bottom drag model: the u^{*+} peaks occur simultaneously with the u' extreme values. The friction velocity feedback is nonlinear with u' , and is approximated by a 2nd degree asymmetric function (Fig. 20). This is confirmed by the asymmetric slopes of the phase plot in Fig. 20. Sweeps occupy larger scales and mobilize more time than ejections (1.5 larger). In Fig. 19c, the instantaneous shear corresponding to ejection is more intense given the vertical component. These results are in agreement with the statistically based conclusions of Cellino and Lemmin (2004) in the outer layer bursting dynamics, where ejections dominate the shear stress production with low duration but higher amplitude events. The residual hysteresis between the beginning and the end of the cycle results from the measurements and data treatment processes.

The present results show that SVP produces variations in the bottom drag stress well marked in the flow time history though with a maxima enhancement of only 10% of the mean value. Despite its small amplitude, the streamwise velocity oscillations associated with the SVP period may be of major importance in bed-load transport given their relatively long duration when compared with small-scale turbulent interactions, and given the importance that the streamwise components may have in the

process (Nelson et al. 1995). This friction velocity is determined from the shear stress slope within the blending layer of the flow. Thus, the u^* cycle from Fig. 18 only reflects the relation u' vs. w' during the passage of an UMR as illustrated in Fig. 19c. Extra instability created by the shear region in the inclined SVP front surely will cause added 3D organized turbulence inside the roughness layer, contributing locally to an enhancement of the riverbed drag. The SVP contribution to bottom drag should therefore take into account the 2D large-scale low-amplitude direct enhancement in phase with the UMR passages estimated here, and the 3D indirect enhancement due to the bursting process triggered by the SVP front shear layer.

4.4 SVP effect in the TKE budget

The turbulent kinetic energy (TKE) transport equation or TKE budget expresses the dynamics of the kinetic energy due to the turbulent velocity fluctuations of a turbulent flow. For an incompressible flow of an isothermal fluid, the TKE equation is (Schlichting (1968), Monin and Yaglom (1971), Hinze (1975), Chassaing (2000) and Pope (2001)):

$$\frac{D\bar{k}'}{Dt} = P + D - \varepsilon \quad (9)$$

\bar{k}' is the temporal mean of the turbulent kinetic energy (TKE: $k' = u'^2 + v'^2 + w'^2$); P , the production rate or generation; D , the diffusive term; and ε , the dissipation rate. The diffusive term encloses the turbulent diffusion, the pressure diffusion, the molecular or viscous diffusion and the diffusion of the Reynolds stress tensor. D is generally negligible for high Reynolds number flows (confirmed for the present measurements in Franca and Lemmin 2005 – 3.8). The production and dissipation terms in TKE, P and ε , are defined by:

$$P = -\overline{v'_i v'_j} \left| \frac{\partial v'_i}{\partial x_j} \right| \quad (10)$$

$$\varepsilon = 2\nu \overline{s'_{ij} s'_{ij}} \quad (11)$$

s'_{ij} is the strain rate defined as $s'_{ij} = \frac{1}{2} \left(\frac{\partial v'_i}{\partial x_j} + \frac{\partial v'_j}{\partial x_i} \right)$. ADVP measurements do not allow direct access to

the instantaneous spanwise gradients ($\frac{\partial}{\partial y}$) in (10) and (11). Assuming that $\frac{\partial u}{\partial y} \approx \frac{\partial v}{\partial x}$, $\frac{\partial w}{\partial y} \approx \frac{\partial v}{\partial z}$, and

$\frac{\partial v}{\partial y} \approx \frac{\partial w}{\partial z}$, we may estimate the instantaneous values of the production P' and dissipation ε' :

$$P' = -v'_i v'_j \left| \frac{\partial v'_i}{\partial x_j} \right| \quad (12)$$

$$\varepsilon' = 2\nu s'_{ij} s'_{ij} \quad (13)$$

We may analyze now the impact of the passage of a UMR in the TKE budget by phase averaging both P' and ε' (Fig. 21). The results are spatially averaged for three different regions of the flow ($z/h < 0.20$, $0.40 < z/h < 0.60$ and $z/h > 0.80$), and are normalized by the temporal mean values.

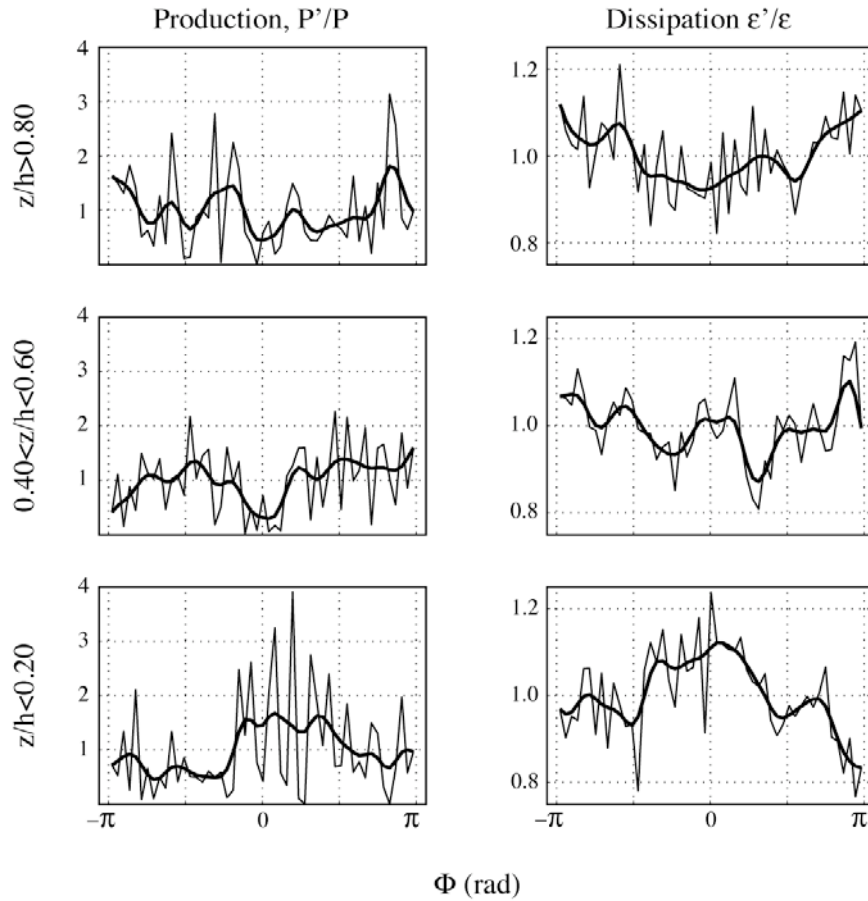


Figure 21 – SVP phase averaged production P' and dissipation ϵ' for three different regions of the flow ($z/h < 0.20$, $0.40 < z/h < 0.60$ and $z/h > 0.80$), normalized by the total temporal mean. The thick line is the mean trend within the SVP period.

Higher frequency interferences are visible in the SVP cycles with a greater enhancement effect than the SVP itself. In the production case it is possible to relate the occurrence of the sweep peak and ejection/sweep transition with an increase in the high frequency peaks mainly near the bottom. Joint behaviour may exist between the SVP and the small-scale turbulence responsible for the larger localized production. SVP works as a trigger for smaller-scale productive activity. This is in accordance with our results where we associate a bursting packet with high- and low-speed fronts (Franca and Lemmin 2005 – 3.6). It agrees with the concept of Adrian et al. (2000) in which large-scale motions (also called inactive motions) nest small-scale turbulence. Lu and Willmarth (1973) observed that these larger organized structures contribute less to Reynolds shear stress. The SVP's direct effect on turbulence production near the bottom is minimal but visible; in the upper layers of the flow it is irrelevant and not conclusive. The ejection seems to be associated to relatively lesser production periods.

Higher frequency fluctuations occurred during the SVP cycle once again and seem to be more important in the dissipation process than the passage of the UMR itself. The variations in dissipation due to the passage of the SVP are very low when compared with the basal dissipation value; as discussed in Franca and Lemmin (2005 – 3.6), background small-scale turbulence constitutes the main source of dissipation. Nevertheless, it is possible to find some interaction between the passage of UMR and the cycle of

instantaneous dissipation. For example, the dissipation distribution within one period changes gradually from a convex shape near the surface to an approximately concave shape near the bottom.

The present observations took into account the vertical phase shift of $3/4\pi$ between the surface and the bottom. The passage of a UMR seems to interact with the small-scale productive processes.

5 THE INTERACTION OF FREE SURFACE WAVES AND SVP

In shallow rivers, the response of the flow to bottom irregularities is evidenced by the wavy free surface pattern. Stationary waves are present in these kinds of flows superimposed by free waves travelling upstream and downstream. This might be due to the inviscid response of the flow to the bed forms (potential flow assumption – barotropic-like flow), stationary or non-stationary hydraulic jumps and wave trains produced by boulders in the riverbed comparable to the effect of ship-waves in still water or geophysical lee waves (Sharman and Wurtele 1983). Having observed *in loco* the existence of free surface waves travelling upstream and downstream, and given the periodic characteristics of the SVP, we hypothesized that free surface waves and the SVP might be related and act jointly. Kirkbride and Ferguson (1995) and Smith (1996) argued that the large-scale outer region velocity fluctuations interact with the free surface.

We observed fluctuations of the water surface ($\eta(t)$) around the mean level (MWL) on a different day but in the same river section and under equivalent hydraulic conditions. The water surface elevation was assessed by a simple video system using a checkerboard plane as background reference (Fig. 22).

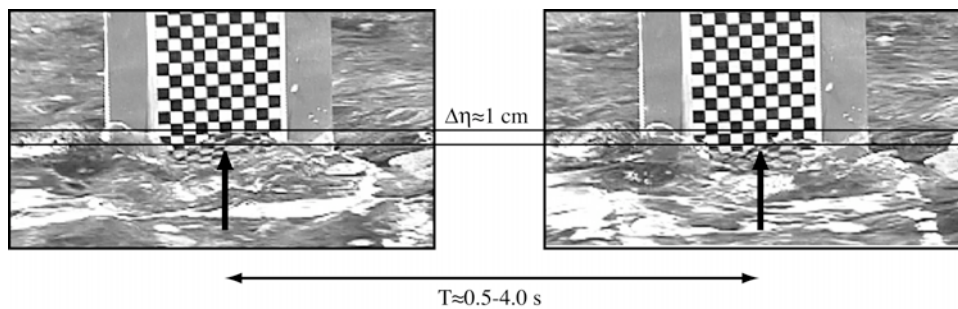


Figure 22 – Record of the water surface elevation; a wave crest and trough, spaced by ≈ 0.72 s and with amplitude of $\Delta\eta \approx 1$ cm.

Although highly irregular due to the variety of surface ripples, it was possible to identify low-frequency oscillations ($f \approx 0.25$ to 2 Hz) with amplitudes scaling with $\Delta\eta \approx 1$ cm. If the SVP is related to travelling surface waves, the u' and w' time series may be related to an idealized sinusoidal-like progressive surface wave such as the one described by USACE (1973) and Kundu and Cohen (2002):

$$\eta(t) = \frac{\Delta\eta}{2} \cos\left(\underbrace{\frac{2\pi}{L} - \frac{2\pi}{T}}_{\phi}\right) \quad (14)$$

L is the wavelength and T the period. The wavelength is related to the period and flow depth,

$$L = \frac{gT^2}{2\pi} \tanh\left(\frac{2\pi h}{L}\right) \quad (15)$$

For $T=1.43$ s and $h=0.17$ m, we obtain $L=1.74$ m. We considered, ideally, that the phase angle Φ corresponds to the cycle of the SVP. According to linear wave theory, the local fluid 2D velocities during the passage of a wave is (USACE (1973), Lighthill (1978) and Kundu and Cohen (2002)):

$$u'(z,t) = \frac{\Delta\eta}{2} \frac{gT}{L} \frac{\cosh\left(\frac{2\pi z}{L}\right)}{\cosh\left(\frac{2\pi h}{L}\right)} \cos(\Phi) \quad (16)$$

$$w'(z,t) = \frac{\Delta\eta}{2} \frac{gT}{L} \frac{\sinh\left(\frac{2\pi z}{L}\right)}{\sinh\left(\frac{2\pi h}{L}\right)} \sin(\Phi) \quad (17)$$

The u' velocity is expected to be in phase with the surface oscillations, whereas the w' is shifted by $\pi/2$. Fig. 23 shows the SVP phase averaged u' and w' data, for a position near the surface, $z/h=0.85$ (at a distance of 0.025 m from the MWL).

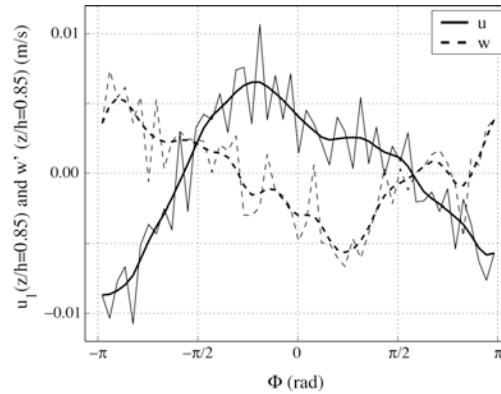


Figure 23 – Near the surface instantaneous streamwise and vertical velocities variations within one SVP cycle ($z/h=0.85$).

Both vertical and streamwise velocity components have approximately a sinus form and the vertical component is actually out-of-phase of the wave with a shift of $\pi/2$.; u' and w' correspond to an orbital trajectory of the fluid due to the passage of a surface wave. The velocity amplitude scales with $\Delta u' \approx 0.014$ m/s (± 0.007 m/s). According to expressions (14) to (16), $\Delta u'$ corresponds to a ripple in the free surface with $\Delta\eta=0.005$ m, which is of the same order of magnitude as the observations made with the video system. The corresponding wave celerity is:

$$c = \frac{L}{T} = 1.22 \text{ m/s} \quad (18)$$

The shallow water wave celerity is similar, $c = \sqrt{gh} = 1.29$ m/s, implying that the surface oscillation associated with the SVP is a shallow water wave.

The SVP may be associated with a periodic oscillation of the water surface compatible with the observed relation between the velocity components u' and w' . According to the linear shallow water theory, the surface fluid particles should describe an orbital trajectory and the u' and w' should be out-of-phase throughout the flow depth. However, as seen in Fig. 19, the sweeps and ejections correspond to in-phase interactions of both velocity components. The velocity fluctuations within the SVP period are damped near the surface (Fig. 19) to values of about 10% when compared with the velocities at $z/h=0.45$. The UMR 2D effect is superimposed on the u' w' relation due to the surface wave, cancelling the orbital trajectories of the fluid particles.

However the nature of the link between the SVP and the surface wave is not clear. The pressure variations due to such a low-amplitude oscillation do not seem to be sufficient to induce a bursting effect capable of generating the sweep-ejection cycle within a SVP period. It is more plausible that the small surface wave is a response of the energy variation in the fluid due to the passage of the UMR's, due to conservation principles. Given the vertical phase shift and the wave direction, this ripple is some kind of approach effect associated with an UMR. The water surface/SVP interaction may be linked to gas transfer processes between the water body and the atmosphere.

6 DISCUSSION AND CONCLUSIONS

In the present paper we identified and isolated large-scale motions, the streamwise velocity pulsation (SVP), which are characterized by the presence of uniform momentum regions (UMR) scaling with the flow depth, where the fluctuating velocity is higher or lower than the time mean. We used space and time correlation analysis to identify the UMR and applied the empirical mode decomposition (EMD) described by Huang et al. (1998) to isolate a narrow frequency band where they exist. Phase averaging of the 3D velocity components within the SVP cycle throughout the flow depth and of the bottom friction velocity allowed us to evaluate the feedback of an UMR passage on the turbulent flow structure and at the free surface. The phase identification of the SVP was made through the Hilbert transform of the streamwise instantaneous velocity at a level situated roughly in the middle of the flow depth.

Space and time correlation analysis of the streamwise instantaneous velocity throughout the flow depth allowed the following conclusions:

- Poor time cross-correlation is observed between vertically adjacent measuring positions in the roughness layer of the flow, $z/h < 0.20$. Inside the roughness or benthic layer, the flow is well mixed and smaller-scale processes hide the correlated large-scale events.
- An enhancement of the vertical correlation is associated with the passage of the positive and negative UMR, indicating that the SVP includes the whole flow depth.

The analysis of the space and time correlations allowed the identification of a narrow frequency band corresponding to the SVP. Refining the original data by the application of the EMD we narrowed and isolated the SVP frequency in a band corresponding to a SVP Strouhal range of $0.13 < S_{SVP} < 0.32$ (this Strouhal number is calculated using the depth averaged velocity). This Strouhal number range contains the Strouhal number corresponding to the time interval between bursting packets estimated in Franca and Lemmin (2005 – 3.6). The UMR related to the SVP seem to correspond to the large-scale regions containing coherent structures packets described in Franca and Lemmin (2005 – 3.6). Using the Hilbert transform for the streamwise velocity in the SVP frequencies at a detection point situated at $z/h=0.45$, we phase-averaged the 3D fluctuating velocities along the profile. The following conclusions can be made about the SVP feedback on the turbulent flow structure:

- There is a high correlation in a SVP cycle throughout the flow depth.
- The SVP have a linear phase shift of $\approx -3/4\pi$ between the bottom and the surface, corresponding to an UMR front geometry of a first quarter moon with the apex situated at $z/h \approx 0.35$. The large UMR scale with 3.1-7.3h horizontally (distance between consecutive SVP fronts) and have a mean angle of 15° in the lower layer.
- The UMR front geometry is conditioned by the vertical phase shift and by the mean velocity profile.
- A large-scale sweep-ejection sequence is associated and in phase with the SVP cycle.
- Compared to sweeps, the ejection effects have shorter time spans within a SVP cycle but dominate the shear stress production with a higher intensity. Sweeps cover 65% of one SVP period.
- A periodic enhancement or reduction of the bottom drag is related with the SVP, varying between 0.90 and 1.10 times the mean value. The friction velocity response to the SVP is nonlinear in the streamwise velocity component due to asymmetry in the time gradients of the drag cycle (apparently a 2nd degree relation exists).
- Two effects of the SVP on bottom drag were found: a 2D large-scale low-amplitude direct enhancement in phase with the UMR; and a 3D indirect enhancement due to the bursting triggered by the SVP.
- A tentative model for the description of the drag cycle is presented in this paper.
- SVP works jointly with smaller scales as a trigger to high frequency production activity; it does not affect the dissipation rate much since this is controlled by background small-scale turbulence, more or less homogeneously distributed within the flow.

Fig. 24 compares the instantaneous velocity profiles with the mean profiles and shows the corresponding events to four key moments in one SVP cycle.

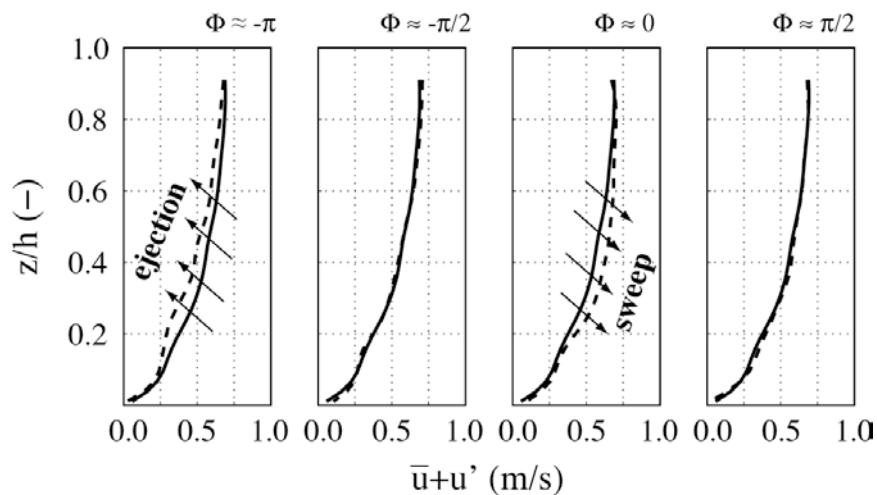


Figure 24 – Instantaneous velocity profiles (dashed line) and indications of the events which occurred at four key moments in the SVP cycle ($\Phi = -\pi, -\pi/2, 0$ and $\pi/2$). The continuous lines represent the mean velocity profile.

Given the perturbed free surface pattern of these flows, filled with signatures of stationary and free waves, we investigated a possible relationship between the SVP cycles and in-phase surface oscillations. Confined to the surface layer of the flow, a u' - w' cycle corresponding to a travelling surface wave is directly associated to the SVP cycle. This surface feature is probably a backwater response to the UMR passage caused by conservation principles. Nevertheless, the relationship between the SVP and the travelling surface wave is not yet clear.

The origin of SVP is still unclear and it is not yet possible to relate SVP occurrence to local conditions. However SVP might be related to a general shedding effect due to the macro-rough bottom, involving all the flow depth. This would be similar to the interaction between coarse elements closely disposed in the bed of the wake interference flow (Morris (1959) and Baiamonte and Ferro (1997)). Randomly distributed elements cause individual vortex shedding due to their intrusion in the flow (Buffin-Bélanger and Roy (1998) and Tritico and Hotchkiss (2005)). Since these are densely distributed in the riverbed, the vortices superimpose and merge into larger-scale motions with frequencies different from the original. This may resemble an ensemble riverbed shedding effect. We showed that the SVP has a regular but non-periodic phase distribution (SVP appears in varied frequencies). The non-periodicity of the SVP might be due to the different boulder sizes in the riverbed and to the interaction and impact between shedding vortices from different boulders (Rubin and McDonald 1995).

According to Schlichting (1968), the relation between the Strouhal number of shedding vortex in the flow around an obstacle of diameter D ($St_D = \frac{fD}{U}$) is constant for high values of the obstacle Reynolds number as in the present case ($Re_D = \frac{\bar{U}D_{84}}{\nu} = 5 \times 10^4$). Considering the diameter D_{84} as representative of the shedding protuberances in the riverbed, and using the depth averaged velocity $U=0.52$ m/s, we have a range of shedding Strouhal numbers of $0.07 < St_D < 0.17$ corresponding to the SVP frequency range (f_{SVP}). St_D is lower than the asymptotic value given by Schlichting (1968) for circular emerged obstacles $St=0.21$, and can be explained by frequency damping due to the cushion effect of the water above the shedding boulders and vortex merging from larger structures.

Similar to the idea expressed by Smith (1996), the large-scale UMR seem to work as a “graveyard” for shedding regions of the flow, randomly distributed and resulting from the extremely rough riverbed. However, in this graveyard, structures do not simply fade away, they merge into one combined non-turbulent effect. Given the limited contribution to the shear stress production, the SVP will correspond to what Lu and Willmarth (1973) referred to as “irrelevant motions”.

Further field and laboratory studies in the SVP should include:

- Determination of the local flow characteristics which condition the vertical phase shift in the SVP and which will define whether UMR should be expected inclined downstream or inclined upstream.
- How are the different UMR geometric configurations related to the bursting process.
- Detailed analysis of the relationship between bursting packets detected by Franca and Lemmin (2005 – 3.6) and the SVP, and evaluation of the indirect contribution of SVP to bottom drag enhancement.
- Synchronized ADV and water surface displacement measurements to evaluate the actual relationship between SVP and free surface waves.
- Analysis of the implications of the passage of a UMR in the occurrence of surface boils or other surface perturbations promoting air-water exchange.

- Determination of the instability conditions for the occurrence of Taylor-Görtler vortices in the curved lower shear layer of the UMR, and observation of eventual vortex signatures in the instantaneous 3D data.
- Analysis of the space correlation of the SVP between profiles across the river.
- Systematic tests to determine the relationship between S_{SVP} and geometric characteristics of the river; a geometric variable should reflect the macro-roughness effect and the merged shedding from the rough bottom.
- Better estimates of the production and dissipation associated with the SVP.

Given the clear interaction between SVP and small-scale processes, we suggest a modified Reynolds decomposition accounting for two frequency bands (\sim refers to large-scale and $''$ to the small-scale processes):

$$v_i = \overline{v_i} + \tilde{v}_i + v_i'' \quad (19)$$

The fluctuating part v_i'' was divided into the two contributory components, \tilde{v}_i and v_i'' . This decomposition will allow determining the large- and small-scale contributions to the Reynolds stress tensor production. For example, the modified Reynolds longitudinal shear stress includes the four following components:

$$\overline{u'w'} = \overline{\tilde{u}\tilde{w}} + \overline{\tilde{u}w''} + \overline{u''\tilde{w}} + \overline{u''w''} \quad (20)$$

Further studies should define the proper filtering for the division between actual large- and small-scales. The lower and higher frequency events correspond to Lu and Willmarth's definition of irrelevant and universal motion, respectively. The SVP is not a random, chaotic and 3D turbulent manifestation but an organized momentum oscillation with a 2D signature.

In our opinion, shallow flows should take a modified characteristic length as a parameter in the description of the large-scale motion which takes into account the low ratio h/D and the density of the large gravel grains in the riverbed. A proper geometric scale characteristic of the SVP is still unknown.

ACKNOWLEDGEMENTS

The authors wish to acknowledge the financial support of the Portuguese Science and Technology Foundation (BD 6727/2001) and the Swiss National Science Foundation (2000-063818). We are most grateful to Tom Osborn for introducing us to Empirical Mode Decomposition, to Huib de Vriend and Wim Uijttewaal for their constructive comments during the elaboration of this paper.

REFERENCES

- Adrian R.J., Meinhart C.D. and Tomkins C.D. (2000), Vortex organization in the outer region of the turbulent boundary layer, *J. Fluid Mech.*, 422, 1-54.
- Antonia R.A., Bisset D.K. and Browne L.W.B. (1990), Effect of Reynolds number on the topology of the organized motion in a turbulence boundary layer, *J. Fluid Mech.*, 213, 267-286.
- Baiamonte G. and Ferro V. (1997), The influence of roughness geometry and Shields parameter on flow resistance in gravel-bed channels, *Earth Surf. Proc. and Landforms*, 22, 759-772.
- Bathurst J.C., Li R.M. and Simons D.B. (1981), Resistance equation for large-scale roughness, *J. Hydr. Eng.*, 107(12), 1593-1613.

- Brown G.L. and Thomas A.S.W. (1977), Large structure in a turbulent boundary layer, *Phys. Fluids*, 20(10), s243-252.
- Buffin-Bélanger T. and Roy A.G. (1998), Effects of a pebble cluster on the turbulent structure of a depth-limited flow in a gravel-bed river, *Geomorphology*, 25, 249-267.
- Buffin-Bélanger T., Roy A.G. and Kirkbride A.D. (2000a), Vers l'intégration des structures turbulentes de l'écoulement dans la dynamique d'un cours d'eau à lit de graviers, *Géogr. Phys. Et Quaternaire*, 54(1), 105-117.
- Buffin-Bélanger T., Roy A.G. and Kirkbride A.D. (2000b), On large-scale flow structures in a gravel-bed river, *Geomorphology*, 32, 417-435.
- Cellino M. and Lemmin U. (2004), Influence of coherent flow structures on the dynamics of suspended sediment transport in open-channel flow, *J. Hydr. Eng.*, 130(11), 1077-1088.
- Chassaing P. (2000), *Turbulence en mécanique des fluides*, Cépadués-Éditions, Toulouse (France).
- Chen T. Que P., Zhang Q. and Liu Q. (2005), Ultrasonic signal identification by empirical mode decomposition and Hilbert transform, *Rev. Scient. Inst.*, 76, 085109.
- Cohen L. (1995), *Time-frequency analysis*, Prentice Hall PTR, Englewood Cliffs (USA).
- Dinehart R.L. (1999), Correlative velocity fluctuations over a gravel river bed, *Water Resour. Res.*, 35(2), 569-582.
- Falco R.E. (1977), Coherent motions in the outer region of turbulent boundary layers, *Phys. Fluids*, 20(10), s124-s132.
- Flandrin P., Gonçalves P. and Rilling G. (2004), Detrending and denoising with empirical mode decompositions, *Eusipco - 12th European Signal Processing Conference*, September 6-10 Vienna (Austria).
- Franca M.J. and Lemmin U. (2004 – A.1), A field study of extremely rough, three-dimensional river flow, *Proc. 4th Int. Symp. Env. Hyd. - IAHR*, Hong Kong (China). Appendix A.1.
- Franca M.J. and Lemmin U. (2005 – 3.4), subchapter “Flow resistance characterization in shallow gravel-bed rivers”.
- Franca M.J. and Lemmin U. (2005 – 3.6), subchapter “Boundary layer bursting packets associated with high- and low-speed wedges detected through a wavelet multiresolution analysis”.
- Franca M.J. and Lemmin U. (2005 – 3.7), subchapter “Evaluation of energetic scales in turbulent gravel-bed rivers based on wavelet analysis”.
- Franca M.J. and Lemmin U. (2005 – 3.8), subchapter “TKE budget analysis in gravel-bed river flow”.
- Hinze J.O. (1975), *Turbulence*, McGraw-Hill, (USA).
- Hofland B. and Booij R.R. (2004), Measuring the flow structures that initiate stone movement, *Proc. Riverflow 2004*, Naples (Italy).
- Hristov T., Friehe C. and Miller S. (1998), Wave-coherent fields in air flow over ocean waves: identification of cooperative behaviour buried in turbulence, *Phys. Rev. Lett.*, 81(23), 5245-5248.
- Huang N.E., Shen Z., Long S.R., Wu M.C., Shih H.H., Zheng Q., Yen N.C., Tung C.C. and Liu H.H. (1998), The empirical mode decomposition and the Hilbert spectrum for nonlinear and non-stationary time series analysis, *Proc. R. Soc. Lond. A*, 454, 903-995.
- Huang N.E., Shen Z. and Long S.R. (1999), A new view of nonlinear water waves: the Hilbert spectrum, *Ann. Rev. Fluid Mech.*, 31, 417-457.

- Jackson R.G. (1976), Sedimentological and fluid-dynamic implications of the turbulent bursting phenomenon in geophysical flows, *J. Fluid Mech.*, 77(3), 531-560.
- Kantha L.H. and Clayson C.A. (2000), *Small scale processes in geophysical fluid flows*. Academic Press, San Diego (USA).
- Kirkbride A.D. and Ferguson R. (1995), Turbulent flow structure in a gravel-bed river: Markov chain analysis of the fluctuating velocity profile, *Earth Surf. Proc. and Landforms*, 20, 721-733.
- Kolmogorov A. (1941), The local structure of turbulence in incompressible viscous fluid for very large Reynold's numbers, *C. R. Acad. Sci. URSS*, XXX(4).
- Kundu P.K. and Cohen I.M. (2002), *Fluid Mechanics*, Academic Press, San Diego (USA).
- Lighthill J. (1978), *Waves in Fluids*, Cambridge University Press, Cambridge (UK).
- Lu S.S. and Willmarth W.W. (1973), Measurements of the structure of the Reynolds stress in a turbulent boundary layer, *J. Fluid Mech.*, 60(3), 481-511.
- Monin A.S. and Yaglom A.M. (1975), *Statistical Fluid Mechanics: Mechanics of Turbulence - Vol. 2*, The MIT Press, Cambridge (USA).
- Morris H.M. (1959), Design methods for flow in rough conduits, *J. Hydr. Eng.*, 85(7), 43-62.
- Nakagawa H. and Nezu I. (1981), Structure of space-time correlations of bursting phenomena in an open-channel flow, *J. Fluid Mech.*, 104, 1-43.
- Nelson J.M., Shreve R.L. and McLean S.R. (1995), Role of near-bed turbulence in bed load transport and bed forms mechanics, *Water Resour. Res.*, 31(8), 2071-2086.
- Nezu I. and Nakagawa H. (1993), *Turbulence in open-channel flows - IAHR monograph*, A.A. Balkema, Rotterdam (The Netherlands).
- Nicholas A.P. (2001), Computational fluid dynamics modelling of boundary roughness in gravel-bed rivers: an investigation of the effects of random variability in bed elevations, *Earth Surf. Proc. and Landforms*, 26, 345-362.
- Nikora V. (1999), Origin of the "-1" spectral law in wall-bounded turbulence, *Phys. Rev. Lett.*, 83(4), 734-736.
- Nikora V. and Smart G.M. (1997), Turbulence characteristics of New Zealand gravel-bed rivers, *J. Hydr. Eng.*, 123(9), 764-773.
- Ooninx P.J. and Hermand J.P. (2004), Empirical mode decomposition of ocean acoustic data with constraint on the frequency range, *Proc. Seventh Eur. Conf. Underwater Acoustics - ECUA*, Delft (The Netherlands).
- Osborn T.R., Nimmo Smith W.A.M., Luznik L., Katz J. (2005), Turbulence and waves in the bottom boundary layer of the coastal ocean, submitted for publication in the *Journal of Physical Oceanography*.
- Pope S.B. (2001), *Turbulent flows*, Cambridge University Press, Cambridge (UK).
- Rilling G., Flandrin P. and Gonçalvès P. (2003), On empirical mode decomposition and its algorithms, *IEEE-EURASIP Workshop on Nonlinear Signal and Image Processing NSIP-03*, Grado (Italy).
- Roy A.G., Buffin-Belanger T., Lamarre H. and Kirkbride A.D. (2004), Size, shape and dynamics of large-scale turbulent flow structures in a gravel-bed river, *J. Fluid Mech.*, 500, 1-27.
- Rubin D.M. and McDonald R.R. (1995), Nonperiodic eddy pulsations, *Water Resour. Res.*, 31(6), 1595-1605.
- Schlichting H. (1968), *Boundary-layer theory*, McGraw-Hill, (USA).

- Sharman R.D. and Wurtele M.G. (1983), Ship waves and lee waves, *J. Atmosph. Sciences*, 40, 396-427.
- Shen C. and Lemmin U. (1999). Application of an acoustic particle flux profiler in particle-laden open-channel flow, *J. Hydr. Res.* 37 (3): 407-419 1999.
- Smith C.R. (1996), Coherent flow structures in smooth-wall turbulent boundary layers: facts, mechanisms and speculation *in* "Coherent flow structures in open channels", ed. Asworth P.J., Bennet S.J., Best J.L. and McLelland S.J., John Wiley & Sons, West Sussex (UK).
- Tritico H.M. and Hotchkiss R.H. (2005), Unobstructed and obstructed turbulent flow in gravel bed rivers, *J. Hydr. Eng.*, 131(8), 635-645.
- USACE – U.S. Army Corps of Engineers (1973), Shore Protection Manual, U.S. Army Coastal Eng. Res. Cent., Virginia (USA).
- Williams J.J., Thorne P.D. and Heathershaw A.D. (1989), Measurements of turbulence in the benthic boundary layer over a gravel bed, *Sedimentology*, 36, 959-971.
- Wolman M.G. (1954), A method of sampling coarse river-bed material, *Trans. Amer. Geoph. Un.*, 35(6), 951-956.
- Yalin M.S. (1992), *River Mechanics*, Pergamon Press Ltd., Exeter (UK).

3.6 BOUNDARY LAYER BURSTING PACKETS ASSOCIATED WITH HIGH- AND LOW-SPEED WEDGES DETECTED THROUGH A WAVELET MULTIREOLUTION ANALYSIS

In this subchapter an innovative method for detecting and reconstructing 3D coherent structures based on wavelet multiresolution analysis is presented. The dynamics of one reconstructed bursting packet composed of five $u'-w'$ interactions is analyzed together with its instantaneous effects on the turbulence structure of the flow, instantaneous velocity profile, Reynolds stress tensor and TKE budget.

	ABSTRACT	3.6.1
1	INTRODUCTION	3.6.1
2	FIELD STUDY	3.6.3
2.1	River characteristics	3.6.3
2.2	Hydraulic characteristics of the detection point	3.6.3
3	INSTRUMENTATION	3.6.4
4	COHERENT STRUCTURES SAMPLING	3.6.5
4.1	Continuous wavelets transform	3.6.5
4.2	Discrete wavelet transform	3.6.6
4.3	Wavelet multiresolution analysis	3.6.6
4.4	Energy partition	3.6.7
4.5	Wavelet-frame conditional quadrant analysis	3.6.9
4.6	Wavelet-frame threshold and cross-correlation conditional sampling	3.6.10
5	RECONSTRUCTION OF THE CONDITIONALLY SAMPLED COHERENT STRUCTURE	3.6.13
5.1	Single point, 3D reconstruction	3.6.13
5.2	Analysis of the instantaneous velocity profile	3.6.15
5.3	Effect of the bursting packet in the Reynolds stress tensor	3.6.20
5.4	Effect of the bursting packet in the instantaneous TKE budget	3.6.22
6	TIME DISTRIBUTION OF THE COHERENT STRUCTURES	3.6.24
7	CONCLUSIONS	3.6.26
	ACKNOWLEDGEMENTS	3.6.28
	REFERENCES	3.6.28

BOUNDARY LAYER BURSTING PACKETS ASSOCIATED WITH HIGH- AND LOW-SPEED WEDGES DETECTED THROUGH A WAVELET MULTIRESOLUTION ANALYSIS

ABSTRACT

Coherent structures are known to play an important role in transport and mixing processes in geophysical fluid mechanics. Using 3D ADV measurements in a river we developed a detection and reconstruction technique of coherent structures based on multiresolution wavelet analysis. The detection of a typical coherent structure is conditioned to the event scale and amplitude. Composite-averaging is then applied to the structures sampled with a correlation-conditioned method. Composite averaging allows the 3D reconstruction of the structure. Its application to a measured profile provided the visualization and characterization of bursting packets composed of sequential ejections and sweeps, E0-S1-E1-S2-E1. Spanwise vortical cells exist and are linked to {x-z} events. Apparently, two central shear events (S1 and E1) are the core of the packet, whereas the remaining ones are due to vortical momentum continuity. Reynolds stresses are enhanced by the bursting packet. The packet is highly energetic and is responsible for a production of twice the peak mean production with low persistence in time. We analyzed the velocity profile deformation resulting from the packet passage. A relationship between the spanwise velocity field and the events in the {x-z} plane is found. Associated with these packets are signatures of large-scale, high- and low-speed wedges exist. The corresponding fronts have a concave shape and near the bottom an angle of 18° with the horizontal. Between the sequential ejections and sweeps, "stop points" exist where all three velocity components have low activity. After analysing the position of the bursting packets over the whole time record, we conclude that the sampled bursting packets are independent. The time interval between packets has an extreme-type statistical distribution and the most probable value corresponds to a Strouhal number of $S_i=2.5$. The bursting Strouhal number is $S_b=12.5$.

Key-words: coherent structures; bursting packet; wavelet multiresolution analysis

1 INTRODUCTION

In geophysical flows momentary variations of the flow velocity are related to such processes as the suspension of sediments and the dispersion of pollutants in the water. Coherent structures consist of macroscale "organized" phenomena, belonging to the productive range of the spectral space. In the inertial and the dissipative ranges, turbulence is essentially composed of fine scale turbulence, such as small scale eddies, essentially random and isotropic. Chassaing (2000) introduced the concept of physical coherence together with the statistical coherence. He states that the physical coherence concept is related to the fact that turbulent structure properties (for example geometric, kinematic and dynamic)

change relatively slowly with respect to its representative scale domain; turbulent structure properties are consequently conveyed by the flow field.

Coherent structures distribute particles and pollutants across the whole water column much faster than small-scale turbulence (Hurther et al. 2002). Cellino and Lemmin (2004) demonstrated the importance of ejections and sweeps in sediment suspension and transport. In open-channel flows, near the surface a link exists between the bursting process and surface boils, which are known as active zones for gas transfer (Kumar et al. (1998), Hurther and Lemmin (2000a), Troiani et al. (2004), and Yoshida and Nezu (2004). State of the art references on coherent structures include Hinze (1975), Yalin (1992), Nezu and Nakagawa (1993), Ashworth et al. (1996), Holmes et al. (1998), Métais and Lesieur (1989) and Chassaing (2000). However, knowledge about the dynamics of coherent structures in rivers is still very limited. The study of 3D instantaneous velocity fields in river flows is essential in order to understand the mixing and transport processes related to flow intermittency. Recent studies based on measurements in rivers (R) or artificial channels (AC), dealing with coherent motion, include Nikora and Goring (2000, AC), Hurther (2001, R), Nikora and Goring (2002, AC), Buffin-Bélanger et al. (2000a and 2000b, R) and Roy et al. (2004, R).

Coherent structures have a short life cycle. They cannot be identified with a time averaged analysis and require an investigation based on time and space correlation measurements or on flow visualization techniques. In laminar and transitional flows, coherent structures occur periodically, whereas turbulent flows occur randomly in space and time. Hence, in addition to flow visualization techniques, conditional sampling and statistics techniques have to be used in the detection and characterization of coherent structures. Conditional statistics techniques may be applied to *quasi*-instantaneous velocity samples obtained from the ADVP measurements. Several authors applied conditional statistics to turbulence studies (Antonia and Atkinson (1973), Nakagawa and Nezu (1977) and Hurther and Lemmin (2000a)). Adrian et al. (2000a) compared Reynolds decomposition, Galilean and LES techniques. In this study we will use Reynolds time-averaged decomposition.

Here we make use of conditional sampling techniques and the wavelet multilevel decomposition of single point instantaneous velocity measurements. Wavelet analysis is a suitable tool for the study of turbulence in geophysical flows. Foufoula-Georgiou and Kumar (1994) presented a compilation of papers dealing with the application of wavelet analysis in geophysics. Other examples include Turner et al. (1994) who examined scales and location of flow structures related with temperature and flux data of atmospheric flow above forest canopy and Yoshida and Nezu (2004) who used wavelet analysis in a study of the importance of the bursting process near the surface to the gas-transfer in open-channel flows.

For this study we use river velocity data obtained with the ADVP instrument to develop a detection algorithm of coherent structures. This is based on the wavelet multilevel decomposition of the 3D instantaneous velocities measured at a single point. A conditioned sample is created with scale, amplitude and cross-correlation threshold methods. Thereafter, the single-point detected structure is reconstructed three-dimensionally by a normalized composite average. We subsequently reconstruct the 3D flow structure in the whole water depth. The reconstructed structure and its time distribution in the instantaneous velocity signal are discussed. The method is demonstrated for Quadrant II (QII) structures (ejections) but it may be generalized to other quadrants. With the detection technique we were able to identify several sequential bursting packets of coherent structures, which were identified and analyzed. Packet dynamics, influence in the velocity profile, TKE production and dissipation rates and time distribution are investigated.

The notation adopted for the Reynolds velocity decomposition is streamwise, $u = \bar{u} + u'$; spanwise, $v = \bar{v} + v'$; vertical, $w = \bar{w} + w'$ ($\bar{\quad}$ time mean and $'$ instantaneous value). When referring to $v_i = \bar{v}_i + v_i'$, v is velocity and the subscript i is one of the 3D Cartesian dimensions $\{1,2,3\} = \{x,y,z\}$.

2 FIELD STUDY

2.1 River characteristics

This research is based on field measurements taken during the summer of 2004, in the Swiss river Venoge (canton of Vaud). The instantaneous velocity profiles were measured in a single day under stationary shallow water flow conditions, as confirmed by the discharge data provided by the Swiss Hydrological and Geological Services. The measuring position was located about 90 m upstream of the Moulin de Lussery. The river's hydraulic characteristics at the time of the measurements are shown in Table 1.

Table 1 - Summary of the river flow characteristics.

Discharge (m ³ /s)	Slope (%)	Mean depth (m)	Width (m)	U (m/s)	Re (x10 ⁴)	Fr (-)	D ₅₀ (mm)
0.76	0.33	0.20	6.30	0.60	5.9 - 8.7	0.32 - 0.61	68

U is the cross-section bulk velocity; Re, the Reynolds number; Fr, the Froude number; D₅₀ the bottom grain size diameter of which 50% of the grain diameters are smaller. The riverbed material grain distribution was sampled according to the Wolman (1954) method. The mean water depth was estimated from local measurements in several positions across the river section. Considering the average water depth, the river aspect ratio B/\bar{h} is 31.5, which corresponds to wide channels. The riverbed is hydraulically rough, with coarse gravel and randomly spaced macro-roughness elements scaling with as much as half the water depth (0.5h). There was no sediment transport during the measurements.

The instantaneous velocity profiles were measured for 211 s, forming a 3x5 rectangular horizontal grid (x-y). 15 velocity profiles were equally spaced in the spanwise direction of 10 cm and in the streamwise of 15 cm. Franca and Lemmin (2005 – 3.4) analyzed the mean velocity field from these measurements. The vertical resolution of the measurements is around 0.5 cm. The bottom position was detected from the sonar-backscattered response. Here only one measured vertical profile is used.

2.2 Hydraulic characteristics of the detection point

The point used in the coherent structure detection was chosen inside the boundary layer of a logarithmic shaped velocity profile. It is located in the bottom shear layer, where instabilities generating turbulent coherent motion are expected. The point is located 1.4 cm above the river bottom, and the flow characteristics of the studied profile are given in Table 2.

Table 2 - Summary of the flow characteristics of the studied profile.

Linear discharge (m ² /s)	Water depth (m)	\bar{U} (m/s)	Re (x10 ⁴)	Fr (-)	u* (m/s)
0.07	0.17	0.38	6.40	0.29	0.040

\bar{U} is the depth-averaged streamwise mean velocity; u^* , shear velocity estimated from the eddy-correlation method (Franca and Lemmin 2005 – 3.4). The time-averaged velocity at the detection point is $\bar{u}=0.24$ m/s. Fig. 1 shows the mean velocity \bar{u} , streamwise turbulence intensity $\overline{u'^2}$, turbulent kinetic energy $\overline{k'^2} = \overline{u'^2} + \overline{v'^2} + \overline{w'^2}$ and shear stress $\overline{u'w'}$ distributions throughout the water depth.

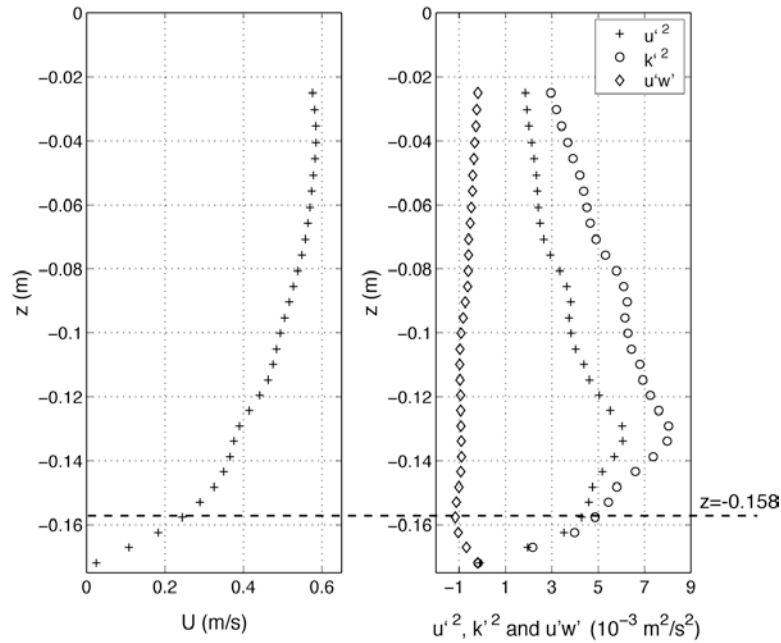


Figure 1 – (a) Mean velocity profile \bar{u} . (b) Distribution of the turbulence intensity $\overline{u'^2}$, turbulent kinetic energy $\overline{k'^2} = \overline{u'^2} + \overline{v'^2} + \overline{w'^2}$ and Reynolds shear stress $\overline{u'w'}$ (x-z). Horizontal dashed line: location of the analyzed gate.

3 INSTRUMENTATION

A deployable ADVP developed at the LHE-EPFL was used for the velocity profile measurements. It allows measuring 3D quasi-instantaneous velocity profiles over the entire depth of the flow in rivers. The ADVP is suitable for field and laboratory measurements. Details on the ADVP are given in chapter 2. A Pulse Repetition Frequency (PRF) of 1666 Hz and a Number of Pulse Pairs (NPP) of 64 were used to estimate the Doppler shift, resulting in a sampling frequency of 26 Hz. A bridge which supported the ADVP instrument allowed the easy displacement of the system across the section and along the river streamwise direction.

4 COHERENT STRUCTURES SAMPLING

4.1 Continuous wavelets transform

Wavelet analysis is a relatively new domain in geophysics fluid mechanics research. It constitutes a powerful mathematical tool since it is capable of localizing signal variability simultaneously both in time and scale (scale here refers to duration of time) (Kantha and Clayson 2000). Contrary to Fourier based analysis, wavelet analysis can deal with non-stationary signals with randomly distributed singularities, such as the occurrence of coherent structures in turbulent time velocity series. In wavelet decomposition, the wavelet functions are scaled locally (dilatation or contraction) in order to represent singularities. Thus, boundaries do not influence the local description of the signal. Fargé (1992) presented an introductory text on the use of wavelet transforms in the study of turbulent signals. In this paper, we give a short introduction to wavelet analysis based on Fargé (1992), Fofoula-Georgiou and Kumar (1994), Kumar and Fofoula-Georgiou (1997) and Mallat (1999). Only 1D wavelet analysis is used.

The continuous wavelet transform \hat{u}_w of a time function $u(t)$ is given by

$$\hat{u}_w(\lambda, t) = \int_{-\infty}^{+\infty} u(\tau) \overline{\psi_{\lambda, t}(\tau)} d\tau \quad (1)$$

λ is a scale parameter; τ , the integration variable (time); and $\overline{\psi_{\lambda, t}(\tau)}$, the conjugate of the wavelet function,

$$\psi_{\lambda, t}(\tau) = \frac{1}{\sqrt{\lambda}} \underbrace{\psi\left(\frac{\tau - t}{\lambda}\right)}_{\psi(t)} \quad (2)$$

$\psi(t)$ defines the wavelet form. Fargé (1992) discusses in detail the conditions for a function to be used as a wavelet. The variable time t is a location parameter, whereas λ defines the time range (scale) where the wavelet function will describe the signal. Kumar and Fofoula-Georgiou (1997) describe the wavelet transform as a microscope, where the magnification is given by $1/\lambda$ and the optics are given by the choice of the wavelet $\psi(t)$. We will use the Daubechies type “D4” wavelet in the present research (Fig. 2), which belongs to a family of wavelet functions defined by Daubechies (1988).

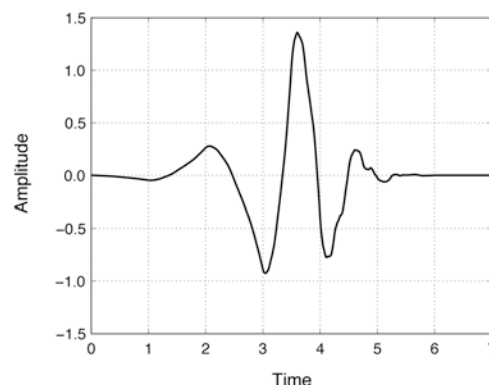


Figure 2 – Daubechies wavelet function of type D4 (Daubechies 1988).

As in the Fourier analysis, we can apply a wavelet transform using appropriate wavelet functions and discrete scale and location parameters (λ and t). The process consists of evaluating the signal locally (the wavelet covering all the time locations) in several modes, each corresponding to a defined scale (the scale is defined by the expansion $\lambda = \lambda_0^m$, where λ_0 is a fixed dilatation step and m an integer).

The time step to analyze the signal is a function of the chosen scale, $t = nt_0\lambda_0^m$. In this way, the time domain is covered by the discrete analysis.

4.2 Discrete wavelet transform

In the continuous wavelet transform, the wavelet function $\psi_{\lambda,t}(t)$ is parameterized by the real values of scale λ and time location t , whereas in the discrete wavelet transform $\psi_{m,n}(t)$ it is parameterized by the integers m and n . These have a similar meaning in both transforms, and can be considered the expansion and location parameters. The discrete wavelet functions thus have the form

$$\psi_{m,n}(t) = \frac{1}{\sqrt{\lambda_0^m}} \psi\left(\frac{t - nt_0\lambda_0^m}{\lambda_0^m}\right) \quad (3)$$

The discrete wavelet transform is defined as

$$\hat{u}_w(m,n) = \frac{1}{\sqrt{\lambda_0^m}} \int_{-\infty}^{+\infty} u(t) \psi\left(\frac{t - nt_0\lambda_0^m}{\lambda_0^m}\right) dt \quad (4)$$

With adequate base dilatations λ_0 and reference time t_0 , the discrete wavelet transform (4) completely describes the original signal. To each of these wavelets, corresponds a wavelet frame, which is characterized by the scale $\lambda = \lambda_0^m$. This is called the wavelet multilevel discretization. The reconstruction formula corresponding to the discrete wavelet transform is given by

$$u(t) = C \sum_{m=-\infty}^{+\infty} \sum_{n=-\infty}^{+\infty} \hat{u}_w(m,n) \psi_{m,n}(t) + \gamma \quad (5)$$

C is a constant, which defines the orthogonal degree of the expansion ($C=1$, orthogonal basis). It also encloses the redundancy of the discrete multilevel wavelet transform (Kumar and Foufoula-Georgiou 1997). γ is the residual term. For an orthogonal decomposition, $C=1$ and $\gamma=0$.

4.3 Wavelet multiresolution analysis

Wavelet multiresolution consists of the decomposition of the original turbulent signal into one coarse approximation set (the approximation) and several others with progressively smaller scale resolution (the details). Once the multilevel wavelet discretization of the signal is made, we reconstruct each level of the signal obtaining several low-resolution data series corresponding to each wavelet frame scale. We then obtain the multiresolution decomposition of our original signal. A scale resolution higher than the scale of the last lower level of decomposition corresponds to the approximation. The signal can thus be successively reconstructed by the addition of the approximation with the consecutive level details (the integer m refers to the frame scale, $\lambda = \lambda_0^m$) (Fig. 3):

$$S_{m-1}(t) = S_m(t) + D_m(t) \quad (6)$$

The symbol S means the successive approximations, and D the successive details.

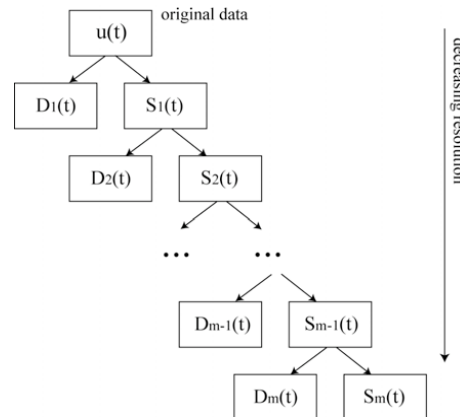


Figure 3 – Schematic representation of the wavelet multiresolution analysis applied to a time data set; successive progression of $S_{m-1}(t) = S_m(t) + D_m(t)$.

Fig. 4 shows the decomposition of the instantaneous streamwise velocity in 8 resolution levels, and the successive corresponding approximations. The wavelet function Daubechies of type ‘D4’ was used for the wavelet multilevel discretization. In Fig. 4b we can see the increasing resolution of the successive approximations calculated from Eq. (6), until the final resolution corresponding to the original data is reached. In Fig. 4a we may see the lower resolution representations of the original signal, each one of them corresponding to a wavelet frame.

4.4 Energy partition

Multiresolution analysis of the data allows to estimate the energy partition throughout the different scale frames associated with each of the decomposition modes. Basically we are now able to independently analyze coherent structures of different scales. A certain scale of coherent structures corresponds to each wavelet frame. We estimated the contribution of each wavelet frame to the streamwise flow energy by calculating the relative variance of the instantaneous velocity signal to each mode (Fig. 5):

$$E_x(\lambda) = \frac{\overline{D_{\lambda,u'}^2}}{\overline{u'^2}} \quad (7)$$

$E_x(\lambda)$ is the relative energy associated with scale λ ; and $\overline{D_{\lambda,u'}^2}$, the variance of the streamwise instantaneous velocity (u') detail associated with the scale λ :

$$\overline{D_{\lambda,u'}^2} = \frac{\sum_{n=1}^{N_{time}} D_{\lambda,u'}(n)}{N_{time}} \quad (8)$$

n is an integer defining the time step; and N_{time} , the total number of time steps (the addition is made for the entire time domain).

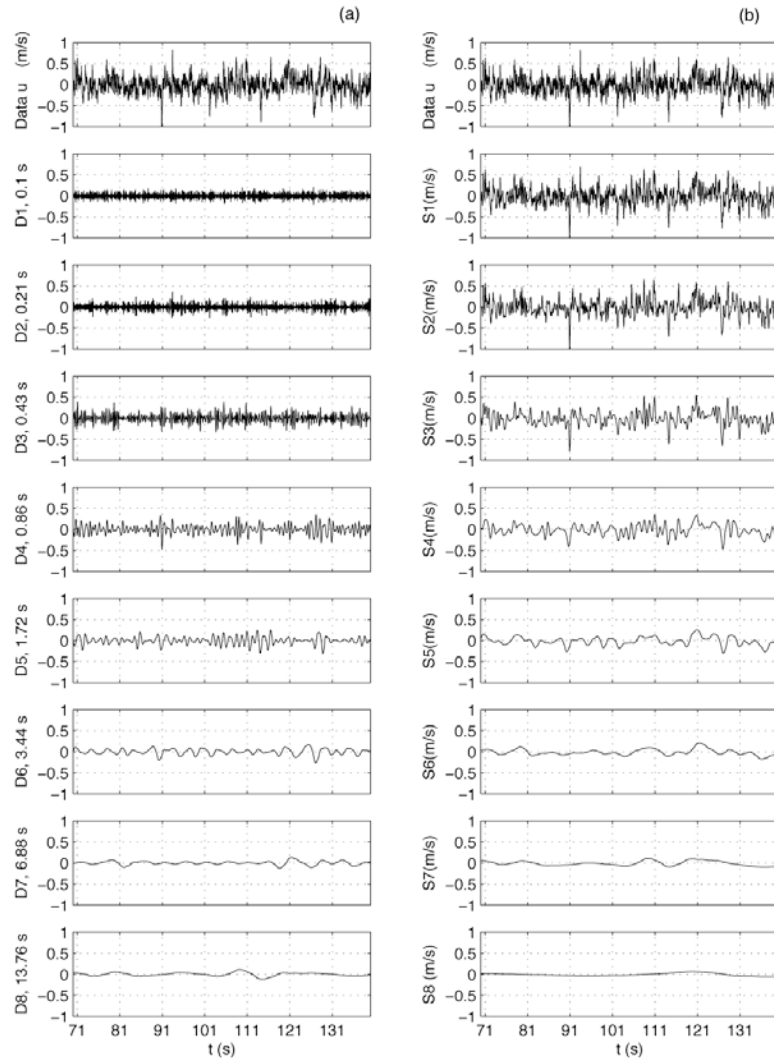


Figure 4 – Multiresolution analysis applied to the instantaneous streamwise velocity data at the detection point, using Daubechies “D4” wavelet function. (a) Data and low-resolution time series $D_m(t)$ corresponding to the time scale λ_0^m . (b) Data and increasing-resolution time series $S_m(t)$ resulting from the progression $S_{m-1}(t) = S_m(t) + D_m(t)$.

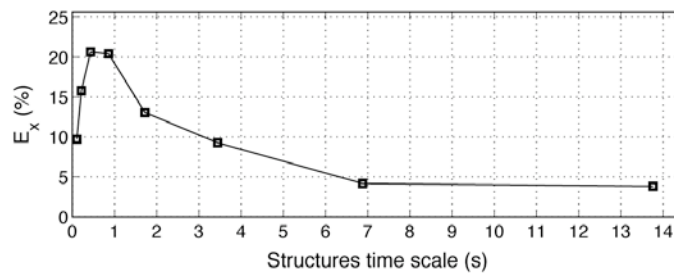


Figure 5 – Partition of the flow energy associated with the streamwise instantaneous velocity field through the different scales of the multi-level decomposition.

The 8-level wavelet decomposition with the Daubechies “D4” function is sufficient to describe the energy partition through the different structure scales present in the flow. The most energetic coherent structures belong to the detail D_3 ($\lambda=0.43$ s), and the maximum energy corresponds to a scale duration within the interval $\lambda=0.43-0.86$ s (Fig. 5). This corresponds to length scales ranging from $\Lambda=\lambda\bar{u}_{(z=0.158)}=0.10$ to 0.20 m (assuming Taylor’s frozen hypothesis using the downstream convective velocity). The energy content is in coherent structures whose scales are between the representative bed grain dimension ($\approx D_{84}$) and the water depth. In the present study we will investigate coherent structures scaling with the most energetic scale. The distribution of the most energetic scales is treated in Franca and Lemmin (2005 – 3.7 and 3.8).

4.5 Wavelet-frame conditional quadrant analysis

The statistical distribution of coherent structures in plane $\{x-z\}$ may be analyzed by means of the threshold-based conditional sampling of instantaneous shear events $\varepsilon'=u'w'$, combined with their quadrant location (Nakagawa and Nezu 1977). The quadrant technique consists of analyzing the distribution of the instantaneous shear events ε' in the four quadrants of the plan, in order to detect coherent motions such as (in plane $\{x-z\}$):

- Outwards interactions, characterized by instantaneous positive streamwise and vertical velocities – Quadrant I;
- Ejections characterized by instantaneous negative streamwise and positive vertical velocities – Quadrant II;
- Inwards interactions, characterized by instantaneous negative streamwise and vertical velocities – Quadrant III;
- Sweeps characterized by instantaneous positive streamwise and negative vertical velocities – Quadrant IV.

The event location in the quadrant depends on the direction of both $\{x-z\}$ components of the event and is summarized by:

$$\begin{array}{lll}
 u'>0 & w'>0 & \varepsilon' \text{ is in the Quadrant I} \\
 u'<0 & w'>0 & \varepsilon' \text{ is in the Quadrant II} \\
 u'<0 & w'<0 & \varepsilon' \text{ is in the Quadrant III} \\
 u'>0 & w'<0 & \varepsilon' \text{ is in the Quadrant IV}
 \end{array} \tag{9}$$

For the positive detection of an event, the direction of the instantaneous velocity field is required, as well as a comparison of the instantaneous shear stress relative amplitude with threshold value H:

$$H_{\varepsilon} = \frac{\varepsilon'}{u'w'} \tag{10}$$

The events where the relative shear stress values are lower than threshold value H are called hole events.

Using wavelet multilevel decomposition of the instantaneous signals, we may condition the analysis of the coherent structures to a wavelet frame, by restricting the quadrant analysis to a certain chosen structure scale. Thus, the threshold H definition is conditioned by the scale corresponding to the mode we are working with:

$$H_{\varepsilon|\lambda} = \frac{D_{\lambda,\varepsilon'}}{D_{\lambda,u'} D_{\lambda,w'}} \quad (11)$$

$D_{\lambda,\varepsilon'}$ is the time series of the instantaneous shear stress detail associated with scale λ , defined as:

$$D_{\lambda,\varepsilon'} = D_{\lambda,u'} D_{\lambda,w'} \quad (12)$$

$D_{\lambda,u'}$ and $D_{\lambda,w'}$ are the instantaneous details of the instantaneous streamwise and vertical velocities, associated with scale λ . In Fig. 6a we show a plot of all the velocity events in the $\{x-z\}$ plane restricted to the wavelet frame defined by the most energetic scale ($\lambda=0.43$ s or $\Lambda=0.10$ m, decomposition mode $m=3$). In Fig. 6b we present the respective quadrant distribution of the shear stress as a function of threshold H .

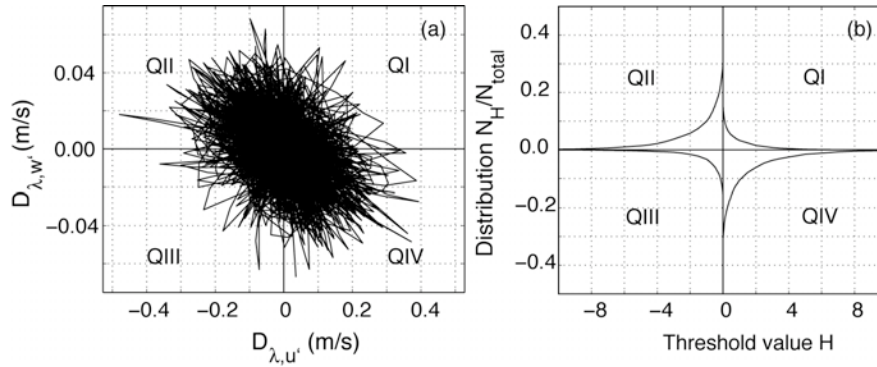


Figure 6 – (a) $\{x-z\}$ plane representation of the partial streamwise velocity time series associated with the most energetic scale ($\lambda=0.43$ s or $\Lambda=0.10$ m). (b) Quadrant repartition of the relative Reynolds shear stress in plane $\{x-z\}$, associated with the most energetic structure scale ($\lambda=0.43$ s or $\Lambda=0.10$ m), as a function of the threshold H .

Negative shear events commonly called ejections and sweeps (Nezu and Nakagawa 1993) and found in QII and QIV are predominant, as confirmed by both plots in Fig. 6. As shown, using wavelet multilevel decomposition the event distribution can be conditioned by a chosen scale range in addition to the analysis of the structure contribution to the flow energy content.

4.6 Wavelet-frame threshold and cross-correlation conditional sampling

The wavelet multiresolution analysis allows conditioning the coherent structure analysis to a determined scale range defined by each of the decomposition modes. In this section we present a conditional sampling technique which combined with the single-point wavelet frame-based structure detection, permits to reconstruct a normalized “typical” turbulent coherent structure. We continue the analysis of $\{x-z\}$ coherent structures corresponding to the most energetic scale previously determined, $\lambda=0.43$ s or $\Lambda=0.10$ m.

We detected coherent structures belonging to the QII (ejections), where the instantaneous shear stress values corresponding to mode 3 (D_3) are above the threshold level of $H_{\varepsilon'}|\lambda=0.43}=5$. All together, 46 events were found in the time series $D_{\lambda=0.43,\varepsilon'}$. Under these conditions, an event occurs in average every 4.60 s during the measuring period (211 s). It is now possible to define a time window around the detected

structures in a determined wavelet frame by isolating structures of the same scale in the complete velocity time signal. A window is centred at the location of the instantaneous shear event detected as relevant (t_e). Its range ($t_e \pm \Delta t_e$) is defined by the window parameter ξ as follows:

$$\Delta t_e = \frac{\xi}{2} \lambda \quad (13)$$

The window parameter ξ represents the actual size of the window. For a window parameter of $\xi=2.2$, we present in Fig. 7 all QII conditionally sampled events in the data time series of the instantaneous streamwise, vertical and spanwise velocity ($v_i' |_{\xi=2.2}$) and the corresponding windowed composite average ($\tilde{v}_i' |_{\xi=2.2}$).

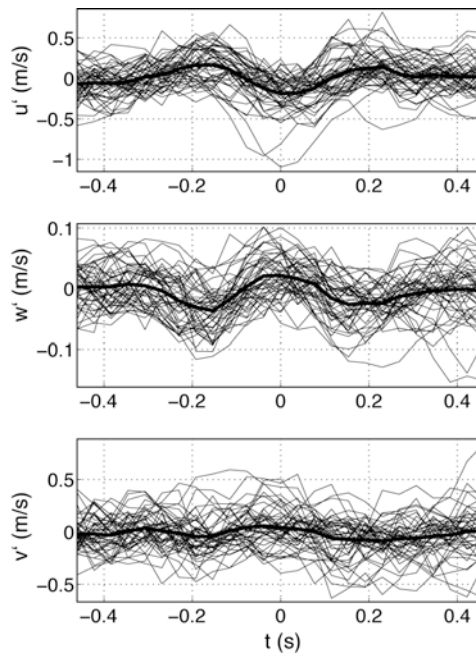


Figure 7 – Instantaneous velocity data ($v_i' |_{\xi=2.2}$) and composite average ($\tilde{v}_i' |_{\xi=2.2}$, thickest line) corresponding to 46 QII coherent events windowed by $\xi=2.2$, restricted to the wavelet frame defined by $\lambda=0.43$ s and conditionally detected by the threshold method with $H_{u',w'} |_{\lambda=0.43}=5$.

Coherence exists between the sampled events in the three Cartesian components. Before and after the occurrence of the detected ejection ($t_e=0$ s), lower amplitude sweeps occur (u' and w' fields). Normally two sweeps are associated with the detected ejections, one before and other after. This is a characteristic of the bursting phenomenon. Some in-phase movement is seen in the spanwise velocity data. However, a high degree of scattering around the mean value is found in the individual windowed data series.

The choice for the event reconstruction may be refined with an analysis based on the cross-correlation between the individual data windows. We define a correlation coefficient threshold H_p below which the windowed instantaneous velocity data are rejected as

$$\left\{ \begin{array}{l} \rho_{\tilde{v}_i|_{\xi}, v_i|_{\xi}} = \frac{C_{\tilde{v}_i|_{\xi}, v_i|_{\xi}}}{\sigma_{\tilde{v}_i|_{\xi}} \sigma_{v_i|_{\xi}}} \\ \text{if } \rho_{\tilde{v}_i|_{\xi}, v_i|_{\xi}} < H_{\rho}, v_i|_{\xi} \text{ is rejected} \end{array} \right. \quad (14)$$

$\rho_{\tilde{v}_i|_{\xi}, v_i|_{\xi}}$ is the correlation coefficient between a windowed instantaneous velocity data ($v_i|_{\xi}$) and the composite average within the window ($\tilde{v}_i|_{\xi}$); $C_{\tilde{v}_i|_{\xi}, v_i|_{\xi}}$ is the covariance between $\tilde{v}_i|_{\xi}$ and $v_i|_{\xi}$; $\sigma_{\tilde{v}_i|_{\xi}}$ and $\sigma_{v_i|_{\xi}}$ are standard deviations of $\tilde{v}_i|_{\xi}$ and $v_i|_{\xi}$, respectively. Setting $H_{\rho}=0.5$, 20 events were chosen (Fig. 8).

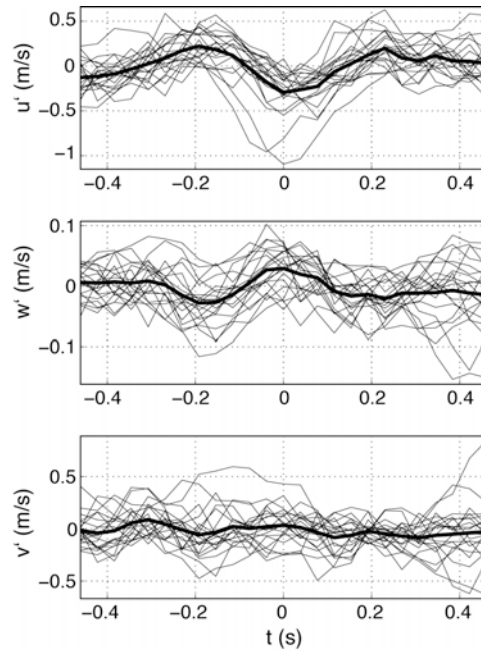


Figure 8 – Instantaneous velocity data ($v_i|_{\xi=2.2}$) and composite average ($\tilde{v}_i|_{\xi=2.2}$, thickest line) corresponding to 20 QII coherent events windowed by $\xi=2.2$, restricted to the wavelet frame defined by $\lambda=0.43$ s, conditionally detected by the threshold method with $H_{|u'w'|_{\lambda=0.43}}=5$ and by the cross-correlation method with $H_{\rho}=0.5$.

Less dispersion is found around the windowed mean velocity series. Proper normalization is required for the representation of the identified coherent events. The time variable was normalized by the scale corresponding to the wavelet frame used as a base to identify the structures (Fig. 9): $t^{\dagger}=t/\lambda$ ($\lambda=0.43$ s); the velocities were normalized by the event amplitude within the time window:

$$v_i^{\dagger} = \frac{v_i|_{\xi=2.2}}{\max(v_i|_{\xi=2.2}) - \min(v_i|_{\xi=2.2})} \quad (15)$$

The existence of sweeps before and after the detected ejection is a coherent event in all selected structures. Thus the detection process allowed isolating a combined sweep-ejection cycle.

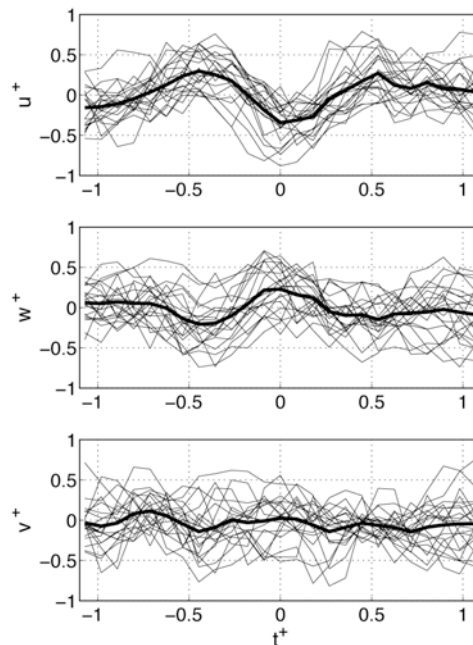


Figure 9 – Instantaneous velocity data ($v_i^+|_{\xi=2.2}$) and composite average ($\tilde{v}_i^+|_{\xi=2.2}$, thickest line) normalized by the local variables λ (time scale of the wavelet frame) and $\max(v_i^+|_{\xi=2.2}) - \min(v_i^+|_{\xi=2.2})$ (event amplitude), corresponding to 20 QII coherent events windowed by $\xi=2.2$, restricted to the wavelet frame defined by $\lambda=0.43$ s, conditionally detected by the threshold method with $H_{u^+w^+|\lambda=0.43}=5$ and by the cross-correlation method with $H_p=0.5$.

5 RECONSTRUCTION OF THE CONDITIONALLY SAMPLED COHERENT STRUCTURE

5.1 Single point, 3D reconstruction

A 3D “typical” coherent structure, normalized by the local event amplitude may be reconstructed by using the composite average of the 20 event detections. Fig. 10 present phase plots of the QII (ejection) structure reconstructed, within the frame defined by the window parameter ξ .

Fig. 11 presents a 3D reconstruction of the normalized coherent structure. The three velocity components present a statistical coherent motion, mainly in the $\{x-z\}$ direction. In Fig. 10a six key moments are identified in the framed process, by chronological order: 1) symbol \circ , when the three instantaneous velocity components have low amplitudes; 2) local maximum amplitude of the u' signal - first sweep (S1); 3) symbol \diamond , before the beginning of the detected ejection when again the three instantaneous velocity components have low amplitudes; 4) corresponds to the detected high amplitude ejection located in the center of the frame (E1); 5) symbol \square , end of the detected ejection, again the

three instantaneous velocity components have low amplitudes; 6) another local maximum of the u' signal amplitude – second sweep (S2).

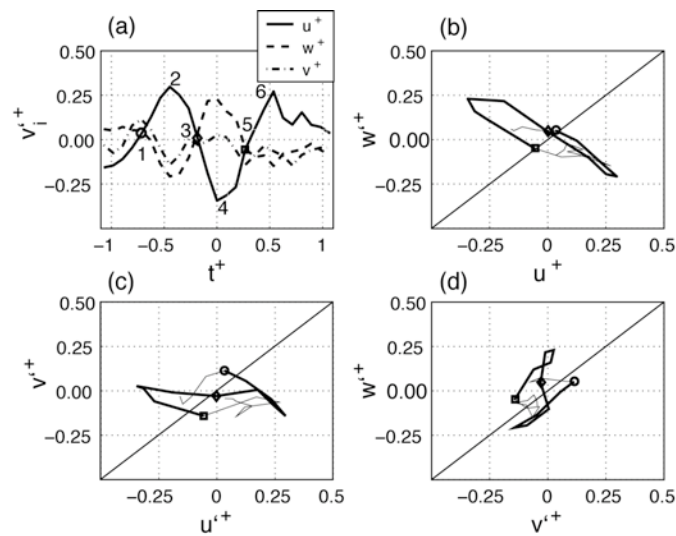


Figure 10 – Reconstruction of the detected coherent structure normalized by the local variables and windowed by $\xi=2.2$. (a) Time plot of the three velocity components. (b) 2D evolution of the coherent structure in the $\{x-z\}$ plane. (c) 2D evolution of the coherent structure in the $\{x-y\}$ plane. (d) 2D evolution of the coherent structure in the $\{y-z\}$ plane. \circ and \square represent the beginning and the end of the sweep-ejection cycle, and \diamond the beginning of the detected ejection.

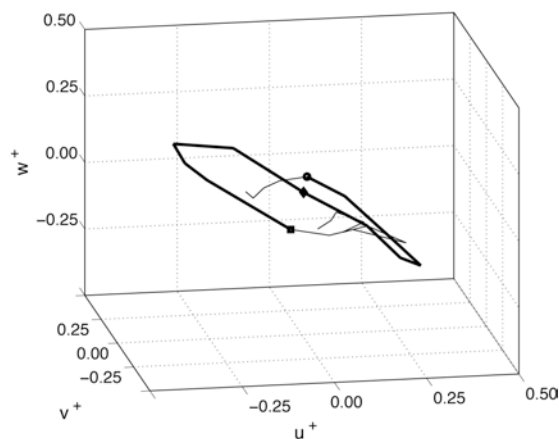


Figure 11 – 3D Reconstruction of the detected coherent structure ejection (QII event) normalized by the local variables and windowed by $\xi=2.2$.

Moments 1, 3 and 5 may be called “stop” points, where the three velocity components have lower amplitudes and roughly the same value. Figures 10b, 10c and 11 show that, although the three components have independent paths in the time evolution, they all seem to converge towards values

close to zero at the end of each sweep or ejection. The spanwise component evolution is in-phase with the vertical component and out-of-phase with the streamwise suggesting an interaction between the three components.

5.2 Analysis of the instantaneous velocity profile

Having reconstructed one sweep-ejection cycle three-dimensionally in a single point, it is now possible to analyze the remaining water column. The same framing and composite averaging methodology is applied to the profile, using the time position detected from the single point analysis (the single point analyzed is considered as the detection point to the velocity profile). In Fig. 12, the mean velocity profiles and the composite-averaged velocity profiles corresponding to the moment $t^+=0$ (center of the detected ejection - E1) are represented together with the instantaneous velocity profiles corresponding to the 20QII detected events.

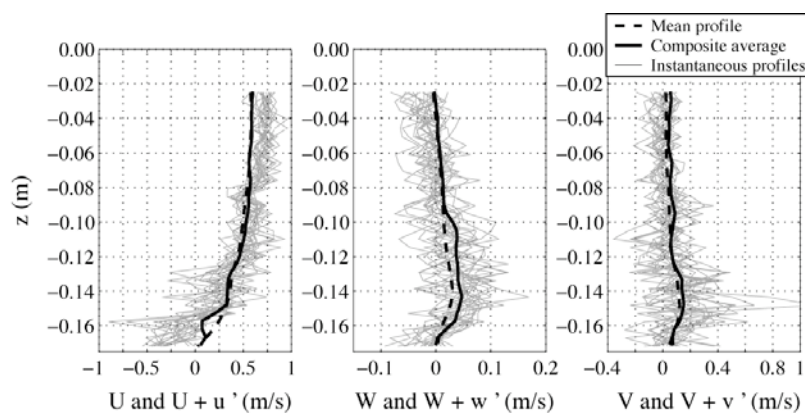


Figure 12 – Mean, instantaneous and composite average of the velocity profiles from the three Cartesian components, for the time step corresponding to $t^+=0$ – E1 (Fig. 10a). The instantaneous profiles correspond to the 20 QII coherent events detected conditionally.

Some coherence between instantaneous velocity profiles is observed. The ejection is not limited to the observed point. It can in fact be observed to some extent in the water column. The negative streamwise velocity variation is limited to the lower layer of the flow, while the positive vertical variation is observed until about half of the water depth. The spanwise velocity has an enhanced variation from the mean value in the positive direction near the detection point. In Fig. 13 the composite averages of the velocity components are represented for the six key moments of the detected cycle indicated in Fig. 10.

The momentary deformation of the velocity profile due to the sweeps and ejections is evident in both the vertical and the streamwise velocity profiles. The streamwise velocity profile acquires its time mean value immediately before and after the events. The events affect the vertical velocity profile to a large extent. For the streamwise component, the effect is more local. This might be explained by the higher streamwise mean momentum that damps the local effects more effectively. Although some in-phase effect between the spanwise and the other components exist, higher deviations from the mean are observed between the sweeps and ejections. Before the sweeps, the spanwise component has its maximum values. During the ejection the spanwise component shows a minimum (confirmed by the phase plots in Figs. 10c and 10d).

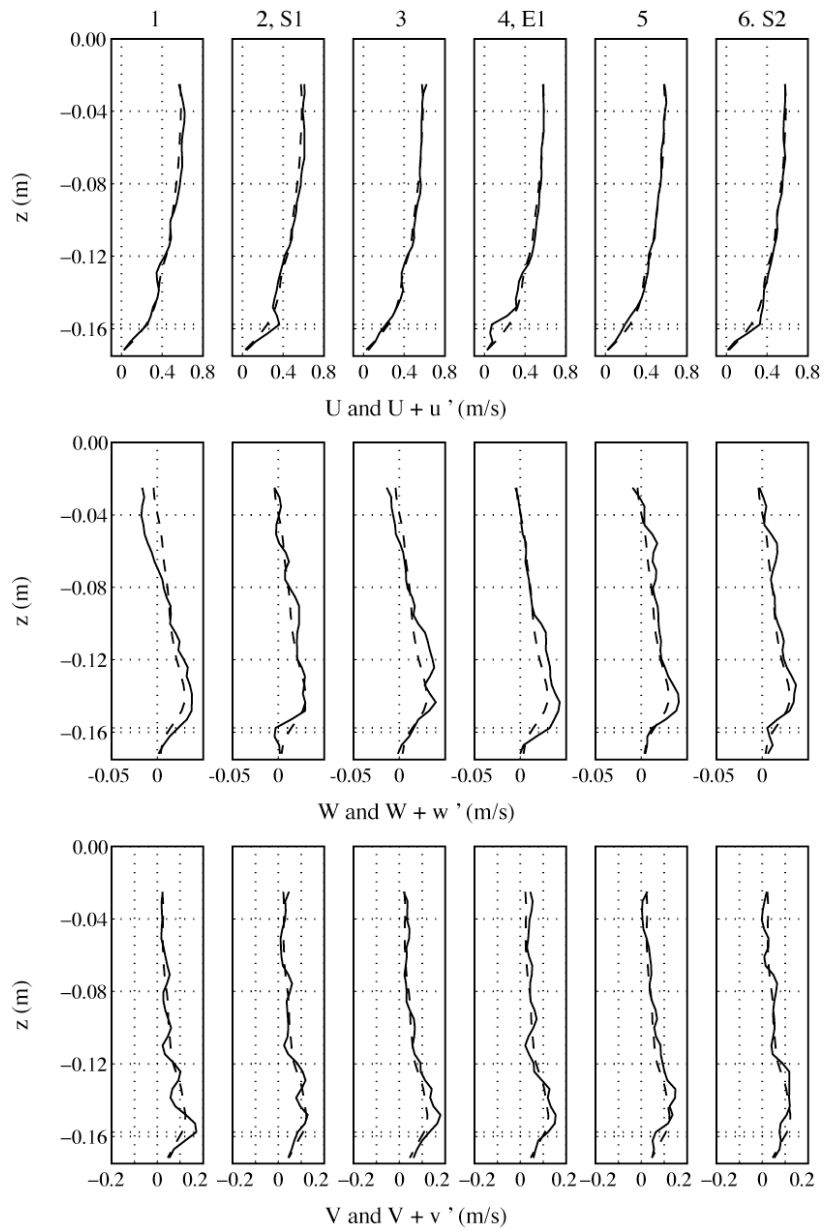


Figure 13 – Mean (dashed line) and composite-averages (continuous lines) of the velocity profiles from the three Cartesian components, corresponding to six “key moments” identified in the 3D time reconstruction of the ejection represented in Fig. 10a (1 to 6 from left to the right).

Fig. 14 shows the time evolution of the composite-average of the three velocity components and of the streamwise plane Reynolds shear stress.

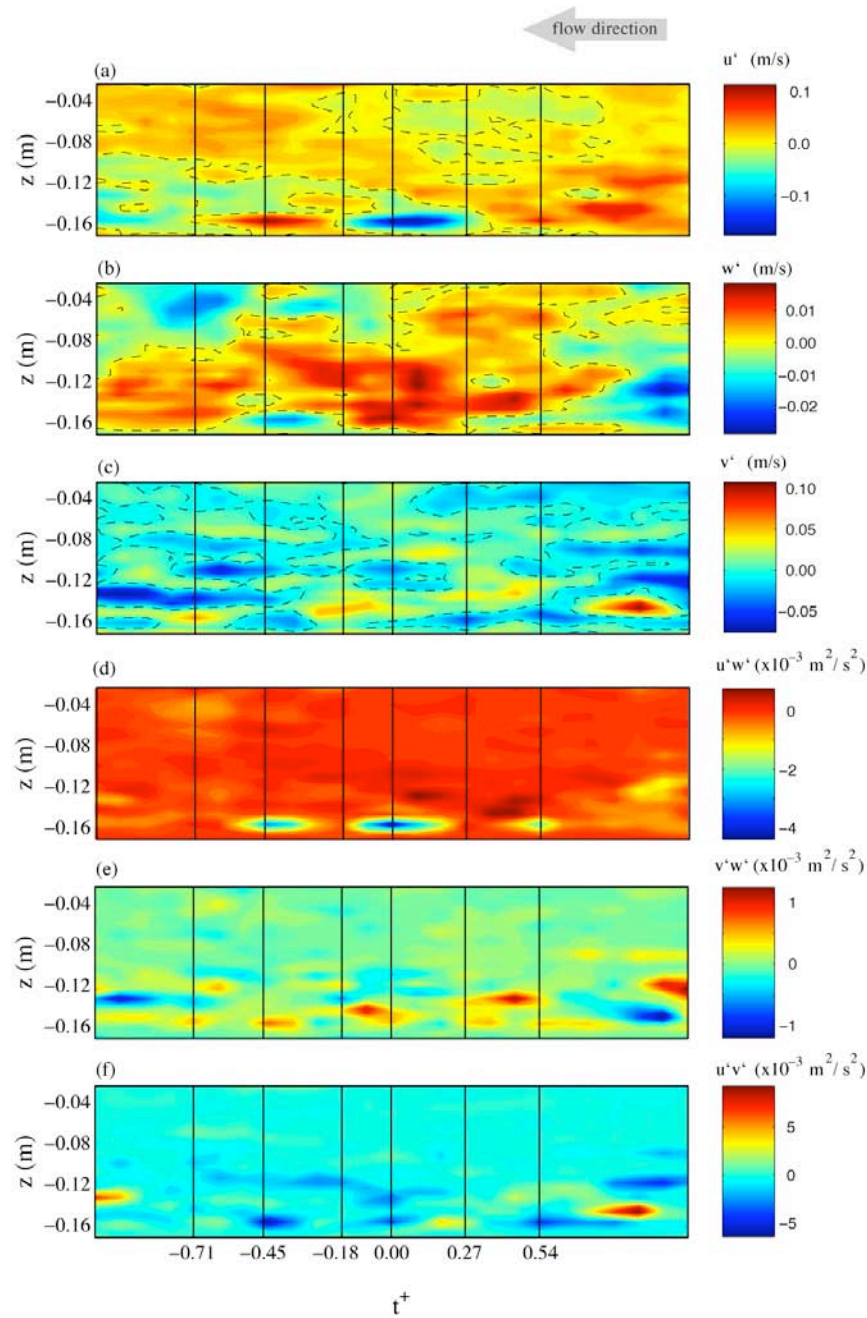


Figure 14 – Instantaneous profiles of the composite average of the three velocity Cartesian components and of the Reynolds shear stresses, within the frame defined by window $\xi=2.2$ (the six key moments are marked on the time axis): (a) streamwise velocity; (b) vertical velocity; (c) spanwise velocity; (d) longitudinal shear stress; (e): transversal shear stress; and (f) horizontal shear stress. The dashed lines (a, b, and c) represent the limit between negative and positive values.

The time plots of the instantaneous streamwise velocity and shear stress profiles clearly show the position of the sweep-ejection-sweep cycle detected previously. In the streamwise fluctuating component (Fig. 14a) we observe that the two main shear events (E1 and S1) are situated above the line

separating negative and positive fluctuations. This division seems to be between two large-scale regions or wedges where the instantaneous velocity is above and below the average (Jackson (1976), Falco (1977), Yalin (1992), Buffin-Bélanger et al. (2000a) and Roy et al. (2004)). Nezu and Nakagawa (1981) referred to these as high- and low-speed regions of the flow as the trigger of the bursting process. The wedge in Fig. 14a may be evidence of the concept described by Adrian et al. (2000b) in which large-scale regions of uniform streamwise momentum nest smaller-scale vortical coherent structures. Although the key moments are also visible in the vertical component, the contour map in Fig. 14b shows widespread variability of the velocity; a local mean trend of the vertical component in the positive direction seems to affect the central area of the window. The spanwise component also shows high variability in the window. The higher variations in the spanwise direction seems to appear before the occurrence of the sweeps. Nevertheless, the spanwise fluctuating velocity is of the same order of magnitude as the streamwise. These observations confirm that the bursting process is highly 3D (Nezu and Nakagawa 1993). In other measurements we observed the occurrence of large-scale motions and indicated that these could be at the origin of the strong anisotropy of the flow (Franca and Lemmin 2004 – A.1). Given their regular time distribution and relatively large duration we call these large-scale motions, Streamwise Velocity Pulsation (SVP) – Franca and Lemmin (2005 – 3.5).

Assuming Taylor's frozen hypothesis, we may compute the spanwise instantaneous vorticity (ω_y') throughout the water depth by:

$$\omega_y'(t_i, z_j) = \frac{u'(t_i, z_{j+1}) - u'(t_i, z_{j-1})}{z_{j+1} - z_{j-1}} - \frac{w'(t_{i+1}, z_j) - w'(t_{i-1}, z_j)}{(t_{i+1} - t_{i-1})u(z_j)} \quad (16)$$

i and j subscripts refer to the position in the grid time/vertical coordinates. Taylor's hypothesis is a good approximation if the mean flow velocity is greater than the turbulent fluctuations ($u'/\bar{u} \ll 1$) (Hinze 1975), which is the case here. The windowed instantaneous spanwise vorticity is presented in Fig. 15 together with the instantaneous velocity vectors from plane $\{x-z\}$.

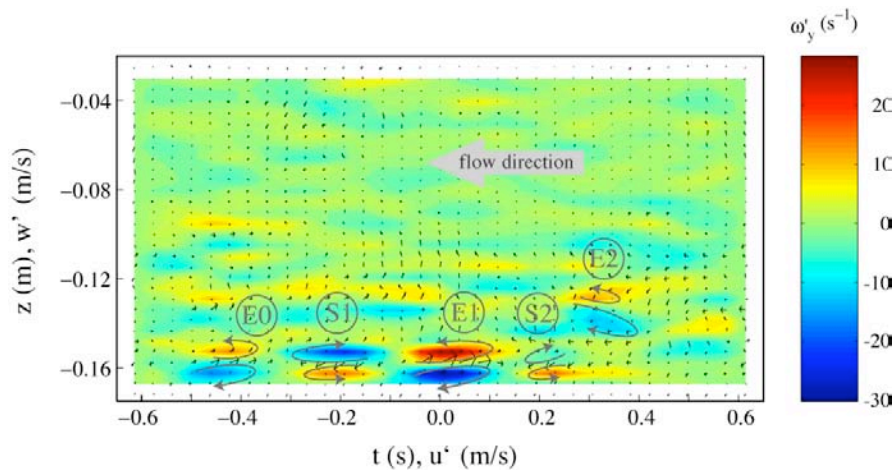


Figure 15 – Instantaneous profile of the spanwise vorticity and instantaneous $\{x-z\}$ velocity vectors, within the frame defined by the parameter $\xi=2.9$. The main vortical movements adjacent to the detected structures are signaled.

In Fig. 15 the observation window was enlarged in order to make two other features visible in the neighbourhood of the detected ejection: a small-scale ejection layer before the first sweep (E0); and a small-scale ejection after the last sweep detached from the lower layer (E2). The visualization of the vorticity

helps to understand the origin of the observed high intensity sweeps and ejections. They are the result of the convergence zones between two adjacent complementary vortical structures where an enhancement of the instantaneous fluid momentum occurs. Fig. 15 presents a sequence of coherent motions with what may be called group or packet behavior, constituted either by sweeps or ejections with adjacent complementary vortical motion (in background): E0) one medium-scale ejection; S1) one large-scale sweep; E1) one large-scale ejection; S2) one sweep; E2) and, apparently related, a third ejection detached from the lower layers of the flow. Fig. 16 shows an interpretation of the observations using as a basis the streamwise velocity profiles. The velocity profiles are represented in the order that they are observed by the ADVP, with the water flowing left to right.

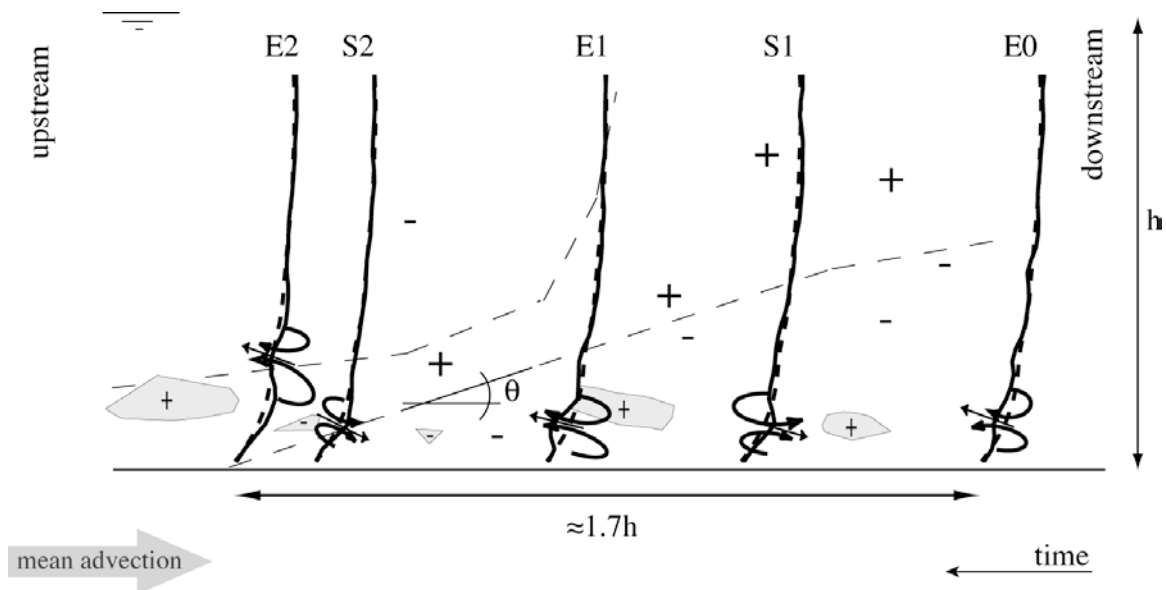


Figure 16 – 3D representation of the sequential packet as it is advected by the mean velocity field, taking as a basis the velocity profile deformation. In the background, in grey, are indicated the regions where the spanwise turbulent velocity is higher; the dashed lines represent the division between high and low speed wedges.

Fig. 16 allows us to further understand the dynamics behind the coherent cycle detected previously. The five profiles in the figure are observed by the ADVP represent the actual sequence advected by the mean flow, from upstream to downstream (left to right).

At the origin of the ejections and sweeps present in the coherent sequence seems to be two adjacent and complementary vortical cells, contributing to the extra momentum seen in those events. The coherent sequence consists of two large-scale and amplitude features: ejection E1 and sweep S1. These seem to constitute marks of a bursting process caused by the passage of a high/low-speed regions division (Nezu and Nakagawa 1981), triggering the sequential process. The observations are not clear, and the Eulerian perspective does not allow us to determine correctly the interdependence between the bursting process and these structures. The interface of the velocity wedges (also observed in Fig. 14a) has a concave shape as described by Nezu and Nakagawa (1981), and an angle with the horizontal of $\theta=18.2^\circ$, which is coherent with the results from Brown and Thomas (1977) $\theta=18^\circ$, Nezu and Nakagawa (1993) $\theta=20^\circ$, and Buffin-Bélanger (2000a) $\theta=15^\circ$ for the near the bed region. An upstream front is also seen in

Fig. 16. Its shape suggests that the fronts do not merge, but instead inflect and diverge in space and time. This characteristic is probably dependent on the vertical velocity gradient.

Bed drag enhances positive vortical structures in the lower layers (Fig. 15). Due to continuity a second, vortex is formed adjacent in an upper layer and both contribute to a momentum boost causing sweep S1. As a reaction, momentum is liberated in the opposite direction from the lower layers upwards into the water column (E1). They are subsequently advected by the mean field and may be captured by a Eulerian observer. We believe that the five observed events are linked by momentum conservation given their complementary vorticity. By continuity, vortical cells form upstream and downstream of the core sequence (S1 and E1), inducing sweep S2 and ejections S0 and S2 due to momentum convergence in between.

The upward trend observed in the vertical mean velocity component (see in Fig. 13) seems to have an uplifting effect on the process. Features S2 and E2 seem to have an uprising movement, and the inclination of the interface between the vortical cells tilts with increasingly slope. The bottom drag influence of the two vortical cells in S2 lessens, resulting in a medium-scale low amplitude sweep. Finally, the last “continuity” response to the structured flow situated in the downstream position (E2) is completely detached from the bottom influence; the medium-scale vortical structure thus has low amplitude and fades away by the background momentum variations.

Spanwise instantaneous components seem to be stronger in between two events in the streamwise plane $\{x-z\}$, and are somehow linked to these structures. This suggests lateral momentum transfer between adjacent ejections and sweeps.

5.3 Effect of the bursting packet in the Reynolds stress tensor

In the Reynolds-averaged Navier Stokes equation (RANS), the stresses due to the turbulent velocity field are included by the Reynolds stress tensor (RST) which for high Reynolds numbers represent the total stress (Hinze 1975):

$$\overline{\tau_{ij}} = -\rho \overline{v'_i v'_j} = - \underbrace{\begin{bmatrix} \overline{\rho u'^2} & \overline{\rho u' v'} & \overline{\rho u' w'} \\ \overline{\rho v' u'} & \overline{\rho v'^2} & \overline{\rho v' w'} \\ \overline{\rho w' u'} & \overline{\rho w' v'} & \overline{\rho w'^2} \end{bmatrix}}_{\text{RST}} \quad (17)$$

ρ is the fluid density. RST is symmetrical. The diagonal terms correspond to normal stresses or turbulent intensities (TI) and the tangential terms to the shear stresses. We analyze the temporary contribution of the sequential group to the different RST components. In Fig. 17 we present the distributions of the RST profiles, total mean and composite-averaged within the window defined in Fig. 15. Both are normalized by the peak values of the respective mean distribution. The composite averaged values are denoted by the symbol \sim .

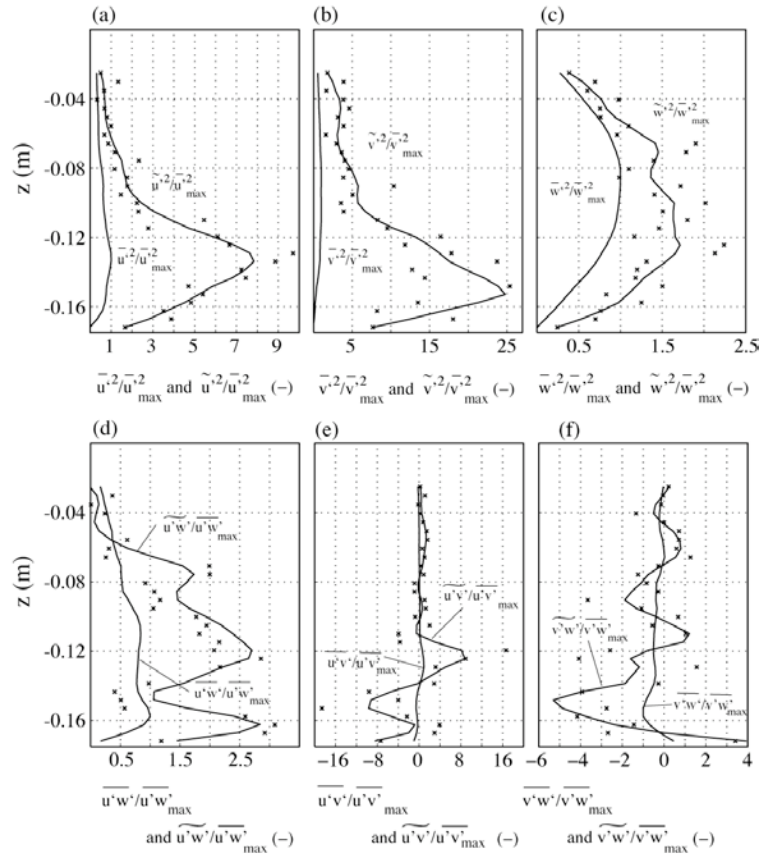


Figure 17 – RST distribution, total mean and composite-averaged TI's and shear stresses profiles, within the frame defined by parameter $\xi=2.9$, both normalized by the local peaks of the total mean distributions: (a) streamwise normal stresses; (b) spanwise normal stresses; (c) vertical normal stresses; (d) longitudinal shear stresses; (e) horizontal shear stresses; (f) transversal shear stresses.

Previous authors suggest that empirical exponential laws universally describe the vertical distribution of TI's in open-channel flows (Nezu and Nakagawa (1993), Kironoto and Graf (1994) and Cardoso et al. (1989)). The present data barely have an exponential distribution, in particular the spanwise and vertical TI profiles. The peak values of the RST components are $\overline{u^2}_{\max}=0.0061 \text{ m}^2\text{s}^{-2}$, $\overline{v^2}_{\max}=0.0015 \text{ m}^2\text{s}^{-2}$, $\overline{w^2}_{\max}=0.0010 \text{ m}^2\text{s}^{-2}$, $\overline{u^1w^1}_{\max}=-0.0012 \text{ m}^2\text{s}^{-2}$, $\overline{u^1v^1}_{\max}=0.0014 \text{ m}^2\text{s}^{-2}$ and $\overline{v^1w^1}_{\max}=0.0005 \text{ m}^2\text{s}^{-2}$. The RST distribution corresponding to the present measurements is analyzed in detail in Franca and Lemmin (2005 – 3.8).

As expected, the TI's are enhanced by the bursting packet sequence. The spanwise normal RST component in particular (Fig. 17b), presents a peak enhancement of about 25 times when compared with the total time mean, suggesting that this direction has a strong component during these events when compared to the background fluctuating field. As to the values of the peak enhancement for both the streamwise (Fig. 17a) and spanwise composite (Fig. 17b) TI's, we have $\frac{\tilde{v}^2_{\max}}{\tilde{u}^2_{\max}} \approx 0.77$. In Fig. 14 we observed that the spanwise velocity fluctuations have the same order magnitude as the streamwise ones. Although on average the turbulence structure of the flow is driven by the streamwise velocity component, strong short time processes in the flow such as this sequential bursting packet are 3D with

important spanwise components. 2D analysis such as the determination of streamwise friction velocities will thus distort the actual estimate of the bottom drag and provide erroneous information on sediment/mass suspension and transport across the boundary layer. These results are in accordance with the observations made in Franca and Lemmin (2005 – 3.4) concerning the inadequacy of the 2D-determined friction velocity in the description of bottom stress. Franca and Lemmin (2005 – 3.8) observed lack of self-similarity of the RST with the friction velocity and stressed the need to determine the predominant momentum transport direction. The vertical TI component distribution (Fig. 17c) is 1 to 2 times the total time averaged value; the increase observed is due to the extra vertical momentum introduced in the flow by the packet process.

The shear stress values indicate the actual drag capacity of the flow. From the peak mean values one observes the importance of both horizontal fluctuations in the profile: the horizontal covariance corresponds to the large Reynolds shear stress. The shear stress distributions are further discussed in Franca and Lemmin (2005 – 3.8). Predictably, the peak composite longitudinal shear stress occurs at the level of the detected x-z events (Fig. 17d). The resulting enhancement is transmitted to the entire profile, except for the adjacent regions corresponding to the center of the vortical cells. At that level an abrupt interruption of the linear trend in the x-z covariance distribution exists. Since the vortices are transversal (y direction), the centers correspond to low correlated $u'w'$ fluctuations. The covariances involving the spanwise component (Figs. 17e and 17.f) have their peak values adjacent to the areas of the packet events. The composite horizontal and longitudinal shear stresses in particular, seem to have a compensatory evolution in the lower layers of the flow. The extra momentum caused by the ejections and sweeps in the $\{x-z\}$ plane, appears to be transmitted to the planes $\{x-y\}$ and $\{x-z\}$ in the adjacent positions.

The shear responsible for the momentum exchanges between the lower and upper regions of the flow must involve the vertical velocity component. The ratio of the composite distribution peaks for the

longitudinal and transversal shear stresses is $\frac{\tilde{v'w'_{\max}}}{\tilde{u'w'_{\max}}} \approx 0.83$. Both are nearly the same order of magnitude.

Therefore the highest intensity of transport/suspension processes may occur along both the streamwise and spanwise directions. These results strengthen the argument given above on the adequacy of the streamwise friction velocity.

5.4 Effect of the bursting packet in the instantaneous TKE budget

The turbulent kinetic energy (TKE) transport equation, also known as the TKE budget, represents the dynamic equilibrium of the energy terms due to the turbulent motion of the flow. For an incompressible flow of an isothermal fluid, the TKE equation is (Schlichting (1968), Monin and Yaglom (1971), Hinze (1975), Chassaing (2000) and Pope (2001)):

$$\frac{D\bar{k}'}{Dt} = P + D - \epsilon \quad (18)$$

\bar{k}' is the temporal mean of the turbulent kinetic energy (TKE – $k' = u'^2 + v'^2 + w'^2$); P, the production rate or generation of TKE by the interaction of Reynolds stress and mean shear; D, the diffusive term; and ϵ , the dissipation rate. The diffusive term includes the turbulent diffusion, the pressure diffusion, the molecular or viscous diffusion and the diffusion of the Reynolds stress tensor. The term D is not considered in the present analysis because it is negligible for high Reynolds number flows. The production and dissipation terms in TKE, P and ϵ , are defined by

$$P = -\overline{v'_i v'_j} \left| \frac{\partial v'_i}{\partial x_j} \right| \quad (19)$$

$$\varepsilon = 2\nu s'_{ij} s'_{ij} \quad (20)$$

s'_{ij} is the strain rate defined as $s'_{ij} = \frac{1}{2} \left(\frac{\partial v'_i}{\partial x_j} + \frac{\partial v'_j}{\partial x_i} \right)$. ADVP measurements do not allow direct access to all the components of (19) and (20), missing the instantaneous spanwise gradients ($\frac{\partial}{\partial y}$). Assuming that $\frac{\partial u}{\partial y} \approx \frac{\partial v}{\partial x}$, $\frac{\partial w}{\partial y} \approx \frac{\partial v}{\partial z}$, and $\frac{\partial v}{\partial y} \approx \frac{\partial w}{\partial z}$, we may estimate the instantaneous values of the production P' and dissipation ε' :

$$P' = -v'_i v'_j \left| \frac{\partial v'_i}{\partial x_j} \right| \quad (21)$$

$$\varepsilon' = 2\nu s'_{ij} s'_{ij} \quad (22)$$

As for the instantaneous vorticity, we may obtain the composite average of the instantaneous production and dissipation, within the same window and under the same conditional sampling conditions (Fig. 15). The streamwise gradients were made using Taylor's frozen hypothesis. The results presented in Fig. 18 are normalized by the window mean value.

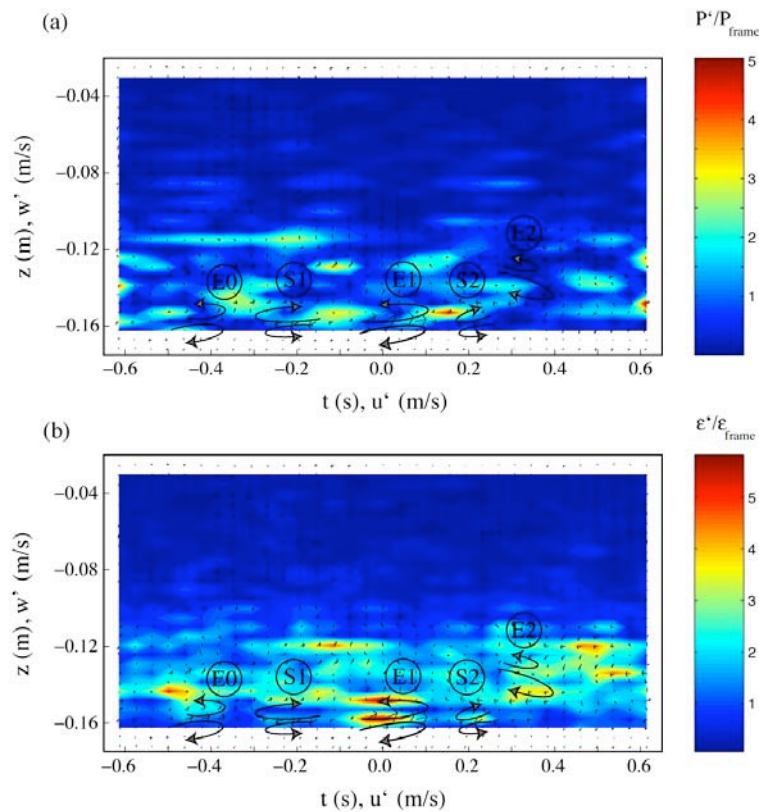


Figure 18 – Instantaneous profile of the relative production and dissipation with instantaneous $\{x-z\}$ velocity vectors, within the window defined by parameter $\xi=2.9$. The main vortical movements and the position of the detected structures are indicated. The instantaneous values are normalized by the mean production and dissipation within the time/space window.

The main turbulent activity is concentrated in the lower half of the flow where the identified structures are located. The dissipation is concentrated at the upper and lower borders of the vortical motion whereas the production is concentrated at the transition zone between ejections and sweeps. The higher values of P' and ε' are associated with the ejection E1. The major production region is observed after the passage of E1 (transition E1 – S2) whereas the major dissipation region is associated with the vortices formed around E1. Nevertheless, dissipation distribution shows little relation with the detected coherent structures packets.

Above $z/h \approx 0.50$ background low amplitude oscillating motions are present but contribute little to TKE dynamics. However, in the production distribution a small enhancement seems to exist correlated with the lower layer coherent structures until roughly $2/3$ of the flow depth. Fig. 19 shows the composite-averaged production \tilde{P} and dissipation $\tilde{\varepsilon}$ profiles in the window defined in Fig. 18.

As stated, the production is enhanced in the lower layer of the flow, where the structures are situated. The bursting packet is responsible for a local increase in the production rate of about two times the mean production peak. The dissipation values are slightly above the peak of the mean dissipation for the whole time record. The observed dissipation is therefore comparable to the basal values, with almost no expression. The coherent structures packets is highly productive, despite their short duration.

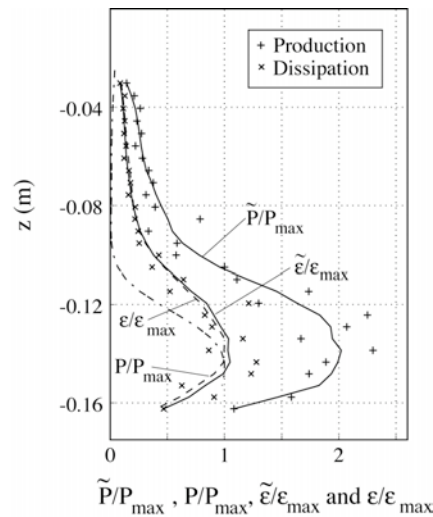


Figure 19 – Composite-averaged production \tilde{P} and dissipation $\tilde{\varepsilon}$, within the frame defined by parameter $\xi=2.9$, normalized by the peak of the mean distributions.

6 TIME DISTRIBUTION OF THE COHERENT STRUCTURES

Knowledge about the intermittency character of the coherent motion in the flow is also important in order to evaluate its effect on mixing and transport processes. In Fig. 20 the time interval between the 46 QII events conditionally first detected by the threshold method (Fig. 7) is indicated in the time series of the instantaneous streamwise velocity of the detection point.

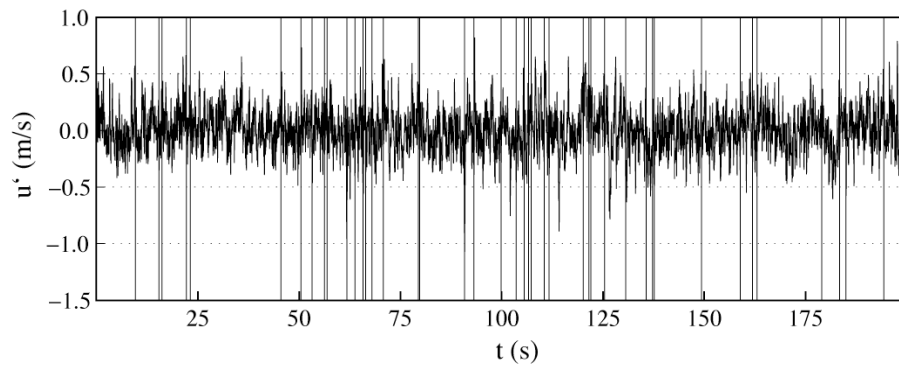


Figure 20 – Time location of the 46 QII detected events, conditionally detected by the wavelet frame defined as $\lambda=0.43$ s by the threshold method with $H_{u'w'}|_{\lambda=0.43}=5$, in the streamwise instantaneous velocity signal of the detection point.

Time distance between consecutive event groups ($T_i=t_{i+1}-t_i$) appears to be random. We thus present the values of T for the 46 QII events (Fig. 21).

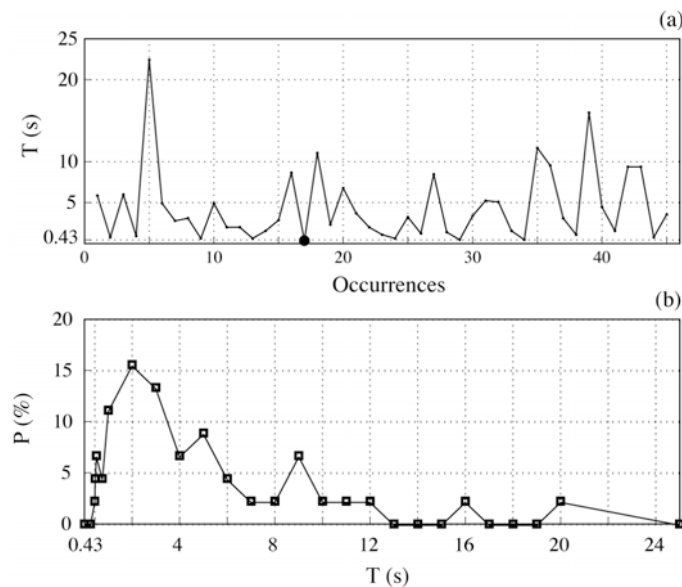


Figure 21 – Time between two consecutive events (T): (a) time between the 46 QII detected events and (b) their distribution.

Although some spurious points exist, the distribution of the time between structures is concentrated in the lower values of the t_i . In Fig. 21a, the distance between consecutive events is only once smaller than the event scale (indicated by a black dot). This means that the detected events and the associated bursting packets are isolated cases and apparently do not interact. Fig. 21b presents the distribution of the time interval between sequential packet distributions T . It has the form of an extreme-type distribution function (Rayleigh for instance), with a maximum roughly corresponding to $T_i=2$ s (≈ 4.6 times the characteristic scale of the events).

The total packet (the 5 events) has a time duration of $t_p \approx 1.2$ s (Fig. 15) which taking into account the number of occurrences corresponds to a persistence in time of $\approx 11.4\%$. The individual vortical cells corresponding to E1 and S1 scale with $t \approx 0.2$ s. If we consider that only the two coherent structures E1 and S1 result from the bursting process, the bursting duration or period of $t_b \approx 0.4$ s is compatible with the large-scale low frequency motion that is part of the bursting process observed by Kirkbride and Ferguson (1995). Taking $T_i = 2$ s as the representative value for the time interval between events, $t_b = 0.4$ s as the total duration of the bursting event, and normalizing both by the friction velocity and the flow depth, we have

$$t_b^+ = \frac{t_b U^*}{h} = 0.08 \quad (23)$$

$$T_i^+ = \frac{T_i U^*}{h} = 0.40 \quad (24)$$

The ratio $t_b/T_i = 0.20$ is equivalent to the one determined by Williams et al. (1989). The bursting Strouhal number corresponding to t_b^+ is $S_b = 12.5$, and an occurrence Strouhal number corresponding to T_i^+ is $S_i = 2.5$. The value of S_i is contained within the range of the SVP Strouhal number defined with the friction velocity $1.54 < S_{SVP}^* < 3.78$ (Franca and Lemmin 2005 – 3.5). The uniform momentum regions containing the bursting packets seem to be due to the SVP phenomenon.

7 CONCLUSIONS

Using ADVP river measurements, we developed a method for identifying and reconstructing coherent structures based on wavelet multiresolution analysis. The coherent structure detection was done by analyzing the turbulent velocity signal at one single point located in the boundary layer. The reconstruction in time and 3D space was carried out using instantaneous velocity profile measurements. The reconstructed signal provides a visualization of a sequential bursting packet of coherent motion.

The single-point instantaneous velocity signal wavelet decomposition was made using a type “D4” Daubechies wavelet function. We observed that eight levels of decomposition were sufficient to describe the energy partition into the different structure scales present in the flow. The length of the most energetic coherent structures corresponds to a macro scale with an order of magnitude between the characteristic bed grain dimension ($\approx D_{84}$) and the water depth (h): its actual value is around $\lambda = 0.43$ - 0.86 s (in length scale, $\Lambda \approx 0.10$ to 0.20 m).

Using the wavelet multilevel decomposition of the signal, a conditional sampling technique was presented that allows the detection and windowing of similar coherent motion in a single point velocity signal. The main steps of the procedure are:

- 1) Wavelet discrete transform of the turbulent velocity signal - multilevel decomposition of the signal into several wavelet-frames;
- 2) Multiresolution decomposition: reconstruction of each wavelet-frame resulting in several low-resolution data series corresponding to different time scales.
- 3) Scale conditional sampling of the decomposed signal with a chosen reference scale (λ).
- 4) Quadrant analysis and threshold-based ($H_{\varepsilon|\lambda}$) sampling of instantaneous shear events conditioned to the chosen scale (λ).
- 5) Windowing and composite averaging of the detected structures with a defined window parameter (ξ).

- 6) Correlation coefficient threshold (H_p) re-sampling: refinement of the windowed events based on the coherence of the different instantaneous events detected within the defined window.
- 7) Normalization and composite averaging of the windowed events: time normalized by the scale λ , and velocities normalized by the events amplitude.

In the present example we used the most energetic motion scale to apply this method ($\lambda=0.43$ s). Negative shear events situated in QII and QIV are predominant for this scale. We restrict our analysis to coherent motion belonging to the QII and to a threshold of $H_{\epsilon|\lambda=0.43}=5$, detecting 46 shear events. After windowing the detected events with a window-parameter $\xi=2.2$, and a refinement using a correlation coefficient threshold of $H_p=0.5$, this number was reduced to 20 events. Under these conditions we reconstructed a composite 3D normalized coherent motion at a single-point using the three components of the instantaneous signal.

The time reconstruction and the phase plots between the three Cartesian components of the reconstruction allowed the following observations:

- The three velocity components present statistical coherent motion.
- A sweep (QIV) was detected before an ejection, with equivalent amplitude and time duration; the compositely reconstructed coherent motion may be a signature of a bursting process.
- A second but subtler sweep (QIV) is observed after the detected ejection.
- Between the sweeps and ejections we observed what may be called a “stop” point where all the three components of the instantaneous velocity simultaneously seem to present low-activity periods.
- The movement inside the window may be defined by six consecutive key moments: 1) “stop” point; 2) first sweep (S1); 3) “stop” point; 4) ejection, located in the centre of the frame (E1); 5) “stop” point; 6) second sweep (S2) (see Fig. 10).

We reconstructed the detected coherent motion in the profile, time-averaging compositely the 3D velocity in the water depth. The instantaneous deformation of the velocity profiles is clear in the vertical and the streamwise components. We observed that the ejection E1 covers a certain scale domain in the water column. The enhancement of the streamwise velocity exists in the lower layer, whereas the vertical component is affected until $z/h \approx 0.50$. The spanwise velocity profiles are not conclusive. Nevertheless, high variations of this component happen before the occurrence of sweeps, suggesting a certain relation with the shear events in plane $\{x-z\}$.

The analysis of the instantaneous vorticity field, the superposition of detected vortical cells with the deformed instantaneous velocity profiles, and an enlargement of the observation window, allowed us to better understand the following characteristics of coherent motion:

- A sequence of three ejections and two sweeps (E0-S1-E1-S2-E1) is formed and may constitute a coherent structure packet. This observation is made with an Eulerian system (ADV), thus the packet was formed somewhere upstream and is convected by the mean velocity field.
- Complementary vortical motion exists between successive events, suggesting a packet activity.
- Ejections and sweeps are the result of extra momentum generated by the convergence of two adjacent and complementary vortical cells.
- The two high amplitude shear events (S1 and E1), probably advected signatures of a bursting process, constitute the core and the origin of the packet.
- The remaining (secondary) events are linked to these by vortical momentum continuity (E0 downstream and S2, E2 upstream).

- Due to rising trend of the flow, the upstream secondary events are lifted and inclined upwards and have low bed-drag influence.
- Lateral momentum transfer seems to exist between adjacent ejections and sweeps.
- Signatures of large-scale motions constituted of high- and low-speed regions travelling downstream are observed and apparently form the trigger for the bursting process that leads to the packet.
- The fronts between high- and low-speed wedges have a concave shape and near the bottom an angle with the horizontal of 18° . Consecutive fronts seem to diverge in space and time in the upper regions of the flow.
- TKE production is concentrated in the transition between events, mainly after the passage of ejection E1.
- The observed packet is highly energetic, and it is responsible for a production of twice the mean peak production during a relatively short period of time.

The distribution of the time between events is studied and we conclude that the observed bursting packets are independent. The time interval between packets has an extreme statistical distribution, where the most probable value corresponds to a Strouhal number of $S_f=2.5$; the bursting Strouhal number is $S_b=12.5$. The bursting Strouhal is of the same order of magnitude as the SVP Strouhal suggesting that the wedges containing the packet described here may correspond to an uniform momentum region of the SVP phenomenon.

Based on the present measurements, further systematic research will be conducted in the 3D measuring grid, in order to develop an overall concept of the influence of bursting events on the transport and mixing processes in rivers similar to the one presented here. A combined analysis of the techniques used by Franca and Lemmin (2005 – 3.5) and the ones herein presented may help to explain the relationship between the SVP and the bursting packets detected. These extremely energetic and rare events are of great importance in the processes described here. Therefore new variables are needed in geophysical modelling in order to take their contribution into account.

ACKNOWLEDGEMENTS

The authors wish to acknowledge the financial support of the Portuguese Science and Technology Foundation (BD 6727/2001) and the Swiss National Science Foundation (2000-063818). We are most grateful to Gene Terray for introducing us to the wavelets analysis.

REFERENCES

- Adrian R.J., Christensen K.T. and Liu Z.C. (2000a), Analysis and interpretation of instantaneous turbulent velocity fields, *Exper. Fluids*, 29, 275-290.
- Adrian R.J., Meinhart C.D. and Tomkins C.D. (2000b), Vortex organization in the outer region of the turbulent boundary layer, *J. Fluid Mech.*, 422, 1-54.
- Antonia R.A. and Atkinson J.D. (1973), High-order moments of Reynolds shear stress fluctuations in a turbulent boundary layer, *J. Fluid Mech.*, 58(3), 581-593.
- Ashworth P.J., Bennett S.J., Best J.L. and McLelland S.J., ed. (1996), *Coherent flow structures in open channels*, John Wiley and Sons Ltd., West Sussex (UK).

- Brown G.L. and Thomas A.S.W. (1977), Large structure in a turbulent boundary layer, *Phys. Fluids*, 20(10), s243-252.
- Buffin-Bélanger T. and Roy A.G. (1998), Effects of a pebble cluster on the turbulent structure of a depth-limited flow in a gravel-bed river, *Geomorphology*, 25, 249-267.
- Buffin-Bélanger T., Roy A.G. and Kirkbride A.D. (2000a), On large-scale flow structures in a gravel-bed river, *Geomorphology*, 32, 417-435.
- Buffin-Bélanger T., Roy A.G. and Kirkbride A.D. (2000b), Vers l'intégration des structures turbulentes de l'écoulement dans la dynamique d'un cours d'eau à lit de graviers, *Géogr. Phys. Et Quaternaire*, 54(1), 105-117.
- Cardoso A.H., Graf W.H. and Gust G. (1989), Uniform flow in a smooth open-channel, *J. Hydr. Res.*, 27(5), 603-616.
- Cellino M. and Lemmin U. (2004), Influence of coherent flow structures on the dynamics of suspended sediment transport in open-channel flow, *J. Hydr. Eng.*, 130(11), 1077-1088.
- Chassaing P. (2000), *Turbulence en mécanique des fluides*, Cépadués-Éditions, Toulouse (France).
- Daubechies I. (1988), Orthonormal bases of compactly supported wavelets, *Comm. Pure Appl. Math.*, XLI, 909-996.
- Dinehart R.L. (1999), Correlative velocity fluctuations over a gravel river bed, *Water Resour. Res.*, 35(2), 569-582.
- Falco R.E. (1977), Coherent motions in the outer region of turbulent boundary layers, *Phys. Fluids*, 20(10), s124-s132.
- Falco R.E. (1979), Comments on "Large structure in a turbulent boundary layer", *Phys. Fluids*, 22(10), 2042.
- Fargé M. (1992), Wavelet transforms and their applications to turbulence. *Ann. Rev. Fluid Mech.*, 24, 395-457.
- Foufoula-Georgiou E. and Kumar P., ed. (1994), *Wavelets in geophysics*. Academic Press, San Diego (USA).
- Franca M.J. and Lemmin U. (2004 – A.1), A field study of extremely rough, three-dimensional river flow, *Proc. 4th Int. Symp. Env. Hyd. - IAHR, Hong Kong (China)*. Appendix A.1.
- Franca M.J. and Lemmin U. (2005 – 2.2), subchapter "Eliminating velocity aliasing in acoustic Doppler velocity profiler data".
- Franca M.J. and Lemmin U. (2005 – 3.4), subchapter "Flow resistance characterization in shallow gravel-bed rivers".
- Franca M.J. and Lemmin U. (2005 – 3.5), subchapter "Streamwise Velocity Pulsation (SVP) in gravel-bed rivers".
- Franca M.J. and Lemmin U. (2005 – 3.7), subchapter "Evaluation of energetic scales in turbulent gravel-bed rivers based on wavelet analysis".
- Franca M.J. and Lemmin U. (2005 – 3.8), subchapter "TKE budget analysis in gravel-bed river flow".
- Hinze J.O. (1975), *Turbulence*, McGraw-Hill, (USA).
- Holmes P., Lumley J.L. and Berkooz G. (1996), *Turbulence, coherent structures, dynamical systems and symmetry*, Cambridge University Press, Cambridge (UK).

- Hurther D. and Lemmin U. (2000a), Shear stress statistics and wall similarity analysis in turbulent boundary layers using a high-resolution 3-D ADVP, *IEEE J. Oc. Eng.*, 25(4), 446-457.
- Hurther D. and Lemmin U. (2000b), A correction method for turbulence measurements with a 3D acoustic Doppler velocity profiler, *J. Atmosph. Ocean. Technol.*, 18, 446-458.
- Hurther D. (2001), 3-D acoustic Doppler velocimetry and turbulence in open-channel flow, PhD dissertation No. 2395, Swiss Federal Institute of Technology, Lausanne.
- Hurther D., Lemmin U. and Blanckaert K. (2002), A field study of transport and mixing in a river using an acoustic Doppler velocity profiler, *Proc. Riverflow 2002*, Louvain-la-Neuve (Belgium).
- Jackson R.G. (1976), Sedimentological and fluid-dynamic implications of the turbulent bursting phenomenon in geophysical flows, *J. Fluid Mech.*, 77(3), 531-560.
- Kantha L.H. and Clayson C.A. (2000), *Small scale processes in geophysical fluid flows*. Academic Press, San Diego (USA).
- Kirkbride A.D. and Ferguson R. (1995), Turbulent flow structure in a gravel-bed river: Markov chain analysis of the fluctuating velocity profile, *Earth Surf. Proc. and Landforms*, 20, 721-733.
- Kironoto B.A. and Graf W.H. (1994), Turbulence characteristics in rough uniform open-channel flow, *Proc. Instn. Civ. Engrs. Wat., Marit. & Energy*, Vol. 106, p. 333-344.
- Kumar P. and Foufoula-Georgiou E. (1997), Wavelet analysis for geophysical applications, *Rev. Geoph.*, 35(4), 385-412.
- Kumar, S., R. Gupta, and S. Banerjee (1998) An experimental investigation of the characteristics of the free surface turbulence in open channel flows, *Phys. Fluids* 10: 437-456.
- Mallat S. (1999), *A wavelet tour of signal processing*. Academic Press, San Diego (USA).
- Métais O. and Lesieur M., ed. (1989), *Turbulence and coherent structures*, Kluwer, Dordrecht (The Netherlands).
- Monin A.S. and Yaglom A.M. (1971), *Statistical Fluid Mechanics: Mechanics of Turbulence - Vol. 1*, The MIT Press, Cambridge (USA).
- Nakagawa H. and Nezu I. (1977). Prediction of the contributions to the Reynolds stress from bursting events in open-channel flows, *J. Fluid Mech.*, 80(1), p. 99.
- Nakagawa H. and Nezu I. (1981), Structure of space-time correlations of bursting phenomena in an open-channel flow, *J. Fluid Mech.*, 104, 1-43.
- Nezu I. and Nakagawa H. (1993), *Turbulence in open-channel flows - IAHR monograph*, A.A. Balkema, Rotterdam (The Netherlands).
- Nikora V. and Goring D. (2000), Flow turbulence over fixed and weakly mobile gravel beds, *J. Hydr. Eng.*, 126(9), 679-690.
- Nikora V. and Goring D. (2002), Fluctuations of suspended sediment concentration and turbulent fluxes in an open-channel flow, *J. Hydr. Eng.*, 128(2), 214-224.
- Pope S.B. (2001), *Turbulent Flows*, Cambridge University Press, Cambridge (UK).
- Rolland T. and Lemmin U., 1997. A two-component acoustic velocity profiler for use in turbulent open-channel flow, *J. Hydr. Res.*, 35(4), p. 545.
- Roy A.G., Buffin-Belanger T., Lamarre H. and Kirkbride A.D. (2004), Size, shape and dynamics of large-scale turbulent flow structures in a gravel-bed river, *J. Fluid Mech.*, 500, 1-27.
- Schlichting H. (1968), *Boundary-layer theory*, McGraw-Hill, (USA).

- Troiani G., Cioffi F. and Casciola C.M. (2004), Free-surface-vorticity interactions in an open channel flow, *J. Hydr. Eng.*, 130(4), 313-323.
- Turner B.J., Leclerc M.Y., Gauthier M., Moore K.E. and Fitzjarrald D.R. (1994), Identification of turbulence structures above a forest canopy using a wavelet transform, *J. Geoph. Res.*, 99(D1), 1919-1926.
- Williams J.J., Thorne P.D. and Heathershaw A.D. (1989), Measurements of turbulence in the benthic boundary layer over a gravel bed, *Sedimentology*, 36, 959-971.
- Wolman M.G. (1954), A method of sampling coarse river-bed material, *Trans. Amer. Geoph. Un.*, 35(6), p. 951.
- Yalin M.S. (1992), *River mechanics*, Pergamon Press Ltd, Exeter (UK).
- Yoshida K. and Nezu I. (2004), Experimental study on air-water interfacial turbulent hydrodynamics and gas transfer in wind-induced open channel-flows, *Proc. 4th Int. Symp. Env. Hyd.*, IAHR, Hong Kong (China).

3.7 EVALUATION OF ENERGETIC SCALES IN TURBULENT GRAVEL-BED RIVERS BASED ON WAVELET ANALYSIS

Based on wavelet multiresolution techniques, the energy partition through the turbulence scales is studied. The distribution curve of energy through the scales and the persistence in time of the most energetic scales are analyzed.

	ABSTRACT	3.7.1
1	INTRODUCTION	3.7.1
2	FIELD STUDY AND INSTRUMENTATION	3.7.2
3	WAVELET BASED ANALYSIS	3.7.3
3.1	Wavelet analysis	3.7.3
3.2	Wavelets multilevel decomposition and multiresolution analysis	3.7.3
4	SINGLE POINT ANALYSIS OF THE ENERGY PARTITION	3.7.4
5	DISTRIBUTION OF THE TURBULENCE SCALES	3.7.7
5.1	Characterization of the energy partition	3.7.7
5.2	Distribution of the most energetic time and length scales (λ_{\max} and Λ_{\max})	3.7.7
5.3	Distribution of the dimensionless energy dispersion by the turbulence scales (σ^+)	3.7.8
5.4	Time distribution of the persistence of the most energetic scales	3.7.9
6	CONCLUSIONS	3.7.10
	ACKNOWLEDGEMENTS	3.7.11
	REFERENCES	3.7.11

EVALUATION OF ENERGETIC SCALES IN TURBULENT GRAVEL-BED RIVERS BASED ON WAVELET ANALYSIS

ABSTRACT

Based on ADV field measurements and recurring to the wavelet multiresolution analysis, we studied the streamwise TKE partition through the eddy scales in a gravel-bed river with low blockage ratio, $h/D_{84}=2.9$. We analyzed monolog, s-shaped and 2xlog profiles which correspond to different velocity distributions in the lower layers. The curve corresponding to the energy distribution through the scales is characterized by the peak value (λ_{\max} or Λ_{\max}), and a dimensionless parameter representing the energy dispersion through the scales (σ^+). Λ_{\max} is situated between the bed grain and the flow depth dimensions. Structures for which $\Lambda_{\max} \gg D_{84}$ contain more than 70% of the energy. The energy content decays rapidly in the small-scale domain. These parameters do not present significant variations within the blending layer of the flow. In the roughness and surface layers however major random deviations occur. σ^+ vary typically between 1 and 3, increasing near the surface. The most energetic scales persist on the average 10 to 20% of the time.

Key-words: turbulence energetic scales; coherent structures; wavelet decomposition

1 INTRODUCTION

Macro-scale organized motion in geophysical flows is responsible for local and strong variations in transport, mixing and gas-transfer processes and has more contribution for these than small-scale background turbulence (Cellino and Lemmin (2004), Kumar et al. (1998), Hurther and Lemmin (2000), Roy et al. (2004), Troiani et al. (2004), and Yoshida and Nezu (2004)). Coherent structures belong to the productive and inertial ranges of the spectral space and are conveyed by the mean flow field. The basic theory of coherent motion is well documented (Hinze (1975), Yalin (1992), Nezu and Nakagawa (1993), Ashworth et al. (1996), Holmes et al. (1998) and Métais and Lesieur ed. (1989) and Chassaing (2000)). The distribution of flow energy by coherent structure scales and the relationship with local geometric conditions are important in the characterization of spreading and convection within the fluid.

Franca (2005 – A.2) and Franca and Lemmin (2005 – 3.4) showed that three types of velocity distribution might be found in shallow macro-rough flows: logarithmic (mono-log), s-shaped and double logarithmic layer (2xlog). The s-shaped profiles are due to the presence of large-scale bed perturbations that inflect the velocity profile. Downstream of the bed perturbation, double boundary layers occur. An inner logarithmic layer is formed near the bottom by the redistribution of the momentum throughout the depth; a second boundary layer is formed due to the upstream wake effect. Mono-log and 2xlog profile flow resistance is determined by riverbed drag, whereas the description of the velocity distribution of 2xlog profiles needs the friction velocity and roughness length of the outer logarithmic layer as parameters. In an intermediate layer of the flow we observed that the shear stress distribution is similar in the measured profiles, independent of the type of profile form. Therefore, the flow may be divided

into three different inviscid layers: 1) the roughness layer ($z < z_{RL} \approx 0.20h$), where the flow is 3D and deviations from a linear shear stress distribution occur; 2) the intermediate blending layer ($z_{RL} \approx 0.30h < z < z_{SL} \approx 0.80h$), where the shear stress distribution is linear and similar in all profiles; and 3) the surface layer ($z > z_{SL} \approx 0.80h$), where the flow is again 3D and deviations from a linear shear stress occur.

The coexistence of the three types of velocity profiles in relatively small areas of the river flow, produces strong local shear zones, and led us to investigate the possible implications in the energetic turbulence scales of the flow. Based on wavelet multiresolution techniques (Fargé 1992), and using ADVP river data, we study the instantaneous velocity signals in order to determine the vertical distribution of the energy partition over the turbulence scales for the three types of profiles. We applied wavelet multilevel decomposition to streamwise instantaneous velocities measured at all points and analyzed the relative contribution of each of the scales corresponding to the decomposition modes in the total energy content of the flow. The distribution curve of the energy through the scales and the persistence in time of the most energetic scales are discussed.

The notation adopted for the Reynolds velocity decomposition is streamwise, $u = \bar{u} + u'$; spanwise, $v = \bar{v} + v'$; vertical, $w = \bar{w} + w'$ ($\bar{\quad}$ is time mean and $'$ is instantaneous value). When referring to $v_i = \bar{v}_i + v_i'$, v is velocity and the subscript i is one of the 3D Cartesian dimensions $\{1,2,3\} = \{x,y,z\}$.

2 FIELD STUDY AND INSTRUMENTATION

The present paper is based on the same data set used by Franca and Lemmin (2005 – 3.4) from the Swiss river Venoge. The main hydraulic characteristics of the river during the measurements are given in Table 1:

Table 1 - Summary of the river flow characteristics.

Discharge	Slope	Mean depth	Width	U	Re	Fr	D ₅₀
(m ³ /s)	%	(m)	(m)	(m/s)	(x10 ⁴)	(-)	(mm)
0.76	0.33	0.20	6.30	0.60	5.9 - 8.7	0.32 - 0.61	68

U is the bulk velocity; Re, the Reynolds number; Fr, the Froude number; D₅₀ the bottom grain size diameter of which 50% of the grain diameters are smaller. The riverbed material grain distribution was determined according to the Wolman (1954) method. Here we use the wavelet multiresolution analysis to evaluate the variation of the turbulence scales in the water column for all 15 profiles. The profiles were divided into three different groups according to the mean velocity profile configuration: logarithmic, s-shaped and double logarithmic (Franca and Lemmin 2005 – 3.4).

The ADVP instrument is described in detail in chapter 2. ADVP allows measuring 3D quasi-instantaneous velocity profiles over the entire depth of the flow in rivers. It is suitable for field and laboratory measurements. A Pulse Repetition Frequency (PRF) of 1666 Hz and a Number of Pulse Pairs (NPP) of 64 were used for the estimate of the Doppler shift, resulting in a sampling frequency of 26 Hz.

3 WAVELET BASED ANALYSIS

3.1 Wavelet analysis

Although wavelet analysis is a relatively new tool, it is potentially useful in geophysical fluid mechanics because a distinct decomposition can be made in time and scale (Kantha and Clayson 2000). Franca and Lemmin (2005 – 3.6) introduced some aspects of wavelet analysis including wavelet continuous and discrete transform, multilevel decomposition and multiresolution analysis in the study of turbulent flows based on Fargé (1992), Fofoula-Georgiou and Kumar (1994), Kumar and Fofoula-Georgiou (1997) and Mallat (1999). Here we only deal with the theory behind the wavelet multilevel decomposition and multiresolution analysis.

3.2 Wavelets multilevel decomposition and multiresolution analysis

In the continuous wavelet transform, the wavelet function is parameterized by the real values of scale λ and time location t . In the discrete transform, the wavelet function $\psi_{m,n}(t)$ is parameterized by the integers m and n . m is an integer defining the scale in the expansion $\lambda = \lambda_0^m$ (where λ_0 is a fixed dilatation step), and n represents the discrete time step ($t = nt_0\lambda_0^m$). The discrete wavelet functions $\psi_{m,n}(t)$ have the form

$$\psi_{m,n}(t) = \frac{1}{\sqrt{\lambda_0^m}} \psi\left(\frac{t - nt_0\lambda_0^m}{\lambda_0^m}\right) \quad (1)$$

In the present study we use the wavelet function of type “D4” (Daubechies 1988). The discrete wavelet transform is defined as

$$\hat{u}_w(m,n) = \frac{1}{\sqrt{\lambda_0^m}} \int_{-\infty}^{+\infty} u(t) \psi\left(\frac{t - nt_0\lambda_0^m}{\lambda_0^m}\right) dt \quad (2)$$

To each of the wavelets, corresponds a wavelet frame, which is characterized by the scale parameter m ($\lambda = \lambda_0^m$); this is called the wavelet multilevel decomposition. The reconstruction formula corresponding to the discrete wavelet transform is given by

$$u(t) = C \sum_{m=-\infty}^{+\infty} \sum_{n=-\infty}^{+\infty} \hat{u}_w(m,n) \psi_{m,n}(t) + \gamma \quad (3)$$

C is a constant, which defines the orthogonal degree of the expansion ($C=1$, orthogonal basis) and also includes the redundancy of the discrete multilevel wavelet transform (Kumar and Fofoula-Georgiou 1997). γ is the residual term. For an orthogonal decomposition we use $C=1$ and $\gamma=0$.

The partial reconstruction of the original signal restricted to a determined m , results in a low-resolution version of our original turbulent signal which corresponds to one wavelet frame scale defined by $\lambda = \lambda_0^m$. The wavelet multiresolution consists of the decomposition of the original turbulent signal into one coarse approximation (the approximation) and several others with a progressively smaller scale resolution (the details associated with the scales present in the signal). The signal can be successively reconstructed by the addition of approximation (S) with consecutive details (D_n) - Fig. 1:

$$S_{m-1}(t) = S_m(t) + D_m(t) \quad (4)$$

The symbol S refers to the successive approximations, and D to the successive details.

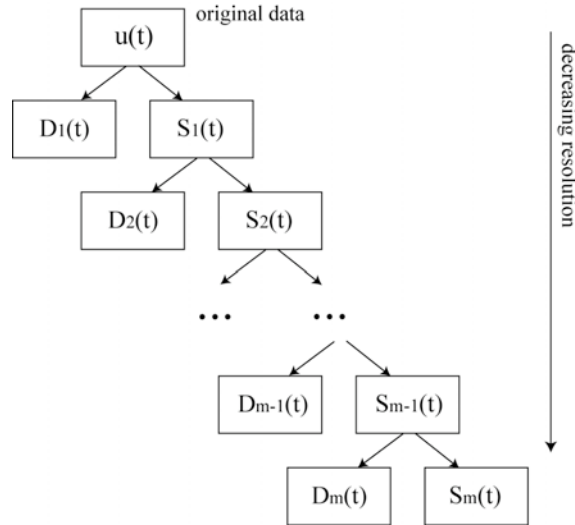


Figure 1 – Schematic representation of the wavelet multiresolution analysis applied to a time series set – successive progression of $S_{m-1}(t) = S_m(t) + D_m(t)$.

Franca and Lemmin (2005 – 3.6) presented the wavelet decomposition into 8 resolution levels and the successive corresponding approximations of the instantaneous streamwise velocity in one single point.

4 SINGLE POINT ANALYSIS OF THE ENERGY PARTITION

Having our signal decomposed into several modes, we may estimate the energy partition over the scales associated with one of the decomposition modes. The contribution of each wavelet frame scale to the streamwise flow energy may be inferred by the relative variance of the instantaneous velocity signal to each mode:

$$E_x(\lambda) = \frac{\overline{D_{\lambda,u'}^2}}{\overline{u'^2}} \quad (5)$$

$E_x(\lambda)$ is the relative energy associated with scale λ and $\overline{D_{\lambda,u'}^2}$ is the variance of the streamwise instantaneous velocity (u') detail associated with scale λ :

$$\overline{D_{\lambda,u'}^2} = \frac{\sum_{n=1}^{N_{time}} D_{\lambda,u'}^2(n)}{N_{time}} \quad (6)$$

n is an integer defining the time step and N_{time} is the total number of time steps (the addition is made over the entire time domain). Fig. 2 shows a typical curve of energy partition over the wavelet scales for a single point analysis presented already in Franca and Lemmin (2005 – 3.6).

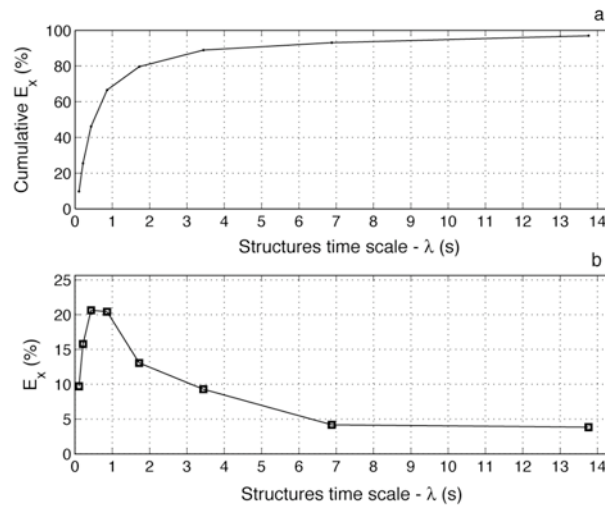


Figure 2 – Partition of the flow energy associated with the streamwise instantaneous velocity field over the different scales of the multi-level decomposition (single point analysis): (a) cumulative and (b) distribution curves.

8-levels of decomposition adequately describe the energy partition over the structure scales present in the flow. In this case the most energetic mode is D_3 , corresponding to scale $\lambda=0.43$ s; the most energetic scale is within the interval $\lambda=0.43-0.86$ s (length scales ranging from $\Lambda=\lambda \bar{u}_{(z=0.158)}=0.10$ to 0.20 m, assuming Taylor's frozen hypothesis). Most of the energy content is found in coherent structures, whose scale is between the representative bed grain dimension ($\approx D_{84}$) and the water depth. These large scales ($\Lambda \approx D_{84}$) contain more than 70% of the energy. The energy content of the signal decays rapidly in the small-scale region. In Fig. 3 we present a reconstruction of the energy content partition by the frequency associated with the coherent structures (represented in terms of power spectra density), using standard FFT techniques.

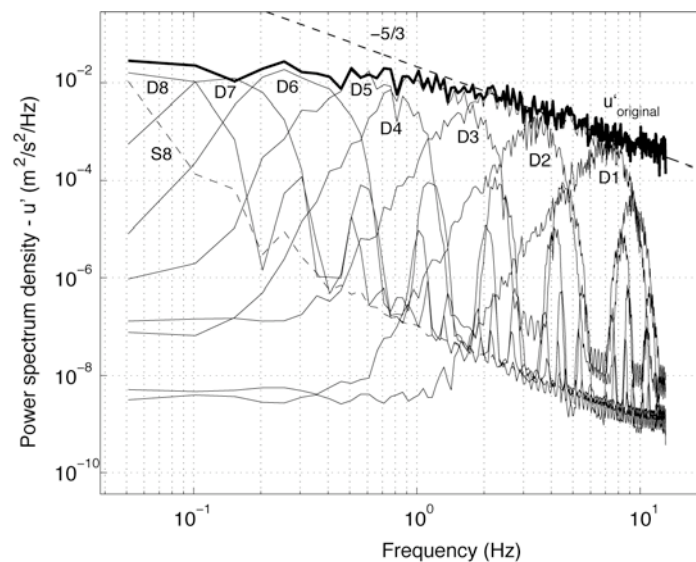


Figure 3 – Reconstruction of the Fourier-based power spectral density of the signal energy with the individual spectra of each of the multi-level decomposition scales for the instantaneous streamwise velocity data (single point analysis). For the calculation of the power spectral density we used the Welch method with 50% overlapping. The data was split into blocks of about 20 s duration.

It can be seen in this figure that the total energy of the signal within the production and the inertia reaches is not lost, and that the wavelet frames represent well the frequency partition of the energy for each scale range. The most energetic scales which belong to the decomposition modes D_4 and D_3 are in the transition region between the production plateau and the inertial $-5/3$ slope subrange.

The integral time scales (τ) for the monolog profile, to which belongs the data in Fig. 3, were calculated in Franca (2005 – A.2). The integral time scale represents the time span with an important correlation between instantaneous velocity values; it is a characteristic time scale for structures advected with the mean flow and captured by the ADVP:

$$\tau = \int_0^{\infty} R_x(t) dt \quad (7)$$

R_x is the autocorrelation function for the time series of the instantaneous streamwise velocity signal obtained by:

$$R_x(t) = \frac{\overline{u'(t_0)u'(t_0+t)}}{u'(t_0)^2} \quad (8)$$

In Fig. 4 we show the autocorrelation function for the instantaneous streamwise velocity signal as a function of the determined time lags, with the wavelet frame scales and the integral time scale indicated.

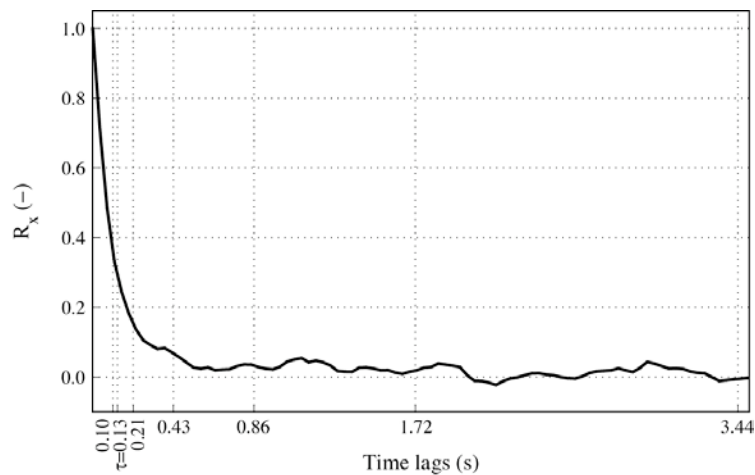


Figure 4 – Autocorrelation function of the instantaneous streamwise velocity signal (single point analysis). Wavelet frame scales corresponding to the signal decomposition and the integral scale τ are indicated.

The integral scale is about 20% of the scale corresponding to the most energetic coherent structures determined by wavelet decomposition. The frequency corresponding to the integral scale ($f_{int}=7.7$ Hz) is beyond the production plateau and clearly situated in the inertial range of the energy density spectrum (Fig. 3). Given the shape of the autocorrelation function (Fig. 4), a relatively small correlation value corresponds to the time lag equivalent to scale $\lambda=0.43$ s. Background small-scales processes are dominant and apparently hide correlations more remote in time. The integral scale determined from the analysis of function R_x may thus not be interpreted as the typical size of a productive structure but rather as the most frequent scale in the turbulent velocity signal. An individual analysis of the different wavelet frames allows separating the energy content of each scale.

5 DISTRIBUTION OF THE TURBULENCE SCALES

5.1 Characterization of the energy partition

It is now possible to apply the method defined previously to estimate the partition of energy over the turbulent scales throughout the 15 measured velocity profiles. Observing a large number of results, we found in all of them that the distribution of the energy by the scales had a shape similar to the one shown in Fig. 2b. We may characterize the energy distribution curve by two representative values: the scale corresponding to the peak value of the energy (λ_{\max}), and the herein called dimensionless energy dispersion by the turbulence scales (σ^+), which is an indicator of the curve shape (or of the variability of the observed energy scales around the most energetic one, Fig. 5):

$$\sigma^+ = \frac{\sigma}{\lambda_{\max}} = \frac{\lambda_{E_{\max}-3\%}^+ - \lambda_{E_{\max}-3\%}^-}{\lambda_{\max}} \quad (9)$$

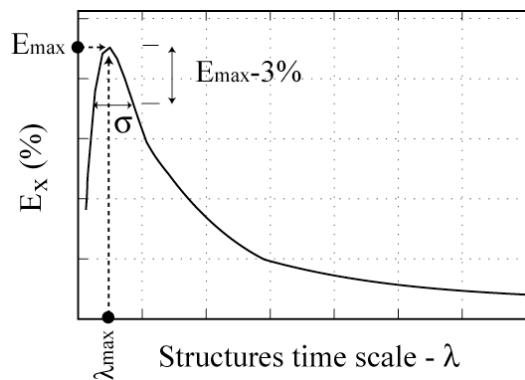


Figure 5 – Definition of the characteristic parameters (λ_{\max} and σ^+) on the analysis of the energy partition over the turbulent scales.

5.2 Distribution of the most energetic time and length scales (λ_{\max} and Λ_{\max})

Fig. 6 shows the vertical distribution of the most energetic time and length scales (λ_{\max} and Λ_{\max}) for all the 15 profiles, divided into three groups: monolog, s, and 2xlog. Length scales were obtained by applying Taylor's frozen hypothesis; Hinze (1975) refers to Taylor's hypothesis as a good approximation when mean flow velocity is large compared to the turbulent fluctuations ($u'/\bar{u} \ll 1$), which is the case.

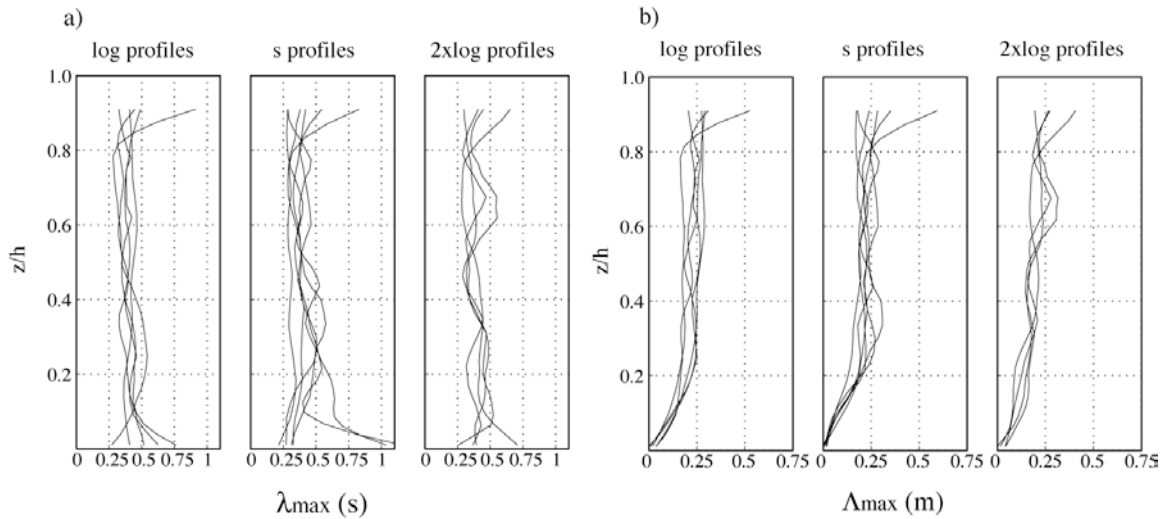


Figure 6 – Distribution of the most energetic scales throughout the water depth for the three profile types (monolog, s and 2xlog): (a) λ_{max} - time scales and (b) Λ_{max} - length scales (by Taylor's frozen hypothesis).

The variation of the time scales throughout the water depth is not related to the profile type, i.e. no significant differences are observed between the three groups. The most energetic time scales in the central part of the water column are on average between 0.25 and 0.50 s. The length scales only show a distortion introduced by the profile shape in the lower layers, converging to nearly constant values beyond $z/h \approx 0.20$. In the 2xlog profiles this convergence happens later due to the presence of the outer boundary layer. Near the surface and near the riverbed, major deviations in the vertical distributions are observed. These are due to local constraints existing in flows with a high variability of the free surface (response to the extreme bed roughness) and randomly distributed rough boundary elements.

Franca and Lemmin (2005 – 3.4) and Franca and Lemmin (2005 – A.3) observed an intermediate blending layer (Wieringa 1976) in the flow between the roughness layer (Nikora and Smart 1997) and the surface layer (or SLOM layer, $z/h > 0.80$). Riverbed and surface boundary effects are smoothed out and merge in one combined and unique drag effect transmitted to this intermediate layer. Apparently, the distribution of the most energetic scales throughout the water column also reflects a blending effect (uniform scales beyond $z/h \approx 0.20$).

5.3 Distribution of the dimensionless energy dispersion by the turbulence scales (σ^+)

Fig. 7 shows the vertical distribution of the dimensionless energy dispersion by the turbulence scales (σ^+) in the three profile groups.

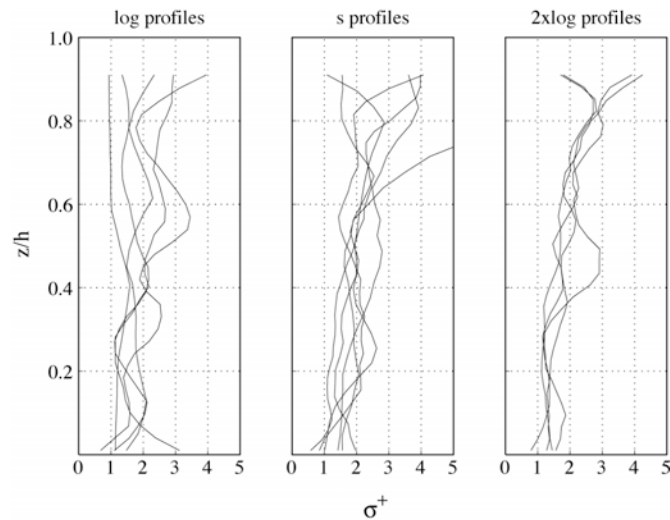


Figure 7 – Variation of the dimensionless energy dispersion by the turbulence scales (σ^+) throughout the water depth for monolog, s-shaped and 2xlog profiles.

The s-shaped profiles show some variation of the energy dispersion coefficient σ^+ distribution. Upwards in the water column however, a larger spreading of the dispersion results exists, indicating a lower uniformity of the turbulence scale distribution. Near the riverbed, the actual length scales are smaller (Fig. 6b). The typical energy partition in Fig. 5 shows that when the higher energy value corresponds to smaller scales, there is less dispersion over the scales.

Generally, an increasing trend towards the surface is observed in the dispersion distribution. S-shaped profiles are due to large-scale bed obstacles that induce the velocity profile inflection in the lower layers. Franca (2005 – A.2) showed that in the regions of the flow where the velocity profile is s-shaped, momentum convergence in the upper layers of the flow is associated with a mean advection towards the surface. According to those results, an average upward convection still exists in the areas corresponding to the 2xlog profiles. This process may thus be responsible for the upward transport of the smaller structures from the lower layers to the surface. It causes higher dispersion of energy through the turbulence scales in the upper layers of the flow. The dispersion coefficients are generally between $\sigma^+=1$ and 3.

In all the cases, major deviations from the mean values are observed once again outside of the intermediate blending layer of the flow.

5.4 Time distribution of the persistence of the most energetic scales

Fig. 8 shows the distribution over the flow depth of the time persistence of the most energetic scales in the three profile groups. The persistence in time (P_λ) of a determined scale (λ) in the turbulent velocity signal is defined as

$$P_\lambda = \frac{f_\lambda}{f_a} \quad (10)$$

where f_λ is the occurrence frequency of coherent motion with scale λ (determined from a Fourier analysis of the corresponding wavelet decomposition detail - D_3), and f_a is the acquisition frequency ($f_a = \text{PRF}/\text{NPP} \approx 26$ Hz).

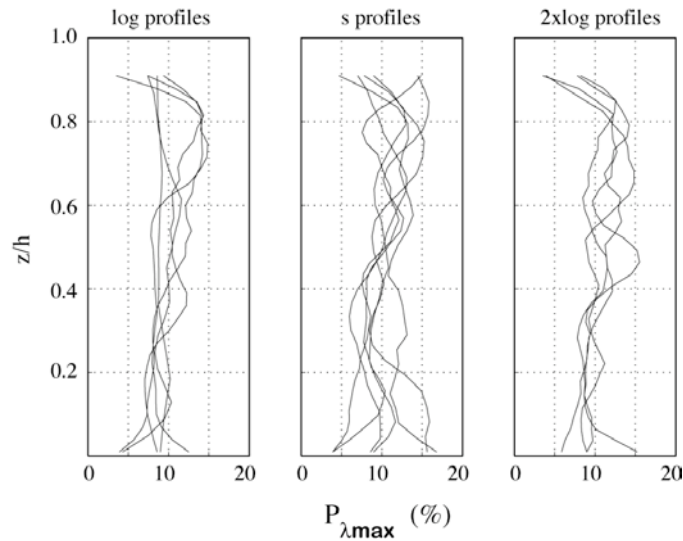


Figure 8 – Distribution of the persistence in time ($P_{\lambda_{\max}}$) of the most energetic turbulent scales throughout the water depth of monolog, s-shaped and 2xlog profiles.

The results of the persistence in time of the most energetic structures for the s profiles show more dispersion. A minor increasing trend in the persistence is noticed from the bottom to $z/h=0.80$. Above this level, the persistence of the scales tends to zero due to the damping effect caused by the water surface. On the average, the most energetic scales persist in the turbulent flow 10 to 20% of the time.

6 CONCLUSIONS

Based on wavelet multiresolution analysis, we studied the turbulent kinetic energy distribution in instantaneous streamwise velocity profiles over turbulence scales. The instantaneous velocity profiles were measured in gravel-bed rivers using the ADVP.

We present an analysis of the kinetic energy scale partition at one single point located in the shear layer of a logarithmic velocity profile. An eight level wavelet decomposition of the turbulent velocity signal, using the Daubechies 'D4' wavelet type, seems to provide enough resolution to describe the energy partition over the turbulent scales. The most energetic scales are found between the bed grain dimension and water depth h . The scales above $\approx D_{84}$ contain more than 70% of the energy; the energy content decays rapidly in the small-scale domain.

Fourier analysis of the energy partition showed that wavelet frames represent the energy partition for each scale range. The most energetic scales belong to the transition between the production plateau and the inertial $-5/3$ slope reach in the energy spectra.

We characterized the energy distribution curve of each level in the flow by the scale corresponding to the energy peak (λ_{\max} or Λ_{\max}), and the dimensionless energy dispersion by turbulence scales (σ^+). Inside

the blending layer a relatively uniform distribution of the scales corresponding to the energy peaks is observed and no significant changes between monolog, s-shaped and 2xlog velocity profiles exist. Major deviations exist in the surface and roughness layers.

In the analysis of the energy dispersion, the following observations can be made: there is an increasing trend in the dispersion values near the surface, especially in the s and 2xlog profiles which might be explained by the momentum advection to the upper layers of the flow existing in the s-shape profiles (momentum concentration due to the flow contraction, Franca (2005 – A.2)). Near the bed, where the energy peak corresponds to smaller scales, the dispersion coefficient decreases. The dispersion coefficients typically vary from $\sigma^+=1$ to 3.

The most energetic scales persist on the average 10 to 20% of the time. Near the water surface, the persistency reduces to zero.

From our results we conclude that the existence of the blending layer between the surface and roughness layers, as discussed by the authors in previous publications, also affects the turbulent scale characteristics throughout the water depth.

ACKNOWLEDGEMENTS

The authors wish to acknowledge the financial support of Portuguese Science and Technology Foundation (BD 6727/2001) and the Swiss National Science Foundation (2000-063818). Acknowledgements are also due to E.A. Terray for introducing us to the wavelet analysis.

REFERENCES

- Ashworth P.J., Bennett S.J., Best J.L. and McLelland S.J., ed. (1996), *Coherent flow structures in open channels*, John Wiley and Sons Ltd., West Sussex (UK).
- Cellino M. and Lemmin U. (2004), Influence of coherent flow structures on the dynamics of suspended sediment transport in open-channel flow, *J. Hydr. Eng.*, 130(11), 1077-1088.
- Chassaing P. (2000), *Turbulence en mécanique des fluides*, Cépadués-Éditions, Toulouse (France).
- Daubechies I. (1988), Orthonormal bases of compactly supported wavelets, *Comm. Pure Appl. Math.*, XLI, 909-996.
- Fargé M. (1992), Wavelet transforms and their applications to turbulence, *Ann. Rev. Fluid Mech.*, 24, 395-457.
- Foufoula-Georgiou E. and Kumar P., ed. (1994), *Wavelet in geophysics*, Academic Press, San Diego (USA).
- Franca M.J. (2005 – A.2), Flow dynamics over a gravel riverbed, *Proc. XXXI IAHR Congress*, Seoul (South Korea). Appendix A.2.
- Franca M.J. and Lemmin U. (2005 – A.3), Cross-Section periodicity of turbulent gravel-bed river flows, *Proc. 4th RCEM. Urbana - Illinois (USA)*. Appendix A.3.
- Franca M.J. and Lemmin U. (2005 – 3.4), subchapter “Flow resistance characterization in shallow gravel-bed rivers”.
- Franca M.J. and Lemmin U. (2005 – 3.6), subchapter “Boundary layer bursting packets associated with high- and low-speed wedges detected through a wavelet multiresolution analysis”.

- Hinze J.O. (1975), *Turbulence*, McGraw-Hill, (USA).
- Holmes P., Lumley J.L. and Berkooz G. (1996), *Turbulence, coherent structures, dynamical systems and symmetry*, Cambridge University Press, Cambridge (UK).
- Hurth D. and Lemmin U. (2000), Shear stress statistics and wall similarity analysis in turbulent boundary layers using a high-resolution 3-D ADVP, *IEEE J. Oc. Eng.*, 25(4), 446-457.
- Kantha L.H. and Clayson C.A. (2000), *Small scale processes in geophysical fluid flows*, Academic Press, San Diego (USA).
- Kumar P. and Foufoula-Georgiou E. (1997), Wavelet analysis for geophysical applications, *Rev. Geoph.*, 35(4), 385-412.
- Kumar, S., R. Gupta, and S. Banerjee (1998) An experimental investigation of the characteristics of the free surface turbulence in open channel flows, *Phys. Fluids* 10: 437-456.
- Mallat S. (1999), *A wavelet tour of signal processing*, Academic Press, San Diego (USA).
- Métais O. and Lesieur M. (ed.) (1989), *Turbulence and coherent structures*, Kluwer, Dordrecht (The Netherlands).
- Nezu I. and Nakagawa H. (1993), *Turbulence in open-channel flows - IAHR monograph*, A.A. Balkema, Rotterdam (The Netherlands).
- Nikora V. and Smart G.M. (1997), Turbulence characteristics of New Zealand gravel-bed rivers, *J. Hydr. Eng.*, 123(9), 764-773.
- Roy A.G., Buffin-Belanger T., Lamarre H. and Kirkbride A.D. (2004), Size, shape and dynamics of large-scale turbulent flow structures in a gravel-bed river, *J. Fluid Mech.*, 500, 1-27.
- Troiani G., Cioffi F. and Casciola C.M. (2004), Free-surface-vorticity interactions in an open channel flow, *J. Hydr. Eng.*, 130(4), 313-323.
- Wieringa, J. (1976), An objective exposure correction method for average wind speeds measured at a sheltered location, *Q. J. R. Meteorol. Soc.*, 102, 241– 253.
- Wolman M.G. (1954), A method of sampling coarse river-bed material, *Trans. Amer. Geoph. Un.*, 35(6), p. 951.
- Yalin M.S. (1992), *River mechanics*, Pergamon Press Ltd, Exeter (UK).
- Yoshida K. and Nezu I. (2004), Experimental study on air-water interfacial turbulent hydrodynamics and gas transfer in wind-induced open channel-flows, *Proc. 4th Int. Symp. Env. Hyd.*, IAHR, Hong Kong (China).

3.8 TKE BUDGET ANALYSIS IN GRAVEL-BED RIVER FLOW

In this subchapter, the study of the mean turbulent structure of gravel-bed river flows is presented, as well as an analysis of the Reynolds stress tensor, eddy viscosity and mixing length, TKE budget (diffusive, productive and dissipative terms), turbulence scales and spectral dynamics.

	ABSTRACT	3.8.1
1	INTRODUCTION	3.8.1
2	FIELD MEASUREMENTS AND INSTRUMENTATION	3.8.2
2.1	River description	3.8.2
2.2	Instrumentation	3.8.3
3	THEORETICAL FRAMEWORK	3.8.3
3.1	Reynolds-averaged equations	3.8.3
3.2	Mixing length and eddy viscosity	3.8.5
3.3	Kolmogorov energy cascade and spectral analysis	3.8.6
4	EXPERIMENTAL RESULTS	3.8.7
4.1	Mean flow characteristics	3.8.7
4.2	Reynolds Stress Tensor: normal stresses	3.8.7
4.3	Reynolds Stress Tensor: shear stresses	3.8.10
4.4	Eddy viscosity and mixing length	3.8.11
4.5	Turbulent Kinetic Energy budget: diffusion terms	3.8.12
4.6	Turbulent Kinetic Energy budget: production and dissipation terms	3.8.13
4.7	Turbulence scales: Kolmogorov (η); Taylor (λ); integral (L); energetic (Λ)	3.8.16
5	CONCLUSIONS	3.8.19
	ACKNOWLEDGEMENTS	3.8.21
	REFERENCES	3.8.21

TKE BUDGET ANALYSIS IN GRAVEL-BED RIVER FLOW

ABSTRACT

River modellers need input on the flow turbulence structure from actual field measurements in order to resolve turbulence equation closures. This paper is based on 3D ADVP gravel-bed river measurements and makes contributions to the Reynolds stress tensor (RST), eddy viscosity and mixing length distributions, TKE budget analysis, turbulence scales, and spectral dynamics. The streamwise turbulent intensity (TI) dominates the TKE, representing between 50 to 80% of the TKE (with maximum at $z/h \approx 0.70$). Spanwise and vertical contributions vary along the flow depth. Empirical formulations given by previous authors to describe RST components are tested and show some limits. The surface and the bottom layers have a strong influence on vertical TI, forcing a convex distribution. Self-similarity of the flow in terms of longitudinal shear stress is only valid in the blending layer. In the roughness layer, the other RST shear stresses acquire more importance and occasionally prevail. Friction velocity u^* estimates must take into account the preferential momentum transport direction. The hypothesis $-\overline{u'w'} = 0.30k$ used for modelling purposes is only valid in the blending layer. The eddy viscosity and mixing length distributions presented atypical forms. Diffusive terms are negligible in the TKE global balance. Thus pseudo-dissipation may be considered equal to the actual dissipation $\tilde{\varepsilon} \approx \varepsilon$. The gradients of the streamwise component have a dominant role in the TKE production. Production mainly happens inside the boundary layer; the dissipation is controlled by the small background structures present throughout the flow depth. Vertical and streamwise production are complementary throughout the flow depth. Production and dissipation follow exponential laws proportional to $e^{-5.1z/h}$ and $e^{-3.9z/h}$, respectively. A catalogue of empirical power laws was made for such turbulence scales as Taylor (λ), Kolmogorov (η), integral (L), energetic (Λ) and mixing length (l_m). The relationship between different scales is also studied. l_m scales with λ until $z/h \approx 0.60$, increasing upwards.

Key-words: gravel-bed rivers; TKE budget; Reynolds stress tensor; turbulence scales

1 INTRODUCTION

Computational fluid mechanics has been widely applied in the simulation of 3D flows with simple geometry and regular bottom roughness. Due to the random variability of the bed elevation caused by large-scale roughness, geophysical flows such as in shallow gravel-bed rivers present additional modelling difficulties.

For low values of the flow-depth to grain-diameter ratio (h/D), the flow is strongly conditioned by the bed geometry formed by the large-scale gravel. Previous studies showed that in these 3D topographically driven flows, self-similarity of the mean turbulence characteristics does not exist in the roughness layer, a restricted lower region of the flow (Nikora and Smart (1997), Smart (1999) and Franca and Lemmin (2005 – 3.4)). The roughness layer is situated below $z_{RL} \approx 0.20h$. Due to the high concentration of coarse elements in the riverbed, a general roughness-wake effect is formed in the flow producing a phenomenon similar to Morris's wake-interference flow (Morris (1959), Kirkbride and Ferguson (1995), Baiamonte and Ferro (1997) and Buffin-Bélanger and Roy (1998)). Nikora et al. (2004) recently presented preliminary simulation results of turbulent flow between the large roughness troughs and tops. Above the roughness layer, and below the surface layer, an intermediate region of the flow exists where self-similarity of the shear stress distribution parameterized with the friction velocity occurs (Franca and Lemmin 2005 – 3.4). This region is similar to the blending layer defined in atmospheric flows (Wieringa 1976). The riverbed roughness and the irregular free surface influences are blended and combined into one single resistance effect, determining a quasi 2D homogeneous shear distribution within the intermediate region of the flow. The interface between the roughness and blending layer of the flow determines the shear resistance.

These features are common in geophysical flows with random bed forms and low blockage ratio h/D , and produce differences in the classic closure methods for turbulence models (Nicholas 2001). One of the main problems in turbulence modelling is the geometric complexity Rodi (1984). Czernuszenko and Rylov (2004) include random bed form effects in turbulence open-channel flow modelling.

The present investigation is based on ADVP field measurements in a gravel-bed river. The paper presents results from a data analysis of Reynolds stress tensor, eddy viscosity and mixing length distributions, TKE budget and turbulence scales distribution.

2 FIELD MEASUREMENTS AND INSTRUMENTATION

2.1 River description

The present measurements were taken during the summer of 2004, in the Swiss river Venoge (canton of Vaud). The instantaneous velocity profiles were measured in a single day under stationary shallow water flow conditions, as confirmed by the discharge data provided by the Swiss Hydrological and Geological Services. The measuring position was located about 90 m upstream of the Moulin de Lussery. The river hydraulic characteristics at the time of the measurements are shown in Table 1.

Table 1 - Summary of the river hydraulic characteristics.

Discharge	Slope	Mean depth	Width	Mean velocity	Re	Fr	D ₅₀	D ₈₄
(m ³ /s)	%	(m)	(m)	(m/s)	(x10 ⁻⁴)	(-)	(mm)	(mm)
0.76	0.33	0.20	6.30	0.60	5.9 - 8.7	0.32 - 0.61	68	89

Re, is the Reynolds number; Fr, the Froude number; D₅₀ and D₈₄, the bed grain size diameter for which 50% and 84% of the grain diameters are smaller. The measurements were made on a 3x5 rectangular horizontal grid (x-y) (Franca and Lemmin, 2005 – 3.4). Fifteen velocity profiles were equally spaced in the spanwise direction with a distance of 10 cm, and in the streamwise direction with a distance of 15 cm. The vertical resolution of the measurements is around 0.5 cm. A measuring grid covering a 3D control volume was defined. The data between all the fifteen positions of the measurement grid were

obtained through 3D interpolation using a cubic spline fitting. The level of the riverbed was determined by the sonar-backscattered response. The profiles were measured for 3.5 min.

2.2 Instrumentation

A deployable ADVP developed at the LHE-EPFL was used for the velocity profile measurements. It allows measuring 3D quasi-instantaneous velocity profiles over the entire depth of the flow in rivers. The ADVP is suitable for field and laboratory measurements. Details on the ADVP are given in chapter 2. A Pulse Repetition Frequency (PRF) of 1666 Hz and a Number of Pulse Pairs (NPP) of 64 were used to estimate the Doppler shift, resulting in a sampling frequency of 26 Hz. A bridge which supported the ADVP instrument allowed the easy displacement of the system across the section and along the river streamwise direction.

3 THEORETICAL FRAMEWORK

3.1 Reynolds-averaged equations

In this subsection we summarize the theoretical developments leading to the TKE budget equation given in detail in Schlichting (1968), Monin and Yaglom (1971), Hinze (1975), Chassaing (2000) and Pope (2001).

To obtain the equation governing turbulent flows where additional stresses are introduced by the fluctuating velocity field, we modify the mean conservation equations by applying the Reynolds decomposition to the variables pressure P , $P_i = \bar{P}_i + P'_i$, and velocity v , $v_i = \bar{v}_i + v'_i$. The subscript i stands for the corresponding 3D Cartesian directions $\{x,y,z\} = \{1,2,3\}$ (1 or x for streamwise, 2 or y for spanwise and 3 or z for vertical). The over-bar is the temporal mean and ' the instantaneous value. For the streamwise, spanwise and vertical velocities we use the symbols u , v and w .

For an incompressible turbulent flow of a Newtonian isothermal fluid, the conservation of mean momentum is expressed by the Reynolds Averaged Navier-Stokes (RANS) equations:

$$\underbrace{\frac{\partial \bar{v}_i}{\partial t} + \bar{v}_j \frac{\partial \bar{v}_i}{\partial x_j}}_{\text{I: total derivative}} = \underbrace{\bar{X}_i}_{\text{II: driving force}} - \underbrace{\frac{1}{\rho} \frac{\partial \bar{P}}{\partial x_i}}_{\text{III: mean pressure}} + \underbrace{\frac{\partial}{\partial x_j} \left(\bar{v} \frac{\partial \bar{v}_i}{\partial x_j} - \overline{v'_i v'_j} \right)}_{\text{IV: viscous and turbulent stresses}} \quad (1)$$

t represents the time variable; x_i , the spatial variable in the direction defined by the index i ; \bar{X}_i (term II), the mean driving force (for open-channel flows corresponds to the gravity term: $g\delta_{i3}$, δ_{i3} is the Kronecker symbol); ν , the fluid kinematic viscosity; ρ , the fluid density. Term I of (1) represents the total derivative of the mean velocity field. Assuming uniform flow conditions, the local term ($\partial/\partial t$) is eliminated. Term III is the stress induced by the mean pressure variation. The last term (IV) represents the viscous (left) and turbulent (right) stresses imposed on the flow. The constraint components due to the pressure gradient and due to viscous and turbulent stresses, can be combined into one tensor ($\bar{\tau}_{ij}$):

$$\frac{\partial \bar{v}_i}{\partial t} + \bar{v}_j \frac{\partial \bar{v}_i}{\partial x_j} = -g\delta_{i3} + \underbrace{\frac{1}{\rho} \frac{\partial}{\partial x_j} \left(-\bar{P} + \mu \frac{\partial \bar{v}_i}{\partial x_j} - \rho \overline{v'_i v'_j} \right)}_{\bar{\tau}_{ij}} \quad (2)$$

μ is the fluid dynamic viscosity ($\mu=\rho\nu$). This equation is similar to Cauchy's equation of motion, except for the element due to the existence of the turbulence field $-\rho v_i v_j$. The pressure gradient was not assessed in the present study; often it may be considered negligible. The viscous dissipation represented by the term $\nu \frac{\partial^2 \bar{v}_i}{\partial x_j \partial x_j}$ is negligible since our measurements were made outside the viscous layer and the flow is fairly turbulent (high Reynolds number). The total stress in the flow may be reduced to $\bar{\tau}_{ij} = -\rho \overline{v'_i v'_j}$, the so-called Reynolds Stress Tensor, RST:

$$\bar{\tau}_{ij} = -\rho \overline{v'_i v'_j} = - \underbrace{\begin{bmatrix} \overline{\rho u'^2} & \overline{\rho u' v'} & \overline{\rho u' w'} \\ \overline{\rho v' u'} & \overline{\rho v'^2} & \overline{\rho v' w'} \\ \overline{\rho w' u'} & \overline{\rho w' v'} & \overline{\rho w'^2} \end{bmatrix}}_{\text{RST}} \quad (3)$$

The RST is symmetric. The diagonal terms correspond to normal stresses and the tangential terms to shear stresses. The total energy (E) balance equation for a flowing fluid may be written considering only the internal energy (E_{int}) and the kinetic energy (E_{kin}):

$$E = E_{\text{int}} + E_{\text{kin}} = E_{\text{int}} + \frac{v_i v_i}{2} = E_{\text{int}} + k \quad (4)$$

In the study of incompressible flow of isothermal fluids, only the evolution of the kinetic energy is considered, making it possible to consider $E=k$. The Reynolds decomposition is also applied to the kinetic energy, $k = \bar{k} + k'$, where \bar{k} is due to the mean and k' to the turbulent velocities. The temporal mean of the turbulent kinetic energy (TKE - \bar{k}') is defined by the trace of RST/2 ρ :

$$2\bar{k}' = \frac{\bar{\tau}_{ii}}{\rho} = \overline{v'_i v'_i} = \overline{(u'^2 + v'^2 + w'^2)} \quad (5)$$

From the RST transport equation it is possible to obtain the TKE transport equation, also known as the TKE budget equation (Gatski 2004):

$$\frac{D\bar{k}'}{Dt} = P + T_D + P_D + V_D - \bar{\epsilon} \quad (6)$$

The TKE budget terms have the following definition (in squared brackets we denote if the term was accessible with our ADVP measurements):

$$\frac{D\bar{k}'}{Dt} = \underbrace{\frac{\partial \bar{k}'}{\partial t}}_{\text{local term}} + \underbrace{v_k \frac{\partial \bar{k}'}{\partial x_k}}_{\text{advective term}} \quad (7)$$

$$P = -\overline{v'_i v'_j} \left| \frac{\partial \bar{v}_i}{\partial x_j} \right| \quad [\text{assessed with the ADVP}] \quad (8)$$

$$T_D = \frac{\partial \overline{v'_j k'}}{\partial x_j} \quad [3^{\text{rd}} \text{ order moment} - \text{limitation of the ADVP}] \quad (9)$$

$$P_D = \frac{1}{\rho} \overline{\frac{\partial v'_j p'}{\partial x_j}} \quad [\text{not assessed}] \quad (10)$$

$$V_D = \nu \overline{\frac{\partial^2 k'}{\partial x_k \partial x_k}} \quad [\text{assessed with the ADVP}] \quad (11)$$

$$\tilde{\varepsilon} = \nu \overline{\frac{\partial v'_i \partial v'_i}{\partial x_j \partial x_j}} = \varepsilon - RST_D \quad [\text{assessed with the ADVP}] \quad (12)$$

$\frac{Dk'}{Dt}$, is the total derivative or the transport of TKE; P, the production or generation of TKE by the interaction Reynolds stress and mean shear; T_D , the turbulent diffusion or TKE advection by the turbulent field; P_D , the pressure diffusion or pressure advection by the turbulent field; V_D , the molecular or viscous diffusion; $\tilde{\varepsilon}$, the pseudo-dissipation, which is the difference between the real dissipation ε and the RST diffusion (RST_D):

$$\varepsilon = 2\nu \overline{s'_{ij} s'_{ij}} \quad [\text{assessed with the ADVP}] \quad (13)$$

$$RST_D = \nu \overline{\frac{\partial^2 v'_i v'_j}{\partial x_j \partial x_j}} \quad [\text{assessed with the ADVP}] \quad (14)$$

s'_{ij} is the strain rate defined as $s'_{ij} = \frac{1}{2} \left(\frac{\partial v'_i}{\partial x_j} + \frac{\partial v'_j}{\partial x_i} \right)$. For simplicity, we replace the diffusive terms in the

TKE budget equation by a single term $D = T_D + P_D + V_D + RST_D$. In the present study we intend to assess the different turbulent terms of the TKE budget using instantaneous velocity profiles measurements made in shallow gravel-bed river flows.

3.2 Mixing length and eddy viscosity

In order to overcome the closure problem due to the presence of the RST in the turbulent RANS (eq. 2) and TKE budget equations (eq. 6), Boussinesq introduced the eddy-viscosity (ν_T) model, also known as the Boussinesq hypothesis (Schlichting 1968). Similar to the laminar flow case, we assume that a relation may be established between shear stress and the mean field through a constant

$$-\overline{v_i v_j} = \nu_T \left(\frac{\partial \overline{v_i}}{\partial x_j} + \frac{\partial \overline{v_j}}{\partial x_i} \right) - \frac{2}{3} \overline{k'} \delta_{ij} \quad (15)$$

ν_i is the apparent, turbulent or eddy viscosity, which is not an actual fluid property but a concept artificially introduced depending on the turbulence flow structure. The second term on the right side of the equation is the sum of the three normal terms of the RST equal to $2\overline{k'}$. In this text we only analyse the eddy viscosity corresponding to the longitudinal shear stress ($\overline{u'w'}$). Due to the three-dimensionality of the studied flow, future investigations should assess a 3D eddy-viscosity. The eddy viscosity can be expressed as the product of a characteristic velocity (U) and a characteristic length scale (l_m)

$$\nu_T = U l_m \quad (16)$$

l_m is currently called the mixing length. From our data, the streamwise variation of the vertical mean velocity is negligible when compared to the vertical gradient of the streamwise velocity ($\frac{\partial \bar{u}}{\partial z} / \frac{\partial \bar{w}}{\partial x} \gg 1$). Taking the friction velocity u^* as the characteristic velocity, Pope (2001) established the following relation between the mixing length l_m and eddy viscosity ν_T :

$$\nu_T = l_m^2 \left| \frac{\partial \bar{u}}{\partial z} \right| \text{ or } l_m = \left(\frac{\nu_T}{\frac{\partial \bar{u}}{\partial z}} \right)^{0.5} \quad (17)$$

The mixing length, as defined in (17), represents a scale of the cross-stream distance travelled by a fluid particle before giving up its momentum (Schlichting (1968) and Kundu and Cohen (2002)).

3.3 Kolmogorov energy cascade and spectral analysis

Kolmogorov's energy cascade theory (Kolmogorov (1941) and Frisch (1995)), describes how energy is transferred from large to small scales: TKE is produced by anisotropic macroscale structures or large eddies in the production range of the spectrum (low wave-numbers); TKE then cascades towards small scale structures in a series of small steps, with no energy change (inertial range of the spectrum); finally, when the eddy structures reach isotropic microscales, on the order of magnitude of the Kolmogorov scale, turbulent energy is dissipated into heat by viscous effects (in the dissipative range of the spectrum). Fig. 1 shows an example of energy cascading presented as eddy-cascade theory by Yalin (1992). A macroturbulent eddy follows a process of successive disintegration in decreasing eddies, in which TKE remains constant until eddies reach the microturbulence length scale where they dissipate due to the viscous stress.

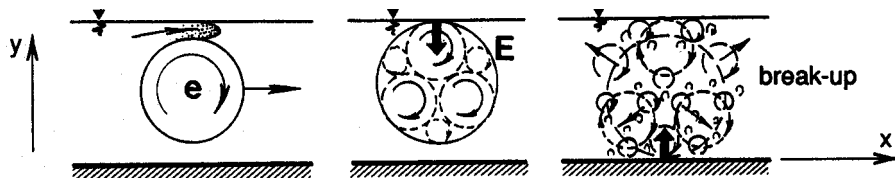


Figure 1 - Example of the cascading theory applied to a large eddy (in Yalin (1992)).

Spectral analysis is applied to turbulence studies, since it allows a better understanding of the scales involved in turbulent processes. Energy cascading is demonstrated in Comte-Bellot and Corrsin (1971) and recently in Katul and Chu (1998). The energy cascade is seen in the velocity, energy and dissipation spectra. The production range is characterized by a peak in the energy spectrum. Macroscale structures associated with this range are of the order of magnitude of the integral scale. In the inertial range energy transfer is described by the power law $S\alpha k^{-5/3}$. The dissipation spectrum has a peak value in the dissipative range characterized by the Kolmogorov scale.

4 EXPERIMENTAL RESULTS

4.1 Mean flow characteristics

Franca (2005 – A.2) and Franca and Lemmin (2005 – 3.4) identified in the present measurements, three kinds of velocity profiles: logarithmic (mono-log), s-type and double logarithmic layer (2xlog). S-shaped profiles are caused by the velocity inflection due to the presence of large-scale bed perturbations. Downstream of the bed perturbation, double boundary-layered profiles occur where the inner logarithmic layer is formed by the redistribution of the momentum throughout the flow depth, whereas the outer boundary layer is due to the upstream wake effect. We verified that the shear stress distribution in an intermediate layer of the flow is similar for the different measured profiles, independent of their type. The flow can be divided into three inviscid layers: 1) the roughness layer, as defined by Nikora and Smart (1997) ($z < z_{RL} \approx 0.20h$); 2) the intermediate blending layer ($z_{RL} \approx 0.20h < z < z_{SL} \approx 0.80h$); and 3) the surface layer ($z > z_{SL} \approx 0.80h$). In the roughness layer the major deviations in the distribution of the mean properties of the flow result from its three-dimensionality. In the intermediate layer, the shear stress distribution is similar in the measured profiles. The flow is again 3D in the surface layer affecting the mean and fluctuating flows. The perturbed surface layer is in response to the large bottom roughness (Franca and Lemmin 2005 – A.3).

4.2 Reynolds Stress Tensor: normal stresses

In this section we analyse the distribution of the three RST normal components corresponding to the velocity variances ($\overline{v_i^2}$), also commonly called turbulent intensities (TI). The normal stresses define the energy content of the flow, since $2\overline{k} = \overline{v_i^2} + \overline{v_i^2}$. In order to understand the turbulence structure of the flow, two analyses for TI terms are presented: TI normalized by the kinetic energy (Fig. 2), and TI normalized by the friction velocity (Fig. 3). The local friction velocities were determined by the eddy-correlation method (Franca and Lemmin 2005 – 3.4), and correspond to the longitudinal shear stress $\overline{u'w'}$ distribution slope in the blending layer.

From Fig. 2a, the main contributor to the TKE is the longitudinal TI ($\overline{u^2}$), representing 50 to 80% of its total value. The turbulence production thus has a strong anisotropy. The occurrence of anisotropic turbulence structures in gravel-bed river flows was documented by other authors (Williams et al. (1989) and Buffin-Bélanger et al. (2000)). The maximum anisotropy is observed near the bottom; it decays to the surface, having a minimum around $z/h \approx 0.70$, increasing again near the surface. The spanwise TI contribution increases constantly from the bottom ($\overline{v^2}/2\overline{k} \approx 0$) to the surface ($\overline{v^2}/2\overline{k} \approx 30\%$). Vertical TI contribution increases from the bottom ($\overline{w^2}/2\overline{k} \approx 0$) to $z/h \approx 0.70$ ($\overline{w^2}/2\overline{k} \approx 20\%$), showing a distribution complementary to the streamwise TI in the region $z/h > 0.20$. Near the bottom, spanwise and vertical TI approach, indicating a tendency to isotropy in the transversal plane $\{y-z\}$.

In Fig. 2b we present the relation between the TI in the streamwise direction and the TI in the other directions. The lines were obtained from the relation between regression curves applied individually to each of the TI distributions. In the intermediate blending layer, the streamwise TI seems to be replaced by the other two components from the bottom to the surface. In the surface layer, the vertical TI decays and the streamwise TI becomes important.

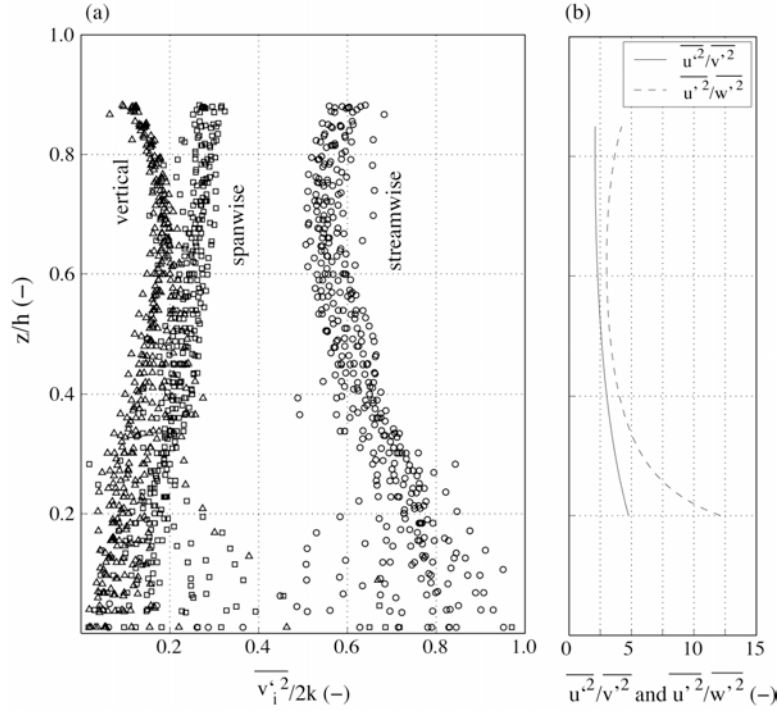


Figure 2 – TI distribution: (a) TI normalized by the TKE ($\overline{v_i'^2}/2k$): ‘ \circ ’ streamwise; ‘ \diamond ’ spanwise; ‘ \triangle ’ vertical; (b) relation between the streamwise TI and the other two components.

Eventually due to large-scale roughness elements present in the lower layer, the spanwise and vertical oscillations are confined, thus resulting in low level contributions to the TKE. Near the bottom we observe major deviations in the TI distribution, mainly below $z/h \approx 0.20$, in the roughness layer. Only in the narrow region between $z/h \approx 0.60$ and $z/h \approx 0.80$ the relative values of TI coincide with the ones suggested by Nezu and Nakagawa (1993) based in empirical exponential TI distributions $\overline{u'^2}/2\overline{k} \approx 0.55$, $\overline{v'^2}/2\overline{k} \approx 0.28$ and $\overline{w'^2}/2\overline{k} \approx 0.17$. The relationship between the different TI components vary throughout the flow depth according to:

$$2.1 < \frac{\overline{u'^2}}{\overline{v'^2}} < 4.8 \quad 3.0 < \frac{\overline{u'^2}}{\overline{w'^2}} < 12.1 \quad (15)$$

The flow is more anisotropic than those observed by Tritico and Hotchkiss (2005) for rivers with high blockage ratios. Both spanwise and vertical TI distribution normalized by the streamwise TI present a concave curve. The evolution of the normalized vertical component presents a parabolic distribution with the curvature apex at $z/h \approx 0.60$. The existence of large-scale uniform streamwise momentum regions pulsating in the flow that has been observed in gravel-bed rivers (Falco (1977), Williams et al. (1989), Kirkbride and Ferguson (1995), Dinehart (1999), Buffin-Bélanger et al. (2000) and Franca and Lemmin (2005 – 3.5)) can be considered an additional cause for the higher contribution of $\overline{u'^2}$.

Several authors presented empirical exponential laws to describe the vertical distribution of TI and TKE in open-channel flows (Nezu and Nakagawa (1993), Kironoto and Graf (1994), and Cardoso et al. (1989)):

$$\frac{v_i'}{u_*'} = D_i \exp(-C_k \frac{z}{h}) \quad (16)$$

$$\frac{\overline{k}'}{u_*'^2} = D_k \exp(-2C_k \frac{z}{h}) \quad (17)$$

D and C are the empirical coefficient and exponent, respectively. In Fig. 3 we compare the actual river data with the relations established by these authors.

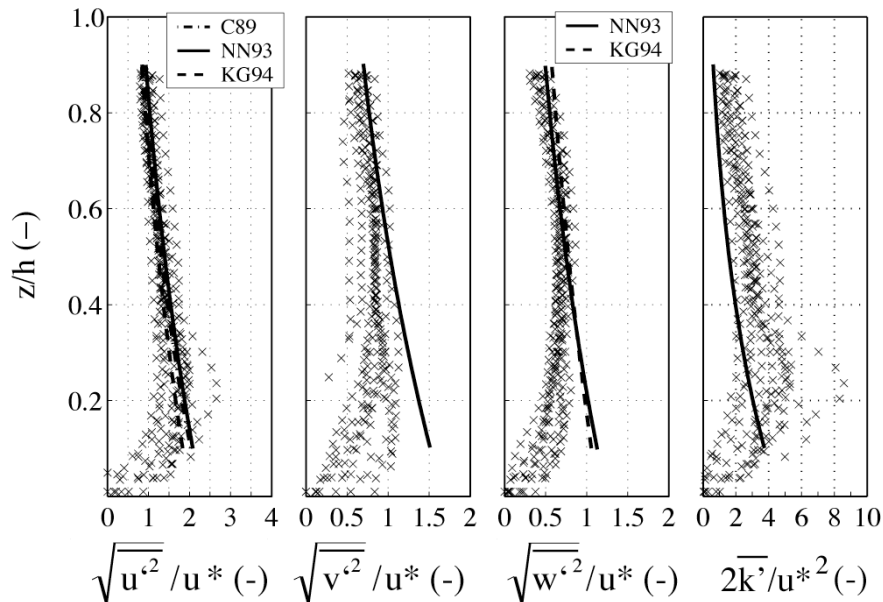


Figure 3 – TI and TKE normalized by the friction velocity ($\sqrt{v_i'^2}/u_*$ and $2k'/u_*'^2$). The continuous lines represent the exponential law adjustments to the measurements as presented in Nezu and Nakagawa (1993).

Near the surface $z/h > 0.60$, observations are of the order of magnitude of the empirical laws (16) and the TI trend is reasonably well described in the streamwise and spanwise cases for $z/h > 0.40$ and $z/h > 0.60$, respectively. However the TI decrease near the bottom, below $z/h \approx 0.20$ and 0.30 for the streamwise and spanwise TI, occurs much earlier than observed by previous authors. From the surface to position $z/h \approx 0.40$, data present the same slope as the empirical curve for the \overline{k}' distribution. The results by Tritico and Hotchkiss (2005) for unobstructed flow are also above the line defined by expression (17). In particular, the vertical TI distribution presents a convex/parabolic shape, different from an exponential law; its maximum is attained roughly in the middle of the water depth. Both the surface and bottom exert a stronger influence on the vertical TI than predicted by empirical laws.

The large roughness in the riverbed induces major changes in the turbulence structure. The TI and TKE values grow from the surface until roughly $z/h = 0.40$. Below this value their distribution is determined by local effects of the randomly distributed bed-forms. The maximum TKE values are situated at $z/h \approx 0.20$, which is the upper limit of the roughness layer (Franca and Lemmin 2005 – 3.4). For larger flow-depth/grain diameter ratios of $h/D_{50} = 35$ and 16, Nicholas (2001) obtained the maximum TKE values at $z/h \approx 0.10$, which is lower than in the present observations. The roughness layer here behaves similarly to the benthic boundary layer (BBL) described for several geophysical flows (Kantha and Clayson 2000) including gravel-bed rivers (Williams et al. 1989).

4.3 Reynolds Stress Tensor: shear stresses

In this section we investigate the distribution of the three RST tangential components ($\overline{v_i'v_j'}$) or shear stresses. Open-channel shear stress is mainly driven by bed shear resulting from the combined effect of the bottom roughness elements and the bed form. In Fig. 4 we plotted the three shear stress components normalized by the friction velocity calculated in Franca and Lemmin (2005 – 3.4) using the eddy-correlation method (Monin and Yanglom 1971). This friction velocity corresponds to the slope of the longitudinal shear stress distribution in the blending layer.

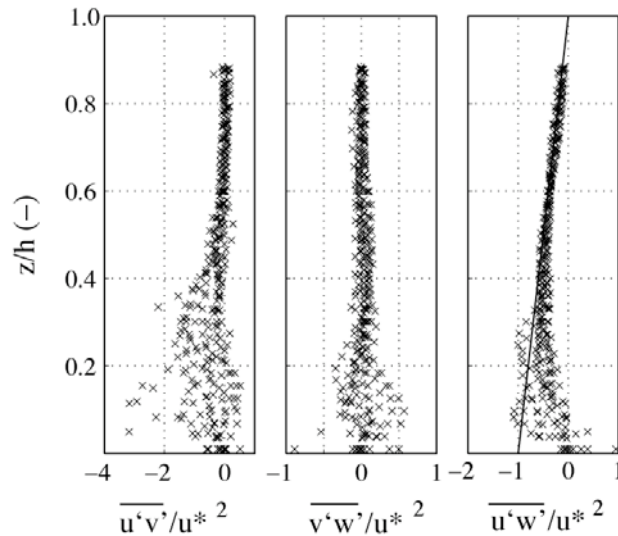


Figure 4 – Shear stresses normalized by the friction velocity ($\overline{v_i'v_j'}/u^{*2}$). The continuous line in the $-\overline{u'w'}/u^{*2}$ graphic represents a hypothetical linear distribution of the longitudinal shear stress, with slope u^* .

As expected, the main shear activity occurs in the lower regions of the flow. The longitudinal shear stress ($\overline{u'w'}$) collapses well with a hypothetical linear distribution above $z/h \approx 0.30$. Below this position it is locally conditioned by the random bed forms. The transversal shear stress distribution ($\overline{v'w'}$) becomes significant below $z/h \approx 0.20$, with maximum values typically around $z/h \approx 0.10$. The distribution of this stress changes randomly and is also locally conditioned by the bed shape. The horizontal shear stress ($\overline{u'v'}$) is important below $z/h \approx 0.40$, occasionally being higher than u^* . Inside the blending layer the surface and bed shear combine into one general effect, and the flow becomes 2D where the $\{x-z\}$ shear dominates the flow resistance. The flow is self-similar only in the blending layer and may be normalized by the variables h and u^* . Near the bed, u^* calculated from the longitudinal shear becomes unsuitable to represent the global shear effect. A friction velocity calculated in the mean momentum direction might be a correct solution corresponding to the self-similarity of the flow. However, the dominant momentum transport direction changes between profiles and within the vertical direction causing additional complexity.

The coefficients $R_k = -\overline{u'w'}/2k$ and $R = \frac{-\overline{u'w'}}{\sqrt{u'^2}\sqrt{w'^2}}$ are indicators for the correlation between the Reynolds shear stress $\overline{u'w'}$ (plane $\{x-z\}$) and the turbulent energy. In Fig. 5, we plot both coefficient

distributions from the data and compare it with the two empirical expressions presented by Nezu and Nakagawa (1993) based on experimental data from several authors:

$$R_k = \frac{-\overline{u'w'}}{2k} = \frac{(1 - z/h) - V_t}{9.56 \exp(-2z/h)} \quad (18)$$

$$R = \frac{-\overline{u'w'}}{\sqrt{u'^2} \sqrt{w'^2}} = \frac{(1 - z/h) - V_t}{2.92 \exp(-2z/h)} \quad (19)$$

V_t is a viscous term that includes the viscous stress in the total shear stress in the flow, negligible outside the viscous layer and in turbulent flows.

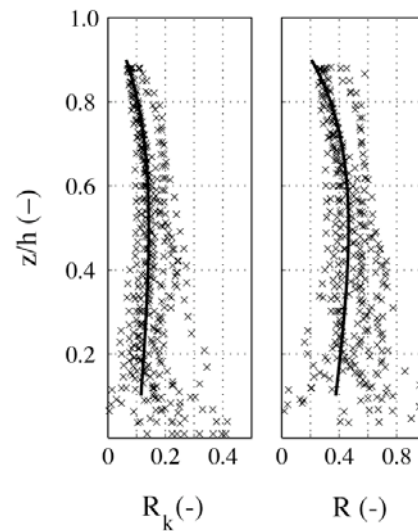


Figure 5 – Correlation factors R_k and R relating shear stress in plane $\{x-z\}$ to normal stress. The continuous lines represent empirical laws (18) and (19) presented by Nezu and Nakagawa (1993).

Both empirical formulas reasonably represent the shear stress correlation coefficient distributions in the upper regions of the flow ($z/h > 0.4$). In the lower layers of the flow, deviations from these theories occur, once again due to the 3D character of the flow. The R coefficient distribution presents more scatter throughout the water depth, increasing near the bottom. Near the surface both coefficients decrease to zero, but not near the bed; Laufer's (1951) R results converge to a similar constant value between 0.4 and 0.5 near the bed.

From the measurements, R_k is around 0.15 in the region $0.30 < z/h < 0.70$, indicating that the assumption $-\overline{u'w'} = 0.30k$ used for modelling purposes (Bradshaw et al. (1967) and Pope (2001)) is only valid within the blending layer. Once again, the abrupt changes of the dominant momentum transport direction condition the correlation between the tangential and the normal components of the RST.

4.4 Eddy viscosity and mixing length

In Fig. 6 we plotted both the normalized eddy viscosity and mixing length distributions. We compare the actual data with the empirical expression presented by Nezu and Nakagawa (1993):

$$v_T = hU^* \frac{\kappa(1 - z/h) - \kappa V_t}{h/z + \pi\Pi \sin(\pi z/h)} \quad (20)$$

Π is the Coles wake parameter defined by these authors to be between 0.0 and 0.2.

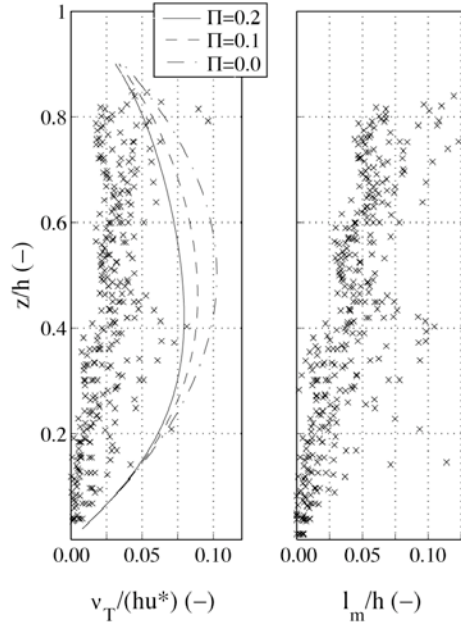


Figure 6 – Eddy viscosity and mixing length normalized by u^* and h . The lines represent the empirical law for eddy viscosity distribution (20) presented by Nezu and Nakagawa (1993).

The calculation of the eddy viscosity and mixing length from the measurements present large scatter, although a general trend allow some observations about Fig. 6. The measured values of eddy viscosity are always below the theoretical curves and their distributions do not present a convex shape as predicted. The empirical law (20) constitutes instead an envelope for the observed data. The values seem to increase towards the surface and do not decrease to zero at $z/h \approx 0.80$ as expected for open-channel flows (Spalart (1988), Nezu and Nakagawa (1993) and Tachie et al. (2004)). The normalized mixing length values present an increasing trend similar to the one obtained by Spalart (1988) with DNS and Tachie et al. (2004) in laboratory flows.

4.5 Turbulent Kinetic Energy budget: diffusion terms

Previously we defined the term $D = T_D + P_D + V_D + RST_D$. Two simplifications in the study of the turbulent dynamic equations were already introduced leading to the simple consideration of the turbulent stresses in the flow. The pressure term P_D is not considered in this investigation. The determination of third order moments is a delicate task when using ADV measurements due to the expansion of phase errors in the conversion of the Doppler signal into the velocity domain. A sufficiently accurate differentiation of the turbulent transport term $\overline{v'_j k'}$ for the evaluation of T_D is thus not possible. In Fig. 7 we present the normalized diffusive terms V_D and RST_D .

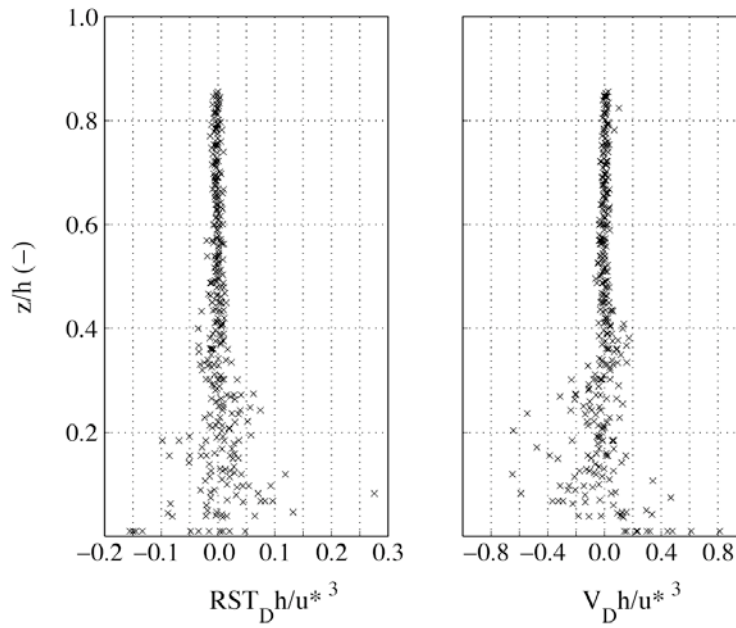


Figure 7 – Distribution of the diffusive terms V_D and RST_D , normalized by u^* and h .

Both diffusive terms remain roughly zero above $z/h \approx 0.40$. Below this, their influence increases in the TKE budget. No apparent trend however is found due to the high scatter of the results. Nevertheless, confirming the simplifications usually introduced for modelling purposes, the influence of the diffusive terms RST_D and V_D is negligible when compared to the production and dissipation terms (see subsection 4.6).

4.6 Turbulent Kinetic Energy budget: production and dissipation terms

In this section we analyze the production P and dissipation ε terms of the TKE equation (6). For sufficiently turbulent flows these two terms dominate turbulence dynamics. The production is due to the action of the mean flow gradients in the RST terms and is responsible for the energy transfer between the mean field and the instantaneous kinetic energy field, acting as a sink ($-P$) in the first field and a source ($+P$) in the second one (Pope 2001). From equation (8), the production may be defined as a 3D vector P_i , where each component relates to the gradient in the corresponding velocity direction

$$P_i = -\overline{v_i' v_k'} \left| \frac{\partial \overline{v_i}}{\partial x_k} \right| \quad (21)$$

Fig. 8 shows the contribution of each flow direction acting against the RST in the generation of TKE.

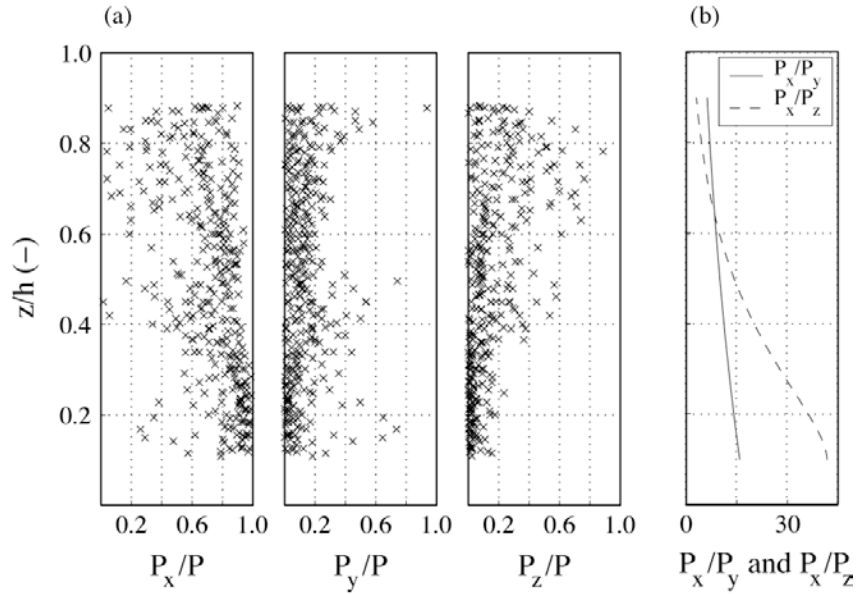


Figure 8 – Components of the production vector in the three Cartesian directions: (a) normalized by the total production P ; (b) relation between the streamwise and the other two components.

As expected from the TI anisotropy (Fig. 2), the streamwise direction prevails in the TKE production, particularly inside the boundary layer where the major mean streamwise velocity gradients occur. Near the surface however, the production is redistributed to the other directions. The spanwise production remains fairly constant throughout the water depth, whereas the vertical production replaces the streamwise as it approaches the surface layer. The vertical contribution seems to have its maximum at $z/h \approx 0.80$, slightly above the occurrence of the maximum TI values in the vertical direction. The relative streamwise production seems to vary on the average between 70% near the surface and 100% near the bottom, whereas the spanwise component between 0% and 10% and the vertical component between 0% and 20%.

In Fig. 8b we present the relationship between the turbulence production in the streamwise and in the other directions. Despite the scatter in Fig. 8a, the lines were obtained from the relation between regression curves. Once again we observe a joint evolution of the vertical and streamwise turbulence characteristics. The relative importance of the productions in both the spanwise and vertical directions relate to the streamwise production according to the following inequalities (Fig. 8b):

$$4.26 < \frac{P_x}{P_y} < 10.69 \quad 2.11 < \frac{P_x}{P_z} < 27.94 \quad (22)$$

ADVP measurements do not allow direct access to the instantaneous gradients which are needed to estimate the turbulence terms of strain rate tensor s'_{ij} . The calculation of dissipation ε may be done by making use of the second Kolmogorov hypothesis that predicts that the equality

$$k_w^{5/3} S_x = C_1 \varepsilon^{2/3} \quad (23)$$

is true in the inertial range (Pope 2001). k_w is the wave number; S_x , the 1D energy spectral density function for the streamwise velocity fluctuations (the main direction responsible for the TKE production, subsection 4.6); and C_1 is a constant approximately equal to 0.50. In Fig. 9 we plotted S_x and the quantity $k_w^{5/3} S_x$ as a function of the wave number. For the calculation of the energy spectral

density the data was divided into blocks of 20 s duration and the Welch method was used with 50% overlapping.

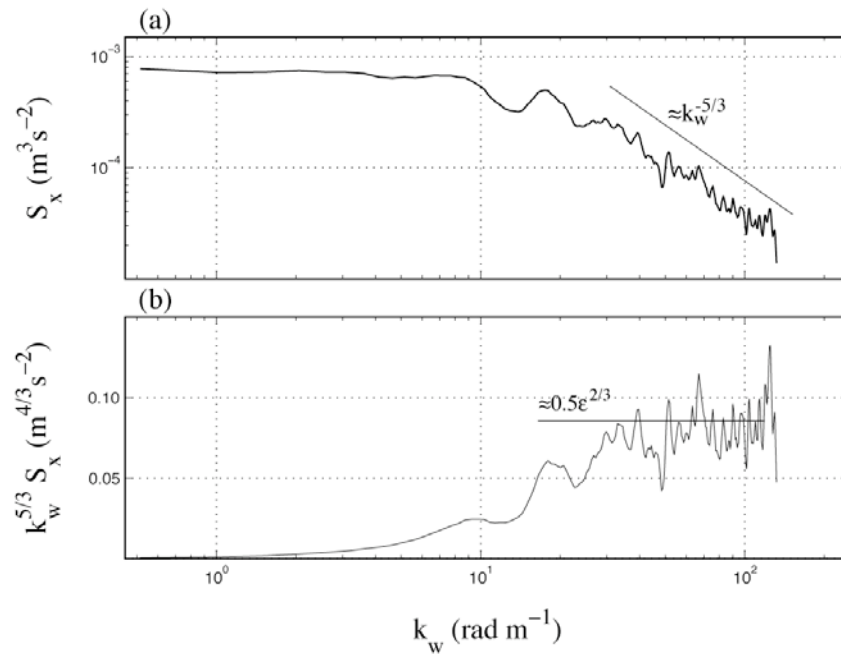


Figure 9 – Streamwise velocity energy spectrum for one position near the bottom ($z/h \approx 0.35$) from the measured profile P5.

The inertial range of the flow characterized by Kolmogorov as a $-5/3$ power law is observed. It corresponds to a range of wave numbers where the quantity $k_w^{5/3} S_x$ is relatively constant. Fig. 10 shows distributions of P and ϵ , normalized by u^* and h .

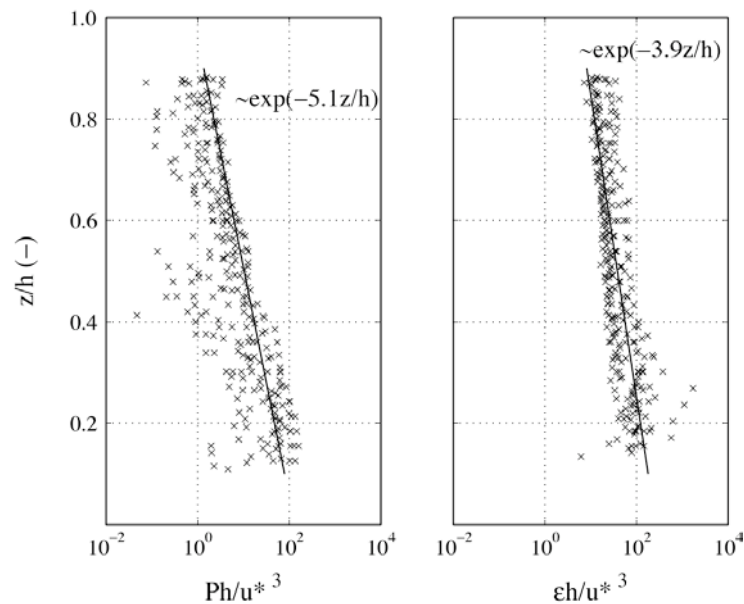


Figure 10 – Production P and dissipation ϵ , normalized by u^* and h .

The production results show more scatter, since the calculation depends on spatial gradients which are sources of errors in the data manipulation. Both production and dissipation terms increase towards the bottom with exponential rates proportional to $e^{-5.1z/h}$ and $e^{-3.9z/h}$, respectively. Production plays the major role near the bottom. The dissipation term distribution presents a lower slope. A comparison of the pseudo dissipation $\tilde{\varepsilon}$ (RST_D in Fig. 7) and the actual dissipation ε (Fig. 10), confirms that RST_D is negligible in the TKE equation, validating the approximation $\tilde{\varepsilon} \approx \varepsilon$ (Chassaing 2000). In the present case both production and dissipation are unbalanced, with the dissipation being higher than the production. TKE flux advected by the mean field (advection term in expression (7)) or by the turbulent field (term T_D in the TKE budget equation) originating in upstream positions might compensate the inequality $\varepsilon > P$.

4.7 Turbulence scales: Kolmogorov (η); Taylor (λ); integral (L); energetic (Λ)

Four scales are important in the study of turbulent flows: Kolmogorov dissipative scale (η); Taylor micro-scale or simply Taylor scale (λ); integral or Taylor macro-scale (L); and the scale corresponding to the higher energy content, herein called energetic scale (Λ). All of them correspond to the size of different repetitive patterns present in the flow. Each one is related to production, transport or dissipation processes.

The Kolmogorov scale (η) characterizes the eddy size of the smallest dissipative motions present in the flow (Pope 2001), for which the viscosity plays the main role in the fluid. It can be estimated from dissipative dynamic scales

$$\eta = \left(\frac{\nu^3}{\varepsilon} \right)^{1/4} \quad (24)$$

The Taylor micro-scale (λ) is related to the values of the 1D velocity auto-correlation function around the zero lag. Physically it constitutes an analysis of the order of magnitude of the fluctuation gradients. It may be considered a measure of the amount of dissipation and can be estimated directly from the value of ε (Chassaing 2000):

$$\lambda = \sqrt{30\nu \frac{\overline{u'^2}}{\varepsilon}} \quad (25)$$

Since $\sqrt{\overline{u'^2}}$ is not associated with the dissipative structures, the Taylor micro-scale cannot be considered as a dissipative pattern scale (Pope 2001).

The integral scale (L) is defined from the 1D velocity auto-correlation function and it represents the lag with an important correlation between consecutive velocity values (Chassaing 2000). From ADV measurements, we may directly calculate the integral time scale τ_{int} in the streamwise direction and relate it to the streamwise integral spatial scale (L), by assuming Taylor's hypothesis and freezing the time domain with the downstream convective velocity:

$$L = \bar{u} \cdot \tau_{int} = \bar{u} \cdot \int_0^\infty R_x(t) dt \quad (26)$$

R_x is the autocorrelation function for the time series of the streamwise instantaneous velocity and t is the time variable. Physically, the integral scale allows an estimate of the mean size of the larger structures in the flow. However it does not represent the most energetic scale as shown by Franca and Lemmin (2005 – 3.7). Instead, the integral scale characterizes a typical size of a structure in the transition between the inertial and the production range in the energy spectra space (low productive scales). As discussed previously, background small scales processes are dominant and apparently hide correlations more remote in time. The integral scale calculated by equation (26) corresponds to the most frequent scale in the turbulent velocity signal.

The most energetic scales (Λ) presented by Franca and Lemmin (2005 – 3.7) were based on a multi-level wavelet decomposition (single point analysis) of the fluctuating signal. This allows the identification of the energy content corresponding to each scale of the decomposition modes. Fig. 11 shows the distribution of all four turbulence characteristic scales.

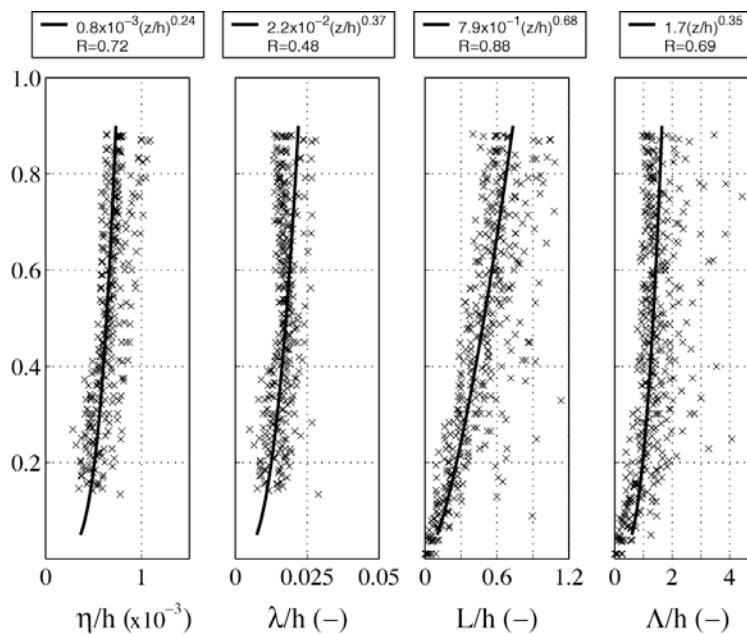


Figure 11 – Turbulence scales normalized by the water depth: Kolmogorov (η); Taylor (λ); integral (L); energetic (Λ).

As shown by previous authors (Nezu and Nakagawa 1993), the characteristic turbulent eddy sizes (l) present a power law distribution

$$\frac{l}{h} = D_1 \left(\frac{z}{h} \right)^{E_1} \quad (27)$$

The best-fit coefficients for these empirical laws are given in Table 1.

Table 1 – Parameterization of the empirical power laws for the distribution of the characteristic turbulent scales

	η	λ	L	Λ
D_1	0.0008	0.022	0.790	1.706
E_1	0.24	0.37	0.68	0.35

All measured scales collapse reasonably well around the regression curves generally with a fairly high correlation coefficient (Fig. 11). The riverbed roughness has a higher restraining effect on the smaller eddies; the scale slope E_1 consequently decreases from the integral to the Kolmogorov scale. The present slope values E_1 are roughly equal those presented by Nezu and Nakagawa (1993). The relation between scale slopes is consequently maintained. From (27) we may express the relation between scales with the following power laws (Fig. 12):

$$\frac{\lambda}{\eta} = 27.5 \left(\frac{z}{h} \right)^{1/8} \quad \text{and} \quad \frac{\Lambda}{L} = 2.16 \left(\frac{z}{h} \right)^{-1/3} \quad (28)$$

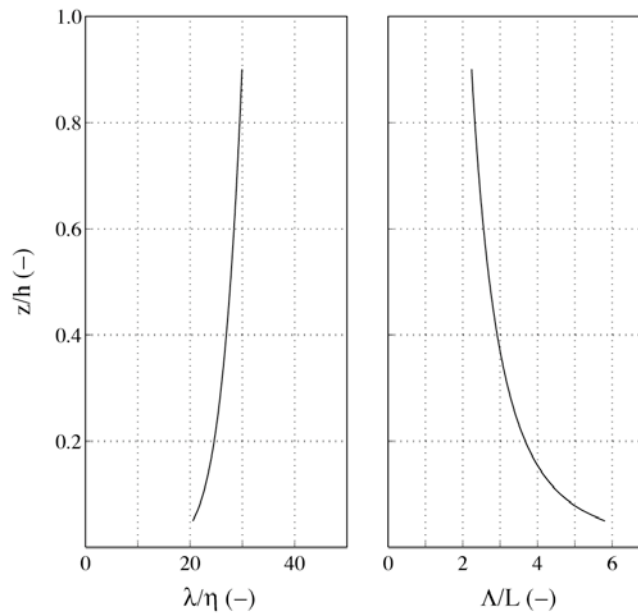


Figure 12 – Empirical relation between the productive and dissipative scales.

If one considers that dissipation occurs at scales smaller than the Taylor scale, then the upper limit of the dissipation range corresponds to scales between 30 and 45 times the Kolmogorov scale. According to Kolmogorov's hypothesis, η scales with a characteristic dissipative eddy size, but it is not equal to it (Pope 2001). We may consider that dissipative scales are typically within the interval $[\eta, \lambda]$ and productive scales within the interval $[L, \Lambda]$. According to Fig. 12, the dissipative range narrows near the bottom, whereas the productive range widens.

Further research should consider the velocity data in the vertical and spanwise directions in the estimate of integral and energetic scales in order to assess the complete geometry of the productive eddies and to analyze distortion and stretching effects in the vertical direction.

5 CONCLUSIONS

Using ADVP measurements made in a 3D grid composed of 15 instantaneous velocity profiles, we analyzed the turbulence structure of a gravel-bed river flow. In previous studies we defined three major outer regions of the flow: 1) the roughness layer ($z < z_{RL} \approx 0.20h$); 2) the intermediate or blending layer ($z_{RL} \approx 0.20h < z < z_{SL} \approx 0.80h$); and 3) the surface layer ($z > z_{SL} \approx 0.80h$). In both the roughness and surface layers, the flow is mainly 3D and the mean turbulence characteristics present major deviations from standard distributions. A lumped analysis was carried out in an attempt to establish general characteristics applicable to these kinds of flows.

We investigated the RST normal and tangential components and we tried to establish useful relations for modelling purposes. The main conclusions on the RST are the following:

- The streamwise TI ($\overline{u'^2}$) dominates the TKE, representing between 50% and 80% of the total amount. Spanwise and vertical TI contributions vary from $\overline{v'^2}/2\overline{k^1} \approx 0$ to $\overline{v'^2}/2\overline{k^1} \approx 30\%$ and from $\overline{w'^2}/2\overline{k^1} \approx 0$ to $\overline{w'^2}/2\overline{k^1} \approx 20\%$. The relation between the several TI distributions is expressed by $2.1 < \frac{\overline{u'^2}}{\overline{v'^2}} < 4.8$ and $3.0 < \frac{\overline{u'^2}}{\overline{w'^2}} < 12.1$.
- The maximum anisotropy happens near the bottom and the minimum is found at $z/h \approx 0.70$. The vertical TI distribution is complementary to the streamwise TI. Near the bottom we observed isotropy in the transversal plane $\{y-z\}$.
- The empirical formulas proposed by previous authors to describe streamwise and spanwise TI distributions are only valid in the range $0.40 < z/h < 0.90$ and $0.60 < z/h < 0.90$, respectively.
- Reduction to zero in the TI occurs earlier than observed by previous authors, i.e. in regions $z/h < 0.20$, 0.30 and 0.40 , respectively for $\overline{u'^2}$, $\overline{v'^2}$ and $\overline{k^1}$.
- The vertical TI distribution has a convex shape. The surface and bottom influence affect the TI distribution, indicating that these two layers determine the turbulence structure of these flows.
- Using the friction velocity as a characteristic velocity scale, the self-similarity of the flow is only valid above the roughness layer. Inside the roughness layer all RST shear stresses increase and acquire equivalent importance indicating that the friction velocity estimated from the longitudinal shear stress $\overline{u'w'}$ does not represent the actual bottom drag. Friction velocity u^* has to be estimated by taking into account the predominant momentum transport direction.
- The distribution of the correlation between the shear stress $-\overline{u'w'}$ and the normal stresses roughly follow the trend suggested by previous authors, although major deviations occur inside the roughness layer. The hypothesis $-\overline{u'w'} = 0.30\overline{k^1}$ used for modelling purposes is valid within the blending layer.

The eddy viscosity distribution did not follow the empirical laws previously suggested. Instead the data showed constantly increasing ν_t values, with no reduction until $z/h = 0.80$.

We individually analyzed the TKE budget equation terms production P , dissipation ϵ , viscous diffusion V_D and Reynolds stress tensor diffusion RST_D , and obtained the following results:

- The diffusive terms V_D and RST_D are negligible in the TKE global balance when compared with the production and dissipation orders of magnitude. The pseudo-dissipation may be considered equal to the actual dissipation $\tilde{\epsilon} \approx \epsilon$.
- The gradients of the streamwise component have a dominant role in the TKE production, especially near the riverbed, representing 70% to 100% of the total amount. Near the surface the

other production components are more important. Spanwise production is kept fairly constant, whereas the vertical production smoothly replaces the streamwise production when approaching the water surface. A link between the vertical and streamwise turbulence distributions exists.

The relation between the different production directions is expressed by $4.26 < \frac{P_x}{P_y} < 10.69$ and

$$2.11 < \frac{P_x}{P_z} < 27.94.$$

- The production and the dissipation distributions follow exponential laws proportional to $e^{-5.1z/h}$ and $e^{-3.9z/h}$, respectively.

The distribution of four specific turbulence scales in the flow dynamics were investigated: Taylor (λ), Kolmogorov (η), integral (L) and energetic (Λ) scales. The scale evolution throughout the flow depth was adapted to power laws. The mixing length (l_m) was related to these. Fig. 13 shows the best-fit curves obtained from the present data, and describes the individual evolution of the turbulent scales and the relationship between them. The relative evolution of the productive and dissipative scales follows the power laws $\frac{\lambda}{\eta} = 27.5 \left(\frac{z}{h}\right)^{1/8}$ and $\frac{\Lambda}{L} = 2.16 \left(\frac{z}{h}\right)^{-1/3}$. The dissipative and productive ranges are thus defined by $[\eta, \lambda=35-40\eta]$ and $[L, \Lambda=2-6L]$.

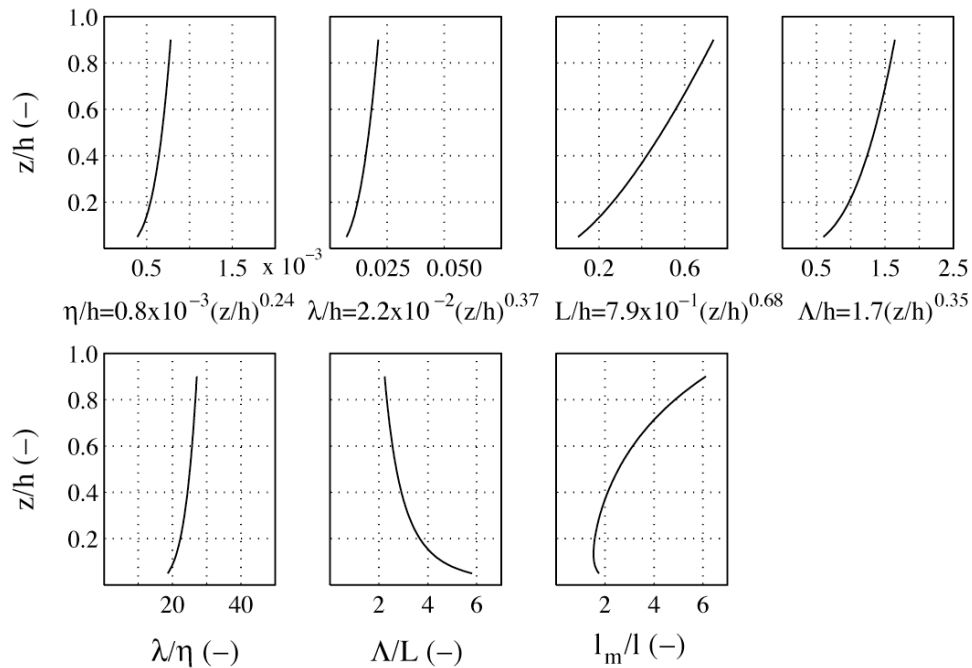


Figure 13 – Catalogue of empirical relations for the turbulent scales.

The mixing length is of the order of magnitude of the Taylor scale until $z/h \approx 0.60$, increasing upwards. l_m is a characteristic eddy size related to the upper limit of the dissipative range or to the inertial range.

The present analysis is based on river measurements. These results contribute to empirical information essential for modelling mixing and transport processes within turbulent gravel-bed river flows.

ACKNOWLEDGEMENTS

The authors acknowledge the financial support of the Portuguese Science and Technology Foundation (BD 6727/2001) and the Swiss National Science Foundation (2000-063818). We are most grateful to Gene Terray for his constructive comments during the elaboration of this paper.

REFERENCES

- Baiamonte G. and Ferro V. (1997), The influence of roughness geometry and Shields parameter on flow resistance in gravel-bed channels, *Earth Surf. Proc. and Landforms*, 22, 759-772.
- Bradshaw P., Ferriss D.H. and Atwell N.P. (1967), Calculation of boundary-layer development using the turbulent energy equation, *J. Fluid Mech.*, 28, 593-616.
- Buffin-Bélanger T. and Roy A.G. (1998), Effects of a pebble cluster on the turbulent structure of a depth-limited flow in a gravel-bed river, *Geomorphology*, 25, 249-267.
- Buffin-Bélanger T., Roy A.G. and Kirkbride A.D. (2000), Vers l'intégration des structures turbulentes de l'écoulement dans la dynamique d'un cours d'eau à lit de graviers, *Géogr. Phys. Et Quaternaire*, 54(1), 105-117.
- Cardoso A.H., Graf W.H. and Gust G. (1989), Uniform flow in a smooth open-channel, *J. Hydr. Res.*, 27(5), 603-616.
- Chassaing P. (2000), *Turbulence en mécanique des fluides*, Cépadués-Éditions, Toulouse (France).
- Comte-Bellot G. and Corrsin S. (1966), The use of a contraction to improve the isotropy of grid-generated turbulence, *J. Fluid Mech.*, 25(4), 657-682.
- Czernuszenko W. and Rylov A. (2004), 3D turbulent flow over irregular bed surfaces, *Proc. Riverflow 2004*, Naples (Italy).
- Dinehart R.L. (1999), Correlative velocity fluctuations over a gravel river bed, *Water Resour. Res.*, 35(2), 569-582.
- Falco R.E. (1977), Coherent motions in the outer region of turbulent boundary layers, *Phys. Fluids*, 20(10), s124-s132.
- Franca M.J. (2005 – A.2), Flow dynamics over a gravel riverbed, *Proc. XXXI IAHR Congress*, Seoul (South Korea). Appendix A.2.
- Franca M.J. and Lemmin U. (2005 – A.3), Cross-Section periodicity of turbulent gravel-bed river flows, *Proc. 4th RCEM. Urbana - Illinois (USA)*. Appendix A.3.
- Franca M.J. and Lemmin U. (2005 – 3.4), subchapter “Flow resistance characterization in shallow gravel-bed rivers”.
- Franca M.J. and Lemmin U. (2005 – 3.5), subchapter “Streamwise Velocity Pulsation (SVP) in gravel-bed rivers”.
- Franca M.J. and Lemmin U. (2005 – 3.7), subchapter “Evaluation of energetic scales in turbulent gravel-bed rivers based on wavelet analysis”.
- Frisch U. (1995), *Turbulence, the legacy of A.N. Kolmogorov*, Cambridge University Press, Cambridge (UK).
- Gatski T.B. (2004), Constitutive equations for turbulent flows, *Theoret. Comput. Fluid Dynamics*, 18, 345-369.

- Hinze J.O. (1975), *Turbulence*, McGraw-Hill, (USA).
- Kantha L.H. and Clayson C.A. (2000), *Small scale processes in geophysical fluid flows*, Academic Press, San Diego (USA).
- Katul G. and Chu C. (1998), A theoretical and experimental investigation of energy-containing scales in the dynamic sublayer of boundary-layer flows, *Boundary-Layer Meteorol.*, 86, 279-312.
- Kirkbride A.D. and Ferguson R. (1995), Turbulent flow structure in a gravel-bed river: Markov chain analysis of the fluctuating velocity profile, *Earth Surf. Proc. and Landforms*, 20, 721-733.
- Kironoto B.A. and Graf W.H. (1994), Turbulence characteristics in rough uniform open-channel flow, *Proc. Instn. Civ. Engrs. Wat., Marit. & Energy*, Vol. 106, p. 333-344, Great-Britain.
- Kolmogorov A. (1941), The local structure of turbulence in incompressible viscous fluid for very large Reynold's numbers, *C. R. Acad. Sci. URSS*, XXX(4).
- Kundu P.K. and Cohen I.M. (2002), *Fluid Mechanics*, Academic Press, San Diego (USA).
- Laufer J. (1951), Investigation of turbulent flow in a two-dimensional channel, NACA – Tech. Report 1053.
- Monin A.S. and Yaglom A.M. (1971), *Statistical Fluid Mechanics: Mechanics of Turbulence - Vol. 1*, The MIT Press, Cambridge (USA).
- Morris H.M. (1959), Design methods for flow in rough conduits, *J. Hydr. Eng.*, 85(7), 43–62 .
- Nezu I. and Nakagawa H. (1993), *Turbulence in open-channel flows - IAHR monograph*, A.A. Balkema, Rotterdam (The Netherlands).
- Nicholas A.P. (2001), Computational fluid dynamics modelling of boundary roughness in gravel-bed rivers: an investigation of the effects of random variability in bed elevations, *Earth Surf. Proc. and Landforms*, 26, 345-362.
- Nikora V. and Smart G.M. (1997), Turbulence characteristics of New Zealand gravel-bed rivers, *J. Hydr. Eng.*, 123(9), 764-773.
- Nikora V., Koll K., McEwan I., McLean S. and Dittrich A. (2004), Velocity distribution in the roughness layer of rough-bed flows, *J. Hydr. Eng.*, 130(10), 1036-1042.
- Pope S.B. (2001), *Turbulent Flows*, Cambridge University Press, Cambridge (UK).
- Rodi W. (1984), Turbulence models and their application in hydraulics - a state of the art review, IAHR - Section of Fundamentals of Division II.
- Schlichting H. (1968), *Boundary-layer theory*, McGraw-Hill, (USA).
- Smart G.M. (1999), Turbulent velocity profiles and boundary shear in gravel bed rivers, *J. Hydr. Eng.*, 125(2), 106-116.
- Spalart P.R. (1988), Direct simulation of a turbulent boundary layer up to $R_q=1410$, *J. Fluid Mech.*, 187, 61-98.
- Tachie M.F., Bergstrom D.J. and Balachandar R. (2004), Roughness effects on mixing properties in open channel turbulent boundary layers, *J. Fluid Eng.*, 126, 1025-1032.
- Tritico H.M. and Hotchkiss R.H. (2005), Unobstructed and obstructed turbulent flow in gravel bed rivers, *J. Hydr. Eng.*, 131(8), 635-645.
- Wieringa, J. (1976), An objective exposure correction method for average wind speeds measured at a shelter location, *Q. J. R. Meteorol. Soc.*, 102, 241– 253.

Williams J.J., Thorne P.D. and Heathershaw A.D. (1989), Measurements of turbulence in the benthic boundary layer over a gravel bed, *Sedimentology*, 36, 959-971.

Yalin M.S. (1992), *River mechanics*, Pergamon Press Ltd, Exeter (UK).

4. CONCLUSIONS

4.1 – Main results

4.2 – Suggestions for future research

4.1 MAIN RESULTS

In this dissertation new insights are given into the dynamics of turbulent flows in shallow gravel-bed rivers. It contributes to the understanding of phenomena related to sediment transport, morphology and mixing in rivers. Differences between theoretical models and observations in the nature are pointed out and explained in view of the local flow conditions, and new turbulent features of the river flow were studied. Two main directions of research were developed: mean velocity distribution and turbulent flow. The analysis of the mean velocity field includes the velocity profile and the distribution of the 3D components. The analysis of the instantaneous velocity field deals with the mean turbulence structure and individual instantaneous features. Improvements of the ADVP data quality are presented as well. The main results of the dissertation are summarized below.

The ADVP was successfully applied in field measurements. The support structure was improved and allowed the intensive profiling of rivers. A simple and easy to implement method to correct aliasing errors in Doppler-based results was developed (subchapter 2.1). This method is based on signal history and can be directly applied to the raw echoed signal, thus correcting the Doppler frequency before its conversion into the velocity domain. Combined with a multistatic configuration, the dealiasing method theoretically provides noise-free estimates of the Reynolds stress tensor. The technique allows several degrees of data aliasing.

During the measurements, the investigated gravel-bed rivers had low blockage ratios of $h/D_{84} \approx 3.0$ and aspect ratios B/h between 23 and 32. The measurements were made during low-water periods. Given the low blockage ratio, the flow response to bed forms is evident on the water surface by the presence of stationary and non-stationary wave patterns. The flow is 3D throughout the flow depth, but especially near the bottom and near the surface.

Mean velocity analysis

The analysis of the mean streamwise velocity profiles, allows the following conclusions to be made:

- The flow may be divided into three different inviscid layers: 1) the roughness layer ($z < z_{RL} \approx 0.20h$), where the flow is 3D and deviations from a linear shear stress distribution occur; 2) the blending layer ($0.20h < z < 0.80h$), where the shear stress distribution is linear and self-similar; and 3) the surface layer ($z > z_{SL} \approx 0.80h$), where the flow is 3D again and deviations from a linear shear stress occur (subchapter 3.4).
- Three types of mean velocity distributions exist in the lower layers of the flow: monologarithmic, s-shaped due to bed perturbations and double logarithmic situated downstream of the bed perturbations. An approximately 2D logarithmic layer is often found in the flow. The level of the profile origin depends on the local roughness conditions (subchapter 3.4).
- Monolog and 2xlog profile flow resistance is determined by riverbed drag. In 2xlog profiles, the friction velocity and roughness length determined for the outer logarithmic layer are required for the velocity profile parameterization. The s-shaped profiles are described by a tangent-hyperbolic function in the lower layers compatible with an external log layer. The tanh function is parameterized by a reference velocity u_0 ($u_0 \approx u_{\infty}/2$) and a geometric parameter L , which is the size of the most frequent eddies inside the roughness sublayer ($L \approx \bar{L}_{int}(z < Z_{RL})$). L may be related to the bottom gravel distribution, $L = \alpha D_{84}$ ($\alpha = 0.25$, to the present data). In order to join the tanh layer with the log layer above, a resistance factor is defined as $C_u = 1/\kappa \cdot \ln(\alpha' D_{84} / z_{0,s})$,

where $\alpha'=0.21$ for the present results and $z_{0,s}$ is the roughness length of the outer layer (subchapter 3.4).

- The use of the log-law applied in the streamwise direction is not sufficient to estimate the friction velocity (u^*). The actual drag occurs in the predominant momentum direction, which changes as a function of the local bed forms. The estimate of u^* has to take into account the actual momentum transport direction which varies with the flow depth (subchapter 3.4 and 3.8).
- Given the variability of the bed roughness throughout the riverbed, a better evaluation of the roughness parameters is obtained through the analysis of the grain diameter distribution curve. Special care shall be given to the log-law parameterization for the equivalent roughness; for $k/h > 0.60$, the profile does not correspond to the log-shape in the lower layers (subchapter 3.1, 3.2 and 3.3).

Based on the analysis of the three mean velocity components the following conclusions can be made for the 3D features of the flow:

- The wall effect of the riverbank is apparent until $B/h \approx 5$ ($y/B \approx 0.15$) and the bottom topography locally produces important secondary mean motion in the flow (subchapter 3.2).
- A permanent flow structure is observed in the upper layer of the flow: local jets (CH regions) compensated by lower velocity regions (CL regions) were detected in the longitudinal velocity field, corresponding to an organized compensatory secondary motion with streamwise vorticity (Surface Layer Organized Movement – SLOM). This mechanism is confined to $z/h > 0.80$. Due to continuity a vortical motion is formed with a streamwise axis implying lateral momentum transfer between adjacent CL and CH regions (subchapter 3.2).
- In one of the studied rivers, the bed forms present a wave-like periodic pattern across the section indicating the possible existence of streamwise ridges. The longitudinal strips, which were produced during high water events may have long-term effects on river processes. The turbulence characteristics of the flow, including the SLOM, respond to the periodic riverbed morphology (subchapter 3.2).
- D-shaped profiles are related to the CH regions and are formed where the velocity is lower near the surface. They were found across the river section; the maximum velocity is situated at around $z_{Umax}/\delta \sim 0.80$. A relationship between the occurrence of D-shaped profiles and the local Froude number is established, indicating that the SLOM might be an inviscid response to the bed forms (subchapter 3.2).
- Only a Froude number based on both horizontal velocity components allows a correct understanding of the local flow regime. A cross-section bulk analysis of the Froude number may hide local effects of bed forms, important in flow dynamics (subchapter 3.2).

Turbulent velocity analysis

Two distinct approaches in the study of the turbulent velocity field are presented. From a lumped analysis of the mean turbulence characteristics, the following conclusions can be drawn on the turbulent structure of the flow including Reynolds stress tensor, TKE budget and turbulence scales:

- The streamwise turbulent intensity (TI) dominates the TKE, representing 50 to 80% of the total energy (with a maximum at $z/h \approx 0.70$). The spanwise and vertical contributions vary along the flow depth. The vertical TI distribution is parabolic with the curvature apex at around $z/h \approx 0.60$, indicating that the surface and the bottom layers exert a strong influence on this (subchapter 3.8).

- Self-similarity of the flow is only found above the roughness layer, inside the blending layer. Inside the roughness layer the longitudinal Reynolds shear stress and the other tangential components become equally important. This supports the theory that the friction velocity u^* calculation must take into account the predominant momentum transport direction. Empirical formula established by previous authors to describe the Reynolds stress tensor components showed certain limitations. The hypothesis $-\overline{u'w'} = 0.30k'$ used for modelling purposes is only valid within the blending layer (subchapter 3.4 and 3.8).
- From the TKE budget analysis, it was confirmed that the diffusive terms are negligible in the TKE global balance and consequently that the pseudo-dissipation may be considered equal to the actual dissipation $\tilde{\varepsilon} \approx \varepsilon$ (subchapter 3.8).
- The gradients of the streamwise component play the dominant role in the TKE production rate. Vertical and streamwise production are complementary throughout the flow depth. Production mainly happens in the boundary layer. Dissipation is more widely spread in the flow, since it is controlled by small background structures. Its maximum is also attained near the bottom. Production and dissipation follow exponential laws proportional to $e^{-5.1z/h}$ and $e^{-3.9z/h}$, respectively (subchapter 3.8).
- The energy distribution over the eddy scales is characterized by a peak value (Λ_{\max}), and a dimensionless parameter representing the energy dispersion through the scales (σ^+). Λ_{\max} is within the bed grain and the flow depth dimensions. Eddies for which $\Lambda_{\max} > \approx D_{84}$ contain more than 70% of the energy. σ^+ varies typically between 1 and 3, increasing near the surface. The most energetic scales persist 10 to 20% of the time (subchapter 3.7).
- Based on the measurements, empirical power laws are presented for the following turbulence scales: Taylor (λ), Kolmogorov (η), integral (L), energetic (Λ) and mixing length (l_m). The relationship between the different scales is also studied: l_m scales with λ until $z/h \approx 0.60$, increasing upwards. (subchapter 3.8).

Based on conditional sampling techniques, it was possible to identify particular features of the turbulent velocity and their role in flow dynamics. These include the detection and analysis of bursting packets in the boundary layer (subchapter 3.6) and the study of the passage of large-scale uniform momentum regions (UMR) which here were called Streamwise Velocity Pulsation (SVP) (subchapter 3.5). Innovative analysis tools were explored and applied with success in this study, namely wavelet decomposition and multiresolution analysis (subchapter 3.6 and 3.7) applied in a conditional sampling technique to detect coherent structures, empirical mode decomposition to isolate SVP regular but non-periodic cycles and phase averaging based on the Hilbert transform phase tracking to reconstruct and investigate the SVP feedback in the instantaneous flow structure (subchapter 3.5). These proved to be powerful tools in the research of turbulent processes in river hydraulics.

- In one of the measured profiles several identical bursting packets composed of sequential ejections and sweeps ($\{x-z\}$ shear events) were visualized and characterized. Spanwise vortical cells can be linked to these events. Two central events seem to be at the core of the packet; the remaining ones probably exist due to vortical momentum continuity (subchapter 3.6).
- The bursting packet locally provokes Reynolds stress enhancement, especially in the horizontal components. Despite its low persistence in time, the packet is highly energetic and is responsible for twice the peak mean production (subchapter 3.6).
- Velocity profile deformation as a consequence of packet passage was analyzed and interpreted. The role of the spanwise component was not clear. However a correlation with the other components exists because the major lateral momentum is consistently observed between the

occurrence of the shear events $\{x-z\}$. Between sequential ejections and sweeps so-called “stop points” exist where all three velocity components have low-activity (subchapter 3.6).

- Associated with the packets, signatures of large-scale high- and low-speed wedges are observed. Near the bottom the fronts have a concave shape, with an angle of 18° with the horizontal (subchapter 3.6).
- The analysis of the occurrence of bursting packets in the total time record allowed to conclude that the sampled bursting packets are independent. The time interval between packets is rather stable and the most probable value corresponds to a Strouhal number of $S_f=2.5$ (Strouhal number defined with the friction velocity). The bursting Strouhal number is $S_b=12.5$ (subchapter 3.6).
- The SVP was identified and isolated; it corresponds to a non-periodic but regular low-frequency occurrence of large-scale UMR of streamwise velocities alternately higher or lower than the mean (positive and negative UMR, respectively). The passage of one positive and one negative UMR constitute a SVP cycle. The SVP Strouhal number is within the range $0.13 < S_{SVP} < 0.32$ (Strouhal number defined with the depth averaged velocity). The Strouhal number corresponding to the time interval between bursting packets in the boundary layer, defined with the same reference velocity, is within this interval. Thus, the UMR containing the detected bursting packets might be due to the SVP (subchapter 3.5 and 3.6).
- The UMR have a vertical linear phase shift of $\approx -3/4\pi$. The front has a first quarter moon shape, with an apex at $z/h \approx 0.35$. It scales with the flow depth (h) in the vertical and with $3.1-7.3h$ in the streamwise direction. In the lower layer the fronts have an average angle of 15° (subchapter 3.5).
- An in-phase cycle of large-scale sweeps and ejections corresponds to the SVP. Though less permanent in the cycle, ejections dominate shear stress production with higher instantaneous amplitudes (subchapter 3.5).
- A periodic variation of the bottom drag between 0.90 and 1.10 times the mean value is related nonlinearly with the SVP. This is called the SVP direct effect on the bottom drag. An enhancement due to the 3D bursting process triggered by the passage of a UMR is the indirect effect of the SVP on bottom drag (subchapter 3.5).
- There is no production cycle directly associated with the passage of an UMR. However this passage triggers high frequency productivity events. The dissipation rate is not affected by the SVP (subchapter 3.5).
- A correlation exists between the SVP and free surface ripples travelling with the UMR (subchapter 3.5).
- The SVP seems to originate in one combined shedding effect produced by large boulders randomly and widely spaced in the riverbed. The regular but non-periodic phase of the SVP is caused by the range of boulder sizes and the interaction between different shedding vortices (subchapter 3.5).

4.2 SUGGESTIONS FOR FUTURE RESEARCH

One of the objectives of this Ph.D. dissertation was to observe, identify and characterize unknown and lesser-known flow phenomena of gravel-bed rivers. These field results should be combined with laboratory and theoretical work in order to study in detail and under controlled conditions the dynamics of these processes.

Possible future research projects based on this dissertation include the following:

- Use the present deployable installation for intensive profiling in rivers, with different ADV configurations adapted to several research purposes (i.e. vertical profiling looking downwards, vertical profiling looking upwards and lateral profiling).
- Implementation of the dealiasing technique in a real time system.
- Definition of a relationship between the grain diameter and the Nikuradse equivalent roughness distributions.
- Investigation of a new indicator for the three-dimensionality of the flow which takes into account the blockage ratio (h/D) and the variability of the bed form expressed as a function of the grain diameter distribution of the bed material. A modified characteristic length should be defined which takes into account the ratio h/D and the density of the large gravel grains in the riverbed.
- Determination of proper correction coefficients in the estimate of the friction velocity from simple in situ methods, taking into account the three-dimensionality of the flow.
- Reproduction and isolation in the laboratory of the Surface Layer Organized Motion (SLOM) in order to investigate its generation and evaluate the interaction with other flow features such as transport, mixing and gas transfer processes.
- Evaluation of the flow regime influence on the SLOM.
- Determine under what conditions the D-shaped profiles occur and the boundary conditions to impose in the surface layer for modelling purposes.
- Reproduction of the three inviscid layers (roughness, intermediate and surface layers) under controlled conditions and subsequent study of the related turbulence structure of the flow namely, the Reynolds stress tensor, TKE budget terms, distribution of the preferential momentum direction, turbulence scales and functionality of the layers within the spectral dynamics. The effect of the roughness variation should be assessed as well as the particularities in the interfaces between layers.
- Reproduction of the SVP in order to study the generation, the dominant scales related to the UMR space and time distribution, influence of the UMR geometry on the associated bottom drag cycle, the indirect contribution of the SVP to the bottom drag, the relation between the SVP and high frequency coherent motion (i.e. bursting packets) and the occurrence of Görtler or Taylor vortices in the curved lower shear layer of the UMR.
- Synchronized ADV and water surface displacement measurements to evaluate the relation between SVP and free surface waves and to investigate possible implications of the passage of a UMR on the occurrence of surface boils or other surface perturbations which may promote air-water exchange.
- Application of the conditional sampling technique based on wavelet analysis to the study of coherent structures in field and laboratory measurements. The influence of local characteristics

in the bursting packet dynamics and the detection of packets with different scales should be assessed.

- Establishment of mean parameters that reflect the influence of large- and small-scale coherent structures on mean turbulence dynamics.
- Investigation of the impact of the highly energetic bursting packets on transport and mixing processes.
- Consideration of the velocity data in the vertical and spanwise directions when estimating the 3D integral and energetic scales in order to assess the full range of productive eddies.
- Continuation of the presented spectral analysis with more detailed data in order to assess the role of each layer in the flow turbulence dynamics.

A modified Reynolds decomposition should be one of the main topics to follow-up the current research. In fact, techniques such as wavelet analysis and empirical mode decomposition should be applied to decompose the turbulent velocities signal into several interacting frequency bands. New dynamic formulations for processes such as bed-load transport, re-suspension and mixing should replace the existing ones based on mean field approaches. The instantaneous processes responsible for these processes have to be statistically included in formulas to be used by practitioners.

The RANS equations are not suitable for irregular rough boundary flows especially in near-bed region, where flows are highly 3D and heterogeneous. Boundary irregularities generate perturbations in ensemble-averaged flows, which have been already detected experimentally in the steady flow. The velocity profiles are determined by the effects of these disturbances. In order to smooth out the flow irregularities, a special, spatial averaging operation is applied to RANS equations. It results in the double-averaged (in both time and space) Navier-Stokes equations, which are used to describe the uniform vertical velocity profile. However, to solve the double-averaged equations we must define so called “form-induced stress” which is a challenging problem. Many papers devoted to this problem have already been published. A series of informal workshops (Belgium/Wavre 2002, Greece/Thessalonica 2003, Spain/Madrid 2004, UK/ Aberdeen 2005) was initiated by an international group of researchers to explore and promote the double-averaging methodology in environmental hydraulics (personal communication by W. Czernuszenko).

A. APPENDICES

A.1 – A field study of extremely rough, three-dimensional river flow (conference paper)

A.2 – Flow dynamics over a gravel riverbed (conference paper)

A.3 – Cross-section periodicity of turbulent gravel-bed river flows (conference paper)

A.4 – Annex to Subchapter 3.2

A.5 – Annex to Subchapter 3.4

A.6 – Curriculum Vitae

A.1 A FIELD STUDY OF EXTREMELY ROUGH, THREE-DIMENSIONAL RIVER FLOW

Appendix A.1 was published in the conference proceedings of the 4th International Symposium on Environmental Hydraulics (IAHR), Hong Kong, December 2004. The authors are M.J. Franca and U. Lemmin.

The results mainly deal with the 3D character of the mean flow, its implication on mixing and transport, and the consequent limits of 2D concepts developed for open-channel flows.

A field study of extremely rough, three-dimensional river flow

M.J. Franca & U. Lemmin

LHE – École Polytechnique Fédérale de Lausanne, Switzerland

ABSTRACT: Field measurements using a deployable 3-D Acoustic Doppler Velocity Profiler were made under stationary conditions, during a low water period in the Swiss lowland river Venoge. The riverbed is hydraulically rough; it is composed of coarse gravel and has randomly spaced protuberances as high as half the water depth. The measurements were made in one half of the cross section of the river. The present analysis focuses on the three-dimensional character of the mean river flow and its implication on mixing and transport. The mean velocity cross river distribution is affected by the riverbank effect and large bottom roughness. The three-dimensionality of the mean flow induces secondary motion due to large-scale bottom roughness. As a consequence, the turbulence distribution across the section and along the water depth is modified. It is concluded that 2-D concepts developed for open-channel flow are of limited value under these conditions.

1 INTRODUCTION

Field measurements of velocity including turbulence features are needed for the validation and calibration of engineering tools in river simulations with respect to sediment transport, morphology evolution, secondary flows and mixing and transport of heat and matter. Only a small number of field studies have been carried out in natural or canalized rivers, mainly due to the lack of suitable instrumentation. Some recent publications give a limited insight into turbulent flow aspects under natural conditions (González et al. (1996); Nikora and Smart (1997); Powell et al. (1999); Smart (1999); Nikora and Goring (2000); Babaeyan-Koopaei et al. (2002); Hurther et al. (2002); Tritico et al. (2002) and Roy et al. (2004)).

In this paper we present the results of a field measurement campaign made on a lowland stretch of the Swiss river Venoge, during the summer of 2003. A deployable three-dimensional Acoustic Doppler Velocity Profiler (ADVP) developed at the LHE was used. The instrument which permits three-dimensional, quasi-instantaneous profiling of the fluctuating velocity flow field along the whole water depth (Rolland and Lemmin, 1997), is positioned at several points across the river section. The flow conditions were stationary and the riverbed was extremely rough. Our results focus on the three-dimensionality of the mean river flow and on the turbulence distribution across the section and along the water depth.

2 FIELD STUDY

The field measurements were made during a low water period, across the Swiss lowland river Venoge (Table 1). They were carried out on a single day and under stationary flow conditions, as confirmed by discharge data provided by the Swiss Hydrological and Geological Services. The chosen cross section was situated along a straight river reach, about 120 m upstream of the Moulin de Lussery (Figure 1).

In Table 1, Re is the Reynolds number; \bar{U} , the vertical mean of the longitudinal velocity; ν , the cinematic viscosity; Fr , the Froude number; g , the gravity acceleration and D_{50} , the bottom grain

Table 1. Summary of the Venoge river flow characteristics.

Mean slope (%)	Discharge Q (m ³ /s)	Av. water depth δ (m)	Width B (m)	Re = $\bar{U}\delta/\nu$ ($\times 10^4$)	Fr = $\bar{U}/\sqrt{sg\delta}$ (-)	D ₅₀ from the riverbed ⁽¹⁾ (mm)
0.13	0.80	0.21	6.30	3.0–14.4	0.2–0.9	40

⁽¹⁾ D₅₀ obtained from a sample of the bottom material using Wolman (1954) method.



Figure 1. View of the study reach and of the deployable support structure for the ADVP field measurements.

size diameter for which 50% of the grain diameters are smaller. Considering the average water depth, one obtains $B/\delta = 30$ which corresponds to shallow water conditions.

The riverbed is hydraulically rough, composed of coarse gravel and randomly spaced protuberances as high as half the water depth (0.5δ). The measurements were made in half the cross section of the river starting from the right riverbank ($y/B = 0$). The deployable 3-D ADVP was used for the measurements. ADVP spatial and time resolutions are sufficient to estimate the main turbulent parameters related to open-channel flows within the production and inertial subranges of the spectral space. In the present study, 25 profiles were measured for 5 min. each with horizontal spacing of 10 to 12.5 cm. A Pulse Repetition Frequency (PRF) of 2000 Hz and a Number of Pulse Pairs (NPP) equal to 32 was used for the estimation of the Doppler shift and subsequently the three-dimensional velocity components, resulting in a sampling frequency of 62.5 Hz. Though a low degree of aliasing was expected, a correcting algorithm developed by the authors was applied to the data. This algorithm rectifies directly the instantaneous values of the Doppler frequencies measured by the receivers through a procedure that follows the signal history and chooses the best correction to be made. A deployable support structure was constructed for the easy displacement of the ADVP along two directions (horizontal and vertical, see Fig. 1). The installation minimizes the disturbance of the flow field and instrumentation vibration. This structure is leveled and aligned and allows to carry out the measurements of the cross section over a short period of time.

3 RESULTS

3.1 Mean velocity field

Figure 2 shows the mean velocity field in the longitudinal, transversal and horizontal planes across the section. Each vertical line corresponds to one measured profile and each vector results from

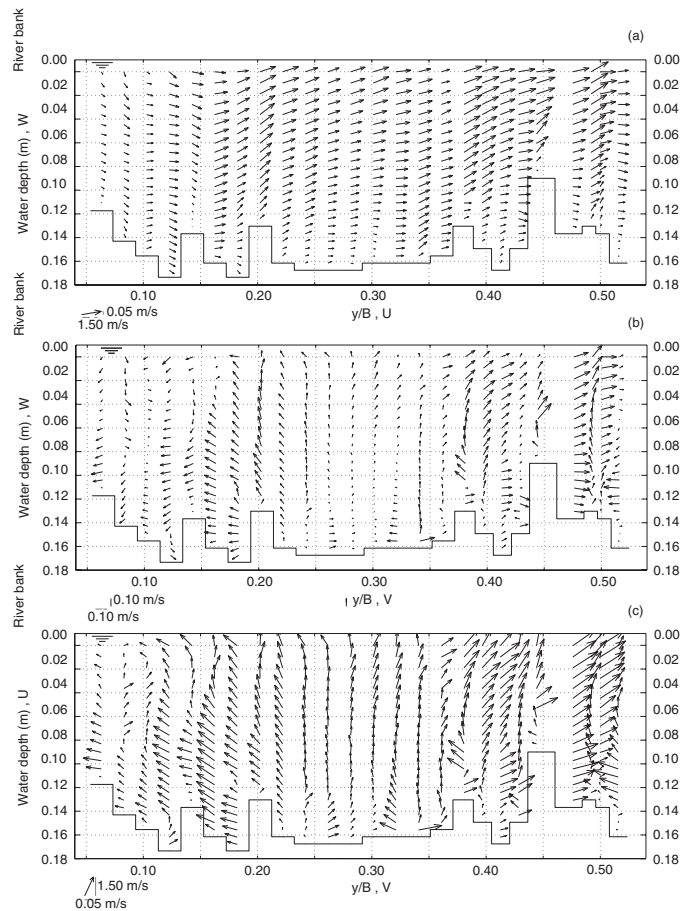


Figure 2. Mean vector fields (U: longitudinal; V: transversal; W: vertical component) in cross section of the river Venoge: (a) longitudinal plane (U-W); (b) transversal plane (V-W); (c) horizontal plane (U-V). Measurements cover half the river width.

one of the ADVP bins. The local water depth is determined from the backscattering echo intensity of the ADVP with a resolution of ± 5 mm.

The high three-dimensionality of the flow is evident from Figure 2, best seen in the near bank zone and around the higher riverbed protuberances. In fact, the large-scale bottom roughness locally produces important secondary mean motion in the flow, as seen from the transversal (V) and vertical (W) components of the mean velocity field (Figure 2b). This leads to a strongly 3-D flow field over most of the cross section (Fig. 2b and c). On a cross section average, the transversal and vertical velocities represent about 5.3% and 7.5% of the longitudinal component, whereas they become locally more important over the large-scale roughness. No structured secondary flow cells were detected. In agreement with observations by Studerus (1982), higher intensity cells in the (U) field are observed across the section where large-scale bottom roughness is found (Fig. 2a). The transversal decrease of the longitudinal velocity component (Fig. 2a) towards the riverbank is associated with a secondary recirculation flow (Fig. 2b and c) and indicates the drag effect of the riverbank occurring for $y/B < 0.15$.

The profiles of the longitudinal component of the mean velocity field measured in the river Venoge were compared to the classical log-law approach. Despite the three dimensional character of the flow, the mean longitudinal velocity distribution shows a logarithmic layer in the lower 40%

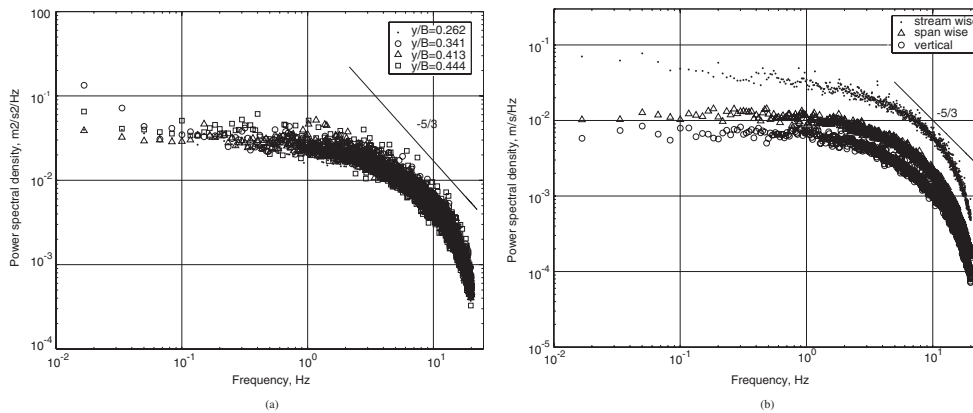


Figure 3. Power spectral density of the turbulent velocity fields: (a) vertically averaged power spectral density of the streamwise velocities for several profiles measured across the section; (b) vertically averaged power spectral density of the streamwise, spanwise and vertical velocity components, for $y/B = 0.282$.

of the water column along most of the section, and classical 2-D boundary layer profiles are found over most of the depth in sections where the bottom is relatively homogeneous ($0.25 > y/B < 0.35$). For all the 25 measured profiles only one did not correspond to hydraulically rough turbulent conditions. The average dimensionless roughness is $k^+ = 9500$; with the dimensionless roughness defined as $k^+ = k_s U^* / \nu$, where U^* is the friction velocity. The computed value of $k_{s,50}$, defined as the equivalent roughness for which 50% of the values are higher, is equivalent to the grain diameter D_{85} taken from the grain size distribution of the riverbed.

Obviously, a 2-D approach of a rough flow is impossible especially in the inner bank zone and near the large-scale bottom roughness. Therefore, concepts developed for open channel flow particularly concerning bottom friction velocities are of limited value in these flows. This is important because sediment transport is controlled by bottom friction and new concepts for the prediction of sediment transport in these flows may be needed. The three-dimensional mean field has its maximum value around the protuberance correspondent to $y/B = 0.45$. In this vertical the mean vertical velocity component assume the highest values, representing about 14% of the maximum longitudinal one. In the profile $y/B = 0.50$ the spanwise velocity acquires its maximum, representing about 10% of the maximum longitudinal one. Taking these two latter values as reference, it is obvious that the secondary mean velocity field introduces an additional advection of about 25% for any physical property present in the flow in its balance equation. The spanwise and the vertical terms should thus be included in this calculation.

The three dimensionality of the flow is confirmed by the inexistence of mass conservation within the cross section. In this flow, mass conservation can only be verified over a river stretch. The secondary mean motion induced by the large-scale bottom roughness is important in the spreading of matter, heat and momentum across the river section. Due to the strong shear zones this may locally be more efficient than background turbulence. Turbulence production is not restricted to the shear due to the bottom roughness. Instead, the shear zones observed in the mean velocity field provide for an additional turbulence production along the whole water column.

3.2 Fluctuating velocity field

Figure 3 presents estimates of the power spectral density of the fluctuating velocity fields. The data was split into blocks of one minute duration and the Welch method with 50% overlapping was used for the calculation of the power spectral density. The vertically averaged spectral density for several measured profiles, representing the bulk average streamwise turbulent energy distribution is shown in Fig. 3a.

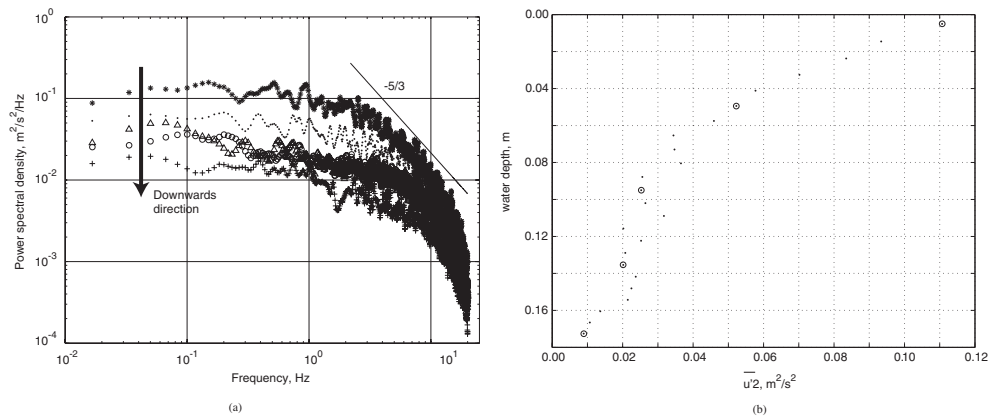


Figure 4. For the streamwise component at $y/B = 0.282$: (a) Power spectral density of the turbulent velocities for several points along the water depth; (b) vertical distribution of turbulence intensity. The points corresponding to the spectral density plots shown in Fig. 4a are represented by a dot surrounded by a circle in Fig. 4b.

No particular tendency of the total bulk energy distribution between $y/B = 0.262$ and $y/B = 0.444$ is detected, despite the difference in roughness and water depth between these two flow zones. The vertically averaged spectral density for the three velocity components for the profile $y/B = 0.282$ is given in Fig. 3b. It shows a strong anisotropy of the flow, with the streamwise velocity component dominating in the energy production, in agreement with the conclusions by Buffin-Bélanger *et al.* (2000). It was also verified that in the transversal plan (y - z), the anisotropy level decreases in the upward direction, towards nearly complete isotropy conditions.

Figure 4 shows the streamwise spectral density for several water depths and the vertical distribution of the streamwise turbulent intensity for $y/B = 0.282$.

High values of the turbulent intensity are found, particularly in the near surface area (Fig. 4). The turbulent energy distribution decreases downwards in the water column, confirmed by the spectral density distribution (Fig. 4a) and by the turbulence intensity profile (Fig. 4b). Thus, in the present flow the bottom production does not seem to be the main source of turbulence. In order to explain the turbulence distribution shown, several other production sources can be envisioned and will be investigated. The flow features here shown for the vertical $y/B = 0.282$ are generally valid for the rest of the cross section.

4 DISCUSSION

Macro roughness and high protuberances present on the riverbed promote mixing in the water mass (pollutants, heat or momentum), due to the existence of secondary mean flow and due to an increase of the turbulence levels within the flow. The effect of the secondary mean flow on the structure of the flow provides for a supplementary advection term in a balance equation, in both the spanwise and vertical directions. This is not considered in exclusively two-dimensional approaches. Furthermore, the high turbulence levels observed are of major importance for mixing.

The strong variation of the mean streamwise velocity field across the section (Fig. 2a) is responsible for additional shear zones that produce horizontal eddies, thus providing for a turbulent energy production all along the water depth. Due to the random distribution of the protuberances and macro-roughness along the studied river reach, the high turbulence levels are equally distributed across the river section. We concluded that in the present flow, sources other than bottom shear contribute to the turbulent energy production.

The presence of macro-roughness elements in the riverbed induces large flow structures with length scales of the water depth. These dominate the turbulence production and are present in

the entire flow depth (Roy 2004). These large structures are conveyed upwards within the water column where the higher longitudinal velocities together with the constraint imposed by the water surface distort them in the streamwise direction. This process explains the high values of streamwise turbulence near the surface and can be considered to be similar to the rapid distortion for which a theory was first developed by Batchelor and Proudman (1954).

At the same time, a regular occurrence of alternating periods of faster and slower streamwise velocity with respect to the mean velocity is observed in the whole water column in the present data, though is not discussed here. This velocity variation induces an additional oscillating component with extremely high amplitude which affects the longitudinal turbulent intensity. This periodic oscillation occurs at a periodicity lower than 1 Hz and can be considered as a quasi-stationary feature of the flow. It will therefore not contribute to the small-scale turbulence. However, the existence of these alternating time cells, suggested by Yalin (1977) can be responsible for the strong anisotropy in the streamwise direction observed in the turbulence intensity analysis.

The authors acknowledge the financial support of the FCT (BD 6727/2001) and the Swiss National Science Foundation (2000-063818).

REFERENCES

- Babaeyan-Koopaei K., Ervine D.A., Carling P.A. and Cao Z. (2002), Velocity and turbulence measurements for two overbank flow events in river, Severn, *J. Hydr. Eng.*, 128(10), 891–900.
- Batchelor G.K. and Proudman I. (1954), The effect of rapid distortion of a fluid in turbulent motion, *Q. J. Mech. Appl. Maths*, 7, 83.
- Buffin-Bélanger T., Roy A.G. and Kirkbride A.D. (2000), Vers l'intégration des structures turbulentes de l'écoulement dans la dynamique d'un cours d'eau à lit de graviers, *Géogr. Phys. Quat.*, 24(1), 105–117.
- González J.A., Melching C.S. and Oberg K.A. (1996), Analysis of open-channel velocity measurements collected with an acoustic doppler current profiler, *Proc. 1st Int. Conf. New/Emerging Conc. Rivers*, Chicago (USA).
- Hurther D., Lemmin U. and Blanckaert K. (2002), A field study of transport and mixing in a river using an acoustic Doppler velocity profiler, *Proc. Riverflow 2002 – Int. Conf. Fluv. Hydr.*, Louvain-la-Neuve (Belgium).
- Nikora V. and Goring D. (2000), Flow turbulence over fixed and weakly mobile gravel beds, *J. Hydr. Eng.*, 126(9), 679–690.
- Nikora V. and Smart G.M. (1997), Turbulence characteristics of New Zealand gravel-bed rivers, *J. Hydr. Eng.*, 123(9), 764–773.
- Powell D.M., Reid I. and Laronne J.B. (1999), Hydraulic interpretation of cross-stream variations in bed load transport, *J. Hydr. Eng.*, 125(12), 1243–1252.
- Rolland T. & Lemmin, U. (1997). A two-component acoustic velocity profiler for use in turbulent open-channel flow, *J. Hydr. Res.* 35(4): 545–561.
- Roy A.G., Buffin-Belanger T., Lamarre H. and Kirkbride A.D. (2004), Size, shape and dynamics of large-scale turbulent flow structures in a gravel-bed river, *J. Fluid Mech.*, 500, 1–27.
- Smart G.M. (1999), Turbulent velocity profiles and boundary shear in gravel bed rivers, *J. Hydr. Eng.*, 125(2), 106–116.
- Studerus, X. (1982), Sekundärströmungen im offenen Gerinne übn rauhen Längsstreifen. Ph.D. thesis, Institut für Hydromechanik und Wasserwirtschaft – ETH, Zurich.
- Tritico H.M., Stone M.C. and Hotchkiss R.H. (2002), Turbulence characterization in the wake of an obstruction in a gravel bed river, *Proc. Hydr. Meas. Exp. Met.*, Estes Park (USA).
- Wolman M.G. (1954), A method of sampling coarse river-bed material, *Trans. Amer. Geoph. Un.*, 35(6), 951–956.
- Yalin, M.S. (1977), *Mechanics of Sediment Transport*. Surrey: Pergamon Press.

A.2 FLOW DYNAMICS OVER A GRAVEL RIVERBED

Appendix A.2 was published in the proceedings of the JFK Student Paper Competition held during the XXXI IAHR Congress, Seoul (South Korea), September 2005. The author is M.J. Franca.

The results deal with the parameterization of the mean velocity profiles of gravel-bed rivers, i.e. monolog, s and 2xlog profiles. The dynamics of the transition between the three types of profiles and the interaction with the turbulence mean characteristics and coherent structures are assessed.

FLOW DYNAMICS OVER A GRAVEL RIVERBED

M.J. FRANCA

Laboratory of Environmental Hydraulics - LHE
École Polytechnique Fédérale de Lausanne, st 18, CH-1015 Lausanne, Switzerland
(e-mail: mario.franca@epfl.ch)

Abstract

Field measurements in a shallow gravel-bed river are analyzed along a streamwise plane where a bed perturbation creates an inflection in the velocity distribution. Three types of velocity profiles may occur in these flows: log (undisturbed profile), s (caused by the perturbation) and double log (after the perturbation). The dynamics of the transition log-s-2xlog is investigated. Three regions of the flow are identified, corresponding to the three mentioned types of profile: (1) convergence of the flow in the outer layers above the boulder; (2) separation of the flow due to the boulder creating a shielded inner zone where the mean velocity distribution is inflected, turbulence levels decrease and coherent structures reorganize; (3) momentum redistribution throughout the water depth. A parameterization of the s-profile with a hyperbolic tangent function is presented, where the main parameter is an energetic eddy size. An analysis of coherent structure scales indicates that this parameter corresponds to the mean integral scale in the roughness sublayer of the flow. Lateral low momentum convection occurs around the obstacle and is responsible for the formation of the inner boundary layer in region (3), whereas the boulder form-drag contributes to the shear in the outer boundary layer. Turbulence mean levels and coherent structures are investigated in the three regions of the flow. Turbulence intensity is modified due to shielding effects and due to the Kelvin-Helmholtz type instability in the inflection of s-profiles. Instantaneous shear stress events are conditionally sampled and the quadrant distribution is investigated.

Keywords: Gravel riverbed; Log-profile; S-profile; double boundary layer; Field measurements.

1. INTRODUCTION

The present research on natural gravel-bed river flows concerns the flow around a bed protuberance. In shallow gravel-bed rivers, the mean velocity in the lower layers of the flow may show two kinds of profiles, logarithmic and s-shaped (Marchand et al., 1984 and Bathurst, 1988). Bathurst (1988) and Ferro and Baiamonte (1994) described the importance of relative roughness for the occurrence of s-profiles. Based on their measurements, Nelson et al. (1993), Baiamonte et al. (1995) and Buffin-Bélanger and Roy (1998) state that the wake effect formed by the bed forms and boulders is responsible for the deviations observed in the velocity profile of gravel-bed rivers. Nikora and Smart (1997) referred to a 3D inner layer of the flow called the roughness sublayer ($z < Z_{RL}$), where deviations from the log-law occur. However, field measurements show that the log-law may be used, in some conditions, to

describe the velocity distribution in gravel-bed river flows (Franca and Lemmin (2004) and Nikora and Smart (1997)). Flow over gravel riverbeds is often compared to atmospheric canopy flow. Katul et al. (2002) described inflected profiles in atmospheric flows above canopy similar to the s-profiles observed in rivers. However, as observed in the present measurements, in the case of gravel riverbeds, a continuous inflection of velocity does not exist, and s and log profiles coexist in the flow. It is thus useful to understand the local conditions causing the s-profiles and the turbulence mechanism involved in the transition between different velocity distributions. In the present measurements several log and s-profiles were detected in the river measurements made on a 3D grid. Double logarithmic layers were observed downstream the bed perturbations. This paper analyzes one streamwise plane where the transition log-s-2xlog exists due to an individual bed perturbation scaling with D_{84} (a “regular” perturbation of the riverbed). The dynamics of the flow are investigated taking into account the spanwise mean velocity. The s profile is parameterized with a tanh function using local turbulent scales. The downstream double boundary layer profile is explained. Coherent structures and their interaction with the measured mean velocity distribution are investigated. The consequences of obstacles on the turbulence distribution are assessed. Structure scales are discussed and related to the velocity decay in the s profile. The notation adopted for the Reynolds velocity decomposition is streamwise, $u = \bar{u} + u'$; spanwise, $v = \bar{v} + v'$; vertical, $w = \bar{w} + w'$ ($\bar{\quad}$ temporal mean and $'$ instantaneous value).

2. FIELD MEASUREMENTS AND INSTRUMENTATION

The present research is based on field measurements made in the Swiss lowland river Venoge, located in the canton of Vaud. The measurements of the velocity profiles were made on a single day, during a shallow water period and under stationary flow conditions (confirmed by the Swiss Hydrological and Geological Services). The gauge position was at the river section situated about 90 m upstream of the Moulin de Lussery (straight reach). The river hydraulic characteristics during the measuring period are shown in Table 1.

Table 1. Summary of the river flow characteristics

Discharge (m^3/s)	Slope (%)	Mean depth (m)	Width (m)	U (m/s)	Re ($\times 10^{-4}$)	Fr (-)	D_{50} (mm)	D_{84} (mm)
0.76	0.33	0.20	6.30	0.60	5.9 - 8.7	0.32 - 0.61	68	89

In Table 1, U is the bulk velocity; Re, the Reynolds number; Fr, the Froude number; D_n the bottom grain diameter for which n% of the grains are smaller. The riverbed was sampled according to Wolman (1954). The ADV, developed at the LHE (Rolland and Lemmin, 1997), was used for the 3D instantaneous velocity measurements over the entire depth of the flow (Fig. 1a). A Pulse Repetition Frequency of 1666 Hz and a Number of Pulse Pairs equal to 64 were used, resulting in a sampling frequency of 26 Hz. An algorithm was applied to correct aliased data (Franca and Lemmin, 2005). 15 velocity profiles were measured for a period of 3.5 min. A 3x5 rectangular horizontal measuring grid was executed with streamwise spacing

of 0.15 m and spanwise spacing of 0.10 m. The distance between consecutive vertical positions is about 5 mm. During the measurements no sediment transport occurred.

3. RESULTS OF THE RIVER MEASUREMENTS

The investigated streamwise plane was positioned 2.85 m from the left riverbank and included three measured profiles (Fig. 1b): $x=-0.30$ m (A), -0.15 m (B) and 0.00 m (C). The bottom position was detected from the sonar-backscattered response. Between the measured profiles, the evolution of the bed was assumed to be step-like. The studied plane comprised a bed indentation from the mean riverbed level scaling with D_{84} . The data between all 15 positions of the measurement grid were obtained through a 3D interpolation (cubic spline). Though the interpolated data is useful for flow dynamics visualization and interpretation, the present discussion is based on the analysis of the individual measured profiles. Based on visual observation and a threshold value defined in terms of difference between the measurements and a theoretical log profile, several s profiles were found in the 15 profiles.

3.1. MEAN VELOCITY

Profiles A, B and C correspond to different kinds of velocity distributions (Fig. 1b): a logarithmic distribution of the velocity (A); an s-shaped profile inside the roughness sublayer, converging to a constant distribution outside the roughness sublayer (B); two logarithmic layers (C). The log law describes the velocity distribution for turbulent open-channel flows in the logarithmic layer of the flow (Graf and Altinakar, 1998), and it is parameterized with the bottom shear velocity (u^*), the Nikuradse equivalent roughness (k), and a geometric parameter B (usually $B=8.5$ for turbulent rough flows). In the profile A, the calculated shear velocity is $u^*=0.071$ m/s and the log profile is a suitable approximation (Fig. 1b).

Local conditions such as the presence of large-scale roughness or the existence of large-scale bed forms inflect the velocity distribution near the bed creating an s-profile (profile B). The layer of the flow where the profile is inflected is called the roughness sublayer, corresponding here to $Z_{RL} \lesssim 0.20h$ for profile B. The inflected profile may be approximated by a tangent-hyperbolic (tanh) profile (Katul et al., 2002), which here is defined as:

$$\frac{\bar{u}}{u_o} = \tanh\left(\frac{z - Z_o}{L}\right) + B' \quad (1)$$

The parameterization of the tanh function requires the definition of the reference depth (Z_o) which corresponds to the inflection point in the tanh function, an energetic eddy size (L ; Katul et al., 2002) representing the velocity decay, and a reference velocity (u_o) at the level $z=Z_o$. L represents a characteristic eddy size produced by Kelvin-Helmholtz type instabilities at the interface Z_o . B' defines the translation imposed on the tanh asymptote, i.e. by making $B'=1$, the positive asymptote will converge to the “quasi” constant velocity in the outer layer of the flow (Fig. 1b), whereas the negative asymptote will converge to zero for $z \rightarrow 0$, a no-slip boundary condition. The velocity distribution slope tends to infinity at the origin. Two relations can thus be defined: $\bar{u} = 0 \Rightarrow \frac{z - Z_o}{L} = a \tanh(-1) \Rightarrow Z_o \approx L\pi$ and

$$\bar{u} = u_o \Rightarrow \frac{z - Z_o}{L} = a \tanh(0) \Rightarrow z = Z_o.$$
 L will determine both, the velocity decay, i.e. the function slope at the inflection point, and the position of the inflection point. The definition of the reference velocity for rough riverbeds, when $B'=1$, must respect the validity limits of the function \tanh $0 < \bar{u} < 2u_o$. Equation (1) is parameterized by the following normalized vertical coordinates $Z_o/h=0.19$, $L/h=0.09$ and $u_o=0.30$ m/s ($u_o=u_\infty/2$, being u_∞ the outer layer velocity). The correlation coefficient (r^2) between the data and the adapted \tanh function is 0.99. The geometric parameter L is of the order of magnitude of 1 cm. In profile C, two boundary layers are found in the velocity distribution. After the boulder, the momentum is redistributed throughout the water depth and the velocity inflection is attenuated. The velocity profile reacquires the log shape near the bottom. Yet, the velocity distribution is still conditioned by the upstream bed form, which forms a second logarithmic layer. Similar to the observations by Sanford and Lien (1999), the shear controlling the inner log layer is due to riverbed drag, whereas the outer log layer is sheared by the upstream boulder. The parameterization of both log layers gives shear velocities of $u^*_{inner}=0.043$ m/s and $u^*_{outer}=0.037$ m/s. The shear effect due to the upstream obstacle has the same order of magnitude as the bottom shear.

Fig. 2a shows the mean 2D velocity vector field (\bar{u} and \bar{w}) and the corresponding stream function lines. In the background the spanwise interpolated mean velocity (\bar{v}) is plotted. In the outer layer of the flow, \bar{v} is low compared to \bar{u} . For downstream and upstream positions, \bar{v} is higher in the inner layer indicating that there is a skirting spanwise motion around the bed protuberance. In Fig. 2b the velocity profiles are plotted with the mean interpolated velocity streamwise gradient in the background. There are two high gradient zones: before (negative gradient) and after (positive gradient) the obstacle. This indicates, by continuity considerations, that the low momentum in the inner layers upstream the obstacle might be transferred to the downstream position around the obstacle by the spanwise velocity field. This momentum relocation may be responsible for the inner log layer in profile C.

The mean velocity field along the downstream plane can be divided into three different regions: (1) upstream of the boulder, where vertical convergence of the flow occurs in the outer layers and an increase in the spanwise velocity field in the inner layers takes place permitting the flow to skirt the obstacle; (2) above the boulder, where takes place the separation of the flow due to the protuberance and the formation of a wake shielding the inner layer of the flow, within which recirculation occurs; (3) downstream of the boulder, where redistribution of the momentum throughout the water column and return of the logarithmic configuration near the bed are observed.

The momentum concentrates in the outer layer of profile B (Figs. 2a); in this layer the velocity distribution is approximately 2D and uniform, making it suitable for the adoption of a \tanh -law. After the boulder, the wake line develops smoothly upwards in the downstream direction. Due to the low ratio water depth/riverbed roughness, the water surface in such flows responds to bed forms. From the configuration of the streamlines, and assuming potential flow hypothesis, the water surface shows a wavy pattern roughly in phase with the bottom bed forms. Visual observation and video recordings corroborate these results.

3.2. TURBULENCE DISTRIBUTION AND COHERENT STRUCTURES

Turbulence is also affected by the presence of riverbed obstacles. Two main consequences are the shielding effect in the layer inside the wake where recirculation of the mean flow exists, and coherent structures production due to the Kelvin-Helmholtz type instabilities in the inflection of the s-profile. In profile A, the turbulence distribution corresponds to that expected for open-channel flows (Fig. 3). The maxima of streamwise turbulence intensity ($\overline{u'^2}$) and Reynolds shear stress ($\overline{u'w'}$) occur in the inner layer of the flow where the log profile presents higher shear. In profile B however, the shear stress is positive inside the shielded zone of the flow ($Z_{RL}/h \approx 0.20$). Here, the turbulence levels are substantially lower than the ones observed in profiles A and C, indicating a shield effect. Hence, the wake has two consequences: it shelters the inner layers of the flow where lower turbulence levels are detected; and it introduces a redistribution of the turbulent structures, where the predominant are responsible for positive shear stress. In profile C, a higher turbulence zone is detected around the shear zone present in the second log layer. This lower peak in the turbulence distribution is due to the boulder effect (form-shear). The shear stresses are negative, thus indicating that the coherent structure distribution is similar to the one in the inner log profiles. Low turbulence levels in the inner boundary layer indicate that this layer is created by lateral low-momentum convection around the riverbed boulder.

In view of the results of the turbulence distribution, it is of interest to study the effect of the boulder on coherent structures. Their distribution is analyzed with conditional sampling of instantaneous shear stress events ($\mathcal{E}' = u'w'$), combined with quadrant analysis (Nakagawa and Nezu, 1977). A threshold value (H) to select the instantaneous shear events \mathcal{E}' and the conditionally sampled mean shear stress vector ($\overline{\mathcal{E}'_i}$) in the i -quadrant are defined:

$$H = \frac{\mathcal{E}'}{u'w'} \quad (2)$$

$$\overline{\mathcal{E}'_i} = \frac{N_i}{\sum_{i=1}^4 N_i} \overline{(u'_i \vec{e}_x + w'_i \vec{e}_z)} \quad (3)$$

N_i is the number of events present in quadrant i ; \vec{e}_x and \vec{e}_z are downstream and vertical unitary vectors. $\overline{\mathcal{E}'_i}$ is a time weighted mean vector, accounting for the event amplitude and persistence in time, thus reflecting the available energy in each of the quadrants. Fig. 4 shows the vertical distribution of magnitude ($\overline{|\mathcal{E}'_i|}$) and the angle with the horizontal ($\tan(\alpha'_{e,i}) = \frac{\overline{\mathcal{E}'_i} \cdot \vec{e}_z}{\overline{\mathcal{E}'_i} \cdot \vec{e}_x}$),

conditionally sampled for the threshold limits $H_1=1$ and $H_2=10$ ($H_1 < u'w' < H_2$). The threshold level $H_1=1$ defines events equal to the Reynolds shear stress, and $H_2=10$ corresponds to the asymptote in the statistical distribution.

In profile A, the events in quadrants II and IV (ejections and sweeps) are dominant near the bed as expected from previous studies on open-channel flows (Nezu and Nakagawa, 1993 and Hurther and Lemmin, 2000). The importance of QII and QIV events decreases towards the water surface. In profile B, until about $z/h=0.20$, the positive shear events (QI and QIII) are slightly stronger than the negative ones (QII and QIV), which is consistent with the positive

Reynolds shear stress zones detected in $z/h < 0.20$ (Fig. 3b). Here, the main coherent structures are inward and outward interactions aligned with the wake direction. In profile C, QII and QIV events are again dominant throughout the water depth. At roughly $z/h = 0.30$, in the shear zone situated between both boundary layers, there is a maximum in the $\overline{\varepsilon'_i}$ distribution. The detected structures may be generated by Kelvin-Helmholtz type instabilities present in the transitions between the two boundary layers and in the upstream s-profile. In this case the structures are advected by the mean flow with a downward mean trend. For all three cases, $\overline{\varepsilon'_i}$ vertical component increases until $z/h \approx 0.75$, dropping to zero near the surface (Fig. 4). For profile B, $\overline{\varepsilon'_i}$ is slightly higher, due to the vertical momentum induced by the upward convergence of the flow.

3.4. INTEGRAL SCALES

Since the velocity decay in the s-profile is related to an energetic eddy scale L (Katul et al., 2002), coherent structure integral scales are investigated. For a measuring position, one may define the integral time scale (τ_{int}), representing the time span with an important correlation between instantaneous velocity values; τ_{int} represents a characteristic time scale for larger coherent structures advected with the mean flow and captured by the ADVP instrumentation. One may relate τ_{int} to the streamwise integral spatial scale (L_{int}), assuming Taylor's hypothesis and freezing the time domain with the downstream convective velocity:

$$\tau_{int}(z) = \int_0^{\infty} R_x(z, t) dt \quad (4)$$

$$L_{int}(z) = \overline{u}(z) \cdot \tau_{int}(z) \quad (5)$$

R_x is the autocorrelation function for the time series of the streamwise instantaneous velocity that varies in depth, and t is the time variable. As expected, the integral scales increase in the vertical direction (Fig. 5). Smaller structures are concentrated near the riverbed, where the main dissipation takes place. Larger structures, which are captured near the surface, originate near the bottom, increasing in size as they are conveyed upwards. In profile B and in the outer layer, coherent structures scales tend to be larger than in profiles A and C, which may be explained by streamwise distortion of the structures due to the momentum convergence. Near the bottom however the structure scales from all three profiles drop to the same limit. In the roughness sublayer of profile B, the integral scale varies from 0 to 20 mm, being 8 mm on average. This value is of the same order of magnitude as the geometric parameter L found in the tanh profile parameterization. Thus, L has the physical meaning of a representative energetic eddy size. For $z/h \approx 0.40$, coherent structures tend to be larger in profile C. The influence of the form seems to also affect the detected structure scales above the second boundary layer. ADVP measurements allow visualizing the turbulent structures advected by the mean flow, created at upstream positions (Eulerian observation). Therefore, observations in profile C present the obstacle form effect. When approaching the bottom, ADVP observations increasingly correspond to locally produced turbulence.

4. CONCLUSIONS

A transition in the velocity distribution of the type log-s-2xlog due to a bed perturbation was investigated (Fig. 6). The double boundary layer corresponds to the transition from s to mono-logarithmic profiles. Three different regions of flow related to the presence of a bed obstacle were identified: (1) convergence, (2) separation and (3) redistribution. Each of these regions corresponding to log, s and double log velocity profiles, were analyzed in terms of mean velocity, mean turbulence and coherent structures.

The s-profile may be described by a tanh function, parameterized with a reference velocity u_0 , which is equal to half the constant velocity in the outer “potential layer” and a geometric parameter of the same order of magnitude as the mean size of the larger coherent structures present inside the roughness sublayer ($L \approx \bar{L}_{int}(z < Z_{RL})$). The low momentum inner layers in region (1) are laterally conveyed into the lee of the obstacle by the mean spanwise field, creating the inner log law layer in the downstream profile (region (3)). In region (2) one finds a “quasi” 2D potential flow above the roughness sublayer and the outer boundary layers where a 2D potential flow approximation is possible. The shear zone in the second logarithmic layer (region (3)) is mainly due to the form drag caused by the upstream obstacle. There is turbulence enhancement due to the existence of coherent structures caused by Kelvin-Helmholtz type instability formed along the wake line (Fig. 6). In the wake of the bed protuberance, a recirculation zone is formed where the mean velocities are low; there is a shielding effect and turbulence reaches lower levels. Inside the wake, the outward and inward interactions aligned with the wake delimitation direction are dominant; the Reynolds shear stress in the inner layer of region (2) is positive. The vertical shear components increase with the vertical, and appear to be higher in the s-profile than in the others, eventually due to the vertical momentum component resulting from the upstream convergence of the flow.

An estimate of river flow energy loss is of major importance in river engineering. When double boundary layered or tanh velocity distributions exist, the estimate of the shear velocity based on the classical log-law approach may no longer be valid. A criterion has therefore to be established in terms of D/h (where D defines a geometric parameter and h , the mean water depth) to define when deviations from the log-law are significant in flow resistance calculations. An understanding of shallow flows around an obstacle is of major importance in geophysical fluid mechanics because of their effect on mixing and transport processes. The present results are an explanation of the processes of mass exchanges between upstream (or upwind) and downstream (downwind) positions from obstacles present in the flow field. They describe the same phenomenon common in shallow river flows, atmospheric flow around mountains, buildings etc, and oceanic currents around underwater obstacles.

ACKNOWLEDGEMENTS

The author acknowledges FCT (BD 6727/2001) and SNSF (2000-063818) financial support, U. Lemmin’s supervision and suggestions made by P. Manso and H. de Vriend.

REFERENCES

- Baiamonte G., Giordano G. and Ferro V., 1995. Advances on velocity profile and flow resistance law in gravel bed rivers. *Excerpta*, 9, p. 41.
- Bathurst J.C., 1988. Velocity profile in high-gradient, boulder-bed channels. *Proc. Int. Conf. Fluv. Hydr.*, Budapest.
- Buffin-Bélanger T. and Roy A.G., 1998. Effects of a pebble cluster on the turbulent structure of a depth-limited flow in a gravel-bed river. *Geomorphology*, 25, p. 249.
- Ferro V. and Baiamonte G., 1994. Flow velocity profiles in gravel-bed rivers. *J. Hydr. Eng.*, 120(1), p. 60.
- Franca M.J. and Lemmin U., 2004. A field study of extremely rough, three-dimensional river flow. *Proc. 4th Int. Symp. Env. Hyd. - IAHR*, Hong Kong.
- Franca M.J. and Lemmin U., 2005. Eliminating velocity aliasing in acoustic Doppler velocity profiler data. (submitted for publication *J. Atmosph. Ocean. Technol.*).
- Graf W. and Altinakar M., 1998. *Fluvial Hydraulics*. p. 56, John Wiley & Sons, West Sussex.
- Hurth D. and Lemmin U., 2000. Shear stress statistics and wall similarity analysis in turbulent boundary layers using a high-resolution 3-D ADVP. *IEEE J. Oc. Eng.*, 25(4), p. 446.
- Katul G., Wiberg P., Albertson J. and Hornberger G., 2002. A mixing layer theory for flow resistance in shallow streams. *Water Resour. Res.*, 38(11), p. 1250.
- Marchand J.P., Jarret R.D. and Jones L.L., 1984. Velocity profile, surface slope, and bed material size for selected streams in Colorado. *U.S. Geol. Surv. Open File Rep.*, 84-733.
- Nakagawa H. and Nezu I., 1977. Prediction of the contributions to the Reynolds stress from bursting events in open-channel flows. *J. Fluid Mech.*, 80(1), p. 99.
- Nelson J.M., McLean S.R. and Wolfe S.R., 1993. Mean flow and turbulence fields over two-dimensional bed forms. *Water Resour. Res.*, 29(12), p. 3935.
- Nezu I. and Nakagawa H., 1993. *Turbulence in open-channel flows - IAHR monograph*. p. 177, A.A. Balkema, Rotterdam.
- Nikora V. and Smart G.M., 1997. Turbulence characteristics of New Zealand gravel-bed rivers. *J. Hydr. Eng.*, 123(9), p. 764.
- Rolland T. and Lemmin U., 1997. A two-component acoustic velocity profiler for use in turbulent open-channel flow. *J. Hydr. Res.*, 35(4), p. 545.
- Sanford T.B. and Lien R.C., 1999. Turbulent properties in a homogeneous tidal bottom boundary layer. *J. Geoph. Res.*, 104(C1), p. 1245.
- Wolman M.G., 1954. A method of sampling coarse river-bed material. *Trans. Amer. Geoph. Un.*, 35(6), p. 951.

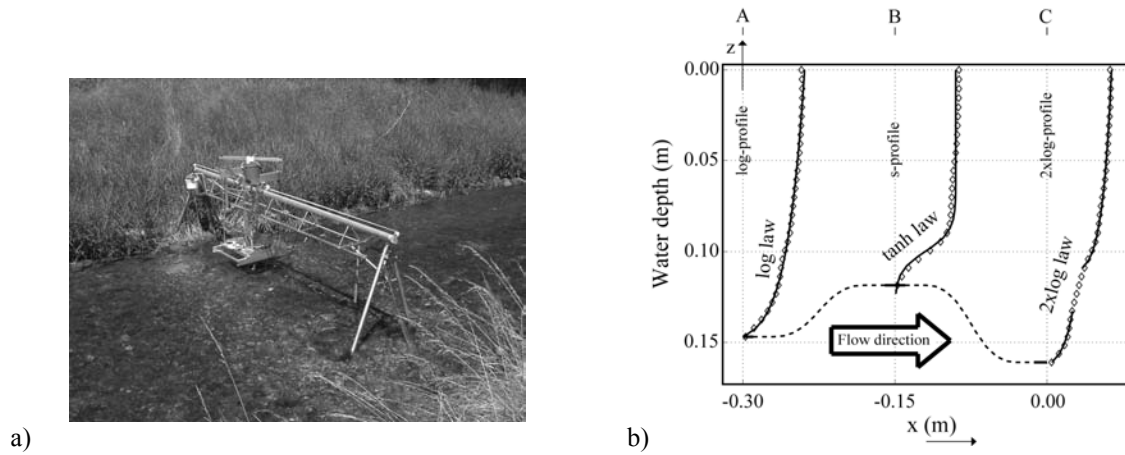


Fig. 1a deployable 3D ADVP system placed for measurements in the river Venoge. 1b streamwise-plane investigated; measured (diamond-shape) and theoretical (continuous lines) mean velocity profiles; Cartesian coordinate convention. The bottom at the measured profiles position is exact; a smoothed step-like bottom was assumed in between (dashed line).

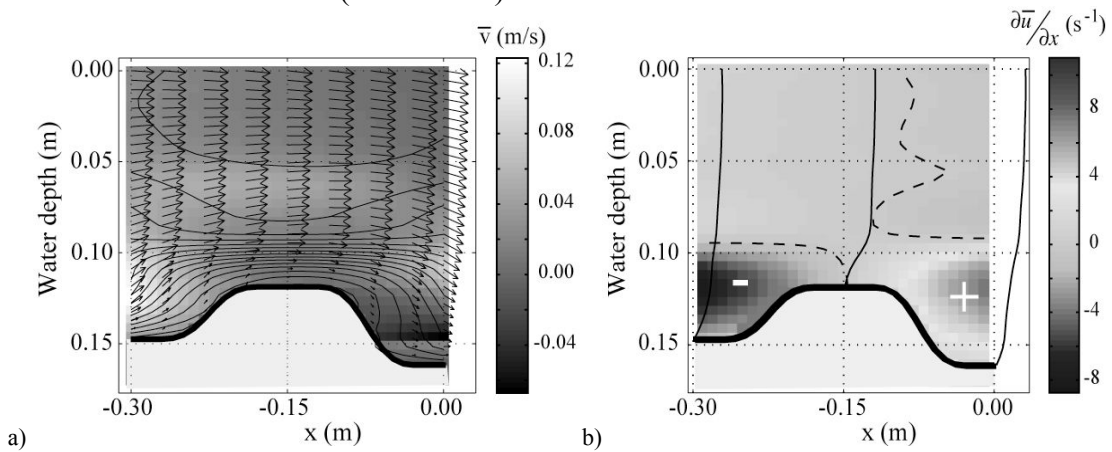


Fig. 2a the vectors represent the mean velocities (vertical velocity is exaggerated 5 times); the contours, the 2D stream lines (x-z); in the background: spanwise mean velocity. 2b the mean velocity profiles are represented for the measured profiles; in the background: the streamwise velocity gradient, whereas dashed contour lines represent the zero limit.

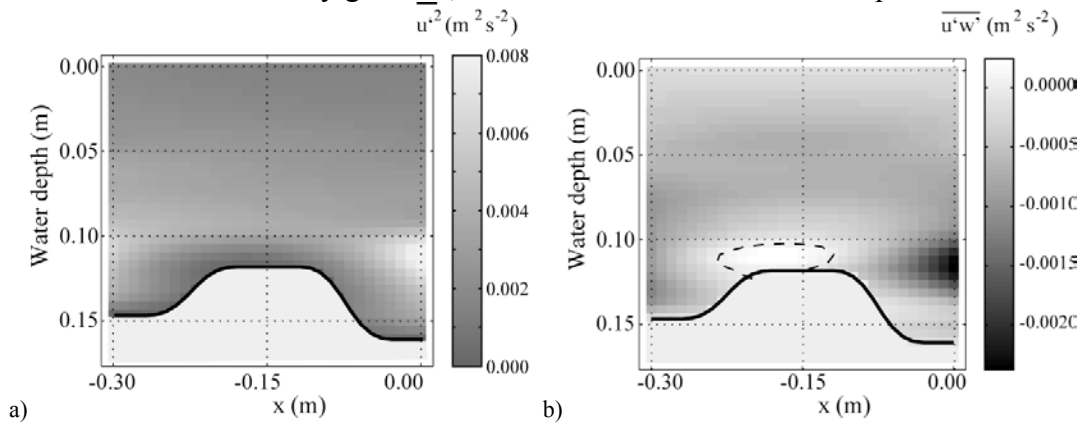


Fig. 3a streamwise turbulence intensity. 3b Reynolds shear stress distribution, whereas dashed contour lines represent the zero limit.

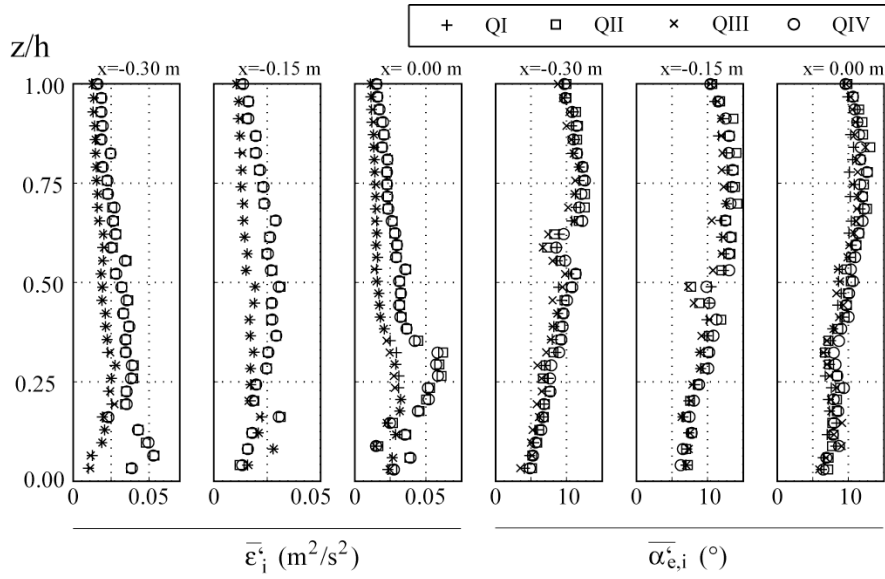


Fig. 4 Vertical distribution of magnitude $\bar{\epsilon}'_i$ and angle $\alpha'_{e,i}$ of the conditionally sampled mean shear stress vectors. Shear stress events were conditionally sampled for $H_1=1$ and $H_2=10$.

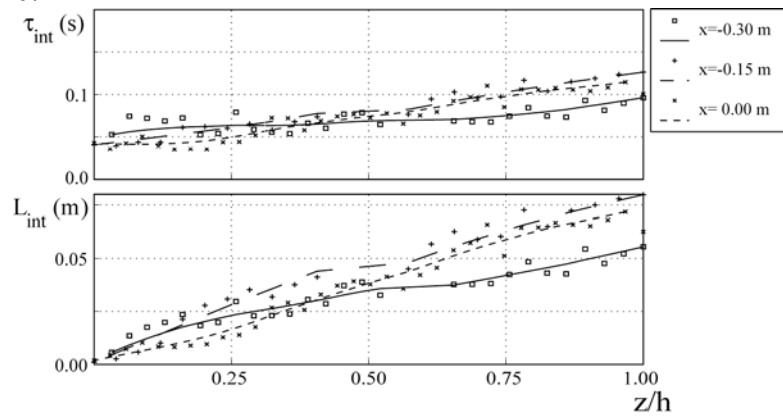


Fig. 5 Vertical distribution of temporal (τ_{int} ; top) and spatial (L_{int} ; bottom) integral scales

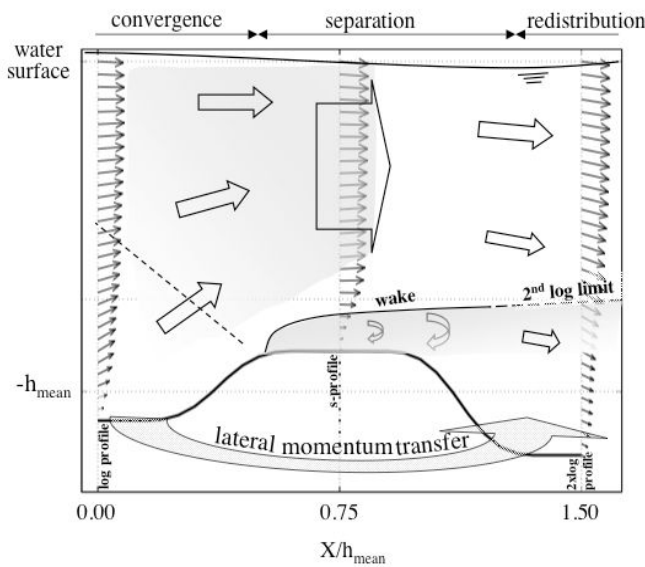


Fig. 6 Interpretation of the investigated flow field.

A.3 CROSS-SECTION PERIODICITY OF TURBULENT GRAVEL-BED RIVER FLOWS

Appendix A.3 was published in the proceedings of the 4th River Coastal and Estuarine Morphodynamics (RCEM), Urbana-Champaign (Illinois-USA), October 2005. The authors are M.J. Franca and U. Lemmin.

The results mainly deal with the 3D character of shallow gravel-bed river flows and focus on the cross-section periodicity of flow features such as bottom shear stress, momentum and low and high velocity regions in the flow outer layer. The Surface Layer Organized Motion (SLOM) is described.

Cross-section periodicity of turbulent gravel-bed river flows

M.J. Franca & U. Lemmin

Laboratory of Environmental Hydraulics (LHE), École Polytechnique Fédérale de Lausanne, Switzerland

ABSTRACT: A 3D wide gravel-bed river flow is investigated using ADVP data from the Swiss river, Chamberonne. The flow aspect ratio was $W/h = 23$, and the relative roughness $D_{84}/h = 0.324$. The flow is mainly 3D near the most important bed forms and near the surface. Bed forms present a wave-like periodic pattern across the section indicating the possible existence of streamwise ridges. All hydraulic characteristics of the flow, such as bed shear, velocity deviations and turbulence production respond to the periodic riverbed morphology. We detected a permanent flow structure in the upper layer of the flow ($z/h > 0.80$), hereinafter called Surface Layer Organized Motion (SLOM), also conditioned by the bed morphology: it consists of periodically distributed low and high velocity regions across the section associated with a mass-compensation secondary motion. This SLOM seems to be an inviscid flow response to the bed forms confined to the layer $z/h > 0.80$ due to a large-scale roughness wake-effect.

1 INTRODUCTION

Wide rivers are generally considered two-dimensional since the bank influence is negligible. However, in the presence of macro bed forms such as boulders and gravel stripes, 2D approaches may no longer be valid and three-dimensionality has to be considered. Recent studies provide some insight into different features of river flow dynamics: mean velocities, turbulence intensities, shear stresses, bed shear, friction velocity, roughness parameters and velocity spectra (Babaeyan-Koopaei et al. 2002); bed-load transport across the river section (Powell et al. 1999); vertical distribution of turbulent energy dissipation and characteristic turbulent scales (Nikora & Smart 1997); turbulence features between weakly mobile and fixed gravel bed cases (Nikora & Goring 2000); coherent structures in rivers and their influence on transport and mixing (Buffin-Bélanger et al. (2000); Hurther et al. (2002)); turbulence in the wake of obstructions (Buffin-Bélanger & Roy 1998); flow structures present in gravel bed rivers (Roy et al. 2004).

Two different regions in the water column have been found to be affected by 3D flow: an inner region, the roughness layer (Nikora & Smart 1997), where wake effects from macro-roughness and skirting effects around the gravel boulders produce deviations from the logarithmic profile (Robert et al. 1992, Nelson et al. 1993, Baiamonte et al. 1995, Buffin-Bélanger & Roy 1998); and an outer region ($z/h > 0.80$) where an organized cellular movement

resulting from a flow response to the bed forms is present. Secondary motion occupying the whole water depth may be associated with a response to the riverbed roughness (Studerus 1982, Nezu & Nakagawa 1993). The hydraulic response to the morphology of the riverbed may be confined to the outer layer of the flow due to a general wake produced by the gravel macro-roughness (Baiamonte & Ferro 1997). This response relates to the occurrence of the so-called d-shaped velocity profiles (Ferro & Baiamonte 1994, Yang et al. 2004). Despite the three-dimensionality of the flow in the lower layers, Nikora & Smart (1997), Smart (1999) and Franca & Lemmin (2004) showed that occasionally the log-law may still be used locally to describe velocity profiles in gravel-bed river flows.

This study is based on field measurements made with the deployable 3D Acoustic Doppler Velocity Profiler (ADVP) in the Swiss river Chamberonne. Several aspects of the flow are assessed: cross-section velocity distribution; influence of bed forms on flow resistance and on velocity distribution; influence of bed morphology on the turbulent flow structure (scales and production).

2 FIELD MEASUREMENTS

3D ADVP field measurements were taken in the Swiss gravel-bed river Chamberonne. They were made on a single day during a low water period, under stationary flow conditions (confirmed by the gauging of

the Swiss Hydrological and Geological Services). The cross-section was at 385 m before the river mouth. The main river characteristics at the time of the measurements are given in Table 1.

S is the mean river slope; Q, the discharge; h, the water depth (corresponding to the deepest profile); W, the river width; Re, the Reynolds number; Fr, the Froude number; D_{50} , D_{50} and D_{84} , the bottom grain size for which 40%, 50% and 84% of the grain diameters are smaller, respectively. The riverbed material was sampled according to the Wolman (1954) technique. The water depth varied between 0.15 and 0.29 cm. Considering the average water depth, the aspect ratio (W/h) is 23, corresponding to shallow water or wide channel. The river slope was determined with topographic data from the Gesrau system (SESA – Canton of Vaud). The riverbed is composed of coarse gravel and randomly spaced macro-roughness producing a rough turbulent flow with no sediment transport during the measurements. The profiles were taken across a section starting from the right riverbank ($y/W = 0$). We assumed symmetrical hydraulic conditions and only measured across half of the river width, taking 24 velocity profiles with a horizontal spacing of 5 to 12.5 cm. Data were acquired during five minutes at each point.

3 INSTRUMENTATION

The 3D Acoustic Doppler Velocity Profiler (ADVP) measures quasi-instantaneous velocity profiles. A detailed description of the ADVP working principle is given in the literature (Rolland & Lemmin 1997). In the present study we used the multistatic configuration of the ADVP: four transducers receive the backscattered signals emitted from one emitter, providing one redundancy in the transformation of the captured Doppler frequency into the three Cartesian velocity components. This redundancy is used for signal noise elimination and for data quality control (Hurther & Lemmin 2000). A Pulse Repetition Frequency (PRF) of 2000 Hz and a Number of Pulse Pairs (NPP) equal to 64 was used resulting in an unfiltered velocity sampling frequency of 31.25 Hz. Even though a low degree of dealiasing was expected in the data, a rectifying algorithm based on the signal time history developed by the authors was applied. A portable metallic structure was used to displace the instrument across the section. The same vertical distance from

Table 1. River Chamberonne flow characteristics.

S (%)	Q (m^3/s)	h (m)	W (m)	Re ($\times 10^4$)	Fr (–)	D_{40} (mm)	D_{50} (mm)	D_{84} (mm)
0.26	0.55	0.29	5.75	4.5–12.3	0.24–0.44	41	49	81

the water surface was maintained during the measurements, and the vibration of the ADVP was minimized by the mounting.

4 BED FORMS

The bed shape is found to be periodic across the section, with a wavelength of about twice the water depth ($\lambda_{b,y} \approx 2h$). This suggests the existence of streamwise sediment stripes which may have formed during higher water periods when the aspect ratio is lower and Prandtl secondary currents of the second kind occur. Flow characteristics during different flood events (provided by SESA – Canton of Vaud) for a cross-section located about 10 m upstream from the measurements are summarized in Table 2.

\bar{U} is the section averaged velocity, and q the unit discharge. The Schoklitsch relation is most appropriate to described bed load conditions in these rivers (Graf & Altinakar 1998), based on the slope S and D_{40} of the bed sediments. Assuming uniform conditions, the critical discharge for incipient sediment motion according to Schoklitsch is given by:

$$q_{cr} = 0.26(s-1)^{5/3} \frac{D_{40}^{3/2}}{S^{7/6}} = 4.8 \text{ m}^2/\text{s} \quad (1)$$

s is the relative density of the sediment particles, here considered equal to 2.6. Given the uncertainty in the empirical formula for the calculation of critical bed load conditions and using the values of unit discharge in Table 2, gravel movement over the riverbed may already occur for low return periods. Second type Prandtl secondary motion (Nezu & Nakagawa 1993) may take place due to the decrease in aspect ratio. Periodic streamwise sediment stripes with a wavelength equivalent to the water depth would appear across the section, generated by lateral sediment transport (Tsujiimoto 1989).

The periodic bed forms detected during the measurements (Fig. 1) might be signatures of streamwise bed stripes, produced during high water periods when

Table 2. Flood event characteristics.

Return period (years)	Q (m^3/s)	h (m)	\bar{U} (m/s)	W/h (–)	q (m^2/s)
2	18.00	0.55	4.52	13.2	2.48
3	20.60	0.59	4.78	12.4	2.82
5	23.35	0.63	4.99	11.8	3.14
10	26.81	0.68	5.24	11.1	3.56
30	30.21	0.72	5.47	10.7	3.93
100	35.00	0.78	5.75	10.0	4.48
300	39.15	0.83	5.97	9.5	4.95

lateral transport conditions by cellular secondary currents are fulfilled. High water events will hence condition the flow characteristics during low water periods.

5 MEAN VELOCITY FIELD

The streamwise velocity distribution in the cross-section is represented by contour lines in Figure 2. In particular near the most important bed forms and in the surface layer ($z/h > 0.80$), strong transversal gradients indicate that the structure of the mean flow is 3-D, making any 2-D approach questionable. The same conclusions were reached in a similar study made in another Swiss river, the Venoge (Franca & Lemmin 2004).

The section-averaged value of the vertical velocity represents 16.5% and the spanwise component 29.1% of the streamwise velocity, respectively. The high spanwise component is mainly orientated towards the right riverbank which corresponds to the outer bank of the river curve and may be explained by the presence of a smooth river bend upstream from the measuring site. No circular cells from Prandtl's secondary flow of the

first kind were observed. This might be due to macro-roughness elements in the riverbed which reorient the flow canceling the vorticity generated by the river curvature.

In Figure 2, the most interesting observation is the periodical occurrence of low velocity regions across the section in the surface layer. In wide channel flows high velocity regions were previously observed near the surface above rougher bed regions (Studerus 1982, Franca & Lemmin 2004). If bed forms mainly determine the roughness, these regions locally compensate the additional bed resistance produced by shallower profiles or those with higher roughness. An increased velocity in the upper layer will compensate for the reduction of the available flow depth. In the present case, however, higher velocity regions are less well developed near the surface ($z/h > 0.80$) compared to the regions of low velocity (Fig. 2). In the following, we call the high and low velocity regions in the upper layer of the flow high velocity cells (CH) and low velocity cells (CL).

Nine CL can be identified which are uniformly and periodically distributed across the section, with a density of about 4 per meter. Due to lateral momentum compensation, weak CH exist adjacent to the CL. Although the CL seem to be distributed independent of the local bed forms, a stronger retarding effect is observed where the water depth is greater and profiles are less rough, corresponding to local minima of k^+ ($k^+ = ku^*/\nu$ is the dimensionless roughness; k is the Nikuradse equivalent roughness, u^* the friction velocity and ν the cinematic viscosity). The periodicity of the CL distribution has a wavelength equal to the water depth ($\lambda_{CL,y} \approx h$). If, however, we consider only the more intense cells this becomes about two times the water depth ($\lambda_{CL+y} \approx 2h$). These two complementary periodicities may occur due to continuity.

CL correspond to a deviation in the velocity profile in the upper layer due to different hydraulic conditions (the so-called velocity dip phenomenon, Yang

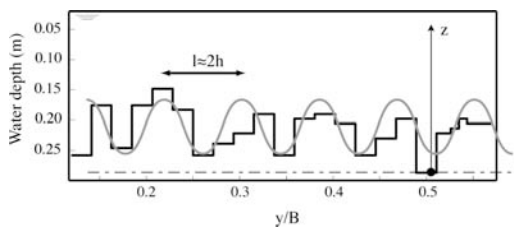


Figure 1. Periodic cross-section variation of the riverbed with hypothetical associated sinusoidal function (gray line) corresponding to an ideal model of the cross-section bed morphology.

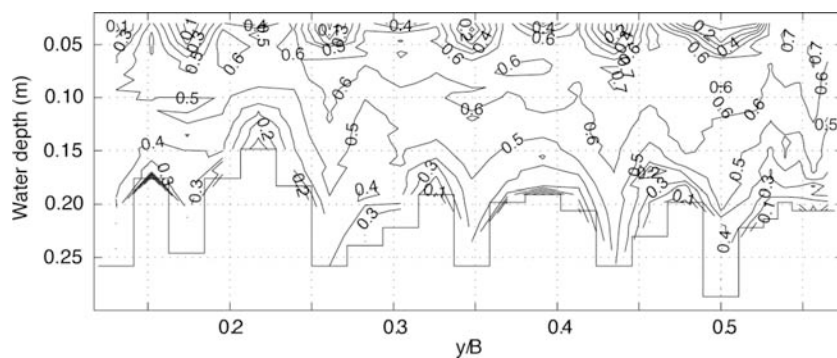


Figure 2. Mean longitudinal velocity field (m/s). The horizontal extent of the measured section is 3.25 m ($y/B = 0.565$). The spanwise and vertical length scales are different.

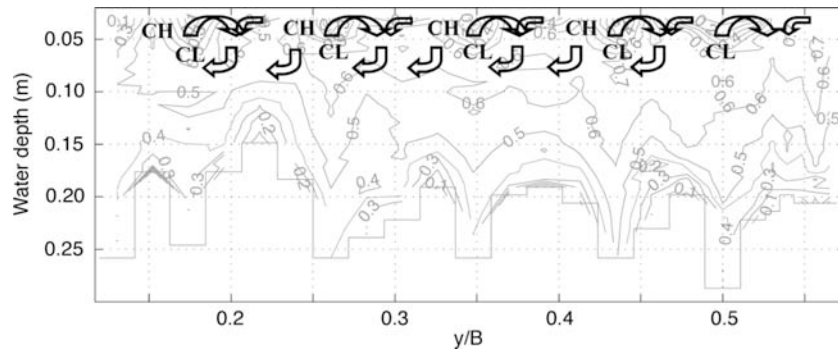


Figure 3. Interpretation of the SLOM (Surface Layer Organized Motion, $z > 0.80 h$) considering all three components of the mean velocity.

et al. (2004)). Velocity profiles with a reduction of the velocity near the surface are known as d-shaped. For mass conservation reasons, the organized co-existence of CH and CL has to be compensated for by secondary motion in the flow (Ferro & Baiamonte 1994).

Eliminating the mean cross-section trend of the time mean vertical and spanwise velocity components (spatial averaging, which corresponds to subtracting the cross-section convective velocity), it is possible to identify a permanent cellular organized structure in the surface layer flow (here called SLOM – Surface Layer Organized Motion), connected to the CL and CH regions suggesting interaction between the three velocity components. An interpretation of this three-dimensional flow is given in Figure 3.

The mechanism involved in the SLOM creates a circulation layer at $z/h > 0.80$ and is described as follows:

- Most of the CL-profiles coincide with an inversion of the vertical mass flux (mainly in the deeper profiles).
- Vertical downward jets coincide with weak CH.
- Lateral mass transfer in the direction of the CH occurs above the CL; this contributes to the CH and to the associated downward jets.
- In the spanwise direction, SLOM cells scale with the water depth (density of 4 cells per meter).
- The lateral mass transfer induces a rotating movement. Clearly symmetrical rotating cells might be found with more accurate measurements under well-controlled laboratory conditions.

As expected in such a rough flow, a boundary layer is formed near the bed around the forms with at least a 2D geometry (Fig. 2). In the roughness sublayer (Nikora & Smart 1997) the flow is highly three-dimensional and deviations from the log-law may occur. These deviations result from a so-called generalized macro-roughness wake and correspond to

s-type profiles (Marchand et al. 1984, Bathurst 1988, Ferro & Baiamonte 1994, Katul et al. 2002, Carravetta & Della Morte 2004 and Franca 2005). Nevertheless, the logarithmic profile still describes reasonably well the velocity distribution in about 65% of the measured profiles up to $z/h < 0.40\bar{u}$. An application of the log-law to the whole cross-section section is difficult due to the high variability of the local parameters. In particular, the local drag conditions vary greatly with the local bed configuration.

6 CROSS-SECTION NIKURADSE ROUGHNESS DISTRIBUTION

The local log-law parameterization (determination of local Nikuradse roughness k and friction velocity u^*) might be used to quantitatively map the roughness across the river section. The logarithmic mean velocity distribution is defined as (Schlichting 1968):

$$\frac{\bar{u}(z)}{u^*} = \frac{1}{\kappa} \ln\left(\frac{z}{k}\right) + A \quad (2)$$

\bar{u} is the time averaged velocity, κ the Von Karman constant (taken as $\kappa = 0.41$), and A is taken as 8.5 for turbulent rough flows (Monin & Yanglom 1971). The friction velocity and Nikuradse roughness were calculated by regressing the velocity against the logarithm of the water depth. Although the application of the log-law and the assumption of the parameter $A = 8.5$ in this flow case may not be without reservation, it may be used to locally approximate the velocity distribution in order to provide an estimate of the respective flow resistance. The majority of the measured profiles corresponds to completely rough bed cases ($k^+ > 70$, Nezu & Nakagawa 1993). The mean k obtained corresponds to D_{84} . Figure 4 shows a plot of the cross-section distribution of the

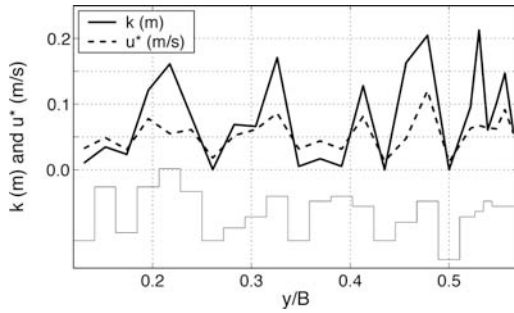


Figure 4. Nikuradse roughness and friction velocity cross-section distribution.

Nikuradse roughness and friction velocity. The riverbed roughness cross-section evolution is found to also have a periodicity, in phase with the bed forms ($\lambda_{k,y} \approx 2h$). This confirms two observations: the flow resistance has a strong form dependence and the cross periodicity of the riverbed is intrinsically related to the flow resistance.

7 FLOW RESPONSE TO THE BOTTOM FORM

A strong dependence of the flow on riverbed morphology was established above. We define a dimensionless variable (the velocity dip, dU) that allows to identify d-type profiles and to evaluate the magnitude of CL, as follows:

$$dU(y) = \frac{\bar{u}_{\max}(y)}{u(y, z = 0.90h)} \quad (3)$$

The level at $z/h = 0.90$ is considered in the middle of the SLOM layer. In Figure 5 we plot the observed velocity dips against the respective local Froude number, defined as:

$$Fr(y) = \frac{U(y)}{\sqrt{gh(y)}} \quad (4)$$

U is the depth-averaged velocity for each profile across the section and g the gravity acceleration. There is clear tendency of a more intense velocity dip for lower local Froude numbers. A limit of around $Fr \approx 0.35$ may be established for the beginning of the occurrence of a significant dip. The local characteristics of the mean flow in the surface layer are thus dependent on the flow regime.

The origin of the d-shaped profiles or CL in this river is not yet clear. Possible reasons for their occurrence are: the presence of stationary breaking surface waves, such as boulder produced waves (ship- and lee-waves) and stationary hydraulic jumps or the inviscid

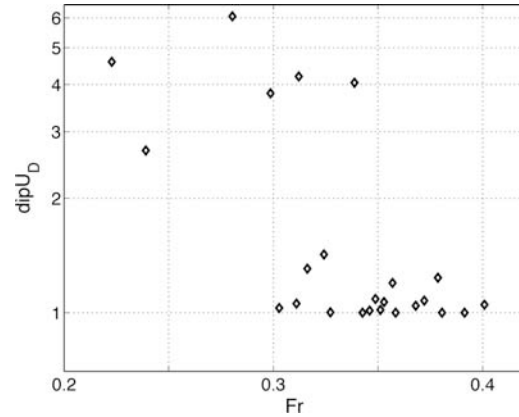


Figure 5. Inviscid response to the bottom shape: relation between the velocity dip (dU ratio) and the Froude number (Fr).

response of the flow to the bed forms (potential flow assumption – barotropic flow). Given the local Froude number dependence, the latter one seems to be the more likely origin.

8 TURBULENCE SCALES

Since the ADVP measurements have sufficient resolution to resolve turbulence scales, a cross section power spectral analysis of the energy distribution has been carried out in order to determine whether periodic bed forms affect the intensity of turbulence. For the calculation of the power spectral density the data was segmented into blocks of 30 s duration. We used the Welch method with 50% overlapping. The results (Fig. 6) are presented for two levels in the water column: ≈ 2 cm from the water surface and ≈ 2 cm from the riverbed. This figure allows to determine the variation of the production plateaus in the spectral domain across the section.

The level of energy in the low frequency production range also varies periodically across the section corresponding to the bed form distribution ($\lambda_{Su,y} \approx 2h$). Depending on the distance to the water surface, two distinct patterns exist: near the surface, the lower production energy levels correspond to the deeper profiles, whereas near the riverbed the opposite occurs. This indicates that bed forms also has a pronounced effect on the generation and the redistribution of turbulence. Close to the riverbed, ADVP observations correspond to locally produced turbulence. It is evident that the redistribution of turbulent energy within the water column is strongly affected by the 3D structure of the flow field. Near the surface, the low energy regions coincide with the larger CL.

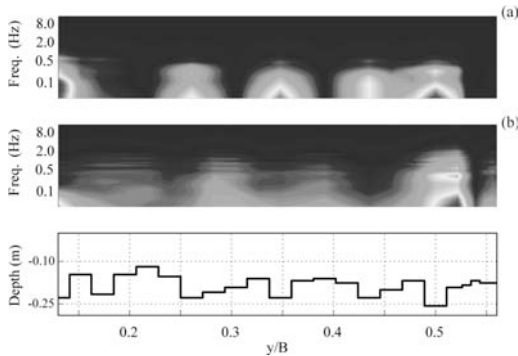


Figure 6. Cross-section variation of the power spectral density ($\text{m}^2/\text{s}^2/\text{Hz}$) of the instantaneous streamwise velocity, as a function of the occurrence frequency, calculated for two levels; (a) ≈ 2 cm from the water surface and (b) ≈ 2 cm from the bottom. Lighter areas indicate higher energy (the plots do not have the same color scale).

9 DISCUSSION

The riverbed morphology presents a periodic character across the section, with a wavelength of two times the water depth ($\lambda_{b,y} \approx 2h$; Fig. 1). Given the flood prediction conditions, the bed forms seem to be signatures of streamwise coarse material stripes which may already be produced during high water events at low return periods.

The measurements show a case of a wide river where two-dimensional open-channel models are no longer valid, due to macro-roughness caused by riverbed forms. A logarithmic form of the velocity profile is occasionally observed near the riverbed. However, a general parameterization of the logarithmic law to the whole cross section becomes impossible, because the studied flow is essentially three-dimensional near the most important bed forms and in the outer layer of the flow (Fig. 2).

The analysis of the three components of the time-averaged velocity indicates a strong dependence of the hydraulic characteristics on the extreme values of the bed morphology. The analysis of the roughness parameters based on the application of the log-law confirmed the roughness dependence on the bed forms (Fig. 4): $\lambda_{k,y} \approx 2h$ and $\lambda_{u^*,y} \approx 2h$. Thus, the flow resistance mainly resulting from bottom drag, presents the same periodic character of the bed forms. Given the relation between friction velocity and shear stress distribution $u^* = u'w'|_{\text{bed}}$, we may conclude that turbulence production across the section is also related to the periodic bed forms.

Figure 7 compares the cross-section variation of several hydraulic characteristics with the bottom variation: dimensionless Nikuradse equivalent roughness (k/D_{84}); local unitary discharge (q/q_{max}), which is

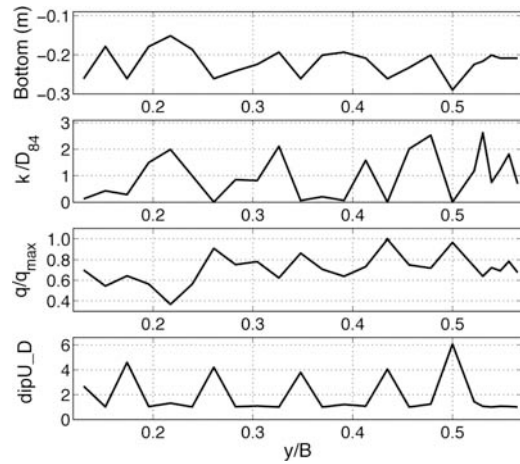


Figure 7. Periodicity of the flow characteristics across the investigated river cross-section.

related to the lateral momentum distribution; and velocity dip as defined above by expression (3). Since the roughness (flow resistance) is in phase with the bottom height variation, the lateral momentum distribution is obviously out of phase with these two, with an expected increasing tendency when moving to the river axis. As indicated above, the bottom shape conditions the occurrence of the d-shaped profiles (associated to the CL cells). The smaller CL regions are visible in Fig. 7 (bottom), situated between the larger CL regions. This reinforces the hypothesis of the origin of the SLOM as an inviscid response of the flow to the riverbed shape.

Based on the observed local Froude number dependence (Fig. 5), we defined the SLOM as an upper layer flow response to bed forms. A low velocity (CL) region in the upper layer of the flow is found to be associated with the periodically spaced deeper profiles ($\lambda_{\text{CL},y} \approx 2h$). Adjacent to these, discrete high-velocity jets (CH) are formed due to a compensatory secondary motion. For continuity reasons, weaker CL occur between two larger ones, reducing the CL periodicity to half the wavelength ($\lambda_{\text{CL},y} \approx h$). As illustrated in Figure 3, the SLOM is thus constituted by alternating large CL/CH and small CL/CH. The turbulent mechanism responsible for the link between the bed forms and the upper layers of the flow is still unknown. Further laboratory work on the turbulence structure of the flow should be done to characterize this interaction.

Based on the observations, in these kinds of macro-rough flows, a general wake is formed by the continuous and superimposed effect of the bed shape/gravel boulders, similar to the wake-interference flow (Baiamonte & Ferro (1997)). An intermediate shielded region of the flow is formed between the roughness

layer as defined by Nikora & Smart (1997) and the SLOM layer, $z/h > 0.80$, similar to the blending layer concept used in atmospheric flows analysis (Wieringa 1976).

10 CONCLUSIONS

From the present field measurements in the river Chamberonne we observed the following main features of the interaction between the bottom profile and the flow characteristics:

- The riverbed cross-section observation highlighted equally spaced roughness elements in the bottom profile with a wavelength of $\lambda_{b,y} \approx 2h$. This indicates the possible existence of streamwise ridges composed of coarse material.
- The structure of the mean flow is essentially 3D near the most important bed forms and in the outer layer of the flow.
- Although the log-law may represent to some extent the velocity distribution in this river, 2D cross-section concepts are not valid and are to be used with caution in shallow gravel-bed flows.
- All river hydraulic characteristics are strongly conditioned by the bed forms, in phase with its periodic cross-section variation, and consequently also the bed-load capacity and transversal momentum distribution.
- We identified a permanent three-dimensional flow structure in the upper layer of the flow ($z/h > 0.80$), the Surface Layer Organized Motion (SLOM), which is strongly conditioned by the bed forms. This motion field consists of periodically distributed low (CL) and high (CH) velocity regions associated with a mass compensation secondary motion. This structured outer layer motion seems to be due to an inviscid response to bed form variations since it is dependent on the local Froude number. A general wake effect might exist due to large-scale roughness, confining this flow response to the layer $z/h = 0.80$.
- The transversal distribution of the turbulence structures is also influenced by the bed morphology. Production intensity changes across the section and changes with water depth depending on the periodic bed shape.

High water events may condition the flow characteristics during low water periods. Bed form changes such as streamwise gravel-stripes which were produced during a high water period, determine the complex 3D flow patterns during shallow water periods.

Mixing is widely present within this flow given the strong shear zones created by the mean flow variability across the river section. Turbulence production is influenced by the existence of shear zones in addition to those resulting from riverbed drag,

thus affecting mixing and transport processes. The SLOM mechanism may have several effects: the creation of a stagnation zone in the upper layers of the flow ($z/\delta > 0.80$) where mass, heat or momentum inputs may be concentrated; promotion of gas transfer through the free surface. Additional studies shall be made to investigate the nature of the permanent structures existing in the layer $z/h > 0.80$ to determine how they might possibly enhance gas transfer between the free surface and the inner flow areas.

The existence of cellular secondary currents in shallow water flows still is an open subject in geophysical fluid mechanics. Thus, 2D concepts are usually considered. We have shown that there are limits to that approach. The bottom roughness height threshold for the onset of 3D flow effects and its influence on mixing and transport processes are not yet well established. Only through further detailed 3D profile measurements as were carried out in this project, progress will be made in understanding and a correct interpretation of the hydraulic processes in such flows.

ACKNOWLEDGEMENTS

The authors acknowledge the financial support of the Swiss National Science Foundation (2000-063818) and the FCT (BD 6727/2001).

REFERENCES

- Babaeyan-Koopaei, K., Ervine, D.A., Carling, P.A. & Cao, Z. 2002. Velocity and turbulence measurements for two overbank flow events in river Severn. *Journal of Hydraulic Engineering* 128(10): 891–900.
- Baiamonte, G. & Ferro, V. 1997. The influence of roughness geometry and Shields parameter on flow resistance in gravel-bed channels. *Earth Surface Processes and Landforms* 22: 759–772.
- Baiamonte, G., Giordano, G. & Ferro, V. 1995. Advances on velocity profile and flow resistance law in gravel bed rivers. *Excerpta* 9: 41–89.
- Bathurst, J.C. 1988. Velocity profile in high-gradient, boulder-bed channels. *Proceedings of the International Conference on Fluvial Hydraulics, Budapest*. 30 May–3 June 1988.
- Buffin-Bélanger, T. & Roy, A.G. 1998. Effects of a pebble cluster on the turbulent structure of a depth-limited flow in a gravel-bed river. *Geomorphology* 25: 249–267.
- Buffin-Bélanger, T., Roy, A.G. & Kirbride, A.D. 2000. On large-scale flow structures in a gravel-bed river. *Geomorphology* 32: 417–435.
- Carravetta, A. & Della Morte, R. 2004. Response of velocity to a sudden change of the bed roughness in sub critical open channel flow. *Proceedings of the Riverflow 2004, Naples*, 23–25 June 2004. Balkema.
- Ferro, V. & Baiamonte, G. 1994. Flow velocity profiles in gravel-bed rivers. *Journal of Hydraulic Engineering* 120(1): 60–80.

- Graf, W.H. & Altinakar, M.S. 1998. *Fluvial Hydraulics*. West Sussex: John Wiley and Sons.
- Franca, M.J. & Lemmin, U. 2004. A field study of extremely rough, three-dimensional river flow. Proceedings of the 4th IAHR International Symposium on Environmental Hydraulics, Hong-Kong, 15–18 December 2004. Balkema.
- Franca, M.J. 2005. Flow dynamics over gravel riverbed. Accepted for the JFK International Student Paper Competition, XXXI IAHR Congress, Seoul.
- Hurther, D., Lemmin, U. & Blanckaert, K. 2002. A field study of transport and mixing in a river using an acoustic Doppler velocity profiler. Proceedings of the Riverflow 2002, Louvain-la-Neuve, 4–6 September 2002. Balkema.
- Katul, G., Wiberg, P., Albertson, J. & Hornberger, G. 2002. A mixing layer theory for flow resistance in shallow streams. *Water Resources Research* 38(11): 1250.
- Marchand, J.P., Jarret, R.D. & Jones, L.L. 1984. Velocity profile, surface slope, and bed material size for selected streams in Colorado. U.S. Geol. Surv. Open File Rep., 84–733.
- Monin, A.S. & Yaglom, A.M. 1971. *Statistical Fluid Mechanics: Mechanics of Turbulence – Vol. 1*. Cambridge (MA): MIT Press.
- Nelson, J.M., McLean, S.R. & Wolfe, S.R. 1993. Mean flow and turbulence fields over two-dimensional bed forms. *Water Resources Research* 29(12): 3935–3953.
- Nezu, I. & Nakagawa, H. 1993. *Turbulence in open-channel flows: IAHR monograph*. Rotterdam: Balkema.
- Nikora, V. & Goring, D. 2000. Flow turbulence over fixed and weakly mobile gravel beds. *Journal of Hydraulic Engineering* 126(9): 679–690.
- Nikora, V. & Smart, G.M. 1997. Turbulence characteristics of New Zealand gravel-bed rivers. *Journal of Hydraulic Engineering* 123(9): 764–773.
- Powell, D.M., Reid, I. & Laronne, J.B. 1999. Hydraulic interpretation of cross-stream variations in bed load transport. *Journal of Hydraulic Engineering* 125(12): 1243–1252.
- Robert, A., Roy, A.G. & De Serres, B. 1992. Changes in velocity profiles at roughness transitions in coarse grained channels. *Sedimentology* 39: 725–735.
- Rolland, T. & Lemmin, U. 1997. A two-component acoustic velocity profiler for use in turbulent open-channel flow. *Journal of Hydraulic Research* 35(4): 545–561.
- Roy, A.G., Buffin-Belanger, T., Lamarre, H. & Kirkbride, A.D. 2004. Size, shape and dynamics of large-scale turbulent flow structures in a gravel-bed river. *Journal of Fluid Mechanics* 500: 1–27.
- Schlichting, H. 1968. *Boundary Layer theory*. New York: McGraw-Hill.
- Smart, G.M. 1999. Turbulent velocity profiles and boundary shear in gravel bed rivers. *Journal of Hydraulic Engineering* 125(2): 106–116.
- Studerus, X. 1982. *Sekundärströmungen im offenen Gerinne über rauhen Längsstreifen*: Ph.D. thesis. Institut für Hydromechanik und Wasserwirtschaft – ETH, Zurich (Switzerland).
- Tsujimoto, T. 1989. Longitudinal stripes of alternate lateral sorting due to cellular secondary currents. Proceedings of the XXIII IAHR Congress, Ottawa, 21–25 August 1989.
- Wieringa, J. 1976. An objective exposure correction method for average wind speeds measured at a shelter location. *Quarterly Journal of the Royal Meteorological Society* 102(431): 241–253.
- Wolman, M.G. 1954. A method of sampling coarse riverbed material. *Transactions American Geophysical Union* 35(6): 951–956.
- Yang, S.Q., Tan, S.K. & Lim, S.Y. 2004. Velocity distribution and Dip-phenomenon in smooth uniform open channel flows. *Journal of Hydraulic Engineering* 130(12): 1179–1186.

A4 ANNEX TO SUBCHAPTER 3.2

This appendix presents speculations on the influence of the instantaneous flow regime and of stationary waves on the mean structure of the flow. The results and discussion are not conclusive. However since they raise important questions in gravel-bed river dynamics, they are included.

1 FROUDE TEMPORAL DISTRIBUTION

The Froude number time distribution was analyzed in order to understand the flow dynamics of each profile across the river sections. The instantaneous Froude number is calculated with the instantaneous average velocity for a whole profile:

$$Fr(y,t) = \frac{\bar{U}(y,t)}{\sqrt{g\delta(y)}} \quad (1)$$

\bar{U} is the vertically averaged velocity. The Froude distributions present a Gaussian shape. In Fig. 1 we represented, for each river, separately the distributions corresponding to profiles where jets occur and where the velocity regions occur (CH and CL regions).

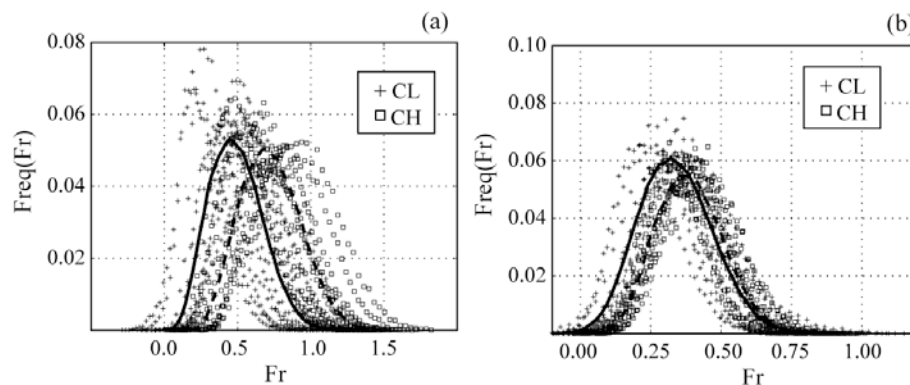


FIGURE 1 – Froude temporal distribution: (a) river Venoge; (b) river Chamberonne. Continuous lines indicate the average Froude distribution of the CL-profiles; dashed lines indicate the average Froude distribution of the CH-profiles.

The distributions corresponding to CH-profiles seem to be located more to the right in the distribution graphics. This is in agreement with the previous results in subchapter 3.2 since they correspond to the shallower profiles. In the Venoge case, the Froude distribution of the CH-profiles includes time where Fr is permanently above 1.0 (supercritical flow), as confirmed by the duration distribution of the supercritical flow (Fig. 2).

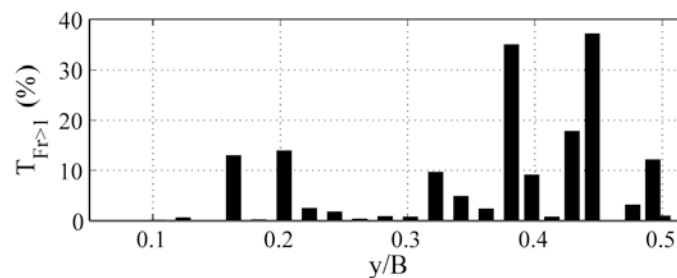


FIGURE 2 – Supercritical Froude duration cross-section distribution of the river Venoge.

There is an intermittent occurrence of supercritical flow in the rougher profiles. This is related to natural oscillations of the instantaneous flow field associated with the local shallow depth of certain profiles that create the conditions for the occurrence of $Fr > 1$. The presence of intermittent supercritical flow implies the existence of intermittent hydraulic jumps in the flow. Surface waves will be important in these kinds of flow, either as free gravity waves or as waves associated with the bottom form (stationary or non-stationary).

2 STATIONARY BREAKING WAVES

Stationary breaking waves (including hydraulic jumps) may explain the occurrence of the reverse flow on top of the D-shaped profiles measured in the river Chamberonne. This structured 2D roll may be due to the presence of a breaking wave such as a hydraulic jump.

In shallow rivers, the response of the flow to bottom irregularities is apparent in the wavy, free surface pattern. Stationary waves are present in these kinds of flows superimposed by free waves travelling upstream and downstream. They may be due to the inviscid response of the flow to the bed forms (potential flow assumption, barotropic-like flow), or a wave train produced by the boulders in the riverbed. These latter might be compared to the effect of ship waves in still water, or the effect of the atmospheric flow over mountains provoking internal waves known as lee waves (Sharman and Wurtele 1983).

The free surface presents an undulated shape where the wavelength is roughly the same as the one corresponding to spanwise periodicity $\lambda = 2\delta$ (visual observation confirms this). The river Chamberonne stationary surface waves are in deepwater, according to Lighthill (1978): $\lambda < 3-5\delta$.

Consider first a potential flow over a riverbed with $\lambda \approx 2\delta$ where the riverbed and the water surface undulation are described by two in-phase sinusoidal functions (barotropic mode). The relation between the riverbed (h) and the water (H) streamwise wave amplitude is (Kundu and Cohen 2002):

$$\frac{h}{H} = e^{-k_w \delta} \quad (2)$$

k_w is the wave number ($k_w = \frac{2\pi}{\lambda}$). Considering $H \approx D_{84}/2 = 40$ mm, and knowing that $k_w = 12.5 \text{ m}^{-1}$, the surface wave amplitude for the river Venoge resulting from a potential flow assumption becomes $h \approx 2$ mm, which underestimates the visual observations ($2h_{\text{obs}} \approx O(1 \text{ cm})$). In analogy to surface gravity waves, these stationary waves have steepness below the maximum for which deep water waves become unstable (USACE 1973): $\frac{2h}{\lambda} = 0.008 \ll 1/7$.

A boulder Froude number (Fr_b), may be proposed similar to the ship wave number defined in ship-wave problems; we assume that a motionless river boulder produces a wave effect similar to the running flow of a ship moving in still water:

$$Fr_b = \frac{U}{\sqrt{gD}} \quad (3)$$

where D represents the length of the obstacle within the river flow. Based on the typical boulder scale $D = \delta$, a low boulder Froude number of $Fr_b = 0.24$ results for the river Chamberonne. In the case of low boulder Froude numbers, longer waves with crests perpendicular to the obstacle prevail. Lighthill (1978) reports that when D is large compared to U^2/g (a low Froude number, which is the case), the dominant wavelength produced by the obstacle is about the maximum possible value of:

$$\lambda_{\max} = 2\pi \frac{U^2}{g} \quad (4)$$

For the Chamberonne we thus have $\lambda_{\max} \approx 9$ cm. Knowing from local observation that the surface wave amplitude is roughly 0.5 cm ($h \approx 5$ mm), we have a wave steepness of 1/9, closer to the theoretical limit of 1/7. These stationary waves are therefore near breaking conditions.

A stationary hydraulic jump may also be responsible for the flow inversion in D-shaped profiles. The riverbed is composed of high elevation (gravel boulders) and low elevation regions. Immediately behind a boulder, the flow will drop causing a hydraulic jump if there is a change in the regime. Since the D-shaped profiles are located in the lower Froude number position, a regime transition (hydraulic jump) after a local drop may exist.

Although the main cause of the D-shaped velocity profiles is not clear, stationary surface waves may play an important role in the flow inversion of those upper layers. A possible superposition of three conditions may be the reason for it, i.e. the inviscid response to the bed form, boulder-induced waves, and the presence of hydraulic jumps.

3 CONCLUSIONS

An analysis of the Froude number distribution showed the importance of waves in these flows. The existence of temporary supercritical flow in some positions across the river indicates that momentary hydraulic jumps exist. This time variation of the flow regime with its associated hydraulic shocks induces stationary or free waves (travelling upstream or downstream), depending on the wavelength.

In the flow, the possibility of stationary breaking waves exists. However it is not possible at this time to establish a relationship with the flow inversion in some of the measured profiles in the river Chamberonne. Three kinds of possible surface waves were considered and a combined effect of these may occur: wavy surface due to potential flow over the bed forms; boulder induced waves; presence of hydraulic jumps due to local regime transitions. These results are speculative and deserve further investigation in the laboratory.

REFERENCES

- Kundu P.K. and Cohen I.M. (2002), Fluid Mechanics, Academic Press, San Diego (USA).
 Lighthill J. (1978), Waves in Fluids, Cambridge University Press, Cambridge (UK).
 Sharman R.D. and Wurtele M.G. (1983), Ship waves and lee waves, J. Atmosph. Sciences, 40, 396-427.
 USACE – U.S. Army Corps of Engineers (1973), Shore Protection Manual, U.S. Army Coastal Eng. Res. Cent., Virginia (USA).

A5 ANNEX TO SUBCHAPTER 3.4

In this appendix it is shown that within the 3D measuring grid used for subchapters 3.4 to 3.8 the flow is overall 2D. The main momentum transport direction is streamwise.

1 MEAN LINEAR-MOMENTUM CONSERVATION

We apply the linear momentum conservation equation in the integral form to the control volume enclosed by the boundaries of the 3D measuring grid used for subchapters 3.4 to 3.8. The linear momentum conservation equation, for a deformable control volume is (Kundu and Cohen 2002):

$$\underbrace{\iiint_{V_c} \frac{\partial(\rho \vec{v})}{\partial t} dV}_I + \underbrace{\iint_{S_c} \rho(\vec{v} \cdot \vec{n}) \vec{v} dS}_{II} = \underbrace{\sum_{III} \vec{F}_e}_{III} \quad (1)$$

Term I represents the local momentum variation, term II, the convective momentum variation and term III, the sum of the external forces acting on the control volume, including the hydrostatic pressure forces and the bottom shear resistance. The measurements were made under steady state conditions. Thus the local momentum variation (term I) is zero. The free surface variations are considered negligible and no vertical momentum flux exists. Thus, equation (1) reduces to the following 2D form:

$$\iint_{S_1} \rho(\vec{v}_{1,x}(y,z) \cdot \vec{n}_1) \vec{v}_{1,x}(y,z) dS + \iint_{S_2} \rho(\vec{v}_{2,x}(y,z) \cdot \vec{n}_2) \vec{v}_{2,x}(y,z) dS = \Delta \Pi_x + \tau_{b,x} \Delta x \Delta B \quad (2)$$

$$\iint_{S_3} \rho(\vec{v}_{3,y}(x,z) \cdot \vec{n}_3) \vec{v}_{3,y}(x,z) dS + \iint_{S_4} \rho(\vec{v}_{4,y}(x,z) \cdot \vec{n}_4) \vec{v}_{4,y}(x,z) dS = \Delta \Pi_y + \tau_{b,y} \Delta B \Delta x \quad (3)$$

$\vec{v}_{j,i}$ is the velocity vector where j indicates the control surface and i the Cartesian direction; \vec{n}_j , the unitary vector normal to the control surface; Π , the hydrostatic pressure force; $\tau_{b,i}$, the bottom shear tension; Δx and ΔB the streamwise and spanwise dimensions of the control volume. Since Δx and ΔB are very small, we may assume quasi-uniform conditions. Thus the pressure terms are equal and the pressure gradient becomes zero ($\Delta \Pi_i = 0$). The control surfaces are defined as: 1 upstream; 2 downstream; 3 facing the right riverbank; and 4 facing the left riverbank. The friction velocity is defined as a function of the bottom shear stress. Table 1 shows the results for the different terms of equations (2) and (3), and the corresponding friction velocity calculation.

Table 3 – Results of the application of the momentum conservation equation to the data; calculation of the bottom shear and the friction velocity.

Streamwise direction			
$\iint_{S_1} \rho(\vec{v}_{1,x}(y,z) \cdot \vec{n}_1) \vec{v}_{1,x}(y,z) dS$	$\iint_{S_2} \rho(\vec{v}_{2,x}(y,z) \cdot \vec{n}_2) \vec{v}_{2,x}(y,z) dS$	$\tau_{b,x}$	u^*_x
(N)	(N)	(N/m ²)	(m/s)
-15.965	17.051	8.832	0.094
Spanwise direction			
$\iint_{S_3} \rho(\vec{v}_{3,y}(x,z) \cdot \vec{n}_3) \vec{v}_{3,y}(x,z) dS$	$\iint_{S_4} \rho(\vec{v}_{4,y}(x,z) \cdot \vec{n}_4) \vec{v}_{4,y}(x,z) dS$	$\tau_{b,y}$	u^*_y
(N)	(N)	(N/m ²)	(m/s)
-0.029	0.053	0.202	0.014

Water fluxes through upstream and downstream boundaries (1 and 2) are: 0.031 and $0.030 \text{ m}^3\text{s}^{-1}$, respectively. The lateral water flux is small, 0.0008 and $0.001 \text{ m}^3\text{s}^{-1}$, for boundaries 3 and 4 respectively. These differences are reflected in the momentum balance and in the value of the bottom resistance to the flow. The streamwise friction velocity result is overestimated when compared to the results in subchapter 3.4.

2 CONCLUSIONS

Given the momentum fluxes through the four control surfaces, within the measuring grid the momentum main transport direction is streamwise and the flow is 2D.

Compared with the results in subchapter 3.4, u^* is overestimated. This may be due to the simplifications introduced by the uniform flow assumption. The reaction to the bed forms is observed throughout the flow and locally imposes important variations in the water surface.

REFERENCES

Kundu P.K. and Cohen I.M. (2002), Fluid Mechanics, Academic Press, San Diego (USA).

A6 CURRICULUM VITAE

Curriculum Vitae

Name:	Mário Jorge Rodrigues Pereira da Franca	Date of birth:	22 nd January 1975
Nationality:	Portuguese	Civil status:	Married
Address:	LHE-ENAC-EPFL, St. 18 1015 – Lausanne, Switzerland	Phone:	+ 41 21 693 23 86
		E-mail:	mario.franca@epfl.ch

DEGREES

- 2005: Ph.D. dissertation entitled "A field study of turbulent shallow flows in gravel-bed rivers", École Polytechnique Fédérale de Lausanne
- 2002: *Post-grad* in Hydraulics and Water Resources, Instituto Superior Técnico - Technical University of Lisbon
- 2001: Member of the *Portuguese Chamber of Engineers*, Civil Engineering College (n. 39102)
- 1998: *Civil Engineering Degree*, Instituto Superior Técnico - Technical University of Lisbon (final classification 16/20)

PROFESSIONAL AND TEACHING ACTIVITY

- 2002 to 2005: PhD student at the Laboratoire d'Hydraulique Environnementale, École Polytechnique Fédérale de Lausanne.
- 2002 to 2005: teaching assistant of Mécanique des Fluides, ENAC - École Polytechnique Fédérale de Lausanne.
- January 2005: guest researcher at the Institute of Geophysics of the Polish Academy of Sciences (Warsaw); collaboration with Włodzimierz Czernuszenko.
- 2003: computational model "RoDaB" for the simulation of breaching conditions on embankment dams.
- 2001 to 2002: research assistant at Instituto Superior Técnico (Lisbon) to pursue the post-grad thesis entitled "Characterization and numerical and experimental modelling of rockfill dam breaking caused by overtopping", under the supervision of António Betâmio de Almeida.
- 1998 to 2002: consultant in the hydraulic and water resources fields.
- 2000: teaching assistant of Hydraulics II, Civil Engineering Department - Instituto Superior Técnico (Lisbon).
- 1998 to 2001: PROCESL – Hydraulic and Environmental Engineering (Algés-Portugal).
- 1998: diploma work with the title: "One and two-dimensional effects of floods on river morphology: a SOBEK model for river Waal; 2D effects of channel narrowing", under the supervision of Huib de Vriend, Technische Universiteit Delft – The Netherlands (classification 8/10).

PUBLICATIONS

- Franca M.J. and Lemmin U., Eliminating velocity aliasing in acoustic Doppler velocity profiler data, *Measurements and Science Technology*, in press.
- Franca M.J. and Lemmin U., Cross-section periodicity of turbulent gravel-bed river flows, *Proc. 4th RCEM - River Coastal and Estuarine Morphodynamics*, Urbana-Champaign, October 2005.
- Franca, M.J., Flow dynamics over a gravel riverbed, *Proc. XXXI IAHR Congress (JFK student paper competition)*, Seoul, September 2005.
- Franca M.J. and Almeida A.B., Discussion of the paper "Modeling of washout of dams" from A. Rozov, *Journal of Hydraulic Research*, Vol. 43 (4), 2005, pp. 439-444.
- Franca M.J. and Lemmin U., A field study of extremely rough, three-dimensional river flow, *Proc. 4th International Symposium Environmental Hydraulics - IAHR*, Hong Kong, December 2004.
- Franca M.J., Braunschweig F. and Almeida A.B., RoDaB: dam breaching model with different breach simulation methodologies, *Proc. Stability and Breaching of Embankment Dams International Seminar*, Oslo, October 2004.
- Franca M.J. and Almeida A.B., Abordagem analítica do fenómeno de ruptura de barragens: determinação do caudal máximo e classificação de albufeiras, *Actas do XXI Congresso Latinoamericano Hidráulica*, Campinas – São Paulo, October 2004 (in Portuguese).

- Franca M.J., Braunschweig F. and Almeida A.B., RoDaB: a user-friendly computational model of dam breaching, *poster presentation at the International Conference Hydraulic of Dams and River Structures*, Teheran, April 2004.
- Franca M.J. and Almeida A.B., A computational model of rockfill dam breaching caused by overtopping (RoDaB), *Journal of Hydraulic Research*, Vol. 42 (2), 2004, pp. 197-206.
- Franca M.J., Braunschweig F. and Almeida A.B., RoDaB: um novo modelo de ruptura de barragens baseado em resultados experimentais, *Actas do 7º Congresso da Agua*, Lisbon, March 2004 (in Portuguese).
- Franca M.J. and Almeida A.B., Experimental tests on rockfill dam breaching process, *Proc. IAHR International Symposium on Hydraulic and Hydrological Aspects of Reliability and Safety Assessment of Hydraulic Structures*, St. Petersburg, May 2002.

AWARDS

- 3rd Prize JFK 2005 Student Paper Competition, International Association of Hydraulic Engineering and Research, Seoul.

COURSES FOLLOWED

- "WATSAN - Water and sanitation engineering from emergency towards development": Centre of Hydrogeology of the University of Neuchâtel (CHYN), International Committee of the Red Cross (ICRC - Wathab Service) and Graduate Institute of Development Studies (IUED), Neuchâtel, October 2005.
- "Mass transport and dispersion in rivers" by G.H. Jirka and W. Uijtewaal: Master Classes of the Riverflow 2004 (IAHR) – Naples, June 2004.
- "LabVIEW Basics 2": École Polytechnique Fédérale de Lausanne/National Instruments, Lausanne, May 2003.
- "Hydraulique Environnementale" by Ulrich Lemmin: ENAC - École Polytechnique Fédérale de Lausanne, July 2002.
- "Instabilité et Turbulence" by Emmanuel Leriche: STI - École Polytechnique Fédérale de Lausanne, July 2002.
- "Fluvial Processes" by M. Selim Yalin: Laboratoire d'Hydraulique Environnementale – École Polytechnique Fédérale de Lausanne, July 2002.
- "Application-oriented introduction to Digital Signal Processing" by Jean-Marc Vesin: Laboratoire d'Hydraulique Environnementale – École Polytechnique Fédérale de Lausanne, May 2002.
- "Research and recent advances in Dam Hydraulics": Fundec – Instituto Superior Técnico (Lisbon), November 2000.
- "Fluvial Hydraulics Course" by W. Graf and M. Altinakar: International Association for Hydraulic Research and Laboratoires de Recherches Hydrauliques – École Polytechnique Fédérale de Lausanne, July 2000.

LANGUAGES

- Portuguese: mother tongue
- English: fluent
- French: fluent
- Castellan: basics

DIVERSE

- Programming languages: Fortran 77 and 90, MatLab, LabView.
- Member of the Portuguese Water Resources Association since 1996.
- Member of the International Association of Hydraulic Engineering and Research since February 2004.
- Co-founder of the local NGO with environmental concerns: Real 21 (<http://www.real21.org>)
- Hobbies: music; photography; literature; painting; rowing; tennis; nature; travel.

December 2005